

Journal of
Mechanics of
Materials and Structures

Special issue

***Tenth Pan American Congress of Applied
Mechanics (PACAM X)***

Volume 4, N° 5

May 2009

 ***mathematical sciences publishers***

JOURNAL OF MECHANICS OF MATERIALS AND STRUCTURES

<http://www.jomms.org>

Founded by Charles R. Steele and Marie-Louise Steele

EDITORS

CHARLES R. STEELE Stanford University, U.S.A.
DAVIDE BIGONI University of Trento, Italy
IWONA JASIUK University of Illinois at Urbana-Champaign, U.S.A.
YASUhide SHINDO Tohoku University, Japan

EDITORIAL BOARD

H. D. BUI École Polytechnique, France
J. P. CARTER University of Sydney, Australia
R. M. CHRISTENSEN Stanford University, U.S.A.
G. M. L. GLADWELL University of Waterloo, Canada
D. H. HODGES Georgia Institute of Technology, U.S.A.
J. HUTCHINSON Harvard University, U.S.A.
C. HWU National Cheng Kung University, R.O. China
B. L. KARIHALOO University of Wales, U.K.
Y. Y. KIM Seoul National University, Republic of Korea
Z. MROZ Academy of Science, Poland
D. PAMPLONA Universidade Católica do Rio de Janeiro, Brazil
M. B. RUBIN Technion, Haifa, Israel
A. N. SHUPIKOV Ukrainian Academy of Sciences, Ukraine
T. TARNAI University Budapest, Hungary
F. Y. M. WAN University of California, Irvine, U.S.A.
P. WRIGGERS Universität Hannover, Germany
W. YANG Tsinghua University, P.R. China
F. ZIEGLER Technische Universität Wien, Austria

PRODUCTION


PAULO NEY DE SOUZA Production Manager
SHEILA NEWBERY Senior Production Editor
SILVIO LEVY Scientific Editor

See inside back cover or <http://www.jomms.org> for submission guidelines.

Regular subscription rate: \$600 a year (print and electronic); \$460 a year (electronic only).

Subscriptions, requests for back issues, and changes of address should be sent to contact@mathscipub.org or to Mathematical Sciences Publishers, 798 Evans Hall, Department of Mathematics, University of California, Berkeley, CA 94720-3840.

©Copyright 2009. Journal of Mechanics of Materials and Structures. All rights reserved.

 mathematical sciences publishers

PREFACE

The Tenth Pan American Congress of Applied Mechanics (PACAM X) was held January 7–11, 2008 in Cancún, Mexico. Its aim, like that of its predecessors, was to promote progress in the broad field of mechanics, including composite materials, computational mechanics, controls, dynamics, fluid mechanics, sensors and monitoring, and solid and structural mechanics. Previous meetings have been held in Rio de Janeiro, Brazil (1989), Valparaiso, Chile (1991), São Paulo, Brazil (1993), Buenos Aires, Argentina (1995), San Juan, Puerto Rico (1997), Rio de Janeiro, Brazil (1999), Temuco, Chile (2002), Havana, Cuba (2004), and Mérida, Mexico (2006). This Tenth PACAM, like the previous gatherings, remains the only conference sponsored by the American Academy of Mechanics (AAM).

PACAM X lived up to its goal of exposing engineers, scientists, and advanced graduate students to new research methods, developments, problems, and potential collaborative opportunities in all the areas mentioned, and provided broad opportunities for personal interactions through means of formal presentations and informal conversations. Participation was not limited to researchers in North, Central and South America; in fact, the PACAM conferences enable individuals to engage with scholars from all over the world during a time when there are few other competing conferences.

A sincere acknowledgment is extended to the National Science Foundation (NSF) for their support of this conference and specifically to Ken Chong at NSF for helping to support several participants and to AAM. Approximately 110 international participants were able to enjoy a very productive gathering in Cancún. The gathering was held at the beautiful Grand Oasis Resort.

Following PACAM X, authors of selected talks were asked to submit extended full-length papers related to their presentation at the conference. The selected papers were then subjected to the normal, peer-review process, and the papers of the best quality were included in this special issue of the *Journal of Mechanics of Materials and Structures*. I thank the Editor-in-Chief and Associate Editor of JoMMS, Charles and Marie-Louise Steele, for the great opportunity to organize this special issue; the individual authors for their excellent contributions; and the anonymous reviewers who put forth a fantastic and detailed effort in helping to choose the best papers for this special issue.

Lastly, in this anxious time for my family, I wish to thank from the bottom of my heart my parents, Constantine and Sofia Attard, for their unwavering support of my career and aspirations in life. Without their unconditional love, nothing in my world would have been possible. Σ'αγαπώ, μπαμπά.

September 2009

THOMAS ATTARD: tattard@utk.edu

Department of Civil and Environmental Engineering, The University of Tennessee, 113 Perkins Hall,
Knoxville, TN 37996-2010, United States

FRACTAL ELEMENTS

SAMER ADEEB AND MARCELO EPSTEIN

Self-similar fractals are geometrically stable in the sense that, when generated by a recursive copying process that starts from a basic building block, their final image depends only on the recursive generation process rather than on the shape of the original building block. In this article we show that an analogous stability property can also be applied to fractals as elastic structural elements and used in practice to obtain the stiffnesses of these fractals by means of a rapidly converging numerical procedure. The relative stiffness coefficients in the limit depend on the generation process rather than on their counterparts in the starting unit. The stiffness matrices of the Koch curve, the Sierpiński triangle, and a two-dimensional generalization of the Cantor set are derived and shown to abide by the aforementioned principle.

1. Introduction

It has been pointed out that many natural structures have a fractal-like composition. These structures are subject to different kinds of loading. Trabecular bones, for instance, which are shown to possess a fractal-like structure [Parkinson and Fazzalari 2000], are responsible for load bearing in vertebrates. Collagen fibers, a major constituent of ligaments and cartilage, are responsible for carrying tensile forces in those structures. The fibers themselves have the self similar fractal like composition; they are, in fact, bundles of fibrils, which in turn are bundles of subfibrils. The subfibrils, under an electron microscope, are seen to be bundles of microfibrils which are bundles of tropocollagen [Frank and Shrive 1999]. The venous and arterial systems within an organism can also be seen as self similar fractals [Peitgen et al. 2004]. While most of the studies focusing on fractals discuss the shape and image properties of fractals [Dyson 1978; Avnir et al. 1998], those studies fail to analyze their structural properties: how fractals would behave under loading and how their behavior is affected by their fractal properties. There are some attempts to analytically determine the deformation of fractals under load [Capitanelli and Lancia 2002; Carpinteri et al. 2001; 2004; Carpinteri and Cornetti 2002; Epstein and Śniatyscki 2006] however, those attempts are based on advanced mathematical techniques beyond the scope of structural analysis.

The generation of a fractal image is geometrically stable as the final image of a fractal is independent of the shape of the initial unit of generation. In the case of the Sierpiński gasket (often called the Sierpiński triangle), for example, the shape of the fractal is recognized after a few iterations of the generation process even if the initial generator is not a triangle. In this paper we report that an analogous behavior is observed in the structural form of the stiffness matrix of an elastic fractal-like structure. The final form of the stiffness matrix is, in a certain sense, independent of the stiffness properties of the unit of generation. We also show that this final form can be obtained by applying the principle of structural self-similarity defined previously in [Epstein and Adeeb 2008].

Keywords: fractals, finite element analysis, stiffness matrix, Koch curve, Sierpiński triangle, Cantor set.

2. Generic stiffness matrices

A *structural element* is a load-carrying solid that can be connected to other elements at a finite number of sites only. At these potential connection points (called *nodes* or *joints*) one or more degrees of freedom (DOFs)—generally translations and/or rotations—are singled out. It is in correspondence with these DOFs that forces and/or couples may be applied to the structural element either directly or via the reactions arising from other elements or structural supports. The ordered set of the DOFs of a structural element can be conceived as a vector \mathbf{U} , called the vector of (element) DOFs. In the theory of linear infinitesimal elasticity, to which we confine our analysis, the *elastic energy* W stored within an element is given by the quadratic form

$$W = \frac{1}{2} \mathbf{U}^t \mathbf{K} \mathbf{U},$$

where \mathbf{K} is a symmetric positive-definite matrix. The physical meaning of the entry k_{ij} of the *stiffness matrix* \mathbf{K} is as follows. Assuming that all the DOFs have been constrained by means of appropriate supports (one support per DOF), this entry represents the reaction in correspondence with the support number i due to a unit displacement of the support number j . The terms *stiffness matrix* and *stiffness coefficient* allude precisely to this physical interpretation.

A necessary condition for a solid to qualify as a structural element is that the stiffness coefficients be bounded in absolute value. Although beyond this limitation and the symmetry of the stiffness matrix (which is a direct consequence of the conservation of energy) it appears that the stiffness coefficients could be arbitrary, it is not difficult to see that this is not the case. Indeed, the elements of each column of the stiffness matrix, corresponding as they do to the complete set of reactions of a structure under no external loads, must constitute a system of forces in equilibrium. Beyond the algebraic conditions resulting from this fact, a structural element may enjoy geometric and material symmetry properties, which may result in further restrictions. The purpose of the remainder of this section is to derive the general reduced forms of the stiffness matrices of a few structural elements taking all these conditions into consideration.

2.1. The stiffness matrix of an equilateral triangle. Our first example consists of an equilateral triangle confined to deform in its plane. The nodes are identified with the vertices of the triangle and the DOFs consist of the components of the nodal displacements of these nodes. These components may be expressed either in terms of a global coordinate system, as shown in [Figure 1](#), right, or in terms of conveniently chosen local directions, as illustrated in the left half of the same figure. The internal constitution of the element is not specified at this point, but it will be assumed that the material properties enjoy at least the same symmetries as the geometry.

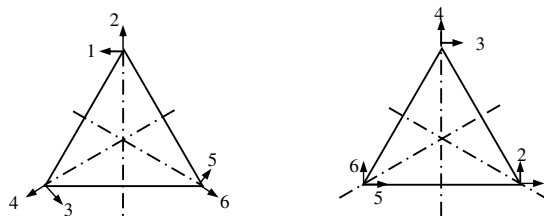


Figure 1. The equilateral triangular element, with local coordinates (left) and global ones (right).

To distinguish between the two options for the DOFs shown in Figure 1, we will denote the corresponding 6×6 stiffness matrices by $\hat{\mathbf{K}}^T$ and \mathbf{K}^T , respectively. (The superscript indicates a triangle and should not be confused with the matrix transposition symbol tr.) By the symmetry of the stiffness matrix, each of these matrices has at most 21 independent coefficients. To implement the extra conditions due to geometric and material symmetry, it is convenient to use the DOFs shown in Figure 1, left. Indeed, it is not difficult to see that in terms of these DOFs the following conditions must hold (assuming that the three axes of geometric symmetry are axes of material symmetry as well):

$$\begin{aligned} \hat{k}_{11}^T = \hat{k}_{33}^T = \hat{k}_{55}^T = A^T, & \quad \hat{k}_{22}^T = \hat{k}_{44}^T = \hat{k}_{66}^T = B^T, & \quad \hat{k}_{12}^T = \hat{k}_{34}^T = \hat{k}_{56}^T = 0, \\ \hat{k}_{13}^T = \hat{k}_{35}^T = \hat{k}_{51}^T = C^T, & \quad \hat{k}_{14}^T = \hat{k}_{36}^T = \hat{k}_{52}^T = D^T, & \quad \hat{k}_{23}^T = \hat{k}_{45}^T = \hat{k}_{61}^T = E^T, \\ & \quad \hat{k}_{24}^T = \hat{k}_{46}^T = \hat{k}_{62}^T = F^T. \end{aligned} \tag{2-1}$$

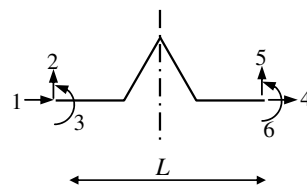
Thus, due to geometrical and material symmetries, the total number of independent entries has been reduced to just 6, indicated by the constants appearing on the right-hand sides of (2-1). Moreover, the equilibrium conditions between the entries of each column (j , say) of the stiffness matrix dictate that the following conditions must hold:

$$\begin{aligned} \hat{k}_{1j}^T - \frac{1}{2}(\hat{k}_{3j}^T + \hat{k}_{5j}^T) + \sqrt{3}\frac{1}{2}(\hat{k}_{4j}^T - \hat{k}_{6j}^T) &= 0, \\ \hat{k}_{2j}^T - \frac{1}{2}(\hat{k}_{4j}^T + \hat{k}_{6j}^T) - \sqrt{3}\frac{1}{2}(\hat{k}_{3j}^T - \hat{k}_{5j}^T) &= 0, \\ \hat{k}_{1j}^T + \hat{k}_{3j}^T + \hat{k}_{5j}^T &= 0. \end{aligned} \tag{2-2}$$

Using (2-2), four of the six coefficients appearing in (2-1) can be written in terms of the other two, say A^t and B^t . The final reduced stiffness matrix with respect to the global DOFs (Figure 1, right) has the form

$$\mathbf{K}^T = \begin{pmatrix} \frac{A^T+3B^T}{4} & \frac{\sqrt{3}(A^T-B^T)}{4} & -\frac{A^T}{2} & \frac{\sqrt{3}(B^T-2A^T)}{2} & \frac{A^T-3B^T}{4} & \frac{\sqrt{3}(3A^T-B^T)}{4} \\ & \frac{3A^T+B^T}{4} & \frac{\sqrt{3}A^T}{2} & -\frac{B^T}{2} & \frac{\sqrt{3}(B^T-3A^T)}{4} & \frac{B^T-3A^T}{4} \\ & & A^T & 0 & -\frac{A^T}{2} & -\frac{\sqrt{3}A^T}{2} \\ & & & B & \frac{\sqrt{3}(2A^T-B^T)}{2} & -\frac{B^T}{2} \\ \text{Symmetric} & & & & \frac{A^T+3B^T}{4} & \frac{\sqrt{3}(B^T-A^T)}{4} \\ & & & & & \frac{3A^T+B^T}{4} \end{pmatrix}. \tag{2-3}$$

2.2. The stiffness matrix of a beam. The diagram on the right shows a beam element with one axis of (geometric and material) symmetry. To take into consideration bending effects, each node is assigned an extra rotational DOF. Thus, the stiffness matrix of the beam element has a hybrid mixture of coefficients of forces and moments per unit displacements and per unit rotations. Consequently, the length L of the beam



plays a role in the relations between the stiffness coefficients. For convenience, we express the stiffness coefficients k_{ij}^B in terms of homogeneous independent constants. A practical choice of units for these constants is that of the product $E \times I$ (Young’s modulus \times moment of inertia \equiv force \cdot length⁴/length²).

By the assumption of one axis of symmetry, the following nine conditions must be satisfied:

$$\begin{aligned} k_{11}^B &= k_{44}^B = A^B, & k_{16}^B &= k_{34}^B = -B^B L, & k_{22}^B &= k_{55}^B = C^B, \\ k_{33}^B &= k_{66}^B = D^B L^2, & k_{13}^B &= k_{46}^B, & k_{12}^B &= -k_{54}^B, \\ k_{15}^B &= -k_{24}^B, & k_{23}^B &= -k_{56}^B, & k_{26}^B &= -k_{35}^B. \end{aligned} \tag{2-4}$$

Moreover, equilibrium of every column of coefficients (equilibrium equations) dictates that, for each j ,

$$k_{1j}^B + k_{4j}^B = 0, \quad k_{2j}^B + k_{5j}^B = 0, \quad k_{3j}^B + k_{5j}^B L + k_{6j}^B = 0. \tag{2-5}$$

Implementing all these conditions, the general stiffness matrix of a beam with one axis of symmetry becomes

$$\mathbf{K}^B = \frac{1}{L^3} \begin{bmatrix} A^B & 0 & B^B L & -A^B & 0 & -B^B L \\ C^B & \frac{C^B L}{2} & 0 & -C^B & \frac{C^B L}{2} & 0 \\ D^B L^2 & -B^B L & -\frac{C^B L}{2} & \left(\frac{C^B}{2} - D^B\right) L^2 & 0 & B^B L \\ \text{Symmetric} & & A^B & 0 & B^B L & \\ & & C^B & -\frac{C^B L}{2} & D^B L^2 & \end{bmatrix}. \tag{2-6}$$

2.3. The stiffness matrix of a square element. Figure 2, left, shows a square element for which every geometric symmetry is also a material symmetry. Each node is assigned two DOFs of displacement in the plane of the square and one rotational DOF in the same plane. Just as in the case of the triangle, it is convenient to implement these symmetries in an adapted coordinate system. The 144 entries of the stiffness matrix \mathbf{K}^S are reduced to 78 by symmetry. Following the same procedure as for the previous examples, the geometric and material symmetry translate into a further reduction to 14 independent stiffness coefficients. The equations due to the four axes of symmetry of the square can be expressed as

$$\begin{aligned} K_{11}^S &= K_{44}^S = K_{77}^S = K_{10\ 10}^S = A^S, & K_{22}^S &= K_{55}^S = K_{88}^S = K_{11\ 11}^S = B^S, \\ K_{33}^S &= K_{66}^S = K_{99}^S = K_{12\ 12}^S = C^S \times L^2, \end{aligned}$$

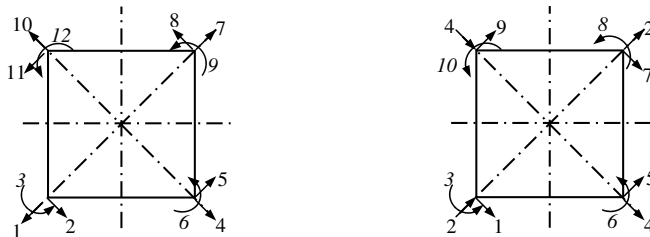


Figure 2. A square element.

$$\begin{aligned}
 K^S_{12} &= K^S_{13} = K^S_{45} = K^S_{46} = K^S_{78} = K^S_{79} = K^S_{10\ 11} = K^S_{10\ 12} = K^S_{18} = K^S_{19} \\
 &= K^S_{4\ 11} = K^S_{4\ 12} = K^S_{27} = K^S_{37} = K^S_{6\ 10} = K^S_{5\ 10} = 0, \\
 K^S_{14} &= K^S_{1\ 10} = K^S_{47} = K^S_{7\ 10} = D^S, \quad K^S_{25} = K^S_{58} = K^S_{8\ 11} = K^S_{2\ 11} = E^S, \\
 K^S_{28} &= K^S_{5\ 11} = F^S, \\
 K^S_{15} &= -K^S_{1\ 11} = K^S_{48} = -K^S_{24} = K^S_{7\ 11} = -K^S_{57} = K^S_{2\ 10} = -K^S_{8\ 10} = G^S, \\
 K^S_{16} &= -K^S_{1\ 12} = K^S_{49} = -K^S_{34} = -K^S_{76} = K^S_{7\ 12} = -K^S_{9\ 10} = K^S_{3\ 10} = H^S \times L, \\
 K^S_{23} &= K^S_{56} = K^S_{89} = K^S_{11\ 12} = I^S \times L, \quad K^S_{17} = K^S_{4\ 10} = J^S, \\
 K^S_{2\ 12} &= K^S_{35} = K^S_{68} = K^S_{9\ 11} = K^S_{26} = K^S_{59} = K^S_{8\ 12} = K^S_{3\ 11} = K^S \times L, \\
 K^S_{29} &= K^S_{5\ 12} = K^S_{38} = K^S_{6\ 11} = L^S \times L, \\
 K^S_{36} &= K^S_{69} = K^S_{9\ 12} = K^S_{3\ 12} = N^S \times L^2, \quad K^S_{39} = K^S_{6\ 12} = O^S \times L^2.
 \end{aligned}$$

Finally, the columnwise equilibrium conditions effect a further and final reduction to just 9 independent coefficients:

$$\begin{aligned}
 K^S_{2j} + K^S_{4j} - K^S_{8j} - K^S_{10j} &= 0, \quad K^S_{5j} + K^S_{7j} - K^S_{1j} - K^S_{11j} = 0, \\
 L \times (K^S_{5j} + K^S_{8j} + K^S_{11j} + K^S_{2j})/\sqrt{2} + K^S_{3j} + K^S_{6j} + K^S_{9j} + K^S_{12j} &= 0.
 \end{aligned} \tag{2-7}$$

Using the equilibrium equations, five coefficients can be written in terms of the remaining nine coefficients as follows:

$$\begin{aligned}
 G^S &= \frac{1}{2}(A^S - J^S), \quad F^S = B^S - A^S + J^S, \quad L^S = I^S - 2H^S, \\
 I^S &= H^S - K^S - \frac{1}{4}\sqrt{2}(-A^S + 2B^S + 2E^S + J^S), \\
 N^S &= -\frac{1}{2}C^S - \frac{1}{2}O^S + \frac{1}{4}(-A^S + 2B^S + 2E^S + J^S).
 \end{aligned} \tag{2-8}$$

As in the case of the beam, the use of hybrid DOFs results in a lack of dimensional homogeneity of the coefficients. For convenience, however, the stiffness coefficients are expressed in terms of 9 constants having the same units and the length of the side, L , makes an explicit appearance wherever needed.

The final reduced stiffness matrix has the form

$$\mathbf{K}^S = \frac{1}{L^3} \begin{bmatrix}
 A^S & 0 & 0 & D^S & G^S & H^S L & J^S & 0 & 0 & D^S & -G^S & -H^S L \\
 B^S & I^S L & -G^S & E^S & K^S L & 0 & F^S & L^S L & G^S & E^S & K^S L & \\
 C^S L^2 & -H^S L & K^S L & N^S L^2 & 0 & L^S L & O^S L^2 & H^S L & K^S L & N^S L^2 & & \\
 & A^S & 0 & 0 & D^S & G^S & H^S L & J^S & 0 & 0 & & \\
 & & B^S & I^S L & -G^S & E^S & K^S L & 0 & F^S & L^S L & & \\
 & & & C^S L^2 & -H^S L & K^S L & N^S L^2 & 0 & L^S L & O^S L^2 & & \\
 & & & & A^S & 0 & 0 & D^S & G^S & H^S L & & \\
 & & & & & B^S & I^S L & -G^S & E^S & K^S L & & \\
 & & & & & & C^S L^2 & -H^S L & K^S L & N^S L^2 & & \\
 & & & & & & & A^S & 0 & 0 & & \\
 & & & & & & & & B^S & I^S L & & \\
 & & & & & & & & & C^S L^2 & &
 \end{bmatrix}. \tag{2-9}$$

Symmetric

(To avoid complicated expressions within this matrix, (2-8) has not been implemented explicitly.)

2.4. Square element with inextensible diagonals. For a square with inextensible diagonals, the diagonal displacement of the two vertices across a diagonal are equal and are assigned a single DOF, as seen in [Figure 2](#), right. The stiffness matrix of such a square with respect to the DOFs shown there has 55 coefficients after employing the symmetry of the matrix. The normalization due to the hybrid combination of moments and forces is again utilized. The axes of symmetry can be used to reduce those fifty five coefficients to twelve coefficients as follows:

$$\begin{aligned}
K^{IS}_{22} &= K^{IS}_{44} = A^{IS}, & K^{IS}_{11} &= K^{IS}_{55} = K^{IS}_{77} = K^{IS}_{99} = B^{IS}, \\
K^{IS}_{33} &= K^{IS}_{66} = K^{IS}_{88} = K^{IS}_{10\ 10} = C^{IS} \times L^2, \\
K^{IS}_{12} &= K^{IS}_{27} = K^{IS}_{28} = K^{IS}_{23} = K^{IS}_{46} = K^{IS}_{45} = K^{IS}_{4\ 10} = K^{IS}_{49} = K^{IS}_{24} = 0, \\
K^{IS}_{13} &= K^{IS}_{56} = -K^{IS}_{78} = -K^{IS}_{9\ 10} = D^{IS} \times L, \\
K^{IS}_{15} &= -K^{IS}_{57} = K^{IS}_{79} = -K^{IS}_{19} = E^{IS}, & K^{IS}_{47} &= K^{IS}_{14} = K^{IS}_{29} = K^{IS}_{25} = F^{IS}, \\
K^{IS}_{2\ 10} &= -K^{IS}_{26} = K^{IS}_{48} = -K^{IS}_{34} = G^{IS} \times L, \\
K^{IS}_{16} &= K^{IS}_{1\ 10} = K^{IS}_{58} = K^{IS}_{53} = -K^{IS}_{76} \\
&= -K^{IS}_{7\ 10} = -K^{IS}_{89} = -K^{IS}_{39} = H^{IS} \times L, \\
K^{IS}_{17} &= K^{IS}_{59} = I^{IS}, & K^{IS}_{18} &= K^{IS}_{5\ 10} = -K^{IS}_{37} = -K^{IS}_{69} = J^{IS} \times L, \\
K^{IS}_{36} &= K^{IS}_{68} = K^{IS}_{8\ 10} = K^{IS}_{3\ 10} = N^{IS} \times L^2, & K^{IS}_{38} &= K^{IS}_{6\ 10} = O^{IS} \times L^2.
\end{aligned}$$

Equilibrium equations for the square in [Figure 2](#), right, have the form

$$\begin{aligned}
K^{IS}_{2j} + K^{IS}_{9j} + K^{IS}_{5j} &= 0, & K^{IS}_{1j} + K^{IS}_{7j} + K^{IS}_{4j} &= 0, \\
L(K^{IS}_{1j} + K^{IS}_{5j} - K^{IS}_{7j} - K^{IS}_{9j})/\sqrt{2} + K^{IS}_{3j} + K^{IS}_{6j} + K^{IS}_{8j} + K^{IS}_{10j} &= 0.
\end{aligned} \tag{2-10}$$

Using the equilibrium equations, five coefficients can be written in terms of the remaining seven coefficients as follows:

$$\begin{aligned}
F^{IS} &= -\frac{1}{2}A^{IS}, & I^{IS} &= -B^{IS} - F^{IS}, & J^{IS} &= D^{IS} - G^{IS}, \\
H^{IS} &= -D^{IS} + \frac{1}{2}G^{IS} + \frac{1}{8}\sqrt{2}(A^{IS} - 4B^{IS} - 4E^{IS}), \\
N^{IS} &= -\frac{1}{2}(\frac{1}{4}A^{IS} - B^{IS} + C^{IS} - E^{IS} + O^{IS}).
\end{aligned} \tag{2-11}$$

The final stiffness matrix has the form

$$\mathbf{K}^{IS} = \frac{1}{L^3} \begin{bmatrix} B^{IS} & 0 & D^{IS}L & F^{IS} & E^{IS} & H^{IS}L & I^{IS} & J^{IS}L & -E^{IS} & H^{IS}L \\ & A^{IS} & 0 & 0 & F^{IS} & -G^{IS}L & 0 & 0 & F^{IS} & G^{IS}L \\ & & C^{IS}L^2 & -G^{IS}L & H^{IS}L & N^{IS}L^2 & -J^{IS}L & O^{IS}L^2 & -H^{IS}L & N^{IS}L^2 \\ & & & A^{IS} & 0 & 0 & F^{IS} & G^{IS}L & 0 & 0 \\ & & & & B^{IS} & D^{IS}L & -E^{IS} & H^{IS}L & I^{IS} & J^{IS}L \\ & & & & & C^{IS}L^2 & -H^{IS}L & N^{IS}L^2 & -J^{IS}L & O^{IS}L^2 \\ & & & & & & B^{IS} & -D^{IS}L & E^{IS} & -H^{IS}L \\ & & & & & & & C^{IS}L^2 & -H^{IS}L & N^{IS}L^2 \\ & & & & & & & & B^{IS} & -D^{IS}L \\ & & & & & & & & & -D^{IS}L & C^{IS}L^2 \end{bmatrix}. \tag{2-12}$$

Symmetric

3. Structural analysis of generated fractals

3.1. Structural analysis of a Sierpiński gasket. The Sierpiński gasket is a fractal generated from an equilateral triangle. The generation process starts by dividing the area inside the equilateral triangle into four similar copies of the original triangle and removing the middle inverted one as shown in Figure 3a. Each of the remaining three copies is again divided into four copies and the middle inverted one is removed and so on ad infinitum. The process is equivalent to starting with a triangle and making two extra copies and placing them as shown in Figure 3b. The new generated structure is then replicated again and the process is repeated ad infinitum. This process of generation is used to generate a Sierpiński gasket from a triangular structural element. A finite element analysis package (ABAQUS 6.6) is utilized to generate a three-node triangle using a plane stress element with a thickness of 1 unit and side dimensions of 1 unit. The three-node triangle is regarded as a structural element rather than a finite element. The stiffness matrix of the generated structure with respect to the three vertices is obtained in every step during the generation process for the triangle by applying a unit deformation in the vertical direction and obtaining the reactions in the corner nodes. Figure 4 shows the generated Sierpiński gasket at the generation step $n = 8$. Since the generated structure obeys the symmetries described in Section 2.1, the generated stiffness matrix has two independent coefficients, A^T and B^T , which can be calculated from the obtained reactions, per (2-2).

As pointed out, the (isotropic) material properties of the originator (namely, the triangular building block) do not affect the final ratios between the stiffness coefficients of the fractal obtained as limit. We have referred to this property as stability. To check that this is indeed the case, we examine two cases separately. In both cases the Young’s modulus of the originator triangle was assumed to be equal to 1 unit, but the Poisson’s ratio was set to 0 for the first case and to 0.4999 for the second. The stiffness matrix of the generated structure converges to one single form for both sets. The ratio B^T/A^T stabilizes and reaches the value 3 after a few steps of the generation process indicating that the details of the stiffness

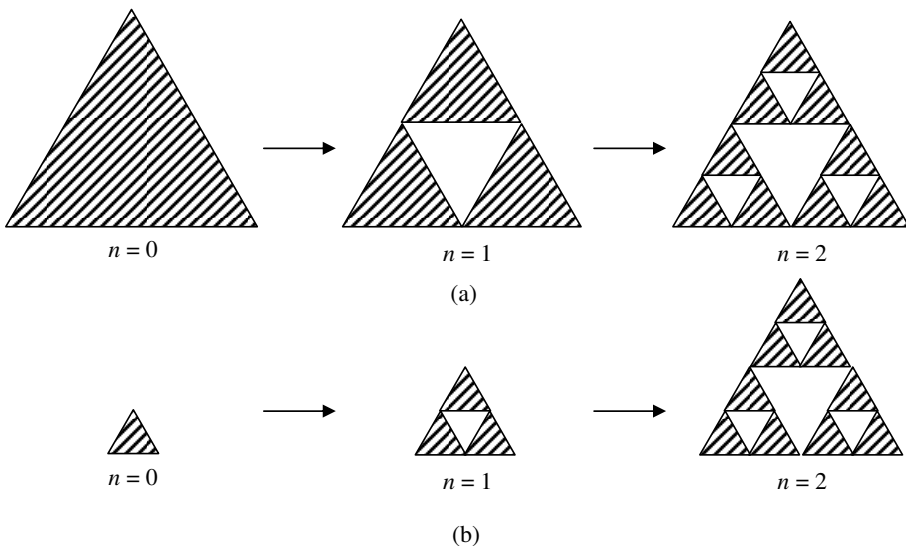


Figure 3. Generation of a Sierpiński gasket by division (a) and by copying (b).

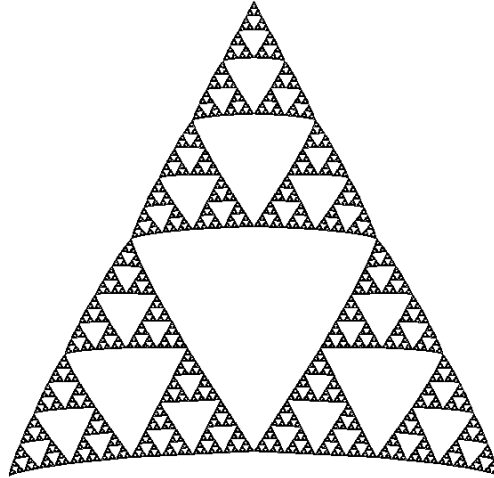


Figure 4. The generated Sierpiński gasket after applying an upward unit deformation at the top vertex while restraining the remaining DOFs. The gasket is shown at the generation step $n = 8$.

of the originator disappear after a few steps of the generation process (see Figure 5a). The generated stiffness matrix for a Sierpiński gasket has only one independent coefficient, namely A^T . The obtained stiffness matrix throughout the generation process appears to be scaled down by the same scaling factor from one step to the next. After a few generation steps, the value of A^T at a generation step n approaches half the value of A^T at the generation step $n - 1$ (see Figure 5b).

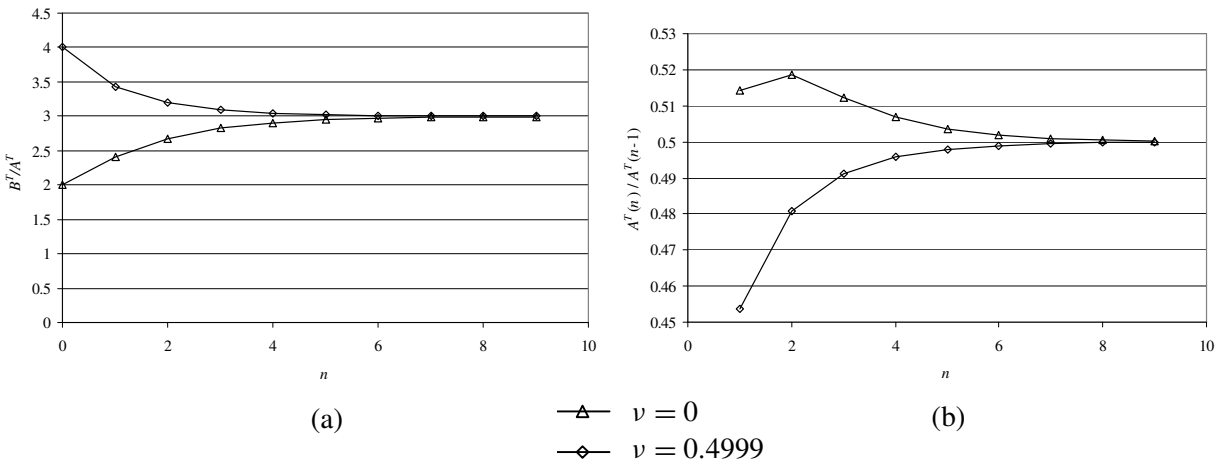


Figure 5. Stability of the stiffness form of a Sierpiński gasket for both sets of stiffness for the originator triangle: (a) the ratio B^T/A^T stabilizes at a value of 3; (b) the ratio $A^T(n)/A^T(n-1)$ stabilizes at a value of 0.5. Each part shows the result for two values of the Poisson's ratio ν .

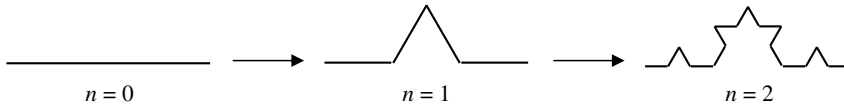


Figure 6. Generation of a Koch curve.

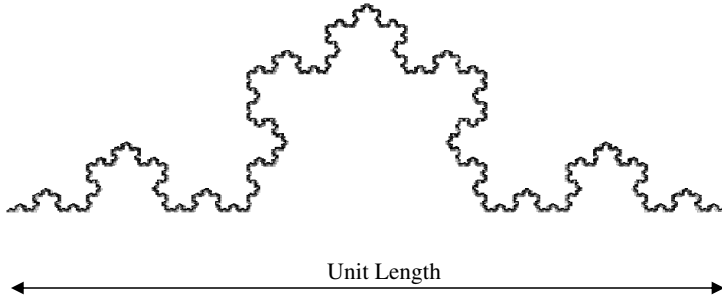


Figure 7. The generated Koch beam at $n = 5$.

3.2. Structural analysis of a Koch beam. The Koch curve is generated by dividing a line segment into three equal parts, removing the middle part, and replacing it by two copies of itself rotated by an angle of sixty degrees. The process is then repeated for the generated four line segments ad infinitum (see Figure 6). The six-DOF structure thus generated is called the Koch beam. ABAQUS 6.6 was used to generate a Koch beam with unit length as a combination of Euler–Bernoulli elastic beams with a Young’s modulus of 1 unit and a moment of inertia of 1 unit. The area of the beams was taken as an arbitrary large number (10000 units) as the deformations are expected to be primarily due to bending. The generated stiffness matrix has four independent coefficients as described in (2-6), namely A^B , B^B , C^B , and D^B . By analyzing (2-6) it is obvious that rows 4 and 6 are sufficient to obtain the four independent coefficients of the stiffness matrix of such a beam. Those independent coefficients can be obtained by applying a unit deformation to DOF number 4 and a unit rotation to DOF number 6 shown (see figure at bottom of page 783). Just as with the Sierpiński gasket, the stiffness form of the generated Koch beam stabilizes after a few generation steps. Each of the ratios of B^B , C^B , and D^B with respect to A^B reaches a limit (see Figure 8a) and the scaling factor (the ratio between the stiffness A^B at a generation step n and the stiffness A^B at the generation step $n - 1$) stabilizes at a value of $3/4$ (see Figure 8b). This factor of $3/4$ is only attainable due to keeping the total length of the Koch beam at each generation step n equal to the length at the previous generation step ($n - 1$). It should be noted here that the ratio between A^B at a generation step n and the value of a^B (being the equivalent stiffness of one of the four legs of the Koch beam during the same generation step) is equal to $1/36$. The leg on its own is considered to be in the generation step $n - 1$, thus having a higher scaling stiffness, with value $4/3$. The length of the leg is three times less than the length of the whole Koch beam and thus the $1/L^3$ term in the stiffness matrix further increases the stiffness of the leg by a value of 27. The total increase in stiffness of the leg compared to that of the whole Koch beam is equal to 36.

3.3. Structural analysis of a two-dimensional modification of the Cantor set. An interesting structural fractal, based on a square and reminiscent of the Cantor set, can be obtained as follows. At the generation

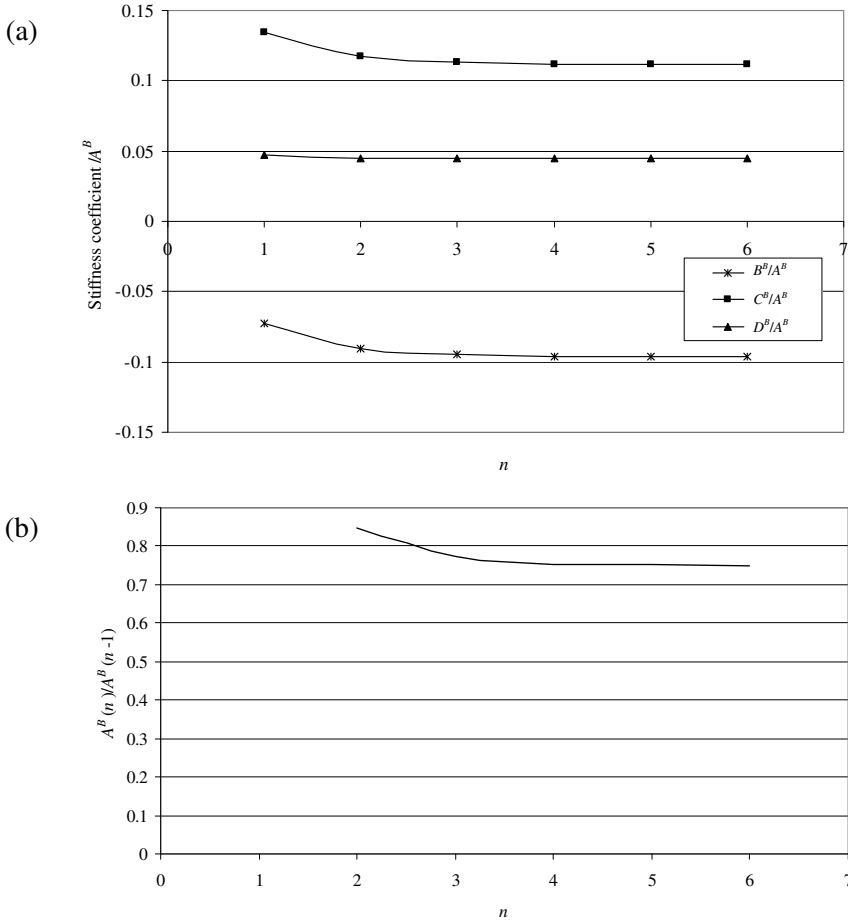


Figure 8. Stability of the stiffness form of a Koch beam. (a) The ratio of each of B^B , C^B , and D^B to A^B stabilizes at a constant value. (b) The ratio $A^B(n)/A^B(n - 1)$ stabilizes at a value of 0.75.

step $n = 1$, the square is divided into nine equal squares, four of which are removed (see Figure 9). The removed squares are those involving the middle third of each side of the original square. Taking a closer look at the side, it can be noticed that at the first generation step, the open set $]1/3, 2/3[$ of the line segment $[0, 1]$ representing each side has been removed. In the following generation steps, the process is repeated for every remaining square. As far as the sides of the original square are concerned, this process results in the generation of the Cantor set.

For this structure to be stable, each square should have a rotational DOF at the corner node; hence the need for the stiffness matrix described in Section 2.3. Nine arbitrary values for the stiffness matrix (2-9) were chosen, ensuring that the matrix is positive definite. The chosen stiffness matrix was rotated to appropriate DOFs that can be implemented in a commercial finite element package using the relationship $\mathbf{K}^{\text{rotated}} = \mathbf{Q}^{\text{tr}} \mathbf{K} \mathbf{Q}$, where \mathbf{Q} is the rotation matrix between the two sets of DOFs. ABAQUS 6.6 was used to generate the model of this fractal at different generation steps. Step $n = 0$ represents a square of unit

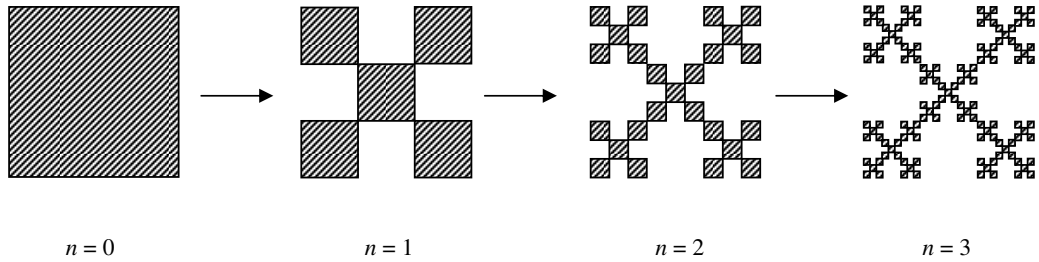


Figure 9. Two-dimensional modification of the Cantor set.

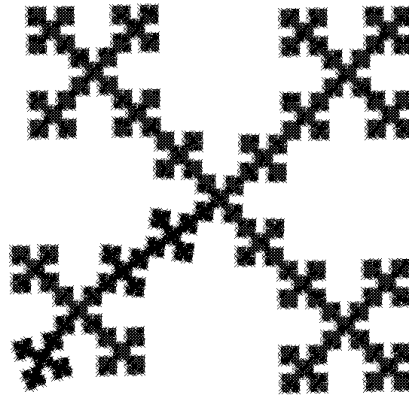


Figure 10. Deformation shape of the two-dimensional Cantor set at $n = 5$ when applying a unit rotation to DOF number 3 and restraining all remaining DOFs at the four corner vertices.

side length with the specified stiffness matrix. Step $n = 1$ represents five squares, each of unit side length and with the specified stiffness matrix. Thus, the total side length of the model grew with the generation steps. The *user element* option was used to input the stiffness matrix for the square unit against the DOFs in a Cartesian coordinate system. By close examination of (2-9), any three columns belonging to the DOFs of one node are sufficient to reproduce the nine coefficients of the matrix. Thus, three separate loading cases were applied on a chosen corner node; two perpendicular unit displacements and a unit rotation. At each generation step and in each loading case, the resulting reactions at the remaining three nodes were obtained and were used to regenerate the stiffness matrix in a Cartesian coordinate system. The stiffness matrix generated was then rotated back to the DOFs shown in Figure 2 and the nine stiffness coefficients of the generated structure were extracted according to (2-9). The ratios of the coefficients with respect to A^S obtained for the different generation steps reveal that seven of the generated coefficients approached zero (see Figure 11). The ratio J^S/A^S on the other hand approached unity. The stiffness entry A^S represents the force needed to extend the diagonal a unit displacement while the stiffness entry J^S represents the reaction to the force A^S on the opposite side of the diagonal. This clearly indicates that the diagonals become infinitely stiff because of the way this fractal is generated; material is always removed during the generation process except from the diagonals. Any force applied in the diagonal direction is totally absorbed by the reaction on the opposite side of the diagonal and all the

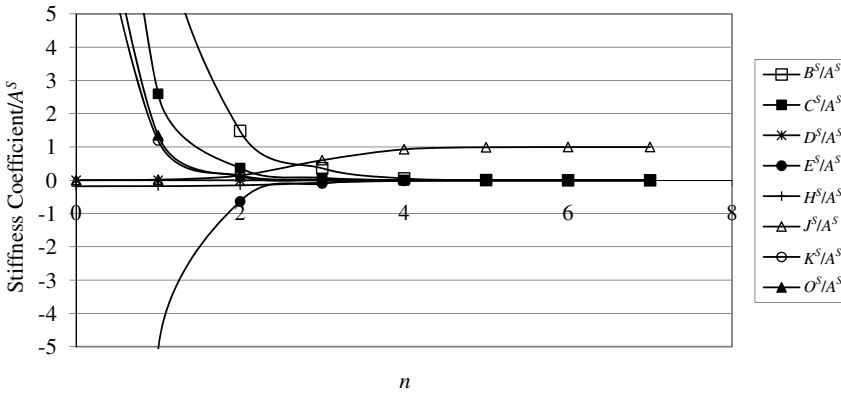


Figure 11. Ratios of stiffness coefficients obtained for the square with respect to the stiffness coefficients A^S .

other reactions to that force are relatively zero. In order to analyze different modes of deformation, the stiffness matrix of a square with inextensible diagonals was introduced in Section 2.4. The new structure with inextensible diagonals will be analyzed in Section 4.3 using the principle of self similarity stated in Section 4.

4. Principle of stiffness self-similarity

It was shown in Section 3 that the stiffness form of fractal structures stabilizes after a few generation steps. It will be shown here that this final form can be achieved by applying the principle of self-similarity to the stiffness matrix of each of the fractals under consideration. A fractal is said to be self-similar if it is an almost disjoint union of shapes that are a reduced copy of the fractal itself. The principle of structural self-similarity was first introduced in [Epstein and Adeeb 2008] and states that for a self-similar fractal the stiffness matrix of \mathbf{K}^f is proportional to the stiffness matrix \mathbf{K}^F of one of its reduced constituent copies with respect to the corresponding DOFs, namely:

$$\mathbf{K}^f = \alpha \mathbf{K}^F, \tag{4-1}$$

where α is a constant.

The $n \times n$ stiffness matrix \mathbf{K}^F with (where n is the number of DOFs chosen for the fractal) as described in Section 3 contains m independent coefficients after employing all the symmetries and equilibrium conditions. The stiffness matrix \mathbf{K}^f of the whole fractal can be constructed by structural analysis assembly procedures of the different units, then condensation to the chosen DOFs of the whole fractal. The assembled stiffness matrix \mathbf{K}^f also has $n \times n$ entries. Since the assembled structure has the same symmetries and equilibrium conditions of its units, it will also have m independent entries. These entries will be nonlinear equations of the m independent entries of the stiffness matrix \mathbf{K}^F . Equation (4-1) can be considered as a system of m equations in $m + 1$ unknowns after the introduction of the scaling factor α . Its solution will, therefore, yield the value of α and of the $m - 1$ independent ratios between the m independent stiffness values. In order to solve this system of equations, a numerical procedure is employed. Starting with initial values for the m independent coefficients of the stiffness matrix \mathbf{K}^F ,

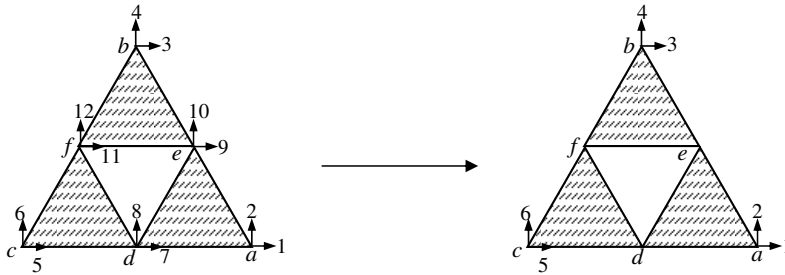


Figure 12. Building up the stiffness of a Sierpiński gasket by assembling three scaled-down copies of the whole structure.

the global stiffness matrix of the whole fractal K^f is assembled. The new m independent coefficients are then extracted from the global stiffness matrix K^f and an average factor α is obtained by dividing the new m independent coefficients of the matrix K^f by the original m independent coefficients of the matrix K^F and averaging the resulting factors. The new independent coefficients divided by the obtained average factor are then used as input for the next step. This process was applied to the fractals under consideration and was shown to lead to the solution obtained in Section 3.

4.1. Stiffness self-similarity of the Sierpiński gasket. The numerical procedure described above was applied to the Sierpiński gasket. As shown in Figure 12, the equilateral triangle abc is assumed to be composed of three smaller equilateral triangles (aed , ebf , and dfc) with identical 6×6 stiffness matrices K^T . Arbitrary positive values are assigned for the coefficients A^T and B^T in (2-3). The global stiffness matrix has 12×12 entries and can be assembled by combining the three smaller stiffness matrices according to their nodal connectivity. The global stiffness matrix can be reduced to a 6×6 matrix K^t by assuming that there are no external forces applied at nodes d , e or f . Thus, the stiffness matrix K^t of the condensed structure abc can be calculated as follows:

$$K_1 \Delta_1 + K_2 \Delta_2 = F, \quad K_2^{tr} \Delta_1 + K_3 \Delta_2 = 0, \quad K^t = K_1 - K_2 K_3^{-1} K_2^{tr}, \quad (4-2)$$

where tr denotes the transpose, K_1 is the first 6×6 entries of the 12×12 global stiffness matrix, Δ_1 is the array of DOFs 1 through 6, K_2 is the submatrix containing the entries of rows 1 to 6 and columns 7 to 12 of the global stiffness matrix, Δ_2 is the array of DOFs 7 through 12, F is the array of external forces applied to DOFs 1 through 6, and K_3 is the submatrix containing the entries of rows 7 to 12 and columns 7 to 12 of the global stiffness matrix.

After the process of assembly and condensation, the entries k^t_{33} and k^t_{44} in the matrix K^t are extracted and are divided by the initial arbitrary values of A^T and B^T to obtain two values that are averaged to obtain a coefficient α . The new values of A^T and B^T for the next iteration are then taken to be k^t_{33}/α and k^t_{44}/α respectively. The process was repeated until the values of B^T and α stabilized. The results obtained are similar to those obtained in Section 3.1. The ratio of B^T/A^T stabilized at a value of 3 while α converged to a value of 0.5.

4.2. Stiffness self-similarity of the Koch beam. The assembly of a Koch beam from four similar parts follows the same procedure used for the Sierpiński gasket described in Section 4.1. The beam ab can be assumed to be composed of the assembly of the four beams ac , cd , de , and eb , each having a stiffness

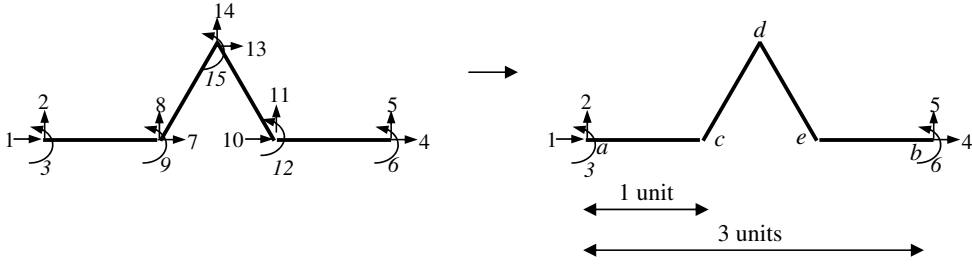


Figure 13. Assembly of a Koch beam from four scaled down copies of the original.

matrix with four independent coefficients according to (2-6). The stiffness matrix K^B for beams cd and de , however, needs to be rotated to the global nodal directions shown in Figure 13. The global assembled stiffness matrix has 15×15 entries and can be reduced to a 6×6 matrix K^b by the equations

$$\mathbf{K}_1 \Delta_1 + \mathbf{K}_2 \Delta_2 = \mathbf{F}, \quad \mathbf{K}_2^{\text{tr}} \Delta_1 + \mathbf{K}_3 \Delta_2 = 0, \quad \mathbf{K}^b = \mathbf{K}_1 - \mathbf{K}_2 \mathbf{K}_3^{-1} \mathbf{K}_2^{\text{tr}}, \quad (4-3)$$

where \mathbf{K}_1 is the first 6×6 entries of the 15×15 global stiffness matrix, Δ_1 is the array of DOFs 1 through 6, \mathbf{K}_2 is the submatrix containing the entries of rows 1 to 6 and columns 7 to 15 of the global stiffness matrix, Δ_2 is the array of DOFs 7 through 15, \mathbf{F} is the array of external forces applied to DOFs 1 through 6, and \mathbf{K}_3 is the submatrix containing the entries of rows 7 to 15 and columns 7 to 15 of the global stiffness matrix.

In the first iteration four arbitrary positive values are assumed for the entries A^B , B^B , C^B , and D^B of the stiffness matrix \mathbf{K}^B . After assembly of the matrix \mathbf{K}^b the entries k_{11}^B and k_{22}^B are extracted and are multiplied by the cube of the length of the whole beam (3 units), then divided by A^B and C^B to obtain two values of the scale factor α . The entry k_{13}^B is multiplied by the square of the length of the whole beam and divided by the entry B^B to obtain another value for the scale factor α . A fourth value for α is then obtained by multiplying the entry k_{33}^B by the length of the whole beam and then dividing the result by the entry D^B . The four values of α are then averaged and the new values for A^B , B^B , C^B , and D^B are used for the next iteration by using the following entries: $k_{11}^B/27\alpha$, $k_{13}^B/9\alpha$, $k_{22}^B/27\alpha$, and $k_{33}^B/3\alpha$ respectively. The results obtained are similar to those obtained in Section 2.2. The values of B^B/A^B , C^B/A^B , D^B/A^B , and α stabilized at -0.09623 , 0.1111 , 0.0444 and $3/4$ respectively.

4.3. Stiffness self-similarity of a two-dimensional modification of the Cantor set. The assembly of the two-dimensional Cantor set (Section 3.3) as a union of five scaled copy of itself is shown in Figure 14. The fractal structure $abcd$ with supports on a , b , c , and d can be considered as a union of the fractal structures $aehg$, $fbji$, $himl$, $klod$, and $mncp$ which have stiffnesses that are a scaled copy of the stiffnesses of the global structure. The principle of self-similarity stated can be applied to this fractal as follows: Arbitrary values are given to the nine stiffness entries of the unit square in (2-9). The stiffness matrix is then rotated to the global DOFs shown in Figure 14. After assembly, the global stiffness matrix had 48×48 entries. The stiffness matrix was then reduced into a 12×12 matrix by eliminating the DOFs at nodes e , f , g , h , i , j , k , l , m , n , o , and p as described in Sections 4.1 and 4.2. After reduction, the stiffness matrix was then rotated to the DOFs shown in Figure 14b. The new stiffness and the ratios were then extracted as described in Sections 4.1 and 4.2. Results similar to those described in Section 3.3

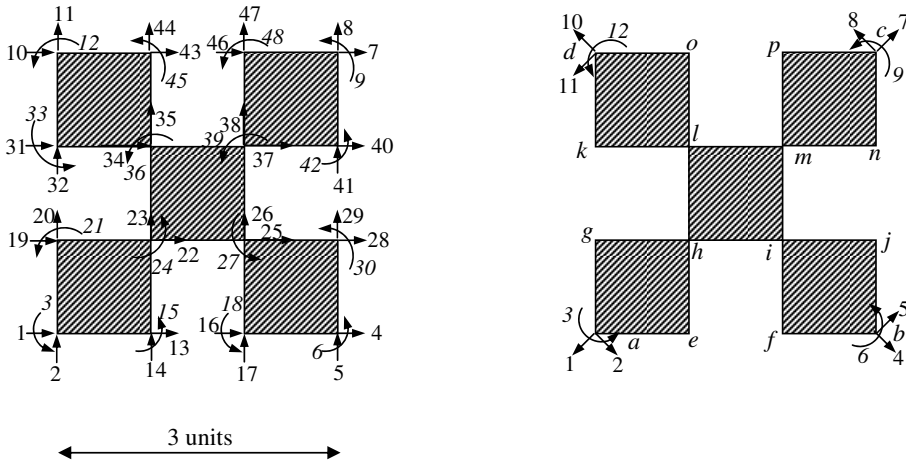


Figure 14. Assembly of the two-dimensional modification of the Cantor set fractal from five scaled down copies of the original.

were obtained using the self-similarity principle. The fractal is infinitely stiff in the diagonal direction with respect to the remaining DOFs. All the stiffness coefficients approached zero except A^S and J^S which had equal values, indicating that the generation of this fractal causes the diagonals to be infinitely stiff compared to other deformation shapes. The ratio between the input stiffness entry k^S_{11} of the unit square and the output stiffness entry K^S_{11} was found to be 3, which is the ratio of the side length of the output structure to the side length of the input unit square.

The stiffness form of the described fractal in modes of deformation other than along the diagonals can be obtained by applying the principle of self-similarity to the assembled fractal structure in [Figure 15](#). In this case, however, the deformations along the diagonals are considered to be single DOFs and

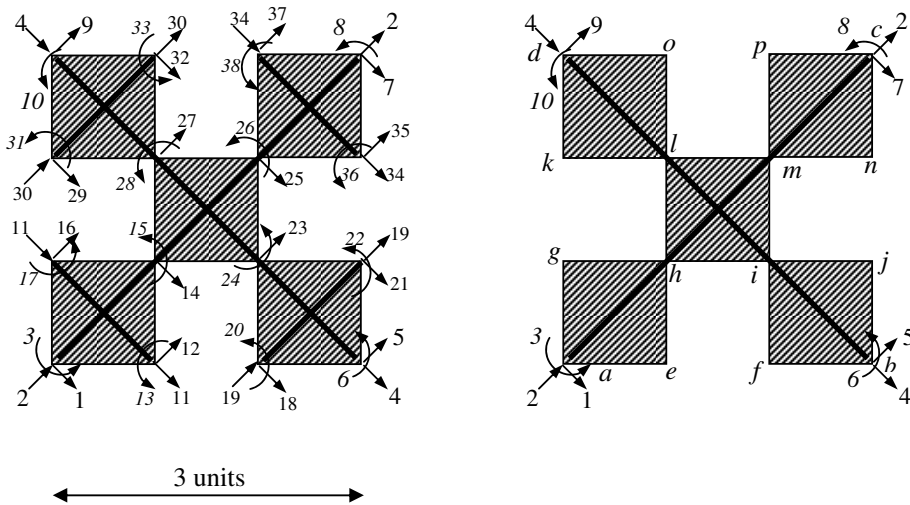


Figure 15. Assembly of the two-dimensional modification of the Cantor set fractal from five scaled down copies of the original, all having inextensible diagonals.

thus the global stiffness matrix has 38×38 entries. The same procedure used for the Koch beam and for the Sierpiński gasket is employed to find the form of the stiffness matrix \mathbf{K}^{IS} shown in Equation (2-12) and the ratios between the stiffness coefficients of the global structure and the stiffness coefficients of the unit structure. The final converged ratios of the seven independent coefficients B^{IS} , C^{IS} , D^{IS} , E^{IS} , G^{IS} , and O^{IS} with respect to A^{IS} were equal to 0.40625, 0.078125, -0.15468 , -0.09375 , -0.17678 , and -0.00521 . The ratio between the stiffness entry k^{IS}_{22} of the initial unit square stiffness matrix \mathbf{K}^{is} and the stiffness entry K^{IS}_{22} of the global stiffness matrix of the whole structure \mathbf{K}^{IS} after assembly and reduction was equal to 27. As the global structure has a length that is 3 times higher than the unit of generation, the length scaling described in Section 3.2 has to be taken into consideration. Thus, the entry k^{IS}_{22} is multiplied by the cube of the length of the unit square to obtain a^{IS} , while the entry K^{IS}_{22} is multiplied by the cube of the length of the global structure to obtain A^{IS} :

$$\frac{k^{IS}_{22}}{K^{IS}_{22}} = 27, \quad \frac{a^{IS}}{L^3_{\text{unit square}}} = k^{IS}_{22}, \quad \frac{A^{IS}}{27L^3_{\text{unit square}}} = K^{IS}_{22} = \frac{k^{IS}_{22}}{27} = \frac{a^{IS}}{27L^3_{\text{unit square}}}. \quad (4-4)$$

Thus, A^{IS} is equal to a^{IS} and the scaling factor α for this fractal is equal to unity.

5. Conclusions

The geometrical stability of self-similar fractals has been shown previously to be reflected in the fact that the final image of a self-similar fractal is not dependent on the image of the building block but rather on the generation procedure [Peitgen et al. 2004]. In this paper we showed that when we consider the fractals as elastic structures, the stiffness form of such structures will also depend on the generation process rather than on the numerical values of the stiffness coefficients of the building block, as long as it is isotropic. This structural-form stability was shown in three fractal-like structures: the Sierpiński triangle the Koch curve, and a two-dimensional generalization of the Cantor set. For each of those fractals, it was shown that there is a final relationship between the independent entries of the stiffness matrix of the generated fractal. This relationship is shown to be independent of the initial relationship among the entries of the stiffness matrix of the building block and to depend only on the generation process and the geometric and material symmetries of the fractal.

In order to find the relationship between the entries and/or the form of the stiffness matrix of a fractal, the principle of structural self similarity has been previously introduced by Epstein and Adeb [2008]. The structural self-similarity principle states that the stiffness matrix of a fractal is proportional to the stiffness matrix of a reduced copy of that same fractal, thus a relationship between the entries can be obtained. In this paper we show a numerical algorithm by which this structural self-similarity principle can be applied to obtain those relationships among the stiffness matrix entries. The principle was applied to the Koch curve, the Sierpiński triangle, and a two-dimensional generalization of the Cantor set. The relationship between the stiffness matrix entries obtained for the three fractal structures using the self-similarity principle exactly match the relationship obtained by the structural analysis of the generated fractals.

The question that poses itself is that self-similar fractals in the strict sense as defined by Mandelbrot [1982] are objects that replicate themselves at all scales, but many of the fractal-like objects found in nature have only a finite range in which they are effectively self-similar [Avnir et al. 1998; Parkinson and

Fazzalari 2000]. The results of our analysis show that the structural properties of a fractal as seen in this work (see Figures 5, 8, and 11) reach a very close approximation to their final stabilized values at the iteration step $n = 4$ or 5. It does not really take long for the originator structural properties to disappear and for the fractal behavior to be dominant.

References

- [Avnir et al. 1998] D. Avnir, O. Biham, D. Lidar, and O. Malcai, “Is the geometry of nature fractal?”, *Science* **279**:5347 (1998), 39–40.
- [Capitanelli and Lancia 2002] R. Capitanelli and M. R. Lancia, “Nonlinear energy forms and Lipschitz spaces on the Koch curve”, *J. Convex Anal.* **9** (2002), 245–257.
- [Carpinteri and Cornetti 2002] A. Carpinteri and P. Cornetti, “A fractional calculus approach to the description of stress and strain localization in fractal media”, *Chaos Solitons Fract.* **13**:1 (2002), 85–94.
- [Carpinteri et al. 2001] A. Carpinteri, B. Chiaia, and P. Cornetti, “Static-kinematic duality and the principle of virtual work in the mechanics of fractal media”, *Comput. Methods Appl. Mech. Eng.* **191**:1–2 (2001), 3–19.
- [Carpinteri et al. 2004] A. Carpinteri, B. Chiaia, and P. Cornetti, “The elastic problem for fractal media: basic theory and finite element formulation”, *Comput. Struct.* **82**:6 (2004), 499–508.
- [Dyson 1978] F. Dyson, “Characterizing irregularity”, *Science* **200**:4342 (1978), 677–678.
- [Epstein and Adeeb 2008] M. Epstein and S. M. Adeeb, “The stiffness of self-similar fractals”, *Int. J. Solids Struct.* **45**:11–12 (2008), 3238–3254.
- [Epstein and Śniatyski 2006] M. Epstein and J. Śniatyski, “Fractal mechanics”, *Physica D* **220** (2006), 54–68.
- [Frank and Shrive 1999] C. B. Frank and N. G. Shrive, “Ligaments”, pp. 107–126 in *Biomechanics of the musculo-skeletal system*, 2nd ed., edited by B. M. Nigg and W. Herzog, Wiley, Chichester, 1999.
- [Mandelbrot 1982] B. Mandelbrot, *The fractal geometry of nature*, W. H. Freeman, San Francisco, 1982.
- [Parkinson and Fazzalari 2000] I. H. Parkinson and N. L. Fazzalari, “Methodological principles for fractal analysis of trabecular bone”, *J. Microsc.* **198**:2 (2000), 134–142.
- [Peitgen et al. 2004] H.-O. Peitgen, H. Jürgens, and D. Saupe, *Chaos and fractals: new frontiers of science*, 2nd ed., Springer, New York, 2004.

Received 28 Dec 2008. Revised 15 May 2009. Accepted 17 May 2009.

SAMER ADEEB: adeeb@ualberta.ca

Department of Civil and Environmental Engineering, University of Alberta, Edmonton, AB T6G 2W2, Canada

MARCELO EPSTEIN: mepstein@ucalgary.ca

Department of Mechanical and Manufacturing Engineering, University of Calgary, 2500 University Drive NW, Calgary, AB T2N 1N4, Canada

APPLICATION AND DESIGN OF LEAD-CORE BASE ISOLATION FOR REDUCING STRUCTURAL DEMANDS IN SHORT STIFF AND TALL STEEL BUILDINGS AND HIGHWAY BRIDGES SUBJECTED TO NEAR-FIELD GROUND MOTIONS

THOMAS L. ATTARD AND KITTINAN DHIRADHAMVIT

The performance of nonlinear lead-core-rubber base isolators (LCR) to passively control highly nonlinear vibrations in two steel buildings and a prestressed concrete bridge under various ground motion inputs is evaluated. The Bouc and Wen model is used to predict the behavior of the lead-core component of the LCR base isolator. Members of the steel buildings that may have yielded are analyzed according to a highly nonlinear constitutive rule used to model the smooth stiffness degradation in the damaged members. The previously developed constitutive rule analyzes kinematically strain-hardened materials under cyclic conditions. The ability of the LCR to reduce displacement, velocity, and acceleration demands is demonstrated numerically using an algorithm developed herein called BISON (base isolation in nonlinear time history analysis). The performance of the LCR isolation is measured for a two story isolated building excited by the El Centro ground motion, a nonstationary signal, and the Northridge ground motion. An eight-story building exhibiting higher-mode influence is also analyzed, and finally the overpass bridge on Highway 99 in Selma, CA is modeled, outfitted with LCR isolation, and also analyzed. The hysteresis of the force-displacement relationships of the structures and the LCR isolators are analyzed parametrically through two LCR design parameters. The results indicate that with an appropriate tuning of these parameters, which affect the inelastic stiffness of the LCR isolator, an appropriate LCR system may be designed to behave with a stationary-like hysteresis and that can very adequately reduce the structural demands under the various excitations.

1. Introduction

In large civil structures, including highway bridges and buildings, passive energy dissipation systems are preferred over active control systems because of lower cost, less maintenance, and lower power consumption. Seismic base isolation implementation remains one of the most widely used and accepted passive methods used to protect buildings and bridges from potential earthquake hazards. The concept of base isolation focuses on altering a structure's natural frequency away from the dominant frequency components of a seismic event [Kikuchi and Aiken 1997; Furukawa et al. 2005]. Base isolation systems are also used to protect the nonstructural components in buildings, including pipes, electrical wires, and various equipment, which may be found in hospitals and communication centers [Pozo et al. 2006; Matsagar and Jangid 2004], by reducing interstory displacement demands and accelerations through hysteretic energy dissipation [Matsagar and Jangid 2008; Dolce et al. 2007]. Some typical base isolators

Keywords: base isolation, passive control, bridge isolation, lead-core rubber base isolation, higher-mode effects, plastic analysis, inelastic structures.

include friction pendulums, rubber bearings, and lead-core-rubber base isolators (LCR) [Dimizas and Koumoussis 2005].

Disadvantages of base isolation systems include their vulnerability to strong pulse-type ground motions generated at near-fault zones [Kelly 1999]. The complementary damping provided by the base isolation may in certain cases induce energy into the higher modes of vibration and increase member deformations and accelerations of an isolated structure resulting in subsequent structural and nonstructural damages [Ramallo et al. 2002].

Examples of base isolated structures include the Los Angeles City Hall, Foothill Law, and the Justice Center in Los Angeles, California [Hart and Wong 2000]. The Bai-Ho Bridge that spans across the Gian-Nan canal in Taiwan utilizes an LCR isolation device [Shen et al. 2004], and the Yama-age Bridge in Japan employs a high-damping-rubber bearing dissipation system [Chaudhary et al. 2001]. The Marga-Marga Bridge in Vina del Mar, which is located in a high seismic risk area in Chile, is protected using high-damping rubber bearings [Boroschek et al. 2003]. Following the Great Hanshin/Awaji earthquake (also referred to as the Hyogo-Ken Nanbu, or Kobe earthquake) on January 17, 1995, the Benten Viaduct Highway Bridge in Kobe City, Japan was rebuilt in 18 months using LCR isolation [Yoshikawa et al. 2000].

Such catastrophes have motivated researchers to develop effective damage mitigation systems to protect various types of structures [Jangid 2004]. Base isolation has become a conventional method for protecting buildings and bridges from seismic events [Choi et al. 2006; Shen et al. 2004; Dicleli 2002]. Base isolation has been used to prevent brittle failure in piers [Hwang and Chiou 1996], to reduce the spectral accelerations in stiff piers, and to reduce the shear force at the bases of bridges [Soneji and Jangid 2006]. In short, it is generally considered a convenient alternative to typical bridge bearings [Chaudhary et al. 2001]. Tsopelas and Constantinou [1997] experimentally studied the use of sliding disc bearings and rubber restoring force devices to isolate bridge models under various types of ground motion excitations. The results showed that these devices resulted in significantly smaller responses than nonisolated bridges. Tsopelas et al. [1996] also performed analytical and experimental studies of elastoplastic isolated systems and concluded that these systems are vulnerable to shock-type seismic motions that result in large displacement demands. Over the last two decades, LCR isolators have been integrated into various buildings and bridges because of their large energy dissipation capability (via their large hysteresis region) and because of their attractive physical compactness [Choi et al. 2006].

In the current investigation, LCR isolators were applied in a benchmark study on the Highway 99 overpass at Second St. in Selma, CA in an effort to improve the performance of the overpass under a ground motion excitation. There are two physical components of LCR isolation that define its constituency. Several layers of rubber that help to support vertical loads while providing lateral flexibility, and the lead core component, which may be represented using the Bouc and Wen model [Wen 1976; Attard and Mignolet 2008], which has a significant physical advantage over bilinear models because of the additional energy dissipation capability that it provides [Ramallo et al. 2002].

The investigation herein focuses on five components. First, dynamic responses of an isolated stiff steel building are examined in order to validate the ability of the LCR isolator to protect structures from far field ground motions. Secondly, the ability of LCR isolators to reduce vibrations in stiff steel buildings subjected to near-field ground motions is analyzed. In this case, the near-field ground motion

is modeled as a nonstationary signal generated as modulated white noise filtered through a Kanai–Tajimi-like spectrum. Thirdly, the procedure is repeated by outfitting the LCR isolator in a building subjected to a component of the 1994 Northridge earthquake. Fourthly, the ability of LCR isolators to control the responses of an eight-story building responding at ‘higher-mode effects’ (HME) of vibration is analyzed under the ground motion of the El Centro ground acceleration record (S00E component) of the 1940 Imperial Valley Earthquake. Finally, a two-span bridge is modeled and analyzed using the El Centro motion.

Two parameters of the LCR isolator, which include the total yield force of the isolator and the pre-yield to post-yield stiffness ratio of the lead-core component, are parametrically varied in order to reduce the responses under the influence of HME or near-field or far-field ground motions and to determine the appropriate design of the LCR isolator. The steel sections of the shear frame buildings are defined using a highly nonlinear material model [Attard 2005], where the member stiffness is assumed to degrade smoothly following a constitutive rule that was developed to assess the behavior of kinematically strain-hardened materials under cyclic conditions. The results are compared to uncontrolled, or as-is, systems that would otherwise degrade highly nonlinearly [Attard 2005]. The yield force of the LCR system was represented using the Bouc and Wen model, whereas the bridge structure was linearly analyzed. The bridge was numerically modeled using site-plan information, and a suitable LCR isolator was designed. Responses of the isolated bridge subjected to the El Centro ground motion were evaluated and compared to those of the nonisolated bridge.

2. Equation of motion and the LCR model

The equation of motion of a structure integrated with LCR isolators and excited by a ground motion acceleration given as \ddot{x}_g is

$$\mathbf{M}\ddot{\mathbf{x}} + \mathbf{C}\dot{\mathbf{x}} + \mathbf{K}\mathbf{x} + \mathbf{F}_R = \mathbf{\Gamma}f - \mathbf{M}\ddot{\mathbf{x}}_g. \quad (1)$$

Here \mathbf{M} and \mathbf{C} are the mass and damping matrices, respectively, where the mass matrix of the structure also includes a grade beam. The Caughey damping matrix [1960], \mathbf{C} , is assembled using all structural modal damping ratios. The displacement vector relative to the ground is defined as $\mathbf{x}(t)$. The stiffness matrix, \mathbf{K} , of the structure and the rubber component of the LCR isolator is elastic and provides a linear nonhysteretic component to the structure-LCR system until yielding occurs. At the point of yielding, the spring force in the post-yielded members remains constant (where $x_i(t) = x_{\text{yield},i}$, where $x_i(t)$ is the individual i -th member displacement, and $x_{\text{yield},i}$ is the respective yield displacement), and the subsequent hysteretic spring force, \mathbf{F}_R , is activated in those members where $x_i(t) > x_{\text{yield},i}$, including the LCR isolator. The nonlinear restoring force, \mathbf{F}_R , accounts for the material anisotropy in inelastic members that undergo cyclic deformations and that may be assumed to kinematically strain harden [Wu 2005; Elnashai and Izzuddin 1993]. The location vector $\mathbf{\Gamma}$ implies the position of the LCR isolator at the grade beam level, and f is a complementary hysteretic force of the lead core component of the LCR isolator of the form

$$f = ZQ_y, \quad (2)$$

where Q_y is the yielding force of the lead core and Z is a hysteretic component of the lead core used to smoothly transition the lead core’s response between the elastic and post-yielded states. Tan and Huang [2000] used a bilinear hysteretic model to evaluate the behavior of LCR isolators in bridges, whereas in

the current investigation, this hysteretic component is represented using the Bouc and Wen model [Bouc 1968; Wen 1976; Attard and Mignolet 2008], the results of which have been shown to consistently match experimental data [Ramallo et al. 2002]. The Bouc and Wen model is given by

$$\dot{Z} = -\alpha |\dot{x}| Z^n - \beta \dot{x} |Z^n| + A\dot{x} \quad \text{for odd values of } n, \quad (3)$$

where α , β , A , and n are shape parameters [Ramallo et al. 2002] and where

$$A = \frac{K_{\text{initial}}}{Q_{\text{total}}}, \quad \alpha = \beta, \quad A = \alpha + \beta. \quad (4)$$

Here K_{initial} is the initial stiffness of the LCR isolator and Q_{total} is the yield force of the LCR isolator which may be calculated as a percentage of a total weight of the structure. The equation of motion (1) is solved herein by marching in time from zero initial conditions by the Newmark Beta scheme assuming a linear change in the acceleration between time steps spread 0.02 s apart. The response simulations are made using an algorithm that was developed as part of this study called BISON (base isolated nonlinear time history analysis) that analyzes the local nonlinear plastic strain and global displacements of any damaged structural members using a nonlinear rule of kinematic strain hardening and formulates the LCR isolator force using the smooth Bouc and Wen model. Because the Bouc and Wen model is intrinsically hysteretic, the parameter n is chosen as ‘one,’ which allows a purely plastic region to exist once the lead core yields and enables a desirable smooth transition between the elastic and inelastic states. The LCR isolator is phenomenologically modeled as shown in Figure 1 and includes a slider that will open to indicate purely plastic behavior of the lead core after it yields ($n = 1$); the relative displacement of the two sides of the closed slider remains zero prior to yielding. Further, the displacement time histories of the lead core would ‘drift’ [Attard 2003; Attard and Mignolet 2005] using the Bouc and Wen model without inclusion of the nonhysteretic rubber components, and thus, these are consequently defined as $k_b x$ and $c_b \dot{x}$ and are included in the model of the LCR isolator as indicated by the equation

$$F_{LCR} = Z Q_y + k_b x + c_b \dot{x}. \quad (5)$$

The total force provided by the LCR isolator is F_{LCR} . The parameters k_b and c_b are the elastic stiffness and damping parameters of the rubber component where the nonhysteretic term, k_b , is included in the build-up of the matrix \mathbf{K} in Equation (1). Once the lead core yields, the inelastic stiffness of the LCR isolator (lead core component + rubber component) is defined as k_b while the Bouc and Wen component of the LCR isolator provides a constant force equal to Q_y that is calculated at $x_i(t) = x_{\text{yield},i}$.

BISON calculates k_b by determining the stiffness of an additional so-called fictitious bottom story (in the case of a building) such that the fundamental period of the entire ‘building + additional fictitious story’ system is equal to 2.5 seconds [Ramallo et al. 2002]. This fictitious bottom story represents the LCR base isolator in the real structure. Caughey damping, which has been used in a previous study by [Attard 2007], is assumed to be 5% in each mode of vibration. The value of K_{initial} is calculated as

$$K_{\text{initial}} = B_{\text{ratio}} \times k_b, \quad (6)$$

where the parameters B_{ratio} and the LCR isolator yield force, Q_{total} , are LCR isolator design parameters that may be appropriately tuned to attain the desired response and controllability of the structure in question. In this study, stiff structures, structures subjected to near-field earthquakes, structures with and

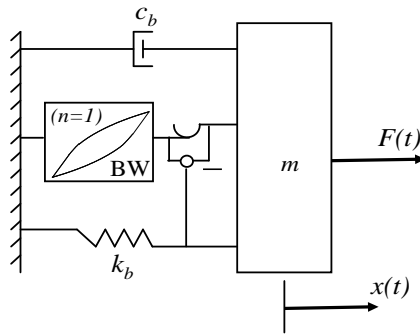


Figure 1. LCR isolator model assuming $n = 1$ in the Bouc and Wen model resulting in a sliding effect (perfectly plastic) after the lead core yields.

without HME, and a 2-span bridge are analyzed parametrically for various values of B_{ratio} and Q_{total} . It has been suggested, however, that the following values be used for the parameter B_{ratio} depending on the peak ground acceleration (PGA) of the ground motion [Spencer et al. 2000]:

$$B_{ratio} = \begin{cases} 6 & \text{if } PGA \leq 0.35 \text{ g,} \\ 10 & \text{if } PGA > 0.35 \text{ g.} \end{cases} \quad (7)$$

3. Numerical examples: Five case studies

3.1. Two-story steel building subjected to the El Centro ground motion. The responses of a two-story steel building designed using LCR isolation were simulated using BISON. The building was excited using the El Centro ground motion with a time-step of 0.02 seconds. The shear frame is supported with a grade beam as shown in Figure 2, and the mass of each story, including the grade beam, is $0.5 \text{ kip}\cdot\text{s}^2/\text{in}$. Each mode of vibration was assumed to have a damping ratio of 5% (assuming Caughey damping), and rock-like soil conditions were considered at the foundation level.

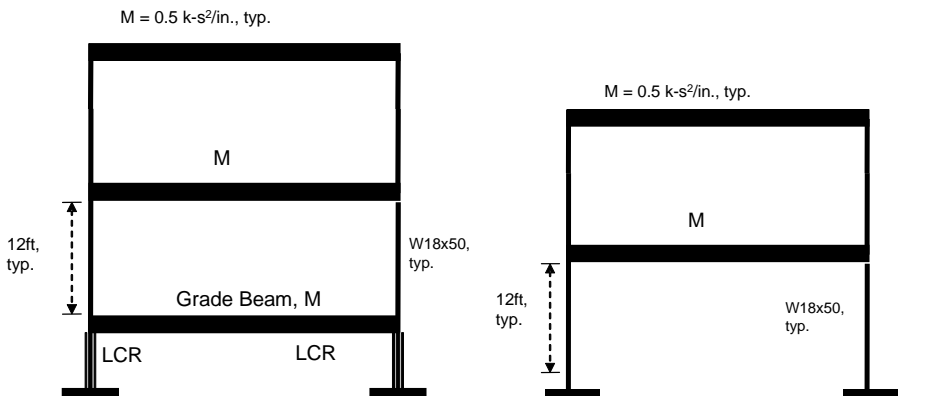


Figure 2. Two story stiff steel building: (a) passively controlled using LCR isolation supported under a grade beam; (b) uncontrolled (“as-is”).

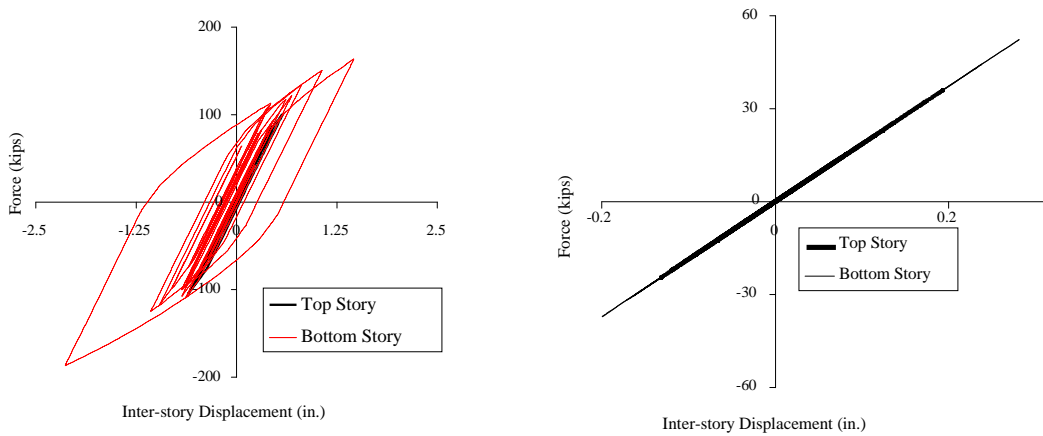


Figure 3. Hysteresis of a 2-story steel building subjected to the 1940 El Centro ground motion: (a) as-is frame [Attard 2005]; (b) isolated frame.

The frame was constructed using $W18 \times 50$ steel sections that were 12 ft tall. The necessary post-yield stiffness of the LCR isolator (k_b) was calculated as 9.87 kip/in, whereby the fundamental period of the isolated structure equaled 2.5 seconds. The LCR isolator was designed to protect the building against moderate ground motions [Ramallo et al. 2002], having a PGA under $0.35 g$'s, with a corresponding B_{ratio} equal to 6; see (7). Skinner et al. [1993] and Spencer et al. [2000] suggest that the value of the yield force of the LCR isolator (Q_{total}) be 5% of the total weight of the structure.

The responses of the building in Figure 2 were marched in time from zero initial conditions using BISON. The force-displacement hysteresis of the as-is, or uncontrolled, frame is shown in Figure 3a, where the $W18 \times 50$ members, especially those of the bottom story, experience significant damage. The nonlinear stiffness degradation model that was embedded in BISON and used to simulate the response time histories was derived following the one proposed by [Attard 2005]. The ability of the LCR isolator to reduce the displacement and velocity time histories is shown in Figures 3b and 4.

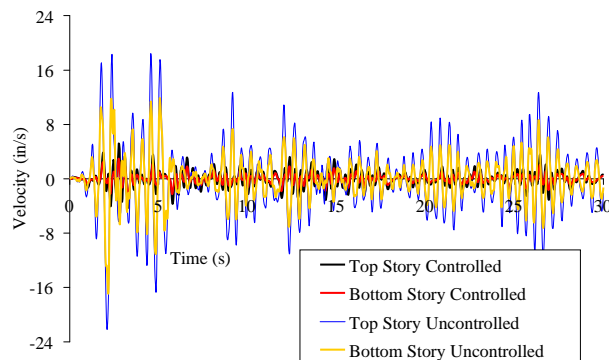


Figure 4. Velocity time histories of top and bottom stories of isolated and as-is frames subjected to the El Centro ground motion.

In [Figure 3b](#), the maximum displacement of the frame with LCR isolation was reduced by over 50% with respect to the maximum displacement of the as-is building, implying that the higher frequencies of the ground motion were adequately filtered through the LCR isolator. Further, the structural members of the isolated frame did not exceed their yield limit (i.e., they remained elastic.). The LCR isolator was also able to significantly reduce the velocity time histories in the two-story building ([Figure 4](#)), which indicates that a significant amount of the input earthquake energy was dissipated, and that the acceleration responses were also reduced.

Finally, [Figure 5a](#) shows the smooth hysteresis of the LCR isolator, which was developed in BISON using the smooth Bouc and Wen model with the following parameters determined for [Equation \(3\)](#): $n = 1$, $A = 3.06$, $\gamma = 1.53$, $\beta = 1.53$.

The perfectly plastic hysteresis of the lead-core component is illustrated in [Figure 5b](#), which shows the smooth transition between the elastic and plastic states ($n = 1$). Finally, [Figure 5c](#) shows that the rubber component remains elastic with a stiffness, k_b , equal to 9.87 kip/in, which is also the post-elastic stiffness of the LCR isolator shown in [Figure 5a](#).

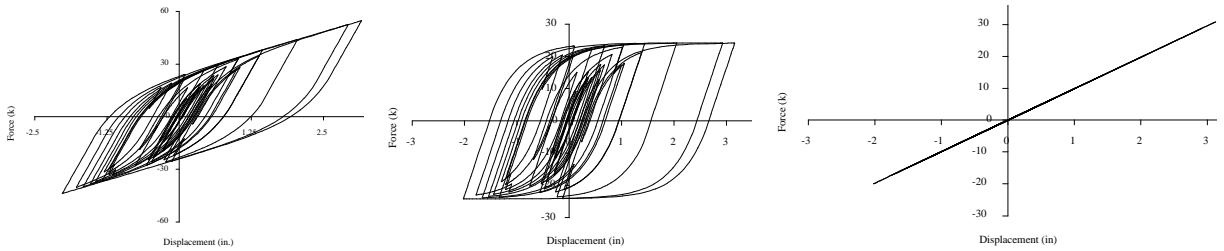


Figure 5. Hysteresis relationships of the (a) LCR isolator, (b) lead-core component using the Bouc and Wen model, and (c) rubber component using $k_b = 9.87$ kip/in.

3.2. Two-story building subjected to an artificial nonstationary excitation. In a second study, BISON was used to simulate the responses of the same two-story building in [Figure 2](#) using a near-field ground excitation that was produced using a nonstationary signal generated as modulated Gaussian white noise filtered through a Kanai–Tajimi-like spectrum, $S_{gg}(\omega)$ equal to

$$S_{gg}(\omega) = G_o \frac{2\pi / \Delta t}{(\omega_g^2 - \omega^2)^2 + (2\zeta_g \omega_g \omega)^2}, \quad (8)$$

where the ground intensity factor of the spectrum, G_o , is 0.126, and the ground frequency and damping terms, ω_g and ζ_g , are 15.6 radians/second and 0.6 [[Clough and Penzien 1993](#)]. It is possible to obtain the time histories of the ground motion (x_g) [[Attard and Mignolet 2008](#)], as the solution response to [Equation \(9\)](#) for a single-degree-of-freedom (single-DOF) ground system subjected to a white noise process, \ddot{x}_{go} , that has a spectral density of $G_o(2\pi / \Delta t)$, where

$$\ddot{x}_g + 2\zeta_g \omega_g \dot{x}_g + \omega_g^2 x_g = -\ddot{x}_{go} \quad (9)$$

and

$$x_g(t) = \int_0^t h(t - \tau) F(\tau) d\tau \quad (10)$$

or

$$x_g(n\Delta t) = - \sum_{m=1}^n \frac{(\ddot{x}_{go}(m\Delta t) + \ddot{x}_{go}((m-1)\Delta t))}{2} h((n-m)\Delta t) \Delta t, \tag{11}$$

where $h(t - \tau)$ is the unit impulse response function, and n is the total number of time steps.

The k_b parameter equals to 9.87 kip/in in order to produce a fundamental period of 2.5 seconds to the isolated structure. The LCR isolator was redesigned with a new value of Q_{total} [Inaudi and Kelly 1993], following the ground excitation, \ddot{x}_g . Park and Otsuka [1999] suggested that the optimal range of Q_{total} be between 14% to 18% of the total weight of the building in order to achieve adequate seismic isolation and control building responses under severe ground motion. Spencer et al. [2000] further suggest that Q_{total} be selected between 13% to 17% of the total building weight and to select the stiffness ratio, B_{ratio} , to be approximately 10 in order to significantly reduce base drifts and moderate the acceleration responses for buildings subjected to severe ground motions. In this light, the LCR yield force, Q_{total} , was selected as 18% and $B_{ratio} = 10$ with due respect of the severe excitation described by (8) and (9). Figure 6 shows the force-displacement hysteresis of the as-is (uncontrolled) and LCR isolated buildings.

A comparison of the two figures indicates that the high energy content of the nonstationary excitation was not adequately dissipated via the lead core component of the LCR isolator. While the displacements of the top story were reduced as was the number of cycles, which indicated that the response remained linear for a longer period of time, the bottom story displacements were only marginally reduced as the structural member stiffness appears significantly nonlinear, which thus implies significant damage. An observation of the velocity time histories in Figure 7a — calculated relative to the LCR isolator velocities, which themselves are calculated relative to the ground — reveals that while the lead core component by definition increases the energy-dissipation capability of the base isolation system, the large velocities in particular indicate that LCR isolation is ineffective in reducing potential structural damages to the W18×50 structural members under this nonstationary excitation. It is in fact observed that the relative velocities of the bottom story of the LCR isolated frame exceed those of the as-is frame (red versus yellow in Figure 7a). In Figure 7b, the LCR isolation appears to have little impact on reducing the displacement

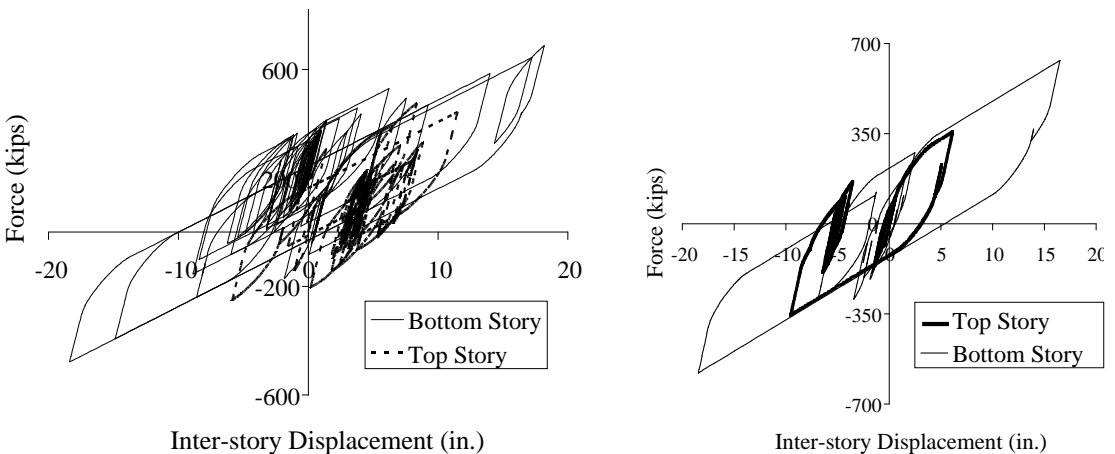


Figure 6. (a) As-is hysteresis. (b) LCR isolated hysteresis of 2-story steel building subjected to a nonstationary ground excitation.

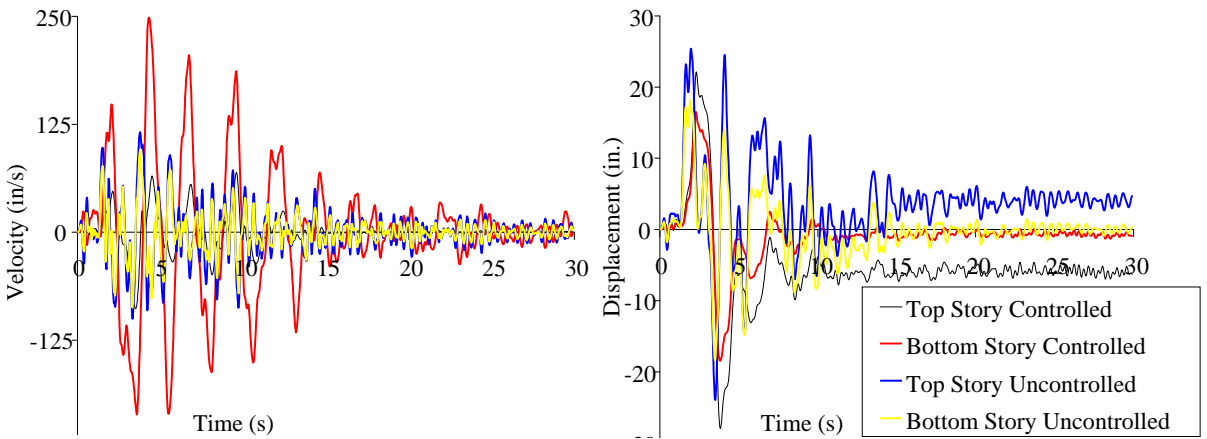


Figure 7. (a) Velocity and (b) displacement time histories of the [Figure 2](#) frame under a nonstationary ground excitation having Kanai–Tajimi-like spectra.

time histories, but does appear to impose an out-of-phase component in the displacement time histories starting at about 6.5 seconds where the frequency abruptly reduces by a factor of about 2.

3.3. Two-story frame subjected to the Northridge (Pacoima Dam) motion. In a third investigation, the frame in [Figure 2](#) was analyzed using the 1994 Northridge ground acceleration record (Pacoima Dam, Upper Left Abutment), which was a near-field ground motion having a PGA of 1.58 g 's. According to (7), B_{ratio} should be equal to 10. Further, the value of Q_y is selected as 0.18. The results are shown in [Figures 8](#) and [9](#), which indicates that LCR isolation is actually effective in reducing damages under this near-field excitation. [Figure 8a](#) shows the degree of structural damage to the $W18 \times 50$ members in the as-is frame, where the damage was significantly reduced ([Figure 8b](#)), when LCR base isolation was integrated into the frame. The force-displacement hysteresis of the LCR isolation system is shown in [Figure 8c](#), and a comparison of [Figures 5a](#) and [8c](#) demonstrates the potential influence that pulse-type, near-field ground motions, such as the Northridge earthquake which was identifiable with historic structural and nonstructural damage, may have on the ability of an LCR isolation system to reduce structural responses, as indicated by the “nonstationary-like” hysteresis shown in [Figure 8c](#). The comparison to [Figure 5a](#), which had been determined using the El Centro earthquake, which was a far-field ground motion, shows that while the lead-core component is to some extent capable of dissipating the energy content of an incoming earthquake, the effects of which may be manifested in the velocity and acceleration time histories of the structural members, this may not necessarily be the case for pulse-type motions (9). In [Figure 9](#), the story-level velocities are calculated relative to the LCR velocities. In this case, LCR isolation ineffectively attenuates the relative velocities, especially in the top story and especially later in the response-history when the velocities are actually shown to increase. This may be correlated to the ‘nonstationary-like’ nature of the LCR hysteresis, and in fact indicates that the velocities are most significantly reduced in either story when the LCR system does not reverse direction which occurs from 4.56 seconds to 5.36 seconds. This would then suggest that LCR isolation in this case precludes a structure from dissipating sufficient energy and reducing the structural velocities.

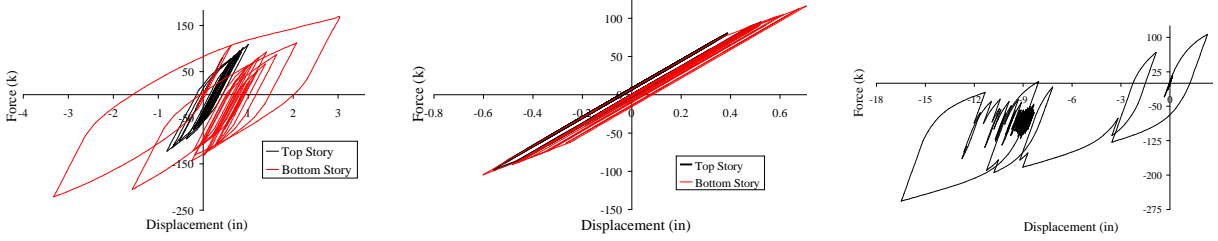


Figure 8. Responses of the LCR isolated 2-story steel frame (Northridge excitation) assuming $B_{ratio} = 10$: (a) as-is force-displacement hysteresis; (b) LCR-controlled hysteresis; (c) LCR hysteresis.

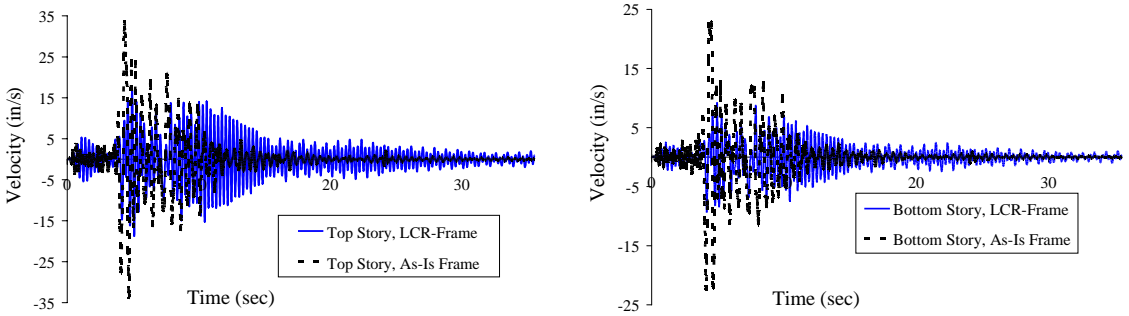


Figure 9. Responses of the LCR isolated 2-story steel frame (Northridge excitation) assuming $B_{ratio} = 10$: (a) top story velocity time histories; (b) bottom story velocity time histories.

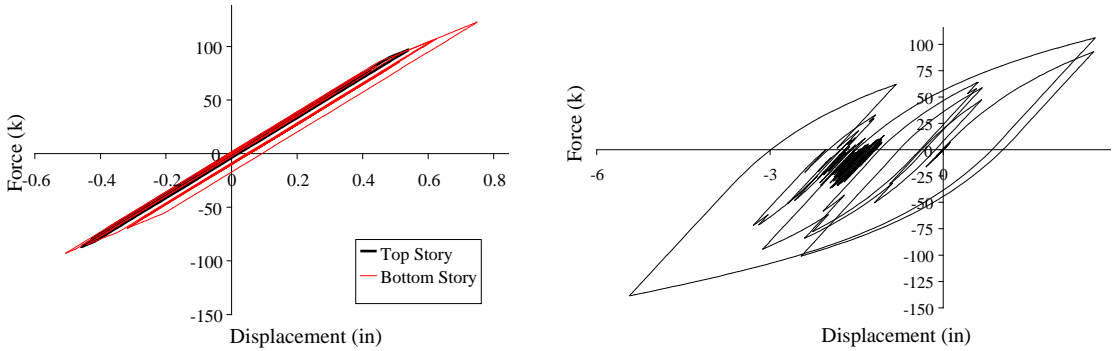


Figure 10. Responses of the LCR isolated 2-story steel frame (Northridge excitation) assuming $B_{ratio} = 6$: (a) force-displacement hysteresis; (b) LCR hysteresis.

In a follow-up to this analysis, a value of $B_{ratio} = 6$, while Q_y was held at 0.18, was used to design a new LCR system to try to mitigate the velocity differences between far-field and near-field excitations. The results are shown in Figures 10 and 11.

While the displacements were again effectively reduced, the structural velocity time histories (Figure 11) calculated relative to the LCR system, are also significantly smaller than those corresponding to

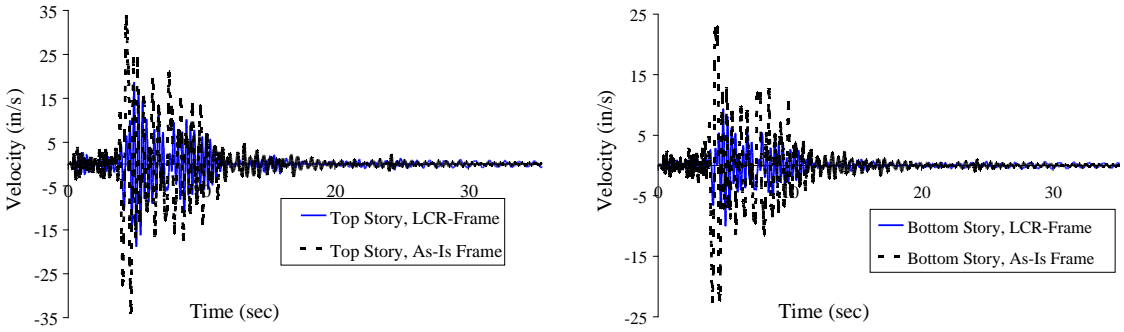


Figure 11. Responses of the LCR isolated 2-story steel frame (Northridge excitation) assuming $B_{\text{ratio}} = 6$: (c) top story velocity time histories; (d) bottom story velocity time histories.

Figure 9, where $B_{\text{ratio}} = 10$. What may be most telling in this comparison is the less nonstationary-like appearance of the LCR hysteresis in Figure 10b.

Finally, Figure 12 shows that the absolute acceleration time histories (structure + LCR isolator + ground accelerations) using a $B_{\text{ratio}} = 10$ versus $B_{\text{ratio}} = 6$. As was the case with the velocity time histories — see Figure 9 versus Figure 11 — a significant disparity exists between top story absolute accelerations for the suggested B_{ratio} of (7), versus the suggested value herein ($B_{\text{ratio}} = 6$). The current findings reveal that at least for near-field motions having large PGAs, LCR isolation systems should be designed using a softer elastic stiffness K_{initial} (i.e., $B_{\text{ratio}} = 6$), which affects energy dissipation of the lead-core component (A) — see (4) and (5) — and which finally results in a more stationary-like hysteresis (where the stiffness of the rubber component, k_b , remains unchanged).

3.4. Eight-story steel building responding with HME. In order to study the influence of HME on the design of an LCR isolation system, an eight story steel shear frame was designed having the properties as shown in Table 1. Each story was designed using W18×50 steel cross sections having a yield stress, σ_{yield} , of 36 ksi. The stiffness of the first story, k_1 , was 9.54 times that of k_7 ; see Table 1. While the stiffness distribution over the height of the building (see 3rd column, Table 1) does not necessarily represent that of an actual building, it does ensure that the building will respond with HME in order to assess the

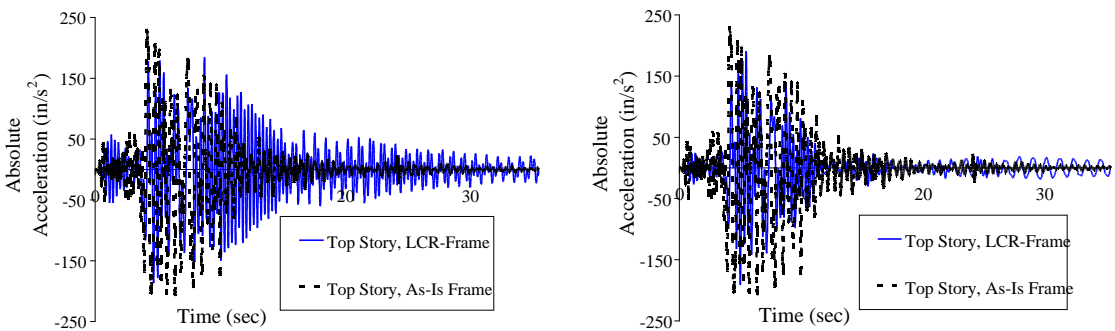


Figure 12. Comparison of absolute accelerations using (a) $B_{\text{ratio}} = 10$ and (b) $B_{\text{ratio}} = 6$.

story	mass (kip·s ² /in)	k_1/k_i	modal mass ratio
8	0.5	8	1.1% (8th mode)
7	0.5	9.54	5.5% (7th mode)
6	0.5	8	0.7% (6th mode)
5	0.5	5.35	0.6% (5th mode)
4	0.5	9.54	8.0% (4th mode)
3	0.5	3.38	8.2% (3rd mode)
2	0.5	1	9.4% (2nd mode)
1	0.5	1	66.4% (1st mode)

Table 1. Property distribution of an eight story stiff steel building with HME.

applicability of LCR isolation in HME-type systems. The modal mass ratio was 66.4%, which was less than 75% [Attard 2007], thus implying the presence of HME. If any of the W18×50 sections were to begin yielding, a smooth nonlinear model previously proposed by [Attard 2005] was assumed to govern the inelastic behavior, which was embedded in BISON. The damping ratio in each mode was assumed to be 5% following the previously mentioned Caughey model for damping.

The elastic stiffness of the LCR rubber component and the post-yield stiffness of the LCR (i.e., k_b) are calculated as 49.5 kip/in by BISON. The eight-story building is subjected to the El Centro ground motion. The value of B_{ratio} is 6, and Q_{total} is 5% of the total weight of the building as previously suggested [Skinner et al. 1993; Spencer et al. 2000].

The responses of the as-is and LCR-controlled buildings are shown in Figure 13. A comparison of the two figures reveals that LCR isolation significantly reduces the absolute maximum displacements (measured relative to the story immediately below, i.e., interstory displacements) on each story in the range of 7.29% to 33.06%, except for the 7th story which showed a slight increase of 0.23% in its interstory displacement, possibly due to the HME.

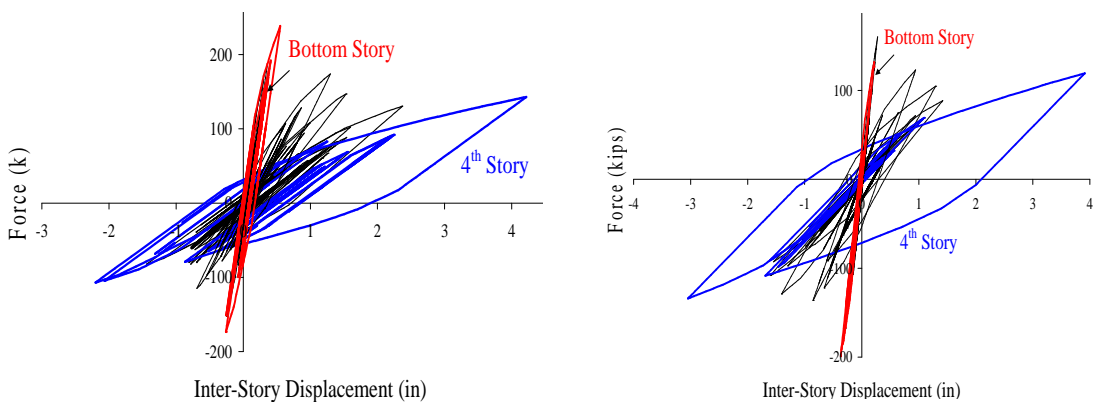


Figure 13. Eight-story steel building subjected to El Centro ground motion: (a) as-is hysteresis; (b) controlled hysteresis.

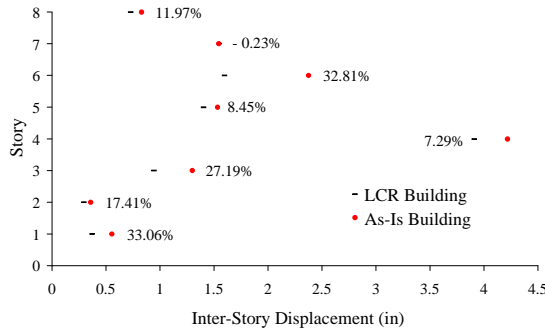


Figure 14. Distribution of interstory displacements between the as-is and LCR-controlled 8-story buildings (with HME); the percent error is shown to the side of each displacement pair per story.

The results are shown graphically in Figure 14, which display the percent error to the side of each interstory displacement. The negative error on story 7 indicates that the interstory displacement increased (0.23%) when LCR isolation was included. All other stories showed a substantial decrease. Note that the stiffness of the 4th story abruptly decreases following the first three ‘stiff’ stories. This sudden difference may be observed in Table 1 between k_1/k_3 and k_1/k_4 , as the structure above the 3rd story in a sense ‘decouples’ from the first three stiff stories, thus enabling the first three stories to behave as a ‘fixed-end’ where stories 4–8 act as a ‘cantilevered end.’ The implication of this is that some dominant lower frequencies (HME exceeding 75%) remain unfiltered by the LCR isolator.

B_{ratio}	Q_{total}	8	7	6	5	4	3	2	1	GB
6	5%	-0.699	-1.501	-1.792	-1.558	3.837	1.016	-0.331	-0.413	-4.436
6	8%	-0.819	-1.734	2.199	-1.352	3.280	0.978	-1.041	0.853	-4.861
6	10%	-0.840	-1.875	-1.927	-1.522	-3.66	-1.078	-0.694	-0.537	-5.711
6	15%	-0.851	1.906	2.905	1.843	5.915	1.590	3.809	-2.459	6.645
6	18%	-0.897	2.696	2.870	1.587	3.388	1.650	1.450	1.355	3.541
10	5%	-0.758	-1.395	1.638	1.027	2.266	-0.815	-1.037	0.689	-3.927
10	8%	0.754	1.378	2.465	1.679	4.388	1.044	0.436	0.474	-10.07
10	10%	-0.891	1.511	2.874	2.168	5.345	1.332	9.817	-10.21	-10.28
10	15%	-0.918	1.821	2.376	1.537	5.063	1.269	0.868	-0.582	10.63
10	18%	-1.152	-2.384	2.210	-1.366	-3.028	3.077	-8.615	7.055	5.815
15	5%	-0.729	-1.677	-2.485	-2.424	-6.414	-3.111	-8.036	9.565	-7.122
15	8%	0.664	1.464	2.478	1.672	4.393	2.694	-5.221	3.863	-5.559
15	10%	-0.823	-1.736	1.741	1.156	-3.049	-1.291	0.642	-0.901	-8.254
15	18%	0.915	1.830	3.189	2.019	4.256	1.229	1.218	0.592	-29.762

Table 2. Maximum interstory displacement as a function of story number, pre-yield to post-yield stiffness ratio, and yield force of the LCR. The last column corresponds to the grade beam.

Table 2 shows the results of a comparative investigation of the influence of parameters B_{ratio} and Q_{total} , where the latter is the yield force of the LCR isolator and is given as a percentage of the total weight of the building, to correlate these parameters to the HME-induced responses, in this case for the 8-story building. The values of B_{ratio} were chosen as 6, 10, and 15, and for each B_{ratio} , the yield forces of the LCR isolator, Q_{total} , were varied between 0.05, 0.08, 0.10, 0.15, and 0.18 (except for $B_{\text{ratio}} = 15$, which did not include $Q_{\text{total}} = 0.15$) as the percentage of the total weight of the building. The responses were marched in BISON for 24 seconds (where the time between time steps, Δt , was assumed to be 0.02 seconds. The maximum displacements of each story in Table 2 include positive and negative signs of the calculated values to indicate the drift direction (right or left) of the maximum absolute displacement. The findings reveal that a combination of $B_{\text{ratio}} = 10$ and $Q_{\text{total}} = 0.05$ produces the smallest collection of interstory displacements and grade beam displacement. To validate these results, the use of $B_{\text{ratio}} = 6$ and $Q_{\text{total}} = 0.05$ will also result in reasonable interstory displacement time histories, although not as good as $B_{\text{ratio}} = 10$ and $Q_{\text{total}} = 0.05$, which is consistent with the findings of [Spencer et al. 2000].

A subsequent examination of the case where $B_{\text{ratio}} = 6$ shows that while an increase in Q_{total} will generally decrease the maximum interstory displacement on the 4th story (except for $Q_{\text{total}} = 0.15$) via a larger dissipative LCR hysteresis and because of the abrupt stiffness change on this floor, the unfiltered incoming lower frequencies tend to excite other pertinent HME resulting in an increase in the maximum displacements of the other stories, including the grade beam. These effects are more apparent as B_{ratio} increases. While a value of $Q_{\text{total}} = 0.18$ provides the best result for the grade beam displacement, this design value typically increases the maximum interstory displacements of many of the other stories. In the case of $B_{\text{ratio}} = 10$, the maximum displacements of many stories increase with an increase in Q_{total} , especially for $Q_{\text{total}} = 0.10$, where the maximum interstory displacements of the stiff 1st and 2nd stories abruptly increase. In this case, the inelastic stiffness of the LCR isolator, k_b , is relatively small and A in (4) and F_{LCR} in (5) are also small indicating that the “stiff” LCR isolator is unable to filter the ground motion frequencies associated with the stiff lower stories of the structure that result in a resonating effect in the response. In the case where $B_{\text{ratio}} = 15$, a decrease in Q_{total} (e.g., $Q_{\text{total}} = 0.05$ or 0.08) needs to be avoided in order to protect and not create a resonant-like response in the stiff lower stories. The results are illustrated in Figure 15, where Q_{total} as indicated is a percentage of the total weight of the building.

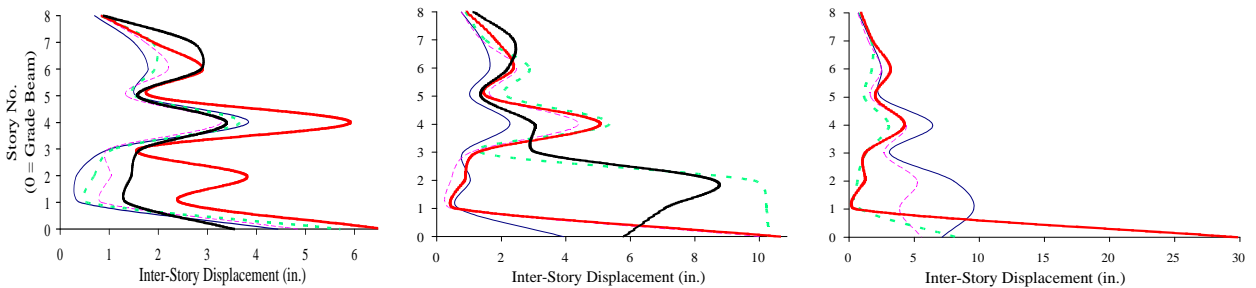


Figure 15. Maximum interstory displacement distributions measuring the impact of Q_{total} (%) on the LCR isolator design, for various B_{ratio} equal to 6 (left), 10 (middle) and 15 (right). The values of Q_{total} are 5 (thin black curve), 8 (magenta dashed curve), 10 (green dashed curve), 15 (red curve), 18 (thick black curve).

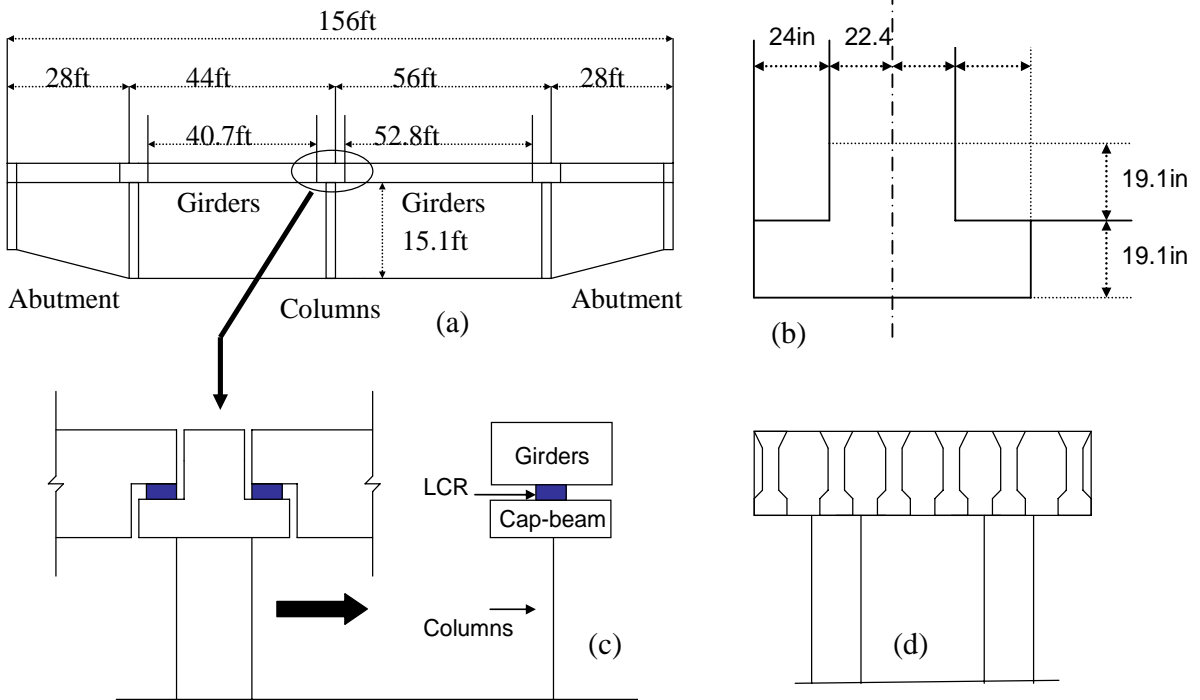


Figure 16. Elevation views of the two-span Highway 99 overpass used in the benchmark and LCR analyses: (a) overpass in the E-W direction; (b) cap girder supporting the LCR isolation pads; (c) 2-DOF model of the girder/cap-beam system; (d) overpass in the N-S direction of traffic.

3.5. Highway bridge protection using LCR isolation. In a final investigation, the highway 99 overpass across Second Street in Selma, CA was outfitted with LCR isolation using a lead core represented by the Bouc and Wen model. The bridge was numerically modeled following specifications of the California Department of Transportation. The LCR isolator was designed for the El Centro earthquake. Figure 16a shows an elevation view of the bridge, which spans 156 ft across two abutments. The bottom flanges of the supporting prestressed concrete girders are 15.1 ft above the ground and are supported by two center columns. An elevation view of the cap-beam is shown in Figure 16b; a detail of the girder-cap connection is shown in Figure 16c. Figure 16d shows the six-girder system together with the two columns aligned perpendicular to the flow of traffic in the North-South direction.

Using a unit weight of concrete of 150 lbs/ft^3 and a compressive concrete strength of 5,000 psi, the modulus of elasticity was calculated as 4,287 ksi, and the weight of the cap-beam was calculated as 89.51 kips. Each of the two columns supports half the weight of each of the two spans, where there are six girders per span; the weight of girders is 115.26 kips, and the diameter of each column is 3.74 ft. To study the effects of LCR base isolation on this bridge, LCR isolators were placed between the cap-beam and the girder to reduce the cap-beam displacement. The isolated bridge was modeled as a two-DOF system composed of the superstructure girders and the substructure cap-beam [Chaudhary et al. 2000; 2001]. The LCR isolator is situated between the cap-beam and the girders; see Figure 16c. The

B_{ratio}	Q_{total}	Girder		Cap-beam	
		displ. (in)	accel. (in/s ²)	displ. (in)	accel. (in/s ²)
6	5%	3.405	161.2	0.0617	163.3
6	10%	3.452	173.4	0.0612	163.3
6	15%	3.643	180.0	0.0604	163.3
10	5%	3.253	156.6	0.0604	163.3
10	10%	2.923	166.3	0.0596	163.2
10	15%	3.057	177.7	0.0589	163.2
15	5%	3.375	151.8	0.0598	163.3
15	10%	2.473	164.7	0.0591	163.2
15	15%	2.520	178.0	0.0584	163.2

Table 3. Maximum absolute displacements and accelerations of the girders and cap-beam (fixed-pin boundary conditions), for various values of B_{ratio} .

as-is system (having no LCR isolation) is modeled as a single-DOF system having mass equal to that of the girders plus the cap-beam. Both systems were analyzed for a fixed-pinned boundary condition, per Caltrans' specs. The parameter B_{ratio} was varied between 6, 10, and 15, and Q_{total} was varied among 0.05, 0.10, 0.15 of the superstructure of the superstructure weight (girders) that was part of a parametric study used to design the LCR isolator for this bridge. For the assumed fixed-pinned boundary conditions, the post-yield stiffness of the LCR isolator was calculated as 1.89 kips/in using BISON that had resulted in a natural period of vibration for the system equal to 2.5 seconds after the lead-core had yielded. The maximum absolute displacements and accelerations of the girders and cap-beam are shown in Table 3, where Q_{total} is again given a percentage of the total weight of the bridge.

Table 3 shows that B_{ratio} has virtually no impact on the cap-beam accelerations and tends to result in a decrease in cap-beam displacements as it increases. The smallest absolute displacements of the girders (2.473 in) and cap-beam (0.0584 in) occur using $Q_{\text{total}} = 0.10$ and $B_{\text{ratio}} = 15$, and $Q_{\text{total}} = 0.15$ and $B_{\text{ratio}} = 15$, respectively. The girder accelerations (164.7 in/s²) were smallest when $Q_{\text{total}} = 0.10$ and $B_{\text{ratio}} = 15$, and the cap-beam displacement (0.0591 in) was also adequately reduced using this combination in an ideal LCR design for a fixed-pinned connection. A comparison of the time history displacements and time history accelerations to those of the as-is case shows that the displacement demands on the cap-beam were reduced by 50% using LCR isolation (Figure 17a), and many of the time history accelerations of the cap-beam were also reduced, as indicated in Figure 17b. Figure 18 shows the hysteresis of the LCR isolator that had been modeled using the Bouc and Wen equations where $Q_{\text{total}} = 0.10$ and $B_{\text{ratio}} = 15$.

4. Conclusions

The ability of lead-core rubber base isolation (LCR) to reduce responses of buildings and bridges is investigated. Five case studies, including parametric analyses, of a stiff two-story structural steel building under (1) the El Centro (S00E component) ground motion, (2) a nonstationary signal, which was modeled

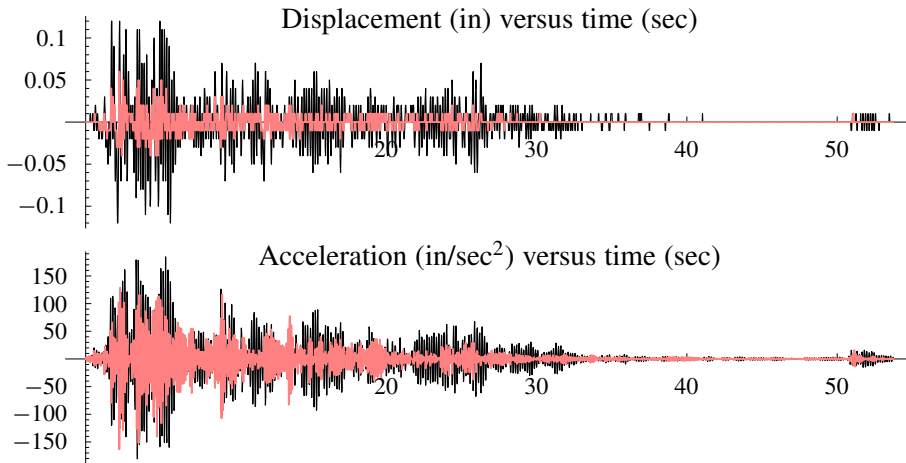


Figure 17. Response of the overpass bridge in Selma, CA with $B_{\text{ratio}} = 15$, $Q_{\text{total}} = 10$. Black curve: as-is response; superimposed lighter curve: LCR-isolated response.

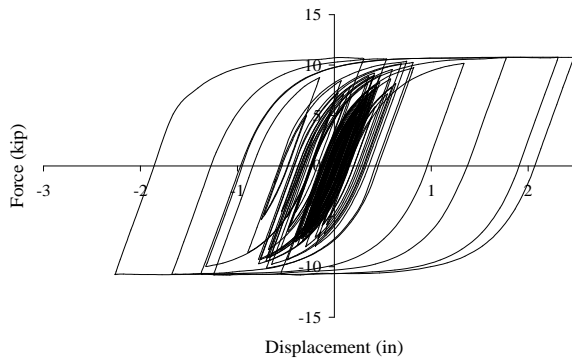


Figure 18. Response of the overpass bridge in Selma, CA with $B_{\text{ratio}} = 15$, $Q_{\text{total}} = 10$: LCR isolator's hysteresis.

as modulated Gaussian white noise passed through a Kanai–Tajimi filter, and (3) the Northridge (Pacoima Dam component) ground motion were analyzed. In addition, an eight-story steel building (4) exhibiting higher-mode effects was also studied, and a prestressed concrete bridge overpass (5) in Selma, CA were also examined using an in-house developed algorithm, called BISON (base isolation in nonlinear time history analysis). It appears that in all five cases, except under the action of the nonstationary signal input, parameters used to design the LCR isolator may be selected to very adequately reduce displacements, velocities, and accelerations by appropriately tuning the ratio of the LCR elastic-to-inelastic stiffness and the LCR yield force. Both parameters affect the LCR hysteresis, which was modeled using the Bouc and Wen model. In the cases where the LCR hysteresis had a stationary-like appearance, the responses were very adequately controlled, which was not the case under the nonstationary signal, where the high energy content associated with the low frequencies of the input appeared to not be adequately dissipated by the LCR isolator. However, in the four other cases, LCR isolation appears to be a very effective means of reducing seismic structural demands if appropriately tuned.

Acknowledgements

The writers gratefully acknowledge the support of this research by the California Department of Transportation (Caltrans) and especially the help of Mr. Mark Der Matoian, Mr. Robert James, and Mr. Alan Vong, and additionally for the support provided by Flatiron Constructors, Inc. (FCI) and Mr. Zeb Lemke.

References

- [Attard 2003] T. L. Attard, *Modeling of higher-mode effects in various structures using a pushover analysis*, Ph.D. Thesis, Arizona State University, Tempe, AZ, 2003.
- [Attard 2005] T. L. Attard, “Post-yield material nonlinearity: optimal homogeneous shear-frame sections and hysteretic behavior”, *Int. J. Solids Struct.* **42**:21–22 (2005), 5656–5668.
- [Attard 2007] T. L. Attard, “Controlling all interstory displacements in highly nonlinear steel building using optimal viscous damping”, *J. Struct. Eng. (ASCE)* **133**:9 (2007), 1331–1340.
- [Attard and Mignolet 2005] T. L. Attard and M. P. Mignolet, “Evolutionary model for random plastic analyses of shear-frame buildings using a detailed degradation model”, pp. 533–540 in *Safety and reliability of engineering systems and structures: proceedings of the 9th International Conference on Structural Safety and Reliability (ICOSSAR 2005)* (Rome, 2005), edited by G. Augusti et al., Millpress, Rotterdam, 2005.
- [Attard and Mignolet 2008] T. L. Attard and M. P. Mignolet, “Random plastic analysis using a constitutive model to predict the evolutionary stress-related responses and time passages to failure”, *J. Eng. Mech. (ASCE)* **134**:10 (2008), 881–891.
- [Boroschek et al. 2003] R. L. Boroschek, M. O. Moroni, and M. Sarrazin, “Dynamic characteristics of a long span seismic isolated bridge”, *Eng. Struct.* **25**:12 (2003), 1479–1490.
- [Bouc 1968] R. Bouc, “Forced vibration of a mechanical system with hysteresis”, pp. 315 in *Proceedings of the Fourth Conference on Nonlinear Oscillations* (Prague, 1967), edited by J. Gonda and F. Jelínek, Academia Publishing, Prague, 1968. Abstract.
- [Caughey 1960] T. K. Caughey, “Classical normal modes in damped linear dynamic systems”, *J. Appl. Mech. (ASME)* **27**:2 (1960), 269–271.
- [Chaudhary et al. 2000] M. T. A. Chaudhary, M. Abe, Y. Fujino, and J. Yoshida, “System identification of two base-isolated bridges using seismic records”, *J. Struct. Eng. (ASCE)* **126**:10 (2000), 1187–1195.
- [Chaudhary et al. 2001] M. T. A. Chaudhary, M. Abe, and Y. Fujino, “Performance evaluation of base-isolated Yama-agé bridge with high damping rubber bearings using recorded seismic data”, *Eng. Struct.* **23**:8 (2001), 902–910.
- [Choi et al. 2006] E. Choi, T. H. Nam, J. T. Oh, and B. S. Cho, “An isolation bearing for highway bridges using shape memory alloys”, *Mater. Sci. Eng. A* **438–440** (2006), 1081–1084.
- [Clough and Penzien 1993] R. Clough and J. Penzien, *Dynamics of structures*, 2nd ed., pp. 599–602, McGraw-Hill, New York, 1993.
- [Dicleli 2002] M. Dicleli, “Seismic design of lifeline bridge using hybrid seismic isolation”, *J. Bridge Eng.* **7**:2 (2002), 94–103.
- [Dimizas and Koumoussis 2005] P. C. Dimizas and V. K. Koumoussis, “System identification of non-linear hysteretic systems with application to friction pendulum isolation systems”, pp. 321–328 in *Proceedings of the 5th GRACM International Congress on Computational Mechanics (GRACM 05)* (Limassol, 2005), vol. 1, edited by G. Georgiou et al., Kantzilaris, Nicosia, 2005.
- [Dolce et al. 2007] M. Dolce, D. Cardone, and G. Palermo, “Seismic isolation of bridges using isolation systems based on flat sliding bearings”, *B. Earthq. Eng.* **5**:4 (2007), 491–509.
- [Elnashai and Izzuddin 1993] A. S. Elnashai and B. A. Izzuddin, “Modelling of material non-linearities in steel structures subjected to transient dynamic loading”, *Earthquake Eng. Struct. Dyn.* **22**:6 (1993), 509–532.
- [Furukawa et al. 2005] T. Furukawa, M. Ito, K. Izawa, and M. N. Noori, “System identification of base-isolated building using seismic response data”, *J. Eng. Mech. (ASCE)* **131**:3 (2005), 268–275.
- [Hart and Wong 2000] C. G. Hart and K. Wong, *Structural dynamics for structural engineers*, Wiley, New York, 2000.

- [Hwang and Chiou 1996] J. S. Hwang and J. M. Chiou, “An equivalent linear model of lead-rubber seismic isolation bearings”, *Eng. Struct.* **18**:7 (1996), 528–536.
- [Inaudi and Kelly 1993] J. A. Inaudi and J. M. Kelly, “Optimum damping in linear isolation system”, *Earthquake Eng. Struct. Dyn.* **22**:7 (1993), 583–598.
- [Jangid 2004] R. S. Jangid, “Seismic response of isolated bridges”, *J. Bridge Eng.* **9**:2 (2004), 156–166.
- [Kelly 1999] J. M. Kelly, “The role of damping in seismic isolation”, *Earthquake Eng. Struct. Dyn.* **28**:1 (1999), 3–20.
- [Kikuchi and Aiken 1997] M. Kikuchi and I. D. Aiken, “An analytical hysteresis model for elastomeric seismic isolation bearings”, *Earthquake Eng. Struct. Dyn.* **26**:2 (1997), 215–231.
- [Matsagar and Jangid 2004] V. A. Matsagar and R. S. Jangid, “Influence of isolator characteristics on the response of base-isolated structures”, *Eng. Struct.* **26**:12 (2004), 1735–1749.
- [Matsagar and Jangid 2008] V. A. Matsagar and R. S. Jangid, “Base isolation for seismic retrofitting of structures”, *Pract. Period. Struct. Des. Constr.* **13**:4 (2008), 175–185.
- [Park and Otsuka 1999] J.-G. Park and H. Otsuka, “Optimal yield level of bilinear seismic isolation devices”, *Earthquake Eng. Struct. Dyn.* **28**:9 (1999), 941–955.
- [Poza et al. 2006] F. Poza, F. Ikhouane, G. Pujol, and J. Rodellar, “Adaptive backstepping control of hysteretic base-isolated structures”, *J. Vib. Control* **12**:4 (2006), 373–394.
- [Ramallo et al. 2002] J. C. Ramallo, E. A. Johnson, and B. F. Spencer, Jr., “‘Smart’ base isolation systems”, *J. Eng. Mech. (ASCE)* **128**:10 (2002), 1088–1099.
- [Shen et al. 2004] J. Shen, M.-H. Tsai, K.-C. Chang, and G.-C. Lee, “Performance of a seismically isolated bridge under near-fault earthquake ground motions”, *J. Struct. Eng. (ASCE)* **130**:6 (2004), 861–868.
- [Skinner et al. 1993] R. I. Skinner, W. H. Robinson, and G. H. McVerry, *An introduction to seismic isolation*, Wiley, Chichester, 1993.
- [Soneji and Jangid 2006] B. B. Soneji and R. S. Jangid, “Effectiveness of seismic isolation for cable-stayed bridges”, *Int. J. Struct. Stabil. Dyn.* **6**:1 (2006), 77–96.
- [Spencer et al. 2000] B. F. Spencer, Jr., E. A. Johnson, and J. C. Ramallo, “‘Smart’ isolation for seismic control”, *Trans. Jpn. Soc. Mech. Eng. C* **43**:3 (2000), 704–711.
- [Tan and Huang 2000] R. Y. Tan and M. C. Huang, “System identification of a bridge with lead-rubber bearings”, *Comput. Struct.* **74**:3 (2000), 267–280.
- [Tsopelas and Constantinou 1997] P. Tsopelas and M. C. Constantinou, “Study of elastoplastic bridge seismic isolation system”, *J. Struct. Eng. (ASCE)* **123**:4 (1997), 489–498.
- [Tsopelas et al. 1996] P. Tsopelas, M. C. Constantinou, S. Okamoto, S. Fujii, and D. Ozaki, “Experimental study of bridge seismic sliding isolation systems”, *Eng. Struct.* **18**:4 (1996), 301–310.
- [Wen 1976] Y. K. Wen, “Method for random vibration of hysteretic systems”, *J. Eng. Mech. (ASCE)* **102**:2 (1976), 249–262.
- [Wu 2005] H. C. Wu, *Continuum mechanics and plasticity*, Chapman and Hall/CRC Press, Boca Raton, FL, 2005.
- [Yoshikawa et al. 2000] M. Yoshikawa, H. Hayashi, S. Kawakita, and M. Hayashida, “Construction of Benten Viaduct, rigid-frame bridge with seismic isolators at the foot of piers”, *Cement Concrete Compos.* **22**:1 (2000), 39–46.

Received 4 Apr 2009. Accepted 16 May 2009.

THOMAS L. ATTARD: tattard@utk.edu

Department of Civil and Environmental Engineering, The University of Tennessee, 113 Perkins Hall, Knoxville, TN 37996-2010, United States

KITTINAN DHIRADHAMVIT: omchin@hotmail.com

Department of Civil and Environmental Engineering, The University of Tennessee, Estabrook Hall, Knoxville, TN 37996-2010, United States

HOMOGENIZATION AND EFFECTIVE PROPERTIES OF PERIODIC THERMOMAGNETOELECTROELASTIC COMPOSITES

JULIAN BRAVO-CASTILLERO, REINALDO RODRÍGUEZ-RAMOS,
HOUARI MECHKOUR, JOSÉ A. OTERO, JOANKA HERNÁNDEZ CABANAS,
LAZARO MAYKEL SIXTO, RAUL GUINOVART-DÍAZ AND FEDERICO J. SABINA

Using asymptotic homogenization, we derive the local problems and the corresponding homogenized coefficients of periodic thermomagnetoelastoelectric heterogeneous media. The theory is applied to obtain analytical expressions for all effective properties of an important class of periodic multilaminated composites. Universal relations involving homogenized thermal coefficients of two-phase laminated and fibrous piezoelectric/piezomagnetic periodic composites, with transversely isotropic constituents, are obtained. Theoretical evidence is shown for the existence of pyroelectric and pyromagnetic effects even if neither phase exhibits them. Numerical calculations and comparisons with others theories are included.

1. Introduction

A coupled effect is the capacity to convert system energy from one type to another (for instance, among magnetic, electric, mechanical, and thermal effects). Composites made of thermopiezoelectric and thermomagnetic components exhibit a magnetoelectric effect that is not present in their individual constituents. The knowledge of the global properties of such composites allows us to address the control of the response of smart structures whose phases are, in general, made of thermomagnetoelastoelectric (TMEE) materials.

Different methods have been employed to estimate the overall properties of TMEE periodic composites. For instance, [Li and Dunn \[1998b\]](#) developed a micromechanical methodology based on the mean field approach of [Mori and Tanaka \[1973\]](#) combined with the Eshelby tensor [[Li and Dunn 1998a](#)] to derive explicit formulae for the effective coefficients of two-phase laminated and fibrous composites. [Aboudi \[2001\]](#) employed a general micromechanical homogenization theory to investigate the global behavior of multiphase TMEE materials. His results show good agreement with those he derived in [[Aboudi 1998](#)], via the generalized method of cells, and those obtained in the work of [Li and Dunn \[1998b\]](#). Using the theory of uniform fields in TMEE heterogeneous media by proper boundary conditions, universal relations between the effective properties of two-phase fibrous composites were derived in [[Benveniste 1995](#)]. In all these works, like in the present paper, the fully coupled constitutive laws for TMEE materials were used. Based on the asymptotic homogenization method, analytical expressions

Keywords: thermomagnetoelastoelectric composites, effective properties, universal relations, laminated, fibrous composites, homogenization, periodic heterogeneous materials.

This work was sponsored by CONACyT Project Number 101489, and CITMA PNCIT IBMFQC Project Number 09-2004. JBC and RRR would like to acknowledge the support of Departamento de Ciencias Básicas at Instituto Tecnológico y de Estudios Superiores de Monterrey, Campus Estado de México. The partial support of COIC-STIA-239-08 UNAM is recognized.

for magnetoelastic unidirectional two-phase fibrous composites with circular cross section fibers and transversely isotropic constituents were derived in [Camacho-Montes et al. 2006].

In this paper, based on the asymptotic homogenization method, the general theory developed in [Bravo-Castillero et al. 2008], for magnetoelastic heterogeneous media, is applied to determine analytical formulae for the effective properties of periodic multilaminated TMEE composites. The formulae obtained generalize those that appear in [Castillero et al. 1998] and in [Galka et al. 1996], where piezoelectric and thermopiezoelectric periodic composites, respectively, were studied. Here a general formula is presented in a unified way which is more adequate for computational implementation. This unified formula is specified for one example of multilayered composites with any finite number of transversely isotropic TMEE constituents to obtain all their effective coefficients. For the particular case of two-laminated media, such effective coefficients prove to satisfy the universal relations derived by Benveniste and Dvorak [1992] for orthotropic fibrous composites. Finally, by using a link between four local problems on the periodic cell for two-phase unidirectional fibrous TMEE composites with transversely isotropic constituents and arbitrary smoothness shape of the fibre cross section, universal relations involving pyromagnetic, pyroelectric, thermoelastic, elastic, piezoelectric, and piezomagnetic effective coefficients are derived [Benveniste 1995]. In particular, a proportion relating the pyromagnetic and pyroelectric components in the direction of the fibers is found. The constant of proportionality involves information relative to the piezoelectric and piezomagnetic constants of both phases.

2. Constitutive laws and equilibrium equations of TMEE materials

Let $\Omega \subset \mathbb{R}^3$ be open, bounded and sufficiently regular, with boundary $\partial\Omega$. The properties of a three-dimensional body, that is, Ω , made of a heterogeneous TMEE material are described by the elasticity four-order tensor c , the piezoelectric coupling third-order tensor e , the piezomagnetic coupling third-order tensor q , the electric permittivity second-order tensor κ , the magnetic permeability second-order tensor μ , the magnetoelastic second-order tensor α , the thermoelastic second-order tensor λ , the pyroelectric vector p , and the pyromagnetic vector m . Also, η stands for the heat conductivity second-order tensor, and $\beta=C_e/T_0$; C_e is the specific heat at constant strain per unit volume and T_0 is the reference (absolute) temperature. Thus, with Y the so-called unit periodic cell and the small parameter $\varepsilon > 0$, the material functions just introduced are εY -periodic in the local variable $y = x/\varepsilon$, and for each $x \in \Omega$ we write, for instance,

$$\begin{aligned} c_\varepsilon^{ijkl}(x) &= c^{ijkl}(x/\varepsilon), & e_\varepsilon^{ikl}(x) &= e^{ikl}(x/\varepsilon), & q_\varepsilon^{ikl}(x) &= q^{ikl}(x/\varepsilon), & \kappa_\varepsilon^{ij}(x) &= \kappa^{ij}(x/\varepsilon), \\ \mu_\varepsilon^{ij}(x) &= \mu^{ij}(x/\varepsilon), & \alpha_\varepsilon^{ij}(x) &= \alpha^{ij}(x/\varepsilon), & \lambda_\varepsilon^{ij}(x) &= \lambda^{ij}(x/\varepsilon), & p_\varepsilon^i(x) &= p^i(x/\varepsilon), \\ m_\varepsilon^i(x) &= m^i(x/\varepsilon), & \eta_\varepsilon^{ij}(x) &= \eta^{ij}(x/\varepsilon), & \beta_\varepsilon(x) &= \beta(x/\varepsilon). \end{aligned}$$

Latin indices run over the set $\{1, 2, 3\}$. The Einstein summation convention will be used throughout. The tensors of material functions satisfy the usual symmetry conditions:

$$\begin{aligned} c_\varepsilon^{ijkl} &= c_\varepsilon^{jikl} = c_\varepsilon^{ijlk} = c_\varepsilon^{klij}, & e_\varepsilon^{ikl} &= e_\varepsilon^{ilk}, & q_\varepsilon^{ikl} &= q_\varepsilon^{ilk}, & \kappa_\varepsilon^{ij} &= \kappa_\varepsilon^{ji}, \\ \mu_\varepsilon^{ij} &= \mu_\varepsilon^{ji}, & \alpha_\varepsilon^{ij} &= \alpha_\varepsilon^{ji}, & \lambda_\varepsilon^{ij} &= \lambda_\varepsilon^{ji}, & \eta_\varepsilon^{ij} &= \eta_\varepsilon^{ji}. \end{aligned}$$

We make the further assumption that *there exists a constant $\delta > 0$ such that, for any $a \in \mathbb{R}^3$ and any*

symmetric 3×3 matrix X ,

$$\left. \begin{aligned} c_\varepsilon^{ijkl}(x)X_{ij}X_{kl} &\geq \delta X_{ij}X_{ij} \\ \kappa_\varepsilon^{ij}(x)a_ia_j &\geq \delta a_ia_i \\ \mu_\varepsilon^{ij}(x)a_ia_j &\geq \delta a_ia_i \\ \lambda_\varepsilon^{ij}(x)a_ia_j &\geq \delta a_ia_i \\ \eta_\varepsilon^{ij}(x)a_ia_j &\geq \delta a_ia_i \end{aligned} \right\} \text{for almost every } x \in \Omega.$$

For a fixed $\varepsilon > 0$, the TMEE behavior of this body is given by the elastic displacement field $u_\varepsilon = (u_\varepsilon^i)$, the electric potential φ_ε , the magnetic potential ψ_ε , and the entropy s_ε , which satisfy the equilibrium equations

$$\left. \begin{aligned} -\operatorname{div} \sigma_\varepsilon(u_\varepsilon, \varphi_\varepsilon, \psi_\varepsilon, s_\varepsilon) &= f \\ -\operatorname{div} D_\varepsilon(u_\varepsilon, \varphi_\varepsilon, \psi_\varepsilon, s_\varepsilon) &= 0 \\ -\operatorname{div} B_\varepsilon(u_\varepsilon, \varphi_\varepsilon, \psi_\varepsilon, s_\varepsilon) &= 0 \\ -\operatorname{div} T_\varepsilon(u_\varepsilon, \varphi_\varepsilon, \psi_\varepsilon, s_\varepsilon) &= 0 \end{aligned} \right\} \text{in } \Omega, \tag{2-1}$$

where $\sigma_\varepsilon = (\sigma_\varepsilon^{ij})$ is the stress tensor, $D_\varepsilon = (D_\varepsilon^i)$ the electric displacement, $B_\varepsilon = (B_\varepsilon^i)$ the magnetic displacement, and $T_\varepsilon = (\eta_\varepsilon^{ij} \partial_j \theta_\varepsilon)$ the flux of the temperature θ_ε . Also $\partial_i = \partial / \partial x_i$, $(\operatorname{div} \sigma_\varepsilon)^i = \partial_j \sigma_\varepsilon^{ij}$, $\operatorname{div} D_\varepsilon = \partial_i D_\varepsilon^i$, $\operatorname{div} B_\varepsilon = \partial_i B_\varepsilon^i$, and $\operatorname{div} T_\varepsilon = \partial_i (\eta_\varepsilon^{ij} \partial_j \theta_\varepsilon)$, $x = (x_i) \in \Omega$. The constitutive equations are given by

$$\begin{aligned} \sigma_\varepsilon^{ij}(u_\varepsilon, \varphi_\varepsilon, \psi_\varepsilon, s_\varepsilon) &= c_\varepsilon^{ijkl} s_{kj}(u_\varepsilon) + e_\varepsilon^{mij} \partial_m \varphi_\varepsilon + q_\varepsilon^{nij} \partial_n \psi_\varepsilon - \lambda_\varepsilon^{ij} s_\varepsilon, \\ D_\varepsilon^i(u_\varepsilon, \varphi_\varepsilon, \psi_\varepsilon, s_\varepsilon) &= e_\varepsilon^{ikl} s_{kl}(u_\varepsilon) - \kappa_\varepsilon^{im} \partial_m \varphi_\varepsilon - \alpha_\varepsilon^{in} \partial_n \psi_\varepsilon + p_\varepsilon^i s_\varepsilon, \\ B_\varepsilon^i(u_\varepsilon, \varphi_\varepsilon, \psi_\varepsilon, s_\varepsilon) &= q_\varepsilon^{ikl} s_{kl}(u_\varepsilon) - \alpha_\varepsilon^{im} \partial_m \varphi_\varepsilon - \mu_\varepsilon^{in} \partial_n \psi_\varepsilon + m_\varepsilon^i s_\varepsilon, \\ \theta_\varepsilon(u_\varepsilon, \varphi_\varepsilon, \psi_\varepsilon, s_\varepsilon) &= -\lambda_\varepsilon^{kl} s_{kl}(u_\varepsilon) + p_\varepsilon^m \partial_m \varphi_\varepsilon + m_\varepsilon^n \partial_n \psi_\varepsilon + \beta_\varepsilon s_\varepsilon, \end{aligned} \tag{2-2}$$

where $s_{kl}(u_\varepsilon)$, $\partial_k \varphi_\varepsilon$, and $\partial_k \psi_\varepsilon$ are, respectively, the linearized strain and the gradients of the electric and magnetic potentials, and $s_{kl}(u_\varepsilon) = \frac{1}{2}(\partial_k u_\varepsilon^l + \partial_l u_\varepsilon^k)$. In (2-1) we have a system of six partial differential equations for finding u_ε , φ_ε , ψ_ε , and s_ε . It has to be completed by suitable boundary conditions. For instance, we can assume homogeneous boundary conditions ($u_\varepsilon = 0$, $\varphi_\varepsilon = 0$, $\psi_\varepsilon = 0$, and $s_\varepsilon = 0$) on the external boundary $\partial\Omega$.

3. Homogenization

The method of two-scale asymptotic expansions will be applied in order to find the homogenized system. The solution of (2-1)–(2-2) can be sought in the form

$$\begin{aligned} u_\varepsilon(x) &= u^0(x, y) + \varepsilon u^1(x, y) + \dots, \\ \varphi_\varepsilon(x) &= \varphi^0(x, y) + \varepsilon \varphi^1(x, y) + \dots, \\ \psi_\varepsilon(x) &= \psi^0(x, y) + \varepsilon \psi^1(x, y) + \dots, \\ s_\varepsilon(x) &= s^0(x, y) + \varepsilon s^1(x, y) + \dots, \end{aligned} \tag{3-1}$$

where $u^0(x, y), u^1(x, y), \dots, \varphi^0(x, y), \varphi^1(x, y), \dots, \psi^0(x, y), \psi^1(x, y), \dots, s^0(x, y), s^1(x, y), \dots$, are Y -periodic functions with respect to the second variable $y = x/\varepsilon$. Similarly, as in the linear thermopiezoelectric or magneto-electroelastic problem (see, for instance, [Galka et al. 1996; Bravo-Castillero et al. 2008]), the functions $u^0(x, y), \varphi^0(x, y)$, and $\psi^0(x, y)$ do not depend on y . However, in general, s^0 depends on both x and y . See [Galka et al. 1992] for a complete description in the thermopiezoelectric case. Due to the linearity of this problem and assuming both regularity of the inclusions' shapes and smoothness in the variation of coefficients, we have

$$\begin{aligned} u^1(x, y) &= s_{rt,x}(u^0(x))w^{rt}(y) + \partial_{m,x}\varphi^0(x)g^m(y) + \partial_{n,x}\psi^0(x)h^n(y) + \theta^h(x)\Gamma(y), \\ \varphi^1(x, y) &= s_{rt,x}(u^0(x))\zeta^{rt}(y) + \partial_{m,x}\varphi^0(x)\pi^m(y) + \partial_{n,x}\psi^0(x)\chi^n(y) + \theta^h(x)Q(y), \\ \psi^1(x, y) &= s_{rt,x}(u^0(x))\eta^{rt}(y) + \partial_{m,x}\varphi^0(x)\xi^m(y) + \partial_{n,x}\psi^0(x)\gamma^n(y) + \theta^h(x)R(y), \end{aligned} \tag{3-2}$$

where $\partial_{m,x}\phi = \partial\phi/\partial x_m$ and $s_{rt,x}(u) = \frac{1}{2}(\partial u_r/\partial x_t + \partial u_t/\partial x_r)$. The functions $u^0(x), \varphi^0(x)$, and $\psi^0(x)$ are, respectively, the mechanical displacement field, the electric potential and the magnetic potential of the effective (homogenized) TMEE body while its temperature field θ^h is given by

$$\theta^h(x) = -\langle \lambda^{kl} \rangle (\partial_{l,x} u_k^0 + \partial_{k,y} u_l^1) + \langle p^k \rangle (\partial_{k,x} \varphi^0 + \partial_{k,y} \varphi^1) + \langle m^k \rangle (\partial_{k,x} \psi^0 + \partial_{k,y} \psi^1) + \langle \beta \rangle s^0(x, y),$$

where $\langle g \rangle = |Y|^{-1} \int_Y g(y) dy$ and the angle brackets denote averaging over the periodic cell Y . Note that in general s^0 depends not only on x but also on the microscopic variable y . The local functions $w^{rt}, \zeta^{rt}, \eta^{rt}; g^m, \pi^m, \xi^m; h^m, \chi^m, \gamma^m$; and Γ, Q, R are Y -periodic solutions of the following problems on the cell Y :

- Problem L_1^{rt} : Find the Y -periodic functions $w^{rt}, \zeta^{rt}, \eta^{rt}$ such that:

$$\left. \begin{aligned} -\partial_{j,y}\sigma^{ij}(w^{rt}, \zeta^{rt}, \eta^{rt}, 0) &= \partial_{j,y}c^{ijrt} \\ -\partial_{i,y}D^i(w^{rt}, \zeta^{rt}, \eta^{rt}, 0) &= \partial_{i,y}e^{irt} \\ -\partial_{i,y}B^i(w^{rt}, \zeta^{rt}, \eta^{rt}, 0) &= \partial_{i,y}q^{irt} \end{aligned} \right\} \text{ on } Y. \tag{3-3}$$

- Problem L_2^m : Find the Y -periodic functions g^m, π^m, ξ^m such that

$$\left. \begin{aligned} -\partial_{j,y}\sigma^{ij}(g^m, \pi^m, \xi^m, 0) &= \partial_{j,y}e^{mij} \\ -\partial_{i,y}D^i(g^m, \pi^m, \xi^m, 0) &= -\partial_{i,y}\kappa^{im} \\ -\partial_{i,y}B^i(g^m, \pi^m, \xi^m, 0) &= -\partial_{i,y}\alpha^{im} \end{aligned} \right\} \text{ on } Y. \tag{3-4}$$

- Problem L_3^m : Find the Y -periodic functions h^m, χ^m, γ^m such that

$$\left. \begin{aligned} -\partial_{j,y}\sigma^{ij}(h^m, \chi^m, \gamma^m, 0) &= \partial_{j,y}q^{mij} \\ -\partial_{i,y}D^i(h^m, \chi^m, \gamma^m, 0) &= -\partial_{i,y}\alpha^{im} \\ -\partial_{i,y}B^i(h^m, \chi^m, \gamma^m, 0) &= -\partial_{i,y}\mu^{im} \end{aligned} \right\} \text{ on } Y. \tag{3-5}$$

- Problem L_4 : Find the Y -periodic functions Γ, Q, R such that

$$\left. \begin{aligned} -\partial_{j,y}\sigma^{ij}(\Gamma, Q, R, 0) &= -\partial_{j,y}\lambda^{ij} \\ -\partial_{i,y}D^i(\Gamma, Q, R, 0) &= -\partial_{i,y}p^i \\ -\partial_{i,y}B^i(\Gamma, Q, R, 0) &= -\partial_{i,y}m^i \end{aligned} \right\} \text{ on } Y. \tag{3-6}$$

- Problem L_5^k : Find the Y -periodic function T^k such that

$$-\partial_{i,y}(\eta^{ij}\partial_{j,y}T^k) = \partial_{i,y}\eta^{ik} \text{ on } Y. \tag{3-7}$$

Here $\partial_{m,y}\phi = \partial\phi/\partial y_m$. The homogenized problem can be written as

$$\left. \begin{aligned} -\operatorname{div} \bar{\sigma}(u^0, \varphi^0, \psi^0, \theta^h) &= f \\ -\operatorname{div} \bar{D}(u^0, \varphi^0, \psi^0, \theta^h) &= 0 \\ -\operatorname{div} \bar{B}(u^0, \varphi^0, \psi^0, \theta^h) &= 0 \\ -\operatorname{div} \bar{T}(u^0, \varphi^0, \psi^0, \theta^h) &= 0 \end{aligned} \right\} \text{ on } \Omega, \tag{3-8}$$

with the homogeneous boundary conditions $u^0 = 0, \varphi^0 = 0, \psi^0 = 0$, and $\theta^h = 0$ on $\partial\Omega$. The effective constitutive laws are given by

$$\begin{aligned} \bar{\sigma}^{ij}(u^0, \varphi^0, \psi^0, \theta^h) &= \bar{c}^{ijkl}s_{kj}(u^0) + \bar{e}^{mij}\partial_m\varphi^0 + \bar{q}^{nij}\partial_n\psi^0 - \bar{\lambda}^{ij}\theta^h, \\ \bar{D}^i(u^0, \varphi^0, \psi^0, \theta^h) &= \bar{e}^{ikl}s_{kl}(u^0) - \bar{\kappa}^{im}\partial_m\varphi^0 - \bar{\alpha}^{in}\partial_n\psi^0 + \bar{p}^i\theta^h, \\ \bar{B}^i(u^0, \varphi^0, \psi^0, \theta^h) &= \bar{q}^{ikl}s_{kl}(u^0) - \bar{\alpha}^{im}\partial_m\varphi^0 - \bar{\mu}^{in}\partial_n\psi^0 + \bar{m}^i\theta^h, \\ \bar{\theta}(u^0, \varphi^0, \psi^0, \theta^h) &= -\bar{\lambda}^{kl}s_{kl}(u^0) + \bar{p}^m\partial_m\varphi^0 + \bar{m}^n\partial_n\psi^0 + \bar{\beta}\theta^h, \end{aligned} \tag{3-9}$$

where the bar indicates an effective property. The local problems must be completed with additional contact conditions on the interfaces between the constituents of the composite of interest. The homogenized effective coefficients have the definitions

$$\begin{aligned} \bar{c}^{ijrt} &= \langle c^{ijkl}[s_{kl,y}(w^{rt}) + \delta_{kl}^{rt}] + e^{kij}\partial_{k,y}\zeta^{rt} + q^{kij}\partial_{k,y}\eta^{rt} \rangle, \\ \bar{e}^{irt} &= \langle e^{ikl}[s_{kl,y}(w^{rt}) + \delta_{kl}^{rt}] - \kappa^{ik}\partial_{k,y}\zeta^{rt} - \alpha^{ik}\partial_{k,y}\eta^{rt} \rangle, \\ \bar{q}^{irt} &= \langle q^{ikl}[s_{kl,y}(w^{rt}) + \delta_{kl}^{rt}] - \alpha^{ik}\partial_{k,y}\zeta^{rt} - \mu^{ik}\partial_{k,y}\eta^{rt} \rangle, \\ \bar{e}^{mij} &= \langle c^{ijkl}s_{kl,y}(g^m) + e^{sij}[\partial_{s,y}\pi^m + \delta_s^m] + q^{sij}\partial_{s,y}\zeta^m \rangle, \\ \bar{\kappa}^{im} &= \langle -e^{ikl}s_{kl,y}(g^m) + \kappa^{is}[\partial_{s,y}\pi^m + \delta_s^m] + \alpha^{is}\partial_{s,y}\zeta^m \rangle, \\ \bar{\alpha}^{im} &= \langle -q^{ikl}s_{kl,y}(g^m) + \alpha^{is}[\partial_{s,y}\pi^m + \delta_s^m] + \mu^{is}\partial_{s,y}\zeta^m \rangle, \\ \bar{\alpha}^{im} &= \langle -e^{ikl}s_{kl,y}(h^m) + \alpha^{ik}[\partial_{s,y}\gamma^m + \delta_k^m] + \kappa^{ik}\partial_{k,y}\chi^m \rangle, \\ \bar{q}^{mij} &= \langle c^{ijkl}s_{kl,y}(h^m) + q^{sij}[\partial_{s,y}\gamma^m + \delta_s^m] + e^{sij}\partial_{s,y}\chi^m \rangle, \\ \bar{\mu}^{im} &= \langle -q^{ikl}s_{kl,y}(h^m) + \alpha^{ik}\partial_{k,y}\chi^m + \mu^{ik}[\partial_{k,y}\gamma^m + \delta_k^m] \rangle, \\ \bar{\lambda}^{ij} &= \langle \lambda^{ij} - c^{ijkl}s_{kl,y}(\Gamma) - e^{kij}\partial_{k,y}Q - q^{ijk}\partial_{k,y}R \rangle, \quad \bar{p}^i = \langle p^i + e^{ikl}s_{kl,y}(\Gamma) - \kappa^{ik}\partial_{k,y}Q - \alpha^{ik}\partial_{k,y}R \rangle, \\ \bar{m}^i &= \langle m^i + q^{ikl}s_{kl,y}(\Gamma) - \alpha^{ik}\partial_{k,y}Q - \mu^{ik}\partial_{k,y}R \rangle, \quad \bar{\beta} = \langle \beta - \lambda^{kl}s_{kl,y}(\Gamma) + p^k\partial_{k,y}Q + m^k\partial_{k,y}R \rangle, \end{aligned} \tag{3-10}$$

and

$$\bar{\eta}^{lj} = \langle \eta^{lj} + \eta^{il} \partial_{l,y} T^j \rangle, \tag{3-11}$$

where $\delta_{ij}^{kl} = \frac{1}{2}(\delta_j^i \delta_l^k + \delta_k^i \delta_l^j)$ and δ_l^j is the Kronecker delta.

4. Closed-form expressions for effective coefficients of multilayered TMEE composites

The local problems above, with equations (3-3)–(3-6), can be written in a unified way as follows: Find a Y -periodic $W_{b'}^{c't}$ such that

$$-\partial_m(C^{a'mb'n} \partial_n W_{b'}^{c't}) = \partial_m(C^{a'mc't}), \tag{4-1}$$

where

$$\begin{aligned} C^{imkn} &\equiv c^{imkn}, & C^{im44} &\equiv -\lambda^{im}, & C^{4mkn} &\equiv e^{mkn}, & C^{4m4n} &\equiv -\kappa^{mn}, & C^{4m44} &\equiv p^m, \\ C^{4444} &\equiv \beta, & C^{5mnk} &\equiv q^{mnk}, & C^{5m4n} &\equiv -\alpha^{mn}, & C^{5j44} &\equiv m^j, & C^{5m5n} &\equiv -\mu^{mn}, \\ W_k^{rt} &\equiv w_k^{rt}, & W_4^{rt} &\equiv \zeta^{rt}, & W_5^{rt} &\equiv \eta^{rt}, & W_k^{4m} &\equiv g_k^m, & W_4^{4m} &\equiv \pi^m, & W_5^{4m} &\equiv \zeta^m, \\ W_k^{5m} &\equiv f_k^m, & W_4^{5m} &\equiv \xi^m, & W_5^{5m} &\equiv \gamma^m, & W_k^{44} &\equiv \Gamma_k, & W_4^{44} &\equiv Q, & W_5^{44} &\equiv R. \end{aligned}$$

The primed Latin indices run from 1 to 5.

The homogenized effective coefficients given by all the Equations (3-10) can be expressed by

$$\bar{C}^{a'mb't} = \langle C^{a'mb't} \rangle + \langle C^{a'mc'n} \partial_n W_{c'}^{b't} \rangle. \tag{4-2}$$

The unified formulation above is very convenient for some specific problems. For instance, let us consider the particular case of a laminated TMEE composite, made of cells which are periodically distributed along the axis y_1 . Each cell may be made of any finite number of homogeneous TMEE layers. The axes of symmetry of each layer are parallel to each other and the y_1 -axis is perpendicular to the layering. In this case, the material functions $C^{a'mb't}$ and the local functions $W^{b't}$ depend only on the fast variable y_1 . Consequently, expressions (4-1) and (4-2) take the form

$$D_1(C^{a'1b'1} D_1 W_{b'}^{c't}) = -D_1(C^{a'1c't}), \tag{4-3}$$

$$\bar{C}^{a'mb't} = \langle C^{a'mb't} \rangle + \langle C^{a'mc'1} D_1 W_{c'}^{b't} \rangle, \tag{4-4}$$

where D_1 denotes the ordinary derivative in the generalized sense with respect to the y_1 coordinate. The angle brackets define the average per unit length of the relevant quantity over the periodic cell, that is, $\langle F \rangle = |Y|^{-1} \int_Y F(y_1) dy_1$, where $|Y|$ denotes the length of Y . For simplicity, a periodic unit cell Y will be considered. This is a one-dimensional homogenization problem which consists in finding the 1-periodic solution of (4-3), with an average of zero on Y , and satisfying the usual contact interface conditions; see, for instance, [Pobedrya 1984, Chapter 5].

Solving the system of ordinary differential equations defined by (4-3), taking into account perfect bonding conditions at the interfaces, and using (4-4), it is possible to obtain a general closed-form formula for all the TMEE effective coefficients:

$$\begin{aligned} \bar{C}^{a'mb't} &= \langle C^{b'mb't} \rangle + \langle C^{b'mc'1} (C^{c'1d'1})^{-1} C^{d'1b't} \rangle \\ &\quad + \langle C^{a'mc'1} (C^{c'1d'1})^{-1} \rangle \langle (C^{d'1e'1})^{-1} \rangle \langle (C^{e'1f'1})^{-1} C^{f'1b't} \rangle. \end{aligned} \tag{4-5}$$

Here $(C^{a'1b'1})^{-1}$ denotes the components of the inverse matrix of $(C^{a'1b'1})$. Equation (4-5) is a generalization of [Pobedrya 1984, Equation (1.11), p. 145] where the purely elastic case was investigated. From (4-5), for the particular case of a two-laminated TMEE composite, the following was derived:

$$\bar{C}^{a'mb't} = C_v^{a'mb't} - v_1(1 - v_1) \llbracket C^{a'mc'1} \rrbracket B_{c'd'}^{-1} \llbracket C^{d'1b't} \rrbracket, \quad (4-6)$$

where v_1 is the volume fraction of phase 1 (BaTiO_3); the material coefficients of such composite are piecewise constants, defined by

$$C^{a'mb't}(y_1) = \begin{cases} C_1^{a'mb't} & \text{for } y_1 \in (0, v_1), \\ C_2^{a'mb't} & \text{for } y_1 \in (v_1, 1), \end{cases}$$

and $C_v^{a'mb't} = v_1 C_1^{a'mb't} + (1 - v_1) C_2^{a'mb't}$, $\llbracket C^{a'mc'1} \rrbracket = C_1^{a'mc'1} - C_2^{a'mc'1}$, a row vector for $a'm$ fixed, $\llbracket C^{d'1b't} \rrbracket = C_1^{d'1b't} - C_2^{d'1b't}$, a column vector for $b't$ fixed, and $\llbracket B_{c'd'} \rrbracket = [v_1 C_2^{c'1d'1} - (1 - v_1) C_1^{c'1d'1}]$, where $B_{c'd'}^{-1}$ is the inverse matrix of $B_{c'd'}$. Equation (4-6) is similar to [Galka et al. 1996, Equation (17), p. 138] for laminated thermopiezoelectric composites.

4.1. Effective properties of a multilaminate with an orthotropic global behavior. We now specialize formula (4-5) for the case of a multilaminated composite whose periodic unit cell can possess any finite number of homogeneous TMEE materials with transversely isotropic properties. Each phase is characterized by the following independent constants:

Five elastic constants:

$$C^{1111} = C^{2222} (\equiv c^{1111} = c^{2222}), \quad C^{1133} = C^{2233} (\equiv c^{1133} = c^{2233}), \\ C^{1122} (\equiv c^{1122}), \quad C^{3333} (\equiv c^{3333}), \quad 2C^{1212} \equiv 2c^{1212} = (c^{1111} - c^{1122}).$$

Three piezoelectric constants:

$$C^{4311} = C^{4322} (\equiv e^{311} = e^{322}), \quad C^{4333} (\equiv e^{333}), \quad C^{4113} = C^{4223} (\equiv e^{113} = e^{223}).$$

Three piezomagnetic constants:

$$C^{5311} = C^{5322} (\equiv q^{311} = q^{322}), \quad C^{5333} (\equiv q^{333}), \quad C^{5113} = C^{5223} (\equiv q^{113} = q^{223}).$$

Two dielectric permittivity constants: $C^{4141} = C^{4242} (\equiv -\kappa^{11} = -\kappa^{22})$ and $C^{4343} (\equiv -\kappa^{33})$.

Two magnetoelectric constants: $C^{5141} = C^{5242} (\equiv -\alpha^{11} = -\alpha^{22})$ and $C^{5343} (\equiv -\alpha^{33})$.

Two magnetic permeability constants: $C^{5151} = C^{5252} (\equiv -\mu^{11} = -\mu^{22})$ and $C^{5353} (\equiv -\mu^{33})$.

Two thermal constants: $C^{1144} = C^{2244} (\equiv -\lambda^{11} = -\lambda^{22})$ and $C^{3344} (\equiv -\lambda^{33})$.

One pyroelectric constant: $C^{4344} (\equiv p^3)$.

One pyromagnetic constant: $C^{5344} (\equiv m^3)$.

The heat capacity: $C^{4444} (\equiv \beta)$.

Using (4-5), the effective coefficients for this composite material are:

Nine elastic effective constants:

$$\begin{aligned}
 \bar{c}^{1111} &= 1/\langle 1/c^{1111} \rangle, & \bar{c}^{1122} &= \langle c^{1122}/c^{1111} \rangle / \langle 1/c^{1111} \rangle, & \bar{c}^{1133} &= \langle c^{1133}/c^{1111} \rangle / \langle 1/c^{1111} \rangle, \\
 \bar{c}^{2222} &= \langle c^{1111} \rangle - \langle (c^{1122})^2/c^{1111} \rangle + \langle c^{1122}/c^{1111} \rangle^2 / \langle 1/c^{1111} \rangle, \\
 \bar{c}^{2233} &= \langle c^{1133} \rangle - \langle c^{1122}c^{1133}/c^{1111} \rangle + \langle c^{1122}/c^{1111} \rangle \langle c^{1133}/c^{1111} \rangle / \langle 1/c^{1111} \rangle, \\
 \bar{c}^{3333} &= \langle c^{3333} \rangle - \langle (c^{1133})^2/c^{1111} \rangle + \langle c^{1133}/c^{1111} \rangle^2 / \langle 1/c^{1111} \rangle, \\
 \bar{c}^{2323} &= \langle c^{1313} \rangle, & \bar{c}^{1313} &= e_1^t \langle M_{13}^{-1} \rangle^{-1} e_1, & \bar{c}^{1212} &= 1/\langle 1/c^{1212} \rangle.
 \end{aligned} \tag{4-7}$$

Five piezoelectric effective constants:

$$\begin{aligned}
 \bar{e}^{322} &= \langle e^{311} \rangle + \langle e^{311}/c^{1111} \rangle \langle c^{1122}/c^{1111} \rangle / \langle 1/c^{1111} \rangle - \langle e^{311}c^{1122}/c^{1111} \rangle, \\
 \bar{e}^{333} &= \langle e^{333} \rangle + \langle e^{311}/c^{1111} \rangle \langle c^{1133}/c^{1111} \rangle / \langle 1/c^{1111} \rangle - \langle e^{311}c^{1133}/c^{1111} \rangle, \\
 \bar{e}^{311} &= \langle e^{311}/c^{1111} \rangle / \langle 1/c^{1111} \rangle, & \bar{e}^{113} &= e_2^t \langle M_{13}^{-1} \rangle^{-1} e_1, & \bar{e}^{223} &= \langle e^{113} \rangle.
 \end{aligned} \tag{4-8}$$

Three dielectric permittivity effective constants:

$$\begin{aligned}
 \bar{\kappa}^{11} &= -e_2^t \langle M_{13}^{-1} \rangle^{-1} e_2, & \bar{\kappa}^{22} &= \langle \kappa^{11} \rangle, \\
 \bar{\kappa}^{33} &= \langle \kappa^{33} \rangle + \langle e^{311} \rangle^2 / \langle c^{1111} \rangle - \langle e^{311}/c^{1111} \rangle^2 / \langle 1/c^{1111} \rangle.
 \end{aligned} \tag{4-9}$$

Five piezomagnetic effective constants:

$$\begin{aligned}
 \bar{q}^{322} &= \langle q^{311} \rangle + \langle q^{311}/c^{1111} \rangle \langle c^{1122}/c^{1111} \rangle / \langle 1/c^{1111} \rangle - \langle q^{311}c^{1122}/c^{1111} \rangle, \\
 \bar{q}^{333} &= \langle q^{333} \rangle + \langle q^{311}/c^{1111} \rangle \langle c^{1133}/c^{1111} \rangle / \langle 1/c^{1111} \rangle - \langle q^{311}c^{1133}/c^{1111} \rangle, \\
 \bar{q}^{311} &= \langle q^{311}/c^{1111} \rangle / \langle 1/c^{1111} \rangle, & \bar{q}^{113} &= e_3^t \langle M_{13}^{-1} \rangle^{-1} e_1, & \bar{q}^{223} &= \langle q^{113} \rangle.
 \end{aligned} \tag{4-10}$$

Three magnetoelectric effective constants:

$$\begin{aligned}
 \bar{\alpha}^{11} &= -e_3^t \langle M_{13}^{-1} \rangle^{-1} e_2, & \bar{\alpha}^{22} &= \langle \alpha^{11} \rangle, \\
 \bar{\alpha}^{33} &= \langle \alpha^{33} \rangle + \langle q^{311}e^{311}/c^{1111} \rangle - \langle q^{311}/c^{1111} \rangle \langle e^{311}/c^{1111} \rangle / \langle 1/c^{1111} \rangle.
 \end{aligned} \tag{4-11}$$

Three magnetic permeability effective constants:

$$\begin{aligned}
 \bar{\mu}^{11} &= -e_3^t \langle M_{13}^{-1} \rangle^{-1} e_3, & \bar{\mu}^{22} &= \langle \mu^{11} \rangle, \\
 \bar{\mu}^{33} &= \langle \mu^{33} \rangle + \langle (q^{311})^2/c^{1111} \rangle - \langle q^{311}/c^{1111} \rangle^2 / \langle 1/c^{1111} \rangle.
 \end{aligned} \tag{4-12}$$

Three thermoelastic effective constants:

$$\begin{aligned}
 \bar{\lambda}^{11} &= \langle \lambda^{11}/c^{1111} \rangle / \langle 1/c^{1111} \rangle, \\
 \bar{\lambda}^{22} &= \langle \lambda^{11} \rangle - \langle c^{1122}\lambda^{11}/c^{1111} \rangle + \langle c^{1122}/c^{1111} \rangle \langle \lambda^{11}/c^{1111} \rangle / \langle 1/c^{1111} \rangle, \\
 \bar{\lambda}^{33} &= \langle \lambda^{33} \rangle - \langle c^{1133}\lambda^{11}/c^{1111} \rangle + \langle c^{1133}/c^{1111} \rangle \langle \lambda^{11}/c^{1111} \rangle / \langle 1/c^{1111} \rangle.
 \end{aligned} \tag{4-13}$$

One pyroelectric effective constant:

$$\bar{p}^3 = \langle p^3 \rangle + \langle e^{311}\lambda^{11}/c^{1111} \rangle - \langle e^{311}/c^{1111} \rangle \langle \lambda^{11}/c^{1111} \rangle / \langle 1/c^{1111} \rangle. \tag{4-14}$$

One pyromagnetic effective constant:

$$\bar{m}^3 = \langle m^3 \rangle + \langle q^{311} \lambda^{11} / c^{1111} \rangle - \langle q^{311} / c^{1111} \rangle \langle \lambda^{11} / c^{1111} \rangle / \langle 1 / c^{1111} \rangle. \tag{4-15}$$

Effective heat capacity:

$$\bar{\beta} = \langle \beta \rangle - \langle (\lambda^{11})^2 / c^{1111} \rangle + \langle \lambda^{11} / c^{1111} \rangle^2 / \langle 1 / c^{1111} \rangle. \tag{4-16}$$

where e_i ($i = 1, 2, 3$) are the vectors of the standard orthonormal basis for the Euclidean space R^3 , and M_{13}^{-1} is the inverse matrix of

$$M_{13} = \begin{pmatrix} c^{1313} & e^{113} & q^{113} \\ e^{113} & -\kappa^{11} & -\alpha^{11} \\ q^{113} & -\alpha^{11} & -\mu^{11} \end{pmatrix}.$$

As we can observe the corresponding homogenized material behaves as a TMEE material with orthorhombic symmetry (2 mm). From the equations involving M_{13}^{-1} in (4-7), (4-8), (4-9), (4-10), (4-11), and (4-12), we can find the expression

$$\bar{M}_{13} = \langle M_{13}^{-1} \rangle^{-1}, \quad \bar{M}_{13} = \begin{pmatrix} \bar{c}^{1313} & \bar{e}^{113} & \bar{q}^{113} \\ \bar{e}^{113} & -\bar{\kappa}^{11} & -\bar{\alpha}^{11} \\ \bar{q}^{113} & -\bar{\alpha}^{11} & -\bar{\mu}^{11} \end{pmatrix}.$$

Consequently,

$$\frac{\bar{c}^{1313}}{\Delta_{11}} = -\frac{\bar{e}^{131}}{\Delta_{12}} = -\frac{\bar{\kappa}^{11}}{\Delta_{22}} = \frac{\bar{q}^{131}}{\Delta_{13}} = \frac{\bar{\alpha}^{11}}{\Delta_{23}} = -\frac{\bar{\mu}^{11}}{\Delta_{33}} = \frac{1}{\Delta}, \tag{4-17}$$

where Δ is the determinant of the $\langle M_{13}^{-1} \rangle$ matrix, and Δ_{ij} is the minor obtained by excluding the i -th row and j -th column. From (4-17), one can observe that if one of the six effective coefficients is known then it is possible to calculate the other ones.

4.2. Two-laminated TMEE composites: Benveniste–Dvorak type relations. In this section we illustrate how Equations (4-7)–(4-16), for the case of two-laminated composites, can be used to derive universal relations of the type obtained in [Benveniste and Dvorak 1992]. In fact, from these formulae we can obtain the following expressions for the effective coefficients:

$$\bar{c}^{1111} - c_v^{1111} = -K \llbracket c^{1111} \rrbracket^2, \quad \bar{c}^{1122} - c_v^{1122} = K \llbracket c^{1111} \rrbracket \llbracket c^{1122} \rrbracket, \quad \bar{c}^{2222} - c_v^{2222} = K \llbracket c^{1122} \rrbracket^2, \tag{4-18}$$

$$\bar{c}^{1133} - c_v^{1133} = K \llbracket c^{1111} \rrbracket \llbracket c^{1133} \rrbracket, \quad \bar{c}^{2233} - c_v^{2233} = K \llbracket c^{1122} \rrbracket \llbracket c^{1133} \rrbracket, \quad \bar{c}^{3333} - c_v^{3333} = K \llbracket c^{1133} \rrbracket^2, \tag{4-19}$$

$$\bar{e}^{311} - e_v^{311} = K \llbracket c^{1111} \rrbracket \llbracket e^{311} \rrbracket, \quad \bar{e}^{322} - e_v^{311} = K \llbracket c^{1122} \rrbracket \llbracket e^{311} \rrbracket, \quad \bar{e}^{333} - e_v^{333} = K \llbracket c^{1133} \rrbracket \llbracket e^{311} \rrbracket, \tag{4-20}$$

$$\bar{q}^{311} - q_v^{311} = K \llbracket c^{1111} \rrbracket \llbracket q^{311} \rrbracket, \quad \bar{q}^{322} - q_v^{311} = K \llbracket c^{1122} \rrbracket \llbracket q^{311} \rrbracket, \quad \bar{q}^{333} - q_v^{333} = K \llbracket c^{1133} \rrbracket \llbracket q^{311} \rrbracket, \tag{4-21}$$

$$\bar{\kappa}^{33} - \kappa_v^{33} = -K \llbracket e^{311} \rrbracket^2, \quad \bar{\alpha}^{33} - \alpha_v^{33} = -K \llbracket e^{311} \rrbracket \llbracket q^{311} \rrbracket, \quad \bar{\mu}^{33} - \mu_v^{33} = -K \llbracket q^{311} \rrbracket^2, \tag{4-22}$$

$$\bar{\lambda}^{11} - \lambda_v^{11} = K \llbracket c^{1111} \rrbracket \llbracket \lambda^{11} \rrbracket, \quad \bar{\lambda}^{22} - \lambda_v^{11} = K \llbracket c^{1122} \rrbracket \llbracket \lambda^{11} \rrbracket, \quad \bar{\lambda}^{33} - \lambda_v^{33} = K \llbracket c^{1133} \rrbracket \llbracket \lambda^{11} \rrbracket, \tag{4-23}$$

$$\bar{p}^3 - p_v^3 = -K \llbracket e^{311} \rrbracket \llbracket \lambda^{11} \rrbracket, \quad \bar{m}^3 - m_v^3 = -K \llbracket q^{311} \rrbracket \llbracket \lambda^{11} \rrbracket, \quad \bar{\beta} - \beta_v = K \llbracket \lambda^{11} \rrbracket^2, \tag{4-24}$$

where $K = v_1(1 - v_1)/(v_1c_2^{1111} + (1 - v_1)c_1^{1111})$. Eliminating K from (4-18)₂, (4-18)₃, and (4-19)₂, and then again from (4-19)_{1,2,3}, from (4-20)_{1,2,3}, from (4-21)_{1,2,3}, and from (4-23)_{1,2,3}, we derive the

universal relations

$$\begin{aligned} \frac{\llbracket c^{1111} + c^{1122} \rrbracket}{\llbracket c^{1133} \rrbracket} &= \frac{\bar{c}^{2222} + \bar{c}^{1122} - (c_v^{2222} + c_v^{1122})}{\bar{c}^{2233} - c_v^{1133}} = \frac{\bar{c}^{1133} + \bar{c}^{2233} - 2c_v^{1133}}{\bar{c}^{3333} - c_v^{3333}} \\ &= \frac{\bar{e}^{311} + \bar{e}^{322} - 2e_v^{311}}{\bar{e}^{333} - e_v^{333}} = \frac{\bar{q}^{311} + \bar{q}^{322} - 2q_v^{311}}{\bar{q}^{333} - q_v^{333}} = \frac{\bar{\lambda}^{11} + \bar{\lambda}^{22} - 2\lambda_v^{11}}{\bar{\lambda}^{33} - \lambda_v^{33}}. \end{aligned} \tag{4-25}$$

Analogously, from expressions (4-18)_{2,3}, (4-19)_{2,3}, (4-20)_{1,2}, (4-21)_{2,3}, (4-22)_{1,3}, (4-23)_{1,2,3}, one can obtain the common constant $\llbracket e^{311} \rrbracket / \llbracket c^{1133} \rrbracket$, and hence the following relations connecting the effective properties:

$$\frac{\llbracket e^{311} \rrbracket}{\llbracket c^{1133} \rrbracket} = \frac{\bar{e}^{311} - e_v^{311}}{\bar{c}^{1133} - c_v^{1133}} = \frac{\bar{e}^{322} - e_v^{311}}{\bar{c}^{2233} - c_v^{1133}} = \frac{\bar{e}^{333} - e_v^{333}}{\bar{c}^{3333} - c_v^{3333}} = \frac{\kappa_v^{33} - \bar{\kappa}^{33}}{\bar{e}^{333} - e_v^{333}} = \frac{\alpha_v^{33} - \bar{\alpha}^{33}}{\bar{q}^{333} - q_v^{333}} = \frac{p_v^3 - \bar{p}^3}{\bar{\lambda}^{33} - \lambda_v^{33}}. \tag{4-26}$$

The following relations are obtained by manipulating (4-18)₂, (4-19)₂, (4-20)_{1,3}, (4-21)₂, (4-22)_{1,2}, (4-23)₂, (4-24)₁:

$$\frac{\llbracket q^{311} \rrbracket}{\llbracket c^{1133} \rrbracket} = \frac{\bar{q}^{311} - q_v^{311}}{\bar{c}^{1133} - c_v^{1133}} = \frac{\bar{q}^{333} - q_v^{333}}{\bar{c}^{3333} - c_v^{3333}} = \frac{\mu_v^{33} - \bar{\mu}^{33}}{\bar{q}^{333} - q_v^{333}} = \frac{\alpha_v^{33} - \bar{\alpha}^{33}}{\bar{e}^{333} - e_v^{333}} = \frac{m_v^3 - \bar{m}^3}{\bar{\lambda}^{33} - \lambda_v^{33}}. \tag{4-27}$$

The universal relations (28) and (29) of [Benveniste and Dvorak 1992] are contained respectively in (4-25) and (4-26). Similarly (12) and (13) of [Benveniste 1995] are included in (4-27). On the other hand these equations illustrate the interrelation between effective thermal terms with other individuals and global elastic, piezoelectric, and piezomagnetic properties. From (4-26) and (4-27) the following relation of proportionality among effective pyromagnetic and pyroelectric properties can be produced:

$$\frac{\llbracket e^{311} \rrbracket}{\llbracket q^{311} \rrbracket} = \frac{\bar{p}^3 - p_v^3}{\bar{m}^3 - m_v^3}. \tag{4-28}$$

This relation can also be obtained from the explicit expressions for the effective moduli \bar{p}^3 and \bar{m}^3 given in [Li and Dunn 1998b, p. 409] for fibrous (circular cylinder) composites.

4.3. Two-phase TMEE fibrous composites: Benveniste type exact connections. Next we determine exact relations (à la [Benveniste 1995]) between the elastic, piezoelectric, piezomagnetic, and thermal effective moduli of two-phase periodic fibrous composite systems characterized by a cylindrical geometry and consisting also of transversely isotropic TMEE constituents. The axis of the cylinder coincides with the axis x_3 . Here such exact connections will be derived in a different way, without solving any local problem, based on certain links among the solutions of the local problems L_1^{33} , L_2^3 , L_3^3 , and L_4 . In order to show that, these local problems will be presented in a compact form as the problem $L^{(q)}$ with $q = 1, 2, 3, 4$. The two-phase periodic cell is denoted by Y , while Σ represents the contact interface between the matrix Y_1 and the inclusion Y_2 (see Figure 1).

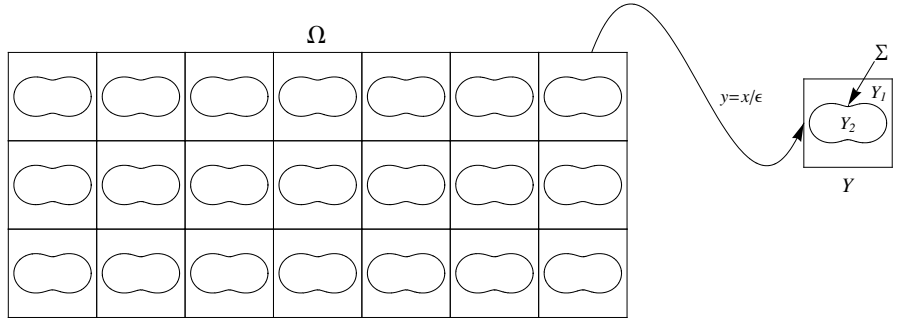


Figure 1. A part of a periodic domain and the unit cell.

The cell problem $L^{(q)}$ consists in finding the Y -periodic functions $w^{(q)}$, $\zeta^{(q)}$, and $\eta^{(q)}$, with an average of zero on Y , satisfying the following equations and continuity conditions on Y :

$$\left. \begin{aligned} \partial_{j,y} \sigma^{ij}(w_\alpha^{(q)}, \zeta_\alpha^{(q)}, \eta_\alpha^{(q)}, 0) &= 0 \\ \partial_{i,y} D^i(w_\alpha^{(q)}, \zeta_\alpha^{(q)}, \eta_\alpha^{(q)}, 0) &= 0 \\ \partial_{i,y} B^i(w_\alpha^{(q)}, \zeta_\alpha^{(q)}, \eta_\alpha^{(q)}, 0) &= 0 \end{aligned} \right\} \text{ in } Y_\alpha, \tag{4-29}$$

$$\left. \begin{aligned} \llbracket w^{(q)} \rrbracket &= 0 \\ \llbracket \zeta^{(q)} \rrbracket &= 0 \\ \llbracket \eta^{(q)} \rrbracket &= 0 \\ \llbracket \sigma^{1\delta}(w_\alpha^{(q)}, \zeta_\alpha^{(q)}, \eta_\alpha^{(q)}, 0)n_\delta \rrbracket &= \kappa^{(q)}n_1 \\ \llbracket \sigma^{2\delta}(w_\alpha^{(q)}, \zeta_\alpha^{(q)}, \eta_\alpha^{(q)}, 0)n_\delta \rrbracket &= \kappa^{(q)}n_2 \\ \llbracket \sigma^{3\delta}(w_\alpha^{(q)}, \zeta_\alpha^{(q)}, \eta_\alpha^{(q)}, 0)n_\delta \rrbracket &= 0 \\ \llbracket D^\delta(w_\alpha^{(q)}, \zeta_\alpha^{(q)}, \eta_\alpha^{(q)}, 0)n_\delta \rrbracket &= 0 \\ \llbracket B^\delta(w_\alpha^{(q)}, \zeta_\alpha^{(q)}, \eta_\alpha^{(q)}, 0)n_\delta \rrbracket &= 0 \end{aligned} \right\} \text{ on } \Sigma, \tag{4-30}$$

where $w^{(1)} \equiv w^{33}$, $\zeta^{(1)} \equiv \zeta^{33}$, $\eta^{(1)} \equiv \eta^{33}$; $w^{(2)} \equiv g^3$, $\zeta^{(2)} \equiv \pi^3$, $\eta^{(2)} \equiv \chi^3$; $w^{(3)} \equiv h^3$, $\zeta^{(3)} \equiv \zeta^3$, $\eta^{(3)} \equiv \gamma^3$; and $w^{(4)} \equiv \Gamma$, $\zeta^{(4)} \equiv Q$, $\eta^{(4)} \equiv R$ are, respectively, the solutions of the local problems L_1^{33} , L_2^3 , L_3^3 , and L_4 . The jump $\kappa^{(p)}$ on the interface Σ is defined for each local problem by the constants $\kappa^{(1)} = -\llbracket c^{3311} \rrbracket$, $\kappa^{(2)} = -\llbracket e^{311} \rrbracket$, $\kappa^{(3)} = -\llbracket q^{311} \rrbracket$, and $\kappa^{(4)} = \llbracket \lambda^{11} \rrbracket$. The structure of the problems (4-29)–(4-30) is very similar to the corresponding ones for elastic [Guinovart-Díaz et al. 2001; Rodríguez-Ramos et al. 2001] and piezoelectric [Bravo-Castillero et al. 2001; Sabina et al. 2001] unidirectional fibrous composites. The unique nonzero solutions of these problems are the elastic plane-strain local functions $w_1^{(q)}(y_1, y_2)$ and $w_2^{(q)}(y_1, y_2)$, for $q = 1, 2, 3, 4$, which are connected by

$$w_\alpha^{(2)} = \frac{\llbracket e^{311} \rrbracket}{\llbracket c^{1133} \rrbracket} w_\alpha^{(1)}, \quad w_\alpha^{(3)} = \frac{\llbracket q^{311} \rrbracket}{\llbracket c^{1133} \rrbracket} w_\alpha^{(1)}, \quad w_\alpha^{(4)} = -\frac{\llbracket \lambda^{11} \rrbracket}{\llbracket c^{1133} \rrbracket} w_\alpha^{(1)}, \tag{4-31}$$

Taking into account the above considerations and notations, and using (3-10), the following expressions for effective properties can be obtained:

- From the problem $L_1^{33} (\equiv L^{(1)})$:

$$\begin{aligned} \bar{c}^{1133} &= \langle c^{1133} \rangle + \langle c^{1111} \partial_{1,1} w_1^{(1)} + c^{1122} \partial_{2,2} w_2^{(1)} \rangle, \\ \bar{c}^{3333} &= \langle c^{3333} \rangle + \langle c^{1133} (\partial_{1,1} w_1^{(1)} + \partial_{2,2} w_2^{(1)}) \rangle, \\ \bar{e}^{333} &= \langle e^{333} \rangle + \langle e^{311} (\partial_{1,1} w_1^{(1)} + \partial_{2,2} w_2^{(1)}) \rangle, \\ \bar{q}^{333} &= \langle q^{333} \rangle + \langle q^{311} (\partial_{1,1} w_1^{(1)} + \partial_{2,2} w_2^{(1)}) \rangle. \end{aligned} \tag{4-32}$$

- From the problem $L_2^3 (\equiv L^{(2)})$:

$$\begin{aligned} \bar{\kappa}^{33} &= \langle \kappa^{33} \rangle - \langle e^{311} (\partial_{1,1} w_1^{(2)} + \partial_{2,2} w_2^{(2)}) \rangle, \\ \bar{\alpha}^{33} &= \langle \alpha^{33} \rangle - \langle q^{311} (\partial_{1,1} w_1^{(2)} + \partial_{2,2} w_2^{(2)}) \rangle, \\ \bar{e}^{311} &= \langle e^{311} \rangle + \langle c^{1111} \partial_{1,1} w_1^{(2)} + c^{1122} \partial_{2,2} w_2^{(2)} \rangle. \end{aligned} \tag{4-33}$$

- From the problem $L_3^3 (\equiv L^{(3)})$:

$$\begin{aligned} \bar{\mu}^{33} &= \langle \mu^{33} \rangle - \langle q^{311} (\partial_{1,1} w_1^{(3)} + \partial_{2,2} w_2^{(3)}) \rangle, \\ \bar{q}^{311} &= \langle q^{311} \rangle + \langle c^{1111} \partial_{1,1} w_1^{(3)} + c^{1122} \partial_{2,2} w_2^{(3)} \rangle. \end{aligned} \tag{4-34}$$

- From the problem $L_4 (\equiv L^{(4)})$:

$$\begin{aligned} \bar{\lambda}^{11} &= \langle \lambda^{11} \rangle - \langle c^{1111} \partial_{1,1} w_1^{(4)} + c^{1122} \partial_{2,2} w_2^{(4)} \rangle, \\ \bar{\lambda}^{33} &= \langle \lambda^{33} \rangle - \langle c^{1133} (\partial_{1,1} w_1^{(4)} + \partial_{2,2} w_2^{(4)}) \rangle, \\ \bar{p}^3 &= \langle p^3 \rangle + \langle e^{311} (\partial_{1,1} w_1^{(4)} + \partial_{2,2} w_2^{(4)}) \rangle, \\ \bar{m}^3 &= \langle m^3 \rangle + \langle q^{311} (\partial_{1,1} w_1^{(4)} + \partial_{2,2} w_2^{(4)}) \rangle, \\ \bar{\beta} &= \langle \beta \rangle - \langle \lambda^{11} (\partial_{1,1} w_1^{(4)} + \partial_{2,2} w_2^{(4)}) \rangle. \end{aligned} \tag{4-35}$$

Now, combining (4-32) and (4-35) and making use of (4-31)₃, the following universal relations can be obtained:

$$\frac{\llbracket c^{1133} \rrbracket}{\llbracket \lambda^{11} \rrbracket} = \frac{\bar{c}^{1133} - c_v^{1133}}{\bar{\lambda}^{11} - \lambda_v^{11}} = \frac{\bar{c}^{3333} - c_v^{3333}}{\bar{\lambda}^{33} - \lambda_v^{33}} = \frac{e_v^{333} - \bar{e}^{333}}{\bar{p}^3 - p_v^3} = \frac{q_v^{333} - \bar{q}^{333}}{\bar{m}^3 - m_v^3}. \tag{4-36}$$

Note that Equations (4-36) involve all thermal global coefficients with the exception of $\bar{\beta}$. However, if the interface Σ is smooth enough so that Green’s formula can be applied, then, from (4-31)₃, (4-32)₃, (4-32)₄, and (4-35)_{3,4,5} one can obtain

$$\begin{aligned} \bar{e}^{333} - e_v^{333} &= -\llbracket e^{311} \rrbracket \Pi, & \bar{q}^{333} - q_v^{333} &= -\llbracket q^{311} \rrbracket \Pi, & \bar{\beta} - \beta_v &= -\frac{\llbracket \lambda^{11} \rrbracket^2}{\llbracket c^{1133} \rrbracket} \Pi, \\ \bar{p}^3 - p_v^3 &= \frac{\llbracket \lambda^{11} \rrbracket \llbracket e^{311} \rrbracket}{\llbracket c^{1133} \rrbracket} \Pi, & \bar{m}^3 - m_v^3 &= \frac{\llbracket \lambda^{11} \rrbracket \llbracket q^{311} \rrbracket}{\llbracket c^{1133} \rrbracket} \Pi, \end{aligned} \tag{4-37}$$

Parameters	Units	BaTiO ₃	CoFe ₂ O ₄	epoxy
c^{1111}	GPa	166.	286.	5.53
c^{1122}	GPa	77.	173.	2.97
c^{1133}	GPa	78.	170.5	2.97
c^{3333}	GPa	162.	269.5	5.53
c^{1313}	GPa	43.	45.3	0
e^{113}	C/m ²	11.6	0	0
e^{311}	C/m ²	-4.4	0	0
e^{333}	C/m ²	18.6	0	0
κ^{11}	10 ⁻¹⁰ C ² /Nm ²	112.	0.8	1
κ^{33}	10 ⁻¹⁰ C ² /Nm ²	126.	0.93	1
q^{113}	N/Am	0	550.	0
q^{311}	N/Am	0	580.3	0
q^{333}	N/Am	0	699.7	0
μ^{11}	10 ⁻⁶ Ns ² /C ²	5.	-590.	1
μ^{33}	10 ⁻⁶ Ns ² /C ²	10.	157.	1

Table 1. Material properties used in the calculations. Taken from [Lee et al. 2005].

where $\Pi = \int_{\Sigma} (w_1^{(1)} dy_2 - w_2^{(1)} dy_1)$. Eliminating Π from these equations, it is possible to obtain relations involving β :

$$\frac{\llbracket c^{1133} \rrbracket}{\llbracket \lambda^{11} \rrbracket} = \frac{\llbracket \lambda^{11} \rrbracket e_v^{333} - \bar{e}^{333}}{\llbracket e^{311} \rrbracket \bar{\beta} - \beta_v} = \frac{\llbracket \lambda^{11} \rrbracket q_v^{333} - \bar{q}^{333}}{\llbracket q^{311} \rrbracket \bar{\beta} - \beta_v}. \quad (4-38)$$

In equations (4-36) and (4-38) nine effective properties are involved. The knowledge of one fixes the values of the others eight. In a similar way, other relations can be derived. For instance, by manipulating (4-37)_{3,4} we can derive (4-28). On the other hand, combining (4-31)₁, (4-32)₃, and (4-33)₂, or again (4-31)₂, (4-32)₄, and (4-34) one can find the relationships

$$\frac{\llbracket c^{1133} \rrbracket}{\llbracket q^{311} \rrbracket} = \frac{\bar{e}^{333} - e_v^{333}}{\alpha_v^{33} - \bar{\alpha}^{33}}, \quad \frac{\llbracket c^{1133} \rrbracket}{\llbracket e^{311} \rrbracket} = \frac{\bar{q}^{333} - q_v^{333}}{\alpha_v^{33} - \bar{\alpha}^{33}}. \quad (4-39)$$

These equations coincide with (13) and (15) of [Benveniste 1995]. Finally, it is interesting to observe that working with expressions (4-31)–(4-35) one can get relations (4-26) and (4-27). All these relations are valid independently of the geometrical cross section of the fibers.

5. Numerical examples

The closed-form formulae for the effective properties of TMEE multilaminated composites, summarized in Section 4.1, were analytically checked in Section 4.2 by means of the derivation (from such formulae) of the universal relations of [Benveniste and Dvorak 1992] and [Benveniste 1995]. For the case of a binary laminated composite, with transversely isotropic piezoelectric constituents, Equations (4-7)–(4-9) yield [Benveniste and Dvorak 1992, (47), p. 1309].

Since TMEE multilaminated composites could be considered as a limit case of unidirectional fibrous composites, formulas of the type described can be useful for checking numerical codes.

To illustrate the performance of the formulae for three-phase magneto-electroelastic composites, we present the results for a three-phase laminate made of a piezoelectric phase (BaTiO₃), a piezomagnetic phase (CoFe₂O₄), and an isotropic linear elastic phase (epoxy). The material properties are given in Table 1. The volume fraction v_3 of the epoxy phase is fixed at 0.4.

In Figures 2 and 3, all effective properties (elastic, piezoelectric, piezomagnetic, electric permittivity, magnetic permeability, and magnetoelectric) of these composites are plotted against the piezomagnetic volume fraction. In Figure 2 we observe that the curves for \bar{c}^{1111} , \bar{c}^{1133} , \bar{c}^{1313} , \bar{c}^{2233} , and \bar{c}^{3333} show the same trend as those appearing in [Lee et al. 2005, Figure 17], where a three-phase fibrous magneto-electroelastic composite was investigated via a finite element model. The same figure also shows that the coefficient \bar{c}^{1212} agrees better with the corresponding one from [Lee et al. 2005, Figure 18] than the one derived from the Mori–Tanaka method of [Li and Dunn 1998b]. The rest of the elastic effective properties \bar{c}^{2222} , \bar{c}^{2233} , and \bar{c}^{1122} also have a linear behavior but cannot be compared because the global behavior of the three-laminate (orthorhombic 2 mm) is different that of the three-phase fibrous composite (tetragonal 4 mm) of [Lee et al. 2005].

A similar situation can be observed in Figure 3, which shows the effective piezoelectric (\bar{e}^{333} , \bar{e}^{113} and \bar{e}^{311}), piezomagnetic (\bar{q}^{333} , \bar{q}^{311} and \bar{q}^{113}), dielectric ($\bar{\kappa}^{33}$, $\bar{\kappa}^{11}$), and magnetic ($\bar{\mu}^{33}$, $\bar{\mu}^{11}$) constants to be practically the same as those in [Lee et al. 2005, Figures 19–22, pp. 810–811]. Finally, the piezomagnetic

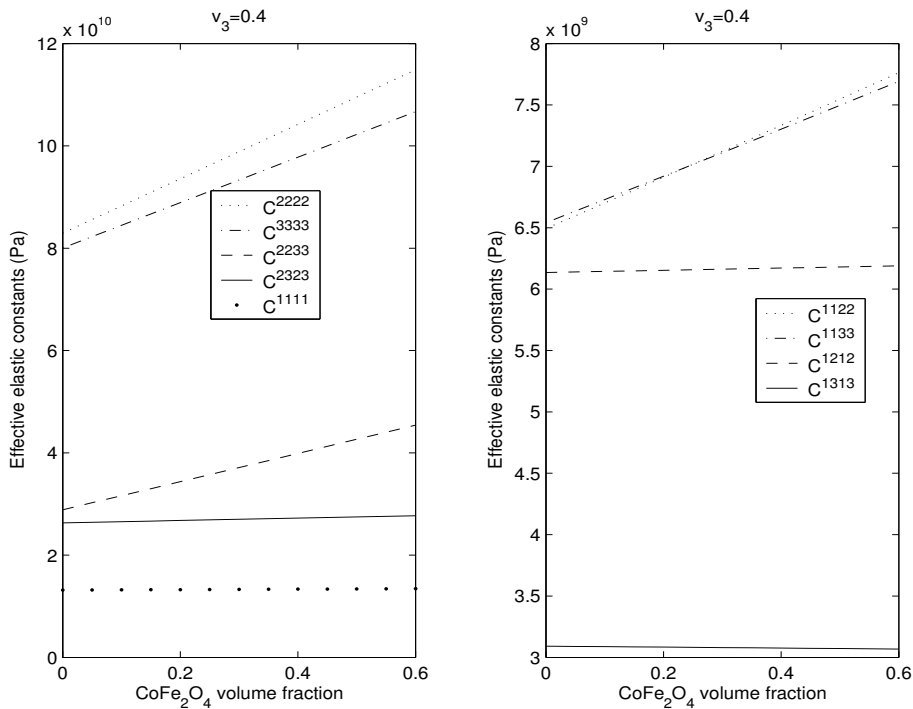


Figure 2. Effective elastic properties of a three-phase magneto-electroelastic laminated composite versus volume fraction of piezomagnetic phase, for $v_3 = 0.4$.

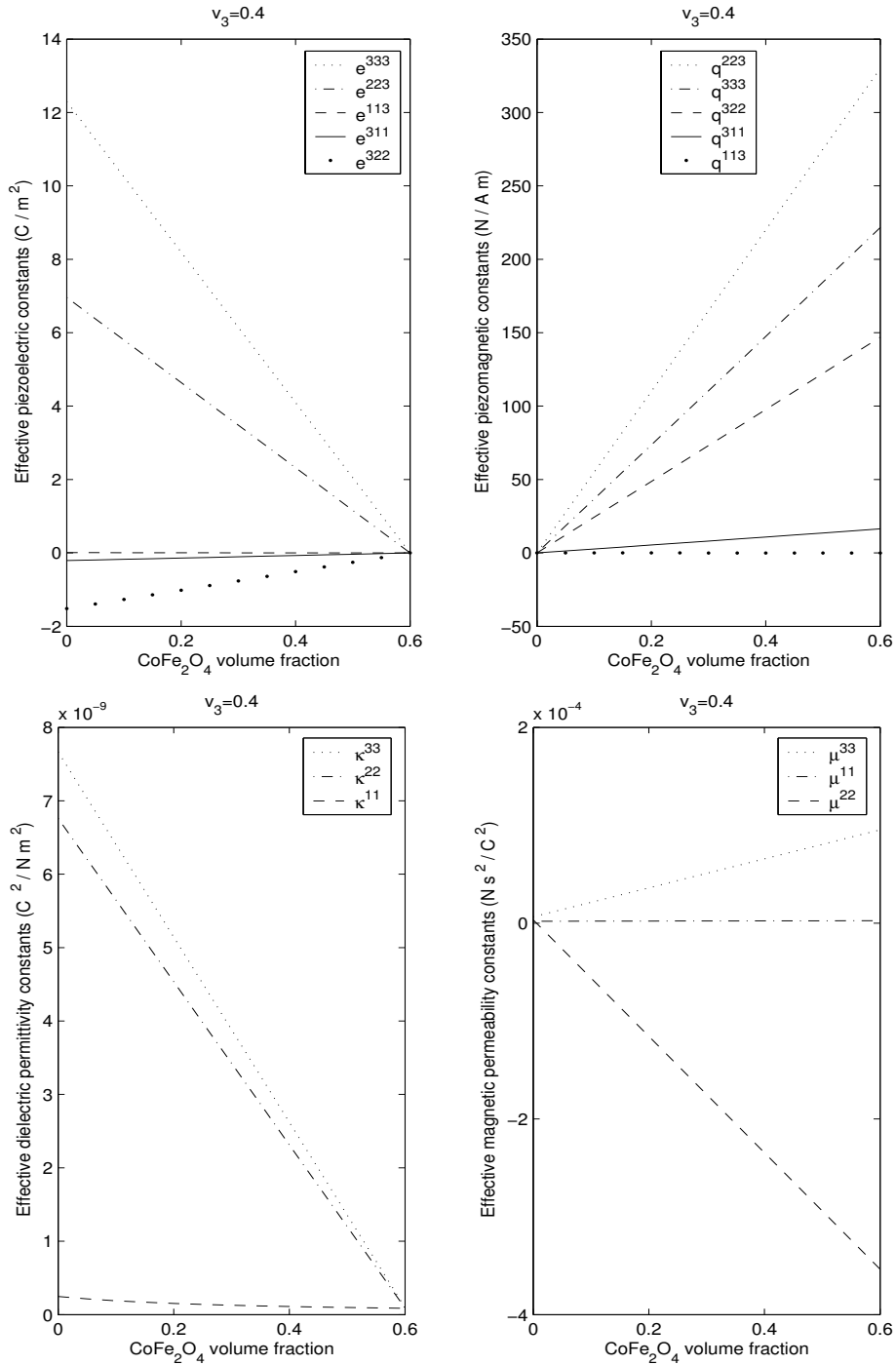


Figure 3. Effective piezoelectric (top left), and piezomagnetic (top right), dielectric (bottom left) and magnetic permeability (bottom right) properties of a three-phase magneto-electroelastic laminated composite versus volume fraction of piezomagnetic phase, for $v_3 = 0.4$.

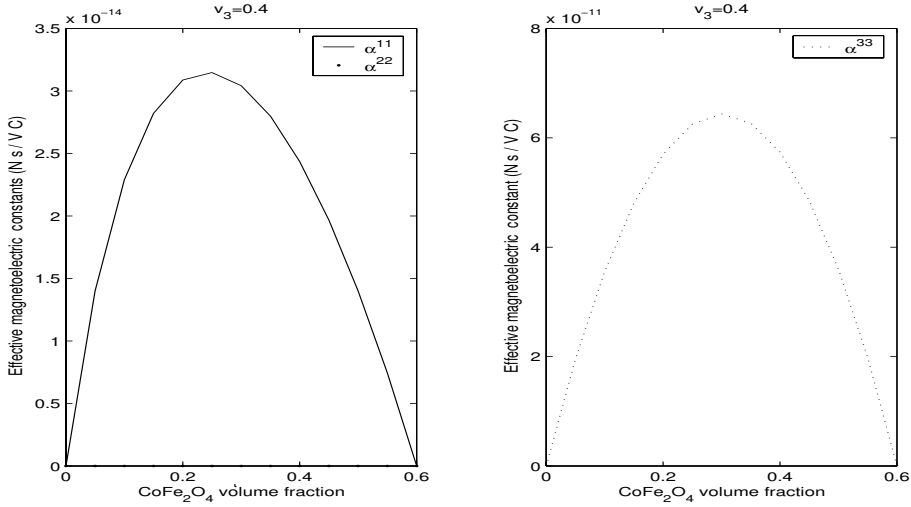


Figure 4. Effective magnetolectric properties of a three-phase magnetoelctroelastic laminated composite versus volume fraction of piezomagnetic phase, for $v_3 = 0.4$.

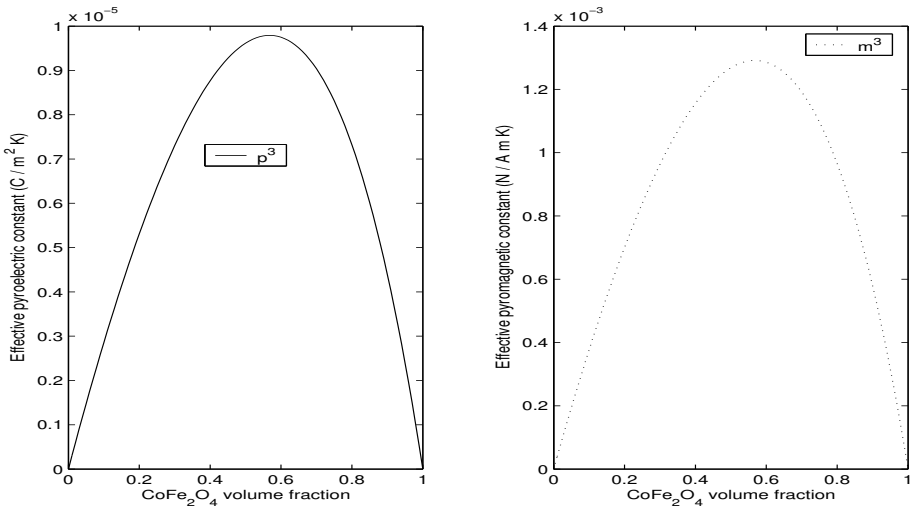


Figure 5. Effective pyroelectric and pyromagnetic properties of a two-phase BaTiO₃-CoFe₂O₄ TMEE laminated composite versus volume fraction of piezomagnetic phase.

effective constants ($\bar{\alpha}^{11}$ and $\bar{\alpha}^{33}$) illustrated in Figure 4 have the same tendency (magnetolectric effect) as those in [Lee et al. 2005, Figures 23 and 24, p. 812].

Figure 5 illustrates the behavior of the pyroelectric and pyromagnetic effective constants of a two-phase (BaTiO₃-CoFe₂O₄) TMEE laminated composite against the piezomagnetic volume fraction. The data for the thermal expansion constants of the constituents were taken from [Ootao and Tanigawa 2005, p. 476]; they are $\theta^{11} = \theta^{22} = 15.7 \times 10^{-6} \text{ K}^{-1}$, $\theta^{33} = 6.4 \times 10^{-6} \text{ K}^{-1}$ (BaTiO₃), and $\theta^{11} = \theta^{22} = \theta^{33} = 10 \times 10^{-6} \text{ K}^{-1}$ (CoFe₂O₄) where $\lambda^{ij} = c^{ijkl} \theta^{kl}$. In this figure, the existence of pyroelectric and pyromagnetic effects is apparently, though neither phase by itself exhibits them.

6. Concluding remarks

In this paper, based on the asymptotic homogenization method, a description of the derivation of the local problems and the formulae to obtain all homogenized effective coefficients of a thermomagneto-electroelastic (TMEE) periodic heterogeneous media are given. The general homogenization model is applied to obtain closed-form formulae for effective (elastic, piezoelectric, piezomagnetic, dielectric, magnetic, magnetoelectric, thermoelastic, pyroelectric, pyromagnetic, and heat capacity) coefficients of periodic multilaminated composites with any finite number of transversely isotropic TMEE constituents. Such formulae are specified for the case of a two-phase laminated composite with an orthotropic global behavior which satisfies the universal relations of [Benveniste and Dvorak 1992]. These relations illustrate the interrelation among magneto-electroelastic and thermal effective properties. In particular, (4-28) shows the proportionality connecting the pyroelectric and pyromagnetic effective coefficients with the proportionality constant given by the ratio of the piezoelectric and piezomagnetic individual properties. Another application of the general homogenization model is devoted to obtaining universal relations (4-36) and (4-38)–(4-39) for two-phase periodic unidirectional fibrous composites with TMEE transversely isotropic individual phases. The derivation of such universal relations does not require the solution of any local problem, and is based on certain links, given by (4-31), among the solutions of four local problems which are expressed in a compact form by (4-29)–(4-30). Several universal relations reported in [Benveniste and Dvorak 1992; Benveniste 1995] are recovered here following a different method. Some numerical calculations for three-phase laminated magneto-electroelastic show a good concordance with similar results obtained for three-phase fibrous composites in [Ootao and Tanigawa 2005]. The magnetoelectric effect expressed by (4-28) is illustrated in Figure 5. The analytical formulae and universal relations of this work can be useful for checking numerical code.

References

- [Aboudi 1998] J. Aboudi, “Micromechanical prediction of the effective coefficients of thermo-piezoelectric multiphase composites”, *J. Intell. Mater. Syst. Struct.* **9**:9 (1998), 713–722.
- [Aboudi 2001] J. Aboudi, “Micromechanical analysis of fully coupled electro-magneto-thermo-elastic multiphase composites”, *Smart Mater. Struct.* **10**:5 (2001), 867–877.
- [Benveniste 1995] Y. Benveniste, “Magnetoelectric effect in fibrous composites with piezoelectric and piezomagnetic phases”, *Phys. Rev. B* **51**:22 (1995), 16424–16427.
- [Benveniste and Dvorak 1992] Y. Benveniste and G. J. Dvorak, “Uniform fields and universal relations in piezoelectric composites”, *J. Mech. Phys. Solids* **40**:6 (1992), 1295–1312.
- [Bravo-Castillero et al. 2001] J. Bravo-Castillero, R. Guinovart-Díaz, F. J. Sabina, and R. Rodríguez-Ramos, “Closed-form expressions for the effective coefficients of a fiber-reinforced composite with transversely isotropic constituents, II: Piezoelectric and square symmetry”, *Mech. Mater.* **33**:4 (2001), 237–248.
- [Bravo-Castillero et al. 2008] J. Bravo-Castillero, R. Rodríguez-Ramos, H. Mechkour, J. A. Otero, and F. J. Sabina, “Homogenization of magneto-electro-elastic multilaminated materials”, *Q. J. Mech. Appl. Math.* **61**:3 (2008), 311–332.
- [Camacho-Montes et al. 2006] H. Camacho-Montes, R. Rodríguez-Ramos, J. Bravo-Castillero, R. Guinovart-Díaz, and F. J. Sabina, “Effective coefficients for two phase magneto-electroelastic fibrous composite with square symmetry cell in-plane mechanical displacement and out-of-plane electric and magnetic field case”, *Integr. Ferroelectr.* **83**:1 (2006), 49–65.
- [Castillero et al. 1998] J. B. Castillero, J. A. Otero, R. R. Ramos, and A. Bourgeat, “Asymptotic homogenization of laminated piezocomposite materials”, *Int. J. Solids Struct.* **35**:5–6 (1998), 527–541.

- [Galka et al. 1992] A. Galka, J. J. Telega, and R. Wojnar, “Homogenization and thermopiezoelectricity”, *Mech. Res. Commun.* **19**:4 (1992), 315–324.
- [Galka et al. 1996] A. Galka, J. J. Telega, and R. Wojnar, “Some computational aspects of homogenization of thermopiezoelectric composites”, *Comput. Assist. Mech. Eng. Sci.* **3**:2 (1996), 133–154.
- [Guinovart-Díaz et al. 2001] R. Guinovart-Díaz, R. Bravo-Castillero, J. Rodríguez-Ramos, and F. J. Sabina, “Closed-form expressions for the effective coefficients of fibre-reinforced composite with transversely isotropic constituents, I: Elastic and hexagonal symmetry”, *J. Mech. Phys. Solids* **49**:7 (2001), 1445–1462.
- [Lee et al. 2005] J. Lee, J. G. Boyd, IV, and D. C. Lagoudas, “Effective properties of three-phase electro-magneto-elastic composites”, *Int. J. Eng. Sci.* **43**:10 (2005), 790–825.
- [Li and Dunn 1998a] J. Y. Li and M. L. Dunn, “Anisotropic coupled-field inclusion and inhomogeneity problems”, *Philos. Mag. A* **77**:5 (1998), 1341–1350.
- [Li and Dunn 1998b] J. Y. Li and M. L. Dunn, “Micromechanics of magneto-electroelastic composite materials: average fields and effective behavior”, *J. Intell. Mater. Syst. Struct.* **9**:6 (1998), 404–416.
- [Mori and Tanaka 1973] T. Mori and K. Tanaka, “Average stress in matrix and average elastic energy of materials with misfitting inclusions”, *Acta Metall. Mater.* **21**:5 (1973), 571–574.
- [Ootao and Tanigawa 2005] Y. Ootao and Y. Tanigawa, “Transient analysis of multilayered magneto-electro-thermoelastic strip due to nonuniform heat supply”, *Compos. Struct.* **68**:4 (2005), 471–480.
- [Pobedrya 1984] B. E. Pobedrya, *Mechanics of composite materials*, Moscow State University Press, Moscow, 1984. In Russian.
- [Rodríguez-Ramos et al. 2001] R. Rodríguez-Ramos, F. J. Sabina, R. Guinovart-Díaz, and J. Bravo-Castillero, “Closed-form expressions for the effective coefficients of a fiber-reinforced composite with transversely isotropic constituents, I: Elastic and square symmetry”, *Mech. Mater.* **33**:4 (2001), 223–235.
- [Sabina et al. 2001] F. J. Sabina, R. Rodríguez-Ramos, J. Bravo-Castillero, and R. Guinovart-Díaz, “Closed-form expressions for the effective coefficients of a fibre-reinforced composite with transversely isotropic constituents, II: Piezoelectric and hexagonal symmetry”, *J. Mech. Phys. Solids* **49**:7 (2001), 1463–1479.

Received 8 Mar 2009. Revised 15 May 2009. Accepted 17 May 2009.

JULIAN BRAVO-CASTILLERO: jbravo@matcom.uh.cu

Facultad de Matemática y Computación, Universidad de La Habana, San Lázaro esq. L, Vedado, Habana 4, CP 10400, Cuba

REINALDO RODRÍGUEZ-RAMOS: reinaldo@matcom.uh.cu

Facultad de Matemática y Computación, Universidad de La Habana, San Lázaro esq. L, Vedado, Habana 4, CP 10400, Cuba

HOUARI MECHKOUR: mechkour@cmapx.polytechnique.fr

École Centrale d'Electronique, Immeuble Pollux, 37 Quai de Grenelle- CS 71520, 75725 Paris Cedex 15, France

JOSÉ A. OTERO: jaotero@icmf.inf.cu

Instituto de Cibernética, Matemática y Física, 15 No. 551, Habana 4, CP 10400, Cuba

JOANKA HERNÁNDEZ CABANAS: joanka@icmf.inf.cu

Instituto de Cibernética, Matemática y Física, 15 No. 551, Habana 4, CP 10400, Cuba

LAZARO MAYKEL SIXTO: sixto@uci.cu

Universidad de Ciencias Informáticas, Departamento de Ciencias Básicas, Boyeros, CP 19370, Cuba

RAUL GUINOVART-DÍAZ: guino@matcom.uh.cu

Facultad de Matemática y Computación, Universidad de La Habana, San Lázaro esq. L, Vedado, Habana 4, CP 10400, Cuba

FEDERICO J. SABINA: fjs@mym.iimas.unam.mx

Instituto de Investigaciones en Matemáticas Aplicadas y en Sistemas, Universidad Nacional Autónoma de México, Delegación Álvaro Obregón, Apartado Postal 20-726, 01000 México, D.F., Mexico

DEPLOYMENT PROCEDURE FOR THE TETRAHEDRON CONSTELLATION

PEDRO A. CAPÓ-LUGO AND PETER M. BAINUM

The NASA Benchmark Tetrahedron Constellation is a four-satellite formation that requires a nominal separation distance at every apogee point. The deployment procedure of a tetrahedron constellation is complex and depends on the separation distance between any pair of satellites within the constellation. In this paper, the deployment procedure of the tetrahedron constellation will be divided into two stages: the deployment from a circular parking orbit to an elliptical orbit, and the correction of the separation distance between pairs of satellites within the constellation. The solution of this problem will be implemented with a combination of Hohmann transfer maneuvers and the digital linear quadratic regulator control scheme showing a minimum consumption of fuel. In summary, the combination of these two techniques will provide a different approach to the deployment procedure of the NASA benchmark tetrahedron constellation.

1. Introduction

One concern in the NASA Benchmark Tetrahedron Constellation problem [Carpenter et al. 2003] is the deployment and reconfiguration procedures. Some papers solved these procedures using different numerical schemes based on pseudospectral methods [Williams and Trivailo 2006; Huntington et al. 2006; Huntington and Rao 2006]. The pseudospectral method solves an optimal control problem by dividing the highly elliptical orbit into sections. In these sections, a two-point boundary value problem will be solved for coasting and thruster burning phases. To solve the pseudospectral method, the problem is transformed into another domain that contains the desired solution of the optimal control problem. After every two-point boundary value problem is solved in every section of the highly elliptical orbit, the control effort and the time for the different coasting and burning phases are mapped into the actual problem to show the solution. This numerical method may take a longer period of time to solve the optimal control problem. In addition, the pseudospectral methods involve a complex mathematical development to include different characteristics of the tetrahedron constellation. For these reasons, the objective of this paper is to present a different solution to the deployment procedure of the NASA Benchmark Tetrahedron Constellation without the use of complex mathematical models.

The satellites will be transferred from a circular orbit to an elliptical orbit with a Hohmann transfer maneuver [Wertz and Larson 1999]. This transfer maneuver represents the most fuel efficient procedure to obtain the desired elliptical orbit for the four satellites. The Hohmann transfer orbit has been used to deploy a different tetrahedron constellation as shown in [Dow et al. 2004]. Also, Bainum et al. [2005] have showed that, by using a modified Hohmann transfer, an along-track constellation can be launched

Keywords: discrete linear quadratic regulator, impulse maneuvers, deployment procedure, tetrahedron constellation.
Research supported by Alliances for Graduate Education and Professoriate (AGEP) Program.

from a circular orbit to an elliptical orbit. With these maneuvers, the satellites in the along-track constellation reach the required configuration at the final apogee point. A similar procedure can be used here to achieve the final formation for the proposed tetrahedron constellation.

After the Hohmann transfer maneuver is used, the digital linear quadratic regulator (DLQR) will be used to correct the drifts in the separation distance and the velocities between any pair of satellites within the constellation. This DLQR control scheme can be used to provide a faster solution to the correction of the separation distances and velocities between any pair of satellites within the proposed constellation. A thrust requirement will be included into the formulation of the DLQR active control scheme to determine the consumption of force during the drift correction.

The purpose of this research work is to present a combination of two techniques to finally deploy the NASA Benchmark Tetrahedron Constellation from an along-track circular orbit to a highly elliptical orbit. With this scheme, a different solution will be provided to obtain the deployment procedure without the use of complex mathematical models and methods.

2. Desired conditions of the satellites in the proposed tetrahedron constellation

The tetrahedron constellation will be used to measure the components of the Earth's magnetic field with the critical data taken at the apogee point by magnetometers. In order to obtain a precise mapping of the Earth's magnetic field, it is important that the positions of all the instruments be accurately placed at or near the apogee point.

According to the NASA Benchmark problem [Carpenter et al. 2003] definition for the tetrahedron constellations, the nominal separation distance between any two of the satellites at apogee is 10 km, and the separation error at subsequent apogees should be within 10%, giving an acceptable range between 9 and 11 km. At other points in the orbit, the minimum separation distance between any pair of satellites should be 1 km. Figure 1 shows a representation of the tetrahedron constellation at the apogee point. SB and SC are assumed to be located along the semimajor axis with a separation distance of 10 km. SA forms the equilateral triangle and is orbiting around the centroid in the equilateral triangle. SH is the fourth satellite located above the centroid of the equilateral triangle which forms the tetrahedron constellation.

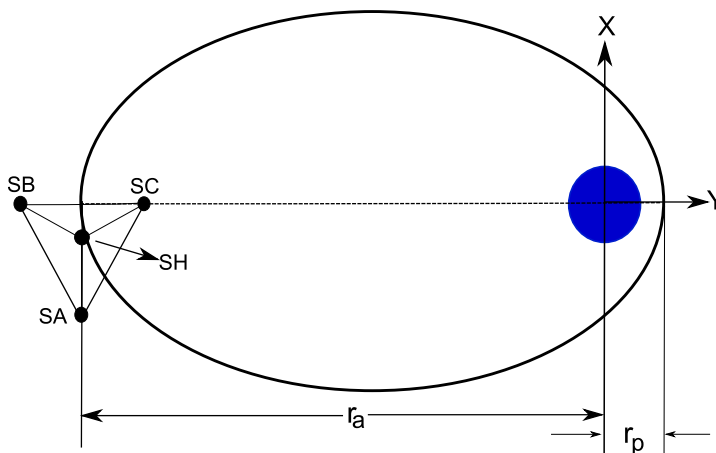


Figure 1. Two dimensional view of the configuration at apogee point.

	SA	SB	SC	SH
X (km)	-8.6602	0	0	-2.8868
Y (km)	-72582.4525	-72587.1941	-72577.7109	-72585.0433
Z (km)	-24285.7489	-24287.3354	-24284.1624	-24278.0058
V_x (km/sec)	0.973083288	0.972733623	0.973432881	0.973083324
V_y, V_z (km/sec)	0	0	0	0

Table 1. Satellite initial positions and velocities for Phase I.

	SA	SB	SC	SH
a (km)	42095.7	42095.7	42095.7	42095.7
e	0.818182	0.818301	0.818064	0.818182
i (degrees)	18.5	18.5	18.5	18.494
Ω (degrees)	0	0	0	0
ω (degrees)	89.9921	90	90	89.9974

Table 2. Orbital elements for the four satellites within the constellation (Phase I).

Using the techniques explained in [Capó-Lugo and Bainum 2005; 2006b], the constellation has a similar configuration at the perigee point, and the tetrahedral formation is obtained with the required separation distance constraints at the apogee point. These techniques were based on the orbital elements of the constellation and did not contain an active control scheme to satisfy the separation distance conditions of the NASA Benchmark Tetrahedron Constellation.

For the first specific size (phase I) of the proposed constellation [Carpenter et al. 2003], the initial positions and velocities for the four satellites are expressed in Table 1. These initial coordinates and velocities are the required conditions such that the final tetrahedron constellation can be obtained at the apogee point. Without perturbations [Capó-Lugo and Bainum 2005; 2006b], the satellites in the constellation satisfied the separation distance constraints for a long period of time, and, with perturbation, the constellation maintains the separation distance conditions for a limited number of complete orbits. For phase I, Table 1 can be used to define the orbital elements for every satellite. Table 2 shows the desired orbital elements at the final apogee point which will be used to calculate the Hohmann transfer maneuvers. In Table 2, a is the semimajor axis, e is the eccentricity, i is the inclination angle, Ω is the right ascension of the ascending node, and ω is the argument of perigee.

3. Transfer from a circular orbit to the elliptical orbit (Stage 1)

The transfer procedure from a circular orbit to an elliptical orbit is complex and may take a period of time before it is achieved. Dow et al. [2004] used a modified Hohmann transfer maneuver to transfer four satellites from a circular orbit to a final elliptical orbit. In their paper, a small consumption of fuel was obtained because the tetrahedron constellation was deployed using intermediate elliptical orbits. If the satellites are in a circular orbit and are transferred to an elliptical orbit with an eccentricity of 0.8, as

an example, the intermediate elliptical orbit is defined as the chosen intermediate values of eccentricity (between 0 and 0.8) used to perform the Hohmann transfer maneuvers.

On the contrary, [Bainum et al. 2005] show that a modified Hohmann transfer orbit can be used to deploy an along-track constellation from a circular parking orbit to an elliptical orbit. In this technique, the satellites are deployed with restrictions on the period of the transfer orbit; in this way, the satellites can reach the apogee point at the same time in the along-track constellation. The required difference in velocity (ΔV) [Bainum et al. 2005] to transfer the satellites from the circular to the elliptical transfer orbit is very similar for all of them which are a characteristic of the modified Hohmann transfer maneuvers.

This section will use similar modified Hohmann transfer maneuvers [Bainum et al. 2005] to transfer the four satellites from a circular orbit into their respective elliptical orbits. After the satellites are released from a rocket, the four satellites will be assumed to be in a circular orbit forming an along-track configuration; also, the separation distance between any pair of satellite within the constellation will be assumed constant. It will be also assumed that the circular orbit will have an inclination angle of 18.5° and a radius equal to $1.2ER$, where ER means Earth radius. As shown in [Capó-Lugo and Bainum 2005; 2006b], this is the radius of perigee and inclination angle for phase I. Before the difference in velocity for the Hohmann transfer maneuvers is calculated, the period of the transfer orbit for every satellite must be studied to determine the order in which the satellites will be deployed. The period of a satellite is defined as

$$T = 2\pi \sqrt{\frac{a^3}{\mu}}. \quad (1)$$

To calculate the semimajor axis (a), the radius of perigee (r_p) for every satellite is set equal to $1.2ER$, and the radius of apogee will be defined for every satellite depending on the desired eccentricity and semimajor axis as shown in Table 2. Table 3 illustrates the radius of apogee (r_a), semimajor axis for the transfer orbit (a_t), and the transfer period for every satellite (T_t).

It can be seen from Table 3 that SB and SC, respectively, has the highest and smallest period in comparison with the satellites SA and SH. The period of the four satellites provides the order in which the satellites will be departing from the circular orbit. The first satellite to depart is SB because it has the highest period. The second satellite is SA because it must be ahead of SH to form the equilateral triangle. The third satellite to depart from the circular orbit will be SH. This satellite will be in the same plane as the other three satellites, but, after the transfer maneuvers, it will be corrected with the DLQR to exhibit out-of-plane motion. The last satellite to depart in the circular orbit is SC which has the smallest period. The separation distance between the satellites in the circular orbit will be considered because, at the final apogee point, it will make a difference in the separation distance between any pair of satellites within the constellation in the final elliptical orbit.

The deployment procedure from the circular orbit to the elliptical orbit is defined as follows:

	SA	SB	SC	SH
r_a (km)	76537.64	76545.388	76532.638	76537.64
a_t (km)	42095.70	42099.58	42093.20	42095.70
T_t (sec)	85910.72	85922.59	85903.07	85910.72

Table 3. Radius of apogee, semimajor axis of the transfer orbit, and period for every satellite.

1. After the four satellites are released from the rocket, these satellites are assumed to be traveling in a circular orbit forming an along-track constellation. The circular orbit has a radius equal to $1.2ER$, and it is assumed that the orbit has an inclination angle equal to 18.5° . Initially, the satellites are assumed to be separated by 0.5° in the true anomaly angle. This difference in the true anomaly angle between any pair of satellites can be changed to larger values, but, at the final apogee point of the transfer ellipse, the separation distance between any pair of satellites will be higher. In addition, the satellites may not reach the apogee point at the same time; for this reason, the separation in the true anomaly angle between some of the pairs of satellites in the along track constellation will be constrained to angles between 0 and 1 degree. Figure 2 shows the difference in the true anomaly angle between the satellites in the along-track constellation in the circular orbit. In Figure 2, δf is the difference in the true anomaly angle, f is the true anomaly angle, and the center of the Earth is denoted by the center of the Cartesian system X and Y . The difference in the true anomaly angle is assumed equal to 0.5° and creates a separation distance of approximately 66.79 km between the pairs SB-SA, SA-SH, and SH-SC in the along-track constellation. The four satellites have a velocity in the circular orbit equal to 7.2166 km/sec. As said earlier, the first satellite to be deployed is SB. The semimajor axis of the transfer orbit for SB is defined in Table 3, and the velocity at the perigee point in the elliptical transfer orbit is equal to

$$V_{p,SB} = \sqrt{\mu \left(\frac{2}{r_p} - \frac{1}{a_t} \right)} = 9.73088 \text{ (km/sec)}. \tag{2a}$$

The necessary ΔV to transfer SB from the circular orbit to the elliptical transfer orbit is equal to

$$\Delta V_{P,SB} = 9.73088 - 7.2166 = 2.5148 \text{ (km/sec)}. \tag{2b}$$

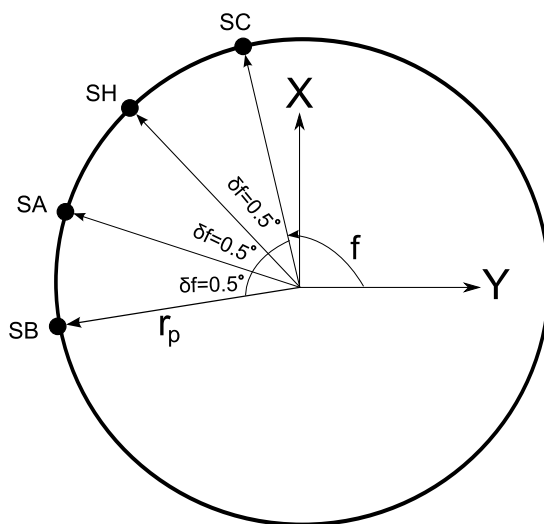


Figure 2. Location and separation of the four satellites in the circular orbit.

This ΔV maneuver is applied in the direction of the motion of the satellite to increase its velocity such that the satellite can be transferred into the elliptical orbit. This ΔV procedure will be performed when the true anomaly angle is equal to 90° because, when the satellite is in the elliptical transfer orbit, the angle at which the satellite departs will be its argument of perigee (ω).

2. 9.25 seconds after SB has departed, SA will be at the transfer point in the circular orbit ($f = 90^\circ$). From Table 3, the difference in the period of the transfer orbit between SB and SA is 11.87 seconds. A correction to the period of the transfer orbit is not necessary because SA will be 2.62 seconds ahead of SB. This difference in time will cause SA to reach the position of SB in a short period of time. For this reason, a correction in the period of the elliptical transfer orbit for SA is not necessary. The velocity and ΔV to change SA from a circular orbit to the elliptical transfer orbit is

$$V_{p,SA} = \sqrt{\mu \left(\frac{2}{r_p} - \frac{1}{a_{t,SA}} \right)} = 9.7308 \text{ km/sec}, \quad \Delta V_{p,SA} = 9.73083 - 7.2166 = 2.5142 \text{ km/sec.} \quad (3)$$

3. 9.25 seconds after SA has departed, SH has reached the transfer point in the circular orbit. The difference in the transfer period between SA and SH is zero (Table 3), but the time that SH takes to reach the transfer point provides the required condition to avoid a collision between these two satellites. For this reason, the transfer period for SH is not altered. The velocity and ΔV to maneuver SH into the elliptical transfer orbit are

$$V_{p,SH} = \sqrt{\mu \left(\frac{2}{r_p} - \frac{1}{a_{t,SH}} \right)} = 9.7307 \text{ km/sec}, \quad \Delta V_{p,SH} = 9.7307 - 7.2166 = 2.5141 \text{ km/sec.} \quad (4)$$

4. 9.25 seconds after SH has departed, SC will reach the transfer point ($f = 90^\circ$). The difference in the transfer period between SB and SC is 19.52 seconds. Once more, a correction to the period of the elliptical transfer orbit is not necessary because the time that SC takes to reach the transfer point will provide enough distance between the other three satellites to avoid a collision. The velocity and the ΔV at the transfer point required to maneuver SC into the elliptical transfer orbit can be defined as

$$V_{p,SC} = \sqrt{\mu \left(\frac{2}{r_p} - \frac{1}{a_{t,SC}} \right)} = 9.7308 \text{ km/sec}, \quad \Delta V_{p,SC} = 9.7308 - 7.2166 = 2.5142 \text{ km/sec.} \quad (5)$$

5. Once the satellites have reached the apogee point, a second ΔV maneuver will be performed to correct the semimajor axis and the eccentricity of the final elliptical orbit. To perform this maneuver, the velocity of the satellite at the apogee point in the elliptical transfer orbit is calculated and, then, is subtracted from the velocity at the apogee point defined in Table 1. Table 4 shows the velocity and ΔV required for the four satellites in the constellation at the apogee point.

	SB	SA	SH	SC
V_a (km/sec)	0.97299	0.9730833	0.973083	0.97343288
ΔV_a (km/sec)	-0.2888×10^{-3}	0	0	0.2828×10^{-3}

Table 4. Velocity at the apogee point in the transfer orbit and the ΔV required to correct the in-plane conditions of the final orbit.

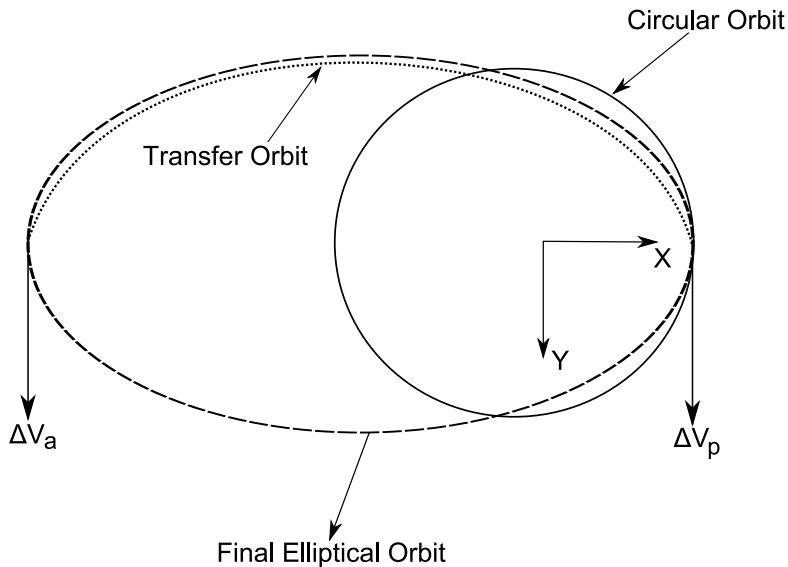


Figure 3. Diagram of the deployment procedure of the constellation.

At the apogee point, this ΔV maneuver will be also applied along the positive or negative tangential direction of the satellite. Figure 3 shows the ΔV maneuvers and the different orbits that will be obtained with these modified Hohmann transfer maneuvers. The Cartesian axis at the center of the Earth is rotated because the elliptical orbit will be created over the X axis in which the true anomaly angle is equal to 90° . This angle will define the argument of perigee of the orbit of the four satellites.

These five steps will define the elliptical orbit of the four satellites using Hohmann transfer maneuvers. Observing the transfer period of the four satellites, these satellites will reach the apogee point at the same time. The tetrahedron formation will not be obtained at the final apogee point; for this reason, a final correction of the separation distance between the satellites is required. This correction can be performed in two ways: solving a two-point boundary value problem (TPBVP) with the linearized Tschauner–Hempel equations, or correcting the drifts in the separation distance between any pair of satellites within the constellation with the DLQR controller [Capó-Lugo and Bainum 2006a].

The solution of a TPBVP is complicated because it involves the theory of primer vector defined in [Lawden 1963]. The linearized Tschauner–Hempel (TH) equations defined by Carter and Humi [1987] satisfy the primer vector relations, and the solution depends on the type of thrust arc. The solution of the TPBVP can be preferred for the formation of the tetrahedron constellation at the apogee point, but there are some other considerations related to the solution of this problem. For these reasons, the correction of the separation distance constraints for the proposed tetrahedron constellation [Carpenter et al. 2003] will be based on the DLQR control scheme [Capó-Lugo and Bainum 2006a]. With this DLQR control scheme, the tetrahedron constellation can be formed with the required separation distance at the following apogee point.

4. Linearized Tschauner–Hempel (TH) equations and thrust capability

The linearized TH equations that define the motion of a pair of satellites in an elliptical orbit about the Earth [Carter and Humi 1987] can be written as

$$y'(f) = [A(f)]y(f) + [B(f)]\vec{a}, \tag{6a}$$

where

$$[A(f)] = \begin{bmatrix} 0 & 0 & 0 & 1 & 0 & 0 \\ 0 & 0 & 0 & 0 & 1 & 0 \\ 0 & 0 & 0 & 0 & 0 & 1 \\ 0 & 0 & 0 & 0 & 2 & 0 \\ 0 & 3\kappa & 0 & 2 & 0 & 0 \\ 0 & 0 & -1 & 0 & 0 & 0 \end{bmatrix}, \quad [B(f)] = \begin{bmatrix} 0 & 0 & 0 \\ 0 & 0 & 0 \\ 0 & 0 & 0 \\ \kappa^3 & 0 & 0 \\ 0 & \kappa^3 & 0 \\ 0 & 0 & \kappa^3 \end{bmatrix}, \tag{6b}$$

$$\begin{aligned} y_j &= (1 + e \cos f)x_j, & y'_j &= (1 + e \cos f)x'_j - (e \sin f)x_j, \\ y''_j &= (1 + e \cos f)x''_j - 2(e \sin f)x'_j - (e \cos f)x_j, \end{aligned} \tag{6c}$$

$$y(f) = [y_1(f) \ y_2(f) \ y_3(f) \ y'_1(f) \ y'_2(f) \ y'_3(f)]^T, \tag{6d}$$

$$\vec{a}(f) = [a_1(f) \ a_2(f) \ a_3(f)]^T, \tag{6e}$$

$$a_j(f) = \frac{\kappa^3 h^6}{\mu^4} \frac{T_j(f)}{m} \quad (j = 1, 2, 3), \quad \kappa = \frac{1}{1 + e \cos f}. \tag{6f}$$

The parameter κ is determined from the well known equation of a Keplerian orbit (or equation of a conic section) where $\mu = GM_E$; h is the angular momentum; f is the true anomaly angle; x_1 is positive against the motion of the spacecraft, x_2 is positive along the radial direction, and x_3 is positive when the right handed system is completed. Equation (6c) is the mathematical transformation used to change from the x_j system to the y_j system. The x_j system contains the actual separation distance between the maneuvering and the reference (or target) spacecraft, and the y_j system has the same specified directions as the x_j system. The maneuvering spacecraft is assumed to have an applied thrust vector along the reference coordinate system, and the reference (or target) spacecraft is initially assumed to be acted on by a Newtonian gravitational force directed toward the center of the Earth.

It is known that the mass inside of the satellite will be changing with respect to the use of thrust for the correction of the drifts between any pair of satellites. The exhaust velocity [Carter and Humi 1987] is written as

$$m' = -\frac{h^3}{\mu^2} \frac{T(f)}{(1 + e \cos f)^2 C_s}, \tag{7}$$

where m is the mass of the satellite, T is the applied thrust for the maneuvering spacecraft and C_s is the effective exhaust velocity. Concerning the present problem, the difference between the initial and final true anomaly angle is assumed to be small enough such that the mass expended is much less in comparison to the initial mass (m_0) of the satellite during the correction of the drifts; hence, the actual mass ($m(f)$) of the satellite can be approximated by its initial mass ($m(f) \approx m_0$). Equation (6f) can be

reduced to

$$a_j = \frac{h^6}{\mu^4} \frac{T_m}{(1 + e \cos f)^3 m_0} u_j(f) = b u_j(f) \kappa^3, \quad (8)$$

where T_m is the maximum thrust, and,

$$b = \frac{h^6}{\mu^4} \frac{T_m}{m_0}, \quad u_j(f) = \frac{T_j(f)}{T_m} \quad (j = 1, 2, 3).$$

Equation (8) will be used to define the transformed thrust accelerations in (6a). If the mass of the satellite changes rapidly with respect to the correction of the drifts, (8) is not valid, and a minimization problem for a varying mass must be solved. Equation (8) will be implemented with the DLQR to determine the thrust consumption for the correction of the separation distance and the velocity drifts between any pair of satellites within the constellation.

Substituting (8) into (6a), the discrete form [Capó-Lugo and Bainum 2006a] of the linearized TH equations is expressed as

$$y(k+1) = \hat{A}(k)y(k) + \hat{B}(k)u(k), \quad (9a)$$

where $\hat{A}(f) = I + \Delta f A(f)$ and $\hat{B} = \Delta f B(f)$ are given by

$$\hat{A}(f) = \begin{bmatrix} 1 & 0 & 0 & \Delta f & 0 & 0 \\ 0 & 1 & 0 & 0 & \Delta f & 0 \\ 0 & 0 & 1 & 0 & 0 & \Delta f \\ 0 & 0 & 0 & 1 & 2\Delta f & 0 \\ 0 & 3\Delta f \kappa & 0 & -2\Delta f & 1 & 0 \\ 0 & 0 & -\Delta f & 0 & 0 & 1 \end{bmatrix}, \quad \hat{B} = \begin{bmatrix} 0 & 0 & 0 \\ 0 & 0 & 0 \\ 0 & 0 & 0 \\ \Delta f \kappa^3 & 0 & 0 \\ 0 & \Delta f \kappa^3 & 0 \\ 0 & 0 & \Delta f \kappa^3 \end{bmatrix}, \quad (9b)$$

and further

$$\kappa(k) = \frac{1}{1 + e \cos(f_L + k \Delta f)}, \quad (9c)$$

$$y(k) = [y_1(k) \ y_2(k) \ y_3(k) \ y'_1(k) \ y'_2(k) \ y'_3(k)]^T, \quad f(k) = f_L + k \Delta f. \quad (9d)$$

Here I is the 6×6 identity matrix, f_L is the initial true anomaly angle, Δf is the sampling in the true anomaly angle, and k is an integer value representing the sample which is obtained at every sampling interval in the true anomaly angle. The integer k ranges from 0 to $N_f - 1$ where N_f is the last sample obtained in the solution of the linearized TH equations defined at the final true anomaly angle and is expressed as

$$N_f - 1 = \frac{f_F - f_L}{\Delta f},$$

where f_F and f_L , respectively, is the final and initial true anomaly angle in which the LQR will be used to correct the drifts between a pair of satellites within the constellation.

5. Station-keeping procedure (Stage 2)

In [Capó-Lugo and Bainum 2007], the LQR approach based on the Carter–Humi (CH) control scheme can be applied to every phase (size) of the tetrahedron constellation. In [Capó-Lugo and Bainum 2006a],

the discrete cost function for the CH was defined and written as

$$J(k) = \frac{\Delta f}{2} \sum_{k=0}^{N_f-1} (y(k) - y_D)^T \tilde{Q}(k)(y(k) - y_D) + (u(k))^T \tilde{R}(k)(u(k)), \quad (10)$$

where $\tilde{Q}(k) = Q\kappa(k)$, $\tilde{R}(k) = R\kappa^2(k)$, and $y(k)$, y_D are the state vector and the desired state vector of the transformed system, respectively. The state and the desired state vector have dimensions of $n \times 1$.

In this case, the system of discrete linear equations can be defined similarly from (9a) as follows:

$$y(k+1) = \hat{A}(k)y(k) + \hat{B}(k)u(k) + \psi(k). \quad (11)$$

The system of linear equations in (9a) is expanded to include a perturbation vector, $\psi(k)$, to take into account outside forces due to the Earth, Moon, and/or Sun. The disturbance column vector in (11) is used to define the J2 perturbation that explains the oblateness of the Earth and is expressed as in [Battin 1999] by

$$\psi(k) = \begin{bmatrix} 0 \\ 0 \\ 0 \\ -\frac{3}{2}J_2\frac{\mu}{r^2}\left(\frac{R_e}{r}\right)^2(1-3\sin^2i\sin^2(f_L+k\Delta f)) \\ -3J_2\frac{\mu}{r^2}\left(\frac{R_e}{r}\right)^2(\sin^2i\sin(f_L+k\Delta f)\cos(f_L+k\Delta f)) \\ -3J_2\frac{\mu}{r^2}\left(\frac{R_e}{r}\right)^2(\sin i\cos i\sin(f_L+k\Delta f)) \end{bmatrix}, \quad (12)$$

where J_2 is approximated [Wertz and Larson 1999] to 1.08263×10^{-3} , R_e is the equatorial radius of the Earth, and i is the inclination angle. Equation (12) will not require a transformation with (6c) because $\psi(k)$ is defined in terms of the mean orbital elements of the satellites in the proposed constellation [Carpenter et al. 2003], as shown in Table 2.

In [Capó-Lugo and Bainum 2006a], the solution of the DLQR problem is obtained but is rewritten here for the y_j system as

$$K(k) = \Delta f \tilde{Q}(k) + \hat{A}^T(k)K(k+1)[I + S(k)K(k+1)]^{-1}\hat{A}(k), \quad (13a)$$

$$g(k) = -\Delta f \tilde{Q}(k)y_D - \hat{A}^T(k)K(k+1)[I + S(k)K(k+1)]^{-1}[S(k)g(k+1) - \psi(k)] + \hat{A}^T(k)g(k+1), \quad (13b)$$

$$y(k+1) = [I + S(k)K(k+1)]^{-1}[\hat{A}(k)y(k) - S(k)g(k+1) + \psi(k)], \quad (13c)$$

$$u(k) = -[\Delta f \tilde{R}(k)]^{-1}\hat{B}^T(k)[K(k+1)y(k+1) + g(k+1)], \quad (13d)$$

where

$$S(k) = \hat{B}(k)[\Delta f \tilde{R}(k)]^{-1}\hat{B}^T(k). \quad (13e)$$

Equations (13a) and (13b) are the digital forms of the Riccati and adjoint Riccati equations. The solution of the DLQR follows the same procedure as explained in [Capó-Lugo and Bainum 2006a]. With this procedure, the satellites will be reconfigured to the proposed tetrahedron constellation at the following apogee point.

6. Results

The complete deployment and station-keeping procedure are defined in the following steps: (1) two ΔV procedures are used to transfer the satellites from a circular orbit to their respective elliptical orbits; (2) then, the DLQR control scheme is used to correct the drifts in the separation distances and velocities between any pair of satellites such that the proposed tetrahedron constellation is obtained at the following apogee point.

Stage 1. The software package used in the simulation for the transfer from a circular to the elliptical orbit is a released version 6.2 of the Satellite Tool Kit software package (STK) [STK 2003]. The company has kindly provided an educational license to use many of the STK capabilities. The STK software is very user friendly and allows simulation in real time. The STK package offers different options for different sets of data input: one for the basic properties, one for the graphic visualization in two dimensions and three dimensions, and other modules for the constraints imposed on the problem.

The STK has different orbit propagators to simulate the NASA Benchmark Tetrahedron Constellation. These orbit propagators are the two body, J2 perturbation, High Precision Orbit Propagator (HPOP), and the Astrogator. In [Capó-Lugo and Bainum 2005; 2006b], the STK was used with the two body, J2 perturbation, and the HPOP orbit propagators to simulate the tetrahedron constellation for a period of time. The Astrogator orbit propagator is used here to input the impulse maneuvers detailed in Steps 1-5 in Section 3 to determine if the satellites reach the final elliptical orbit at the same time. This orbit propagator provides different instructions to define the ΔV maneuvers at the perigee and apogee point for every satellite; in addition, the Astrogator has an instruction that defines the transfer point of the four satellites. Using this instruction in the orbit propagator, the transfer point is defined when the true anomaly angle is equal to 90° ; in this way, the desired argument of perigee for the elliptical orbit can be obtained for every satellite.

In Section 3, the four satellites are located in a circular orbit in which its radius is equal to the radius of perigee for phase I, and the inclination angle is equal to 18.5° . The initial time [Carpenter et al. 2003] for the simulation is June 21, 2009 at 00:00:00 UTCG. This initial date and time was defined in the NASA Benchmark Tetrahedron Constellation problem [Carpenter et al. 2003]. The simulation is performed without perturbations because the satellites will not be in the initial circular orbit for a long period of time such that the perturbations due to the Earth can build up through time. Figure 4 shows the initial



Figure 4. Initial satellite locations in the circular orbit.

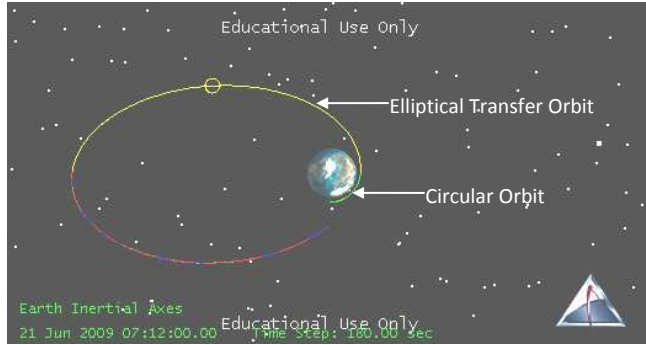


Figure 5. Satellites in the transfer elliptical orbit.

location of the four satellites in the circular orbit. The locations of the satellites are shown with a circle, but the four satellites are not shown because of the vantage point of view used in the STK software. The four satellites have the same separation distance as shown in [Figure 2](#) and mentioned in [Section 3](#). The difference in the true anomaly angle (δf) is assumed to be equal to 0.5° .

When every satellite reaches a true anomaly angle equal to 90° , the first burn at the transfer point is performed such that the satellites are maneuvered into the elliptical transfer orbit. As said earlier, the Astrogator is instructed to perform a ΔV maneuver for every satellite when the true anomaly angle is 90° . [Figure 5](#) shows the satellites in the elliptical transfer orbit. Once more, the position of the satellites is shown with a circle in the elliptical transfer orbit, and, through the simulation, the satellites travel near each other such that the four satellites will arrive at the apogee point at the same time. The STK provides different tables to show various data points like the position, velocity, orbital elements, etc. for any satellite used in the simulation. The data defining the separation distance between any pair of satellites is used to determine if the satellites violate the separation distance constraints of the NASA Benchmark Tetrahedron Constellation [[Carpenter et al. 2003](#)]. This constraint says that the satellites can not have a separation distance less than 1 km at any other point in the orbit, excluding the apogee point. At the apogee point, the nominal separation distance condition is 10 ± 1 km between any pair of satellites within the constellation. With these data tables, it is found that the minimum separation distance in the transfer elliptical orbit between any pair of satellites is greater than 13 km for a difference in the true anomaly angle of 0.5° . This shows that no pair of satellites violates the separation distance constraints in the elliptical transfer orbit.

[Figure 6](#) shows the simulation after the satellites reach the apogee point in the elliptical transfer orbit when the Astrogator is performing the last ΔV maneuver explained in [step 5](#) ([page 842](#)). In [Figure 6](#), the satellites arrive at the apogee point at the same time, but there are drifts in the separation distance between any pair of satellites within the constellation: the separation distances range from 10 to 28 kilometers (for $\delta f = 0.5^\circ$). For this reason, the constellation will be corrected with the DLQR to obtain the proposed tetrahedron constellation at the following apogee point; in addition, SH must be located in its out-of-plane position to obtain the final formation.

The difference in the true anomaly angle (δf) can be analyzed with the STK to determine how δf affects the separation distances between any pair of the satellites at the final apogee point. The difference in the true anomaly angle used in the previous simulations is 0.5° , but this δf will be increased to 1 degree and decreased to 0.3° to determine the effects on the separation distance at the final apogee point.

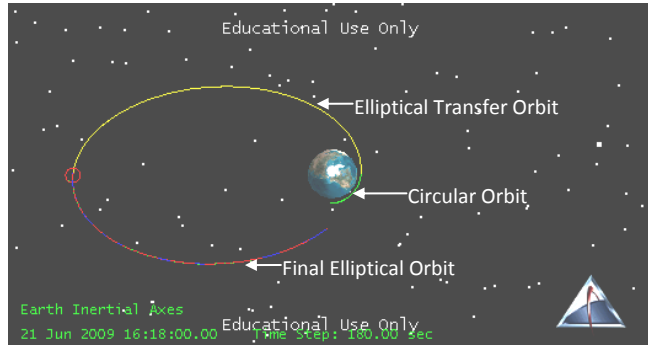


Figure 6. Satellites at the apogee point of the final elliptical orbit.

δf	SA-SB	SA-SC	SA-SH	SB-SC	SB-SH	SC-SH
0.3°	15.276	10.696	5.406	14.459	13.875	5.290
0.5°	14.080	17.960	9.008	20.689	15.258	8.952
1°	15.196	35.958	18.018	44.465	27.970	17.940

Table 5. Separation distances (in km) between pairs of satellites for various δf .

Table 5 shows the separation distance between any pair of satellites within the constellation for the chosen values of δf . In Table 5, δf must be constrained between 0 and 1 degree such that a minimum separation distance can be obtained at the apogee point. For the pair SA-SB, the separation distance does not significantly diminish with a decrease in the δf , but, for the other pairs of satellites, the separation distance is decreased as δf decreases. When $\delta f = 0.3$, the separation distance between any pair of satellites is near the 10 km range; in this way, the DLQR can be efficiently used to correct the drifts between any pair of satellites to obtain the desired configuration at the final apogee point.

Table 6 shows the orbital elements and the position of the four satellites at the final apogee point. It can be seen from Table 6 that the four satellites arrive at the apogee point at the same time. Comparing Table 2 with Table 6, SB can be used as the reference satellite because it has similar orbital elements as in Table 2. For this reason, SB will be used as the target spacecraft to correct the other three satellites such that, at the following apogee point, the proposed tetrahedron constellation can be obtained.

	SA	SB	SC	SH
a (km)	42,091.02	42,095.44	42,093.47	42,091.02
e	0.818162	0.818359	0.818270	0.818124
i (degrees)	18.5	18.5	18.5	18.5
Ω (degrees)	0	0	0	0
ω (degrees)	90	90	90	90
f (degrees)	180.056	180.055	180.043	180.059

Table 6. Initial orbital elements for the four satellites within the constellation (Phase I).

	SA	SB	SC	SH
X (km)	410.539171	404.465887	399.847473	405.135249
Y (km)	-72567.835478	-72581.128031	-72568.133913	-72567.985691
Z (km)	-24280.858097	-24285.305723	-24280.957952	-24280.908358
V_X (km/sec)	0.973120	0.972665	0.973407	0.973122
V_Y (km/sec)	0.027229	0.026829	0.026512	0.026871
V_Z (km/sec)	0.009111	0.008977	0.008871	0.008991

Table 7. Initial coordinates and velocities for the four satellites at the apogee point after the transfer maneuver.

Stage 2. The initial positions and velocities at the apogee point for the four satellites are obtained from the STK data tables to determine the initial conditions for the DLQR active control scheme. Table 7 shows the initial coordinates and velocities of the four satellites at the final apogee point after the final transfer maneuver. The values shown in Table 7 are obtained for a difference in the true anomaly angle of 0.3° and are used to calculate the difference between the reference and the maneuvering satellites because the separation distances are near the 10 km in comparison with the other values for the difference in the true anomaly angle shown in Table 5.

It is known that the reference satellite is SB, and the maneuvering satellites are SA, SC, and SH. The difference between the reference satellite and the maneuvering satellites for the nominal coordinates are known as the nominal separation distance. This difference is obtained from Table 1 that defines the desired coordinates and velocities for the four satellites. The same calculation is performed for the initial coordinates and velocities shown in Table 7. This difference between the initial coordinates and velocities is known as the initial separation distance.

In the DLQR control scheme [Capó-Lugo and Bainum 2006a], the initial conditions are defined from the difference between the satellite initial and nominal coordinates and velocities for these three pairs of satellites. These initial conditions are the drifts that must be corrected such that, at the following apogee point, the NASA Benchmark Tetrahedron Constellation can be obtained with the required separation distance conditions [Carpenter et al. 2003]. Table 8 shows the drifts for the separation distance and velocities for these pairs of satellites.

	SB-SA	SB-SC	SB-SH
$x_1(f_L) = X_S - X_N$ (km)	-14.7335	4.6184	-3.5561
$x_2(f_L) = Y_S - Y_N$ (km)	-8.5510	-2.7640	-10.2446
$x_3(f_L) = Z_S - Z_N$ (km)	-2.8611	-1.1748	4.9325
$x'_1(f_L) = X'_S - X'_N$ (m/sec)	-0.3190	-0.4274	-0.1073
$x'_2(f_L) = Y'_S - Y'_N$ (m/sec)	-0.4000	0.3170	-0.0420
$x'_3(f_L) = Z'_S - Z'_N$ (m/sec)	-0.1340	0.1060	-0.0140

Table 8. Initial conditions for the digital LQR control scheme.

The simulations with the DLQR will begin at the apogee point in which the four satellites arrive after the second ΔV maneuver (Figure 6) and will finish at the following apogee point. At this final apogee point, the separation distance and velocities for the four satellites will be satisfied. In reference [Capó-Lugo and Bainum 2006a], it is demonstrated that the DLQR is better approximated when the sampling in the true anomaly angle is 0.1 radians. The Q and R matrices are 6×6 positive definite and 3×3 positive semidefinite diagonal matrices, respectively. The R matrix is chosen to maintain a minimum consumption of fuel, and the Q matrix is obtained from different simulations to determine a minimum time problem as shown in reference [Capó-Lugo and Bainum 2007]. In this simulation, the weights for the Q and R matrices are $\text{diag}[20 \ 20 \ 20 \ 1 \ 1 \ 1]$ and $\text{diag}[1 \ 1 \ 1]$, respectively. As explained in reference [Capó-Lugo and Bainum 2006a], the positions are weighted more than the velocities because the DLQR will compensate more the positions that are multiplied by the varying coefficient term, κ .

The thrust system assumed for this simulation is the ion thruster. The ion thruster has a maximum thrust range between 5×10^{-5} and 0.5 N [Wertz and Larson 1999]. In these simulations, it is assumed that the maximum thrust is equal to 0.5 N. After the final Hohmann transfer maneuvers, the satellites will be in the elliptical orbit defined by the orbital elements of phase I (Table 6). For all the simulations, y_D is set to zero.

Figure 7 shows the correction of the drifts in the separation distance and velocity for the X direction for the three pairs of satellites. It can be seen that SB-SC requires less amount of thrust than SB-SH and SB-SA. For the three cases, the maximum value of the optimal control is 10^{-3} N in which the DLQR provides a very good response and optimal use of the thrust in the satellite. The assumption taken between the initial and final mass in the satellite is approximately correct because of this small expenditure of thrust. In addition, the maximum thrust for the ion propulsion can be reduced, or the R matrix can be changed to a different weight forcing the maximum value of the thrust level in Figure 7 to decrease. For this case, the correction of the drifts and the optimal control came to rest in less than half of an orbit.

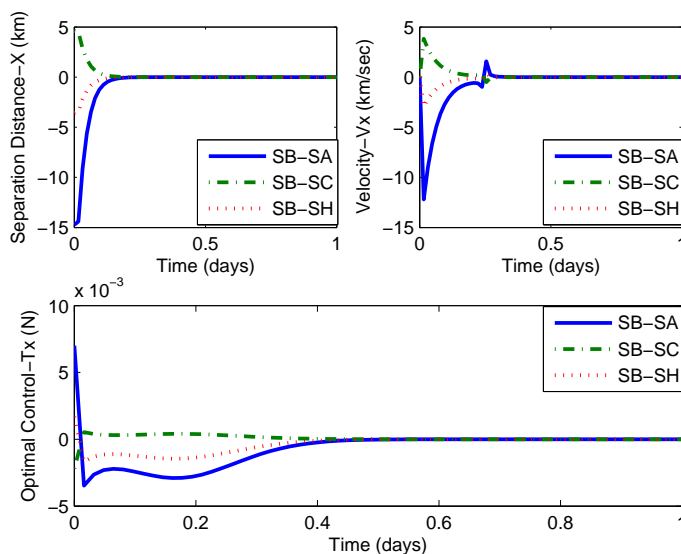


Figure 7. Correction of the separation distance and velocity for the satellites in the X direction.

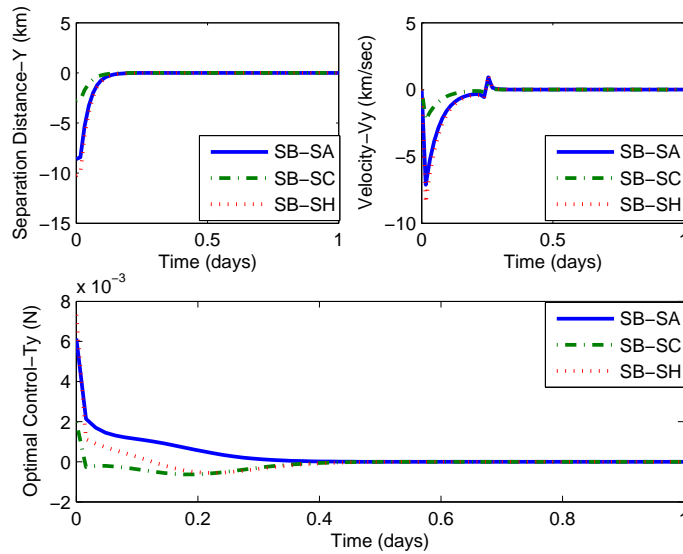


Figure 8. Correction of the separation distance and velocity for the satellites in the Y direction.

Figure 8 shows the correction for the separation distance and velocity for the three pairs of satellites in the Y direction. In this case, SB-SH requires a higher amount of thrust in comparison to SB-SC and SB-SA because SH is moving to its out-of-plane position to form the tetrahedron constellation. The correction of the separation distance for the three cases happens near the apogee point because of the weight chosen for the Q matrix. With this weight, the positions, which are multiplied by the varying term (κ), are corrected faster than the velocities because, in the TH equations, the coefficients in the velocity terms are multiplied by constants. The maximum value for the optimal control is 10^{-3} N, and the optimal control comes into rest in less than 0.5 days; in other words, the controller comes to rest before the satellites reaches the first perigee point after the correction begins.

Figure 9 shows the correction for the separation distance and the velocity for the satellites along the Z direction. In this case, SB-SH also requires a higher consumption of thrust than SB-SC and SB-SA because, as said earlier, SH will move into a different orbital plane to form the proposed tetrahedron constellation [Carpenter et al. 2003]. It is also seen that the corrections of the separation distance, the velocity, and the optimal control take less than half of an orbit. In addition, the maximum value of the optimal control is approximately 10^{-3} N and comes to rest in less than half of an orbit.

In all the simulations, the correction for the separation distances and the velocities will be performed before the satellites reach the first perigee point after the correction begins. In addition, the optimal control shows a small consumption of fuel for the three pairs of satellites. The assumption made about the mass inside of the satellite can be used in the DLQR active control scheme for the correction of the separation distance and velocity drifts. Hence, the NASA Benchmark Tetrahedron Constellation will be reconfigured at the following apogee point, and, in [Capó-Lugo and Bainum 2007], it was shown that the satellites will maintain the separation distance constraints for a limited number of complete orbits when the perturbations due to the Earth are acting on the satellites.

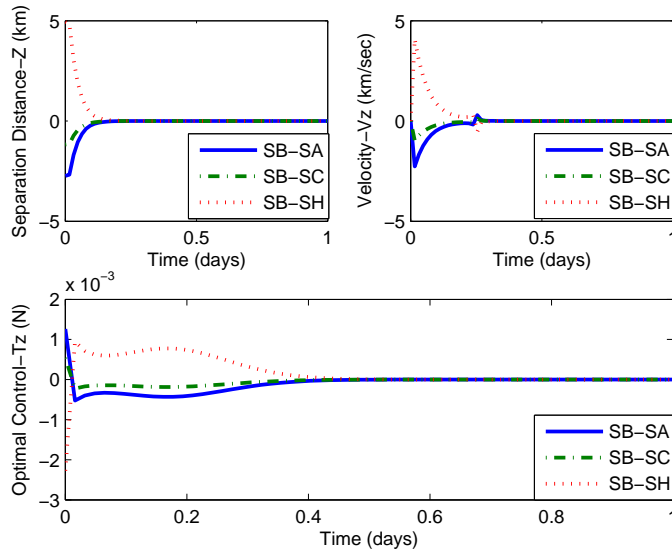


Figure 9. Correction of the separation distance and velocity for the satellites in the Z direction.

7. Remarks

A different solution for the deployment of the NASA Benchmark Tetrahedron Constellation is provided. The mathematical procedures are much simpler than in [Williams and Trivailo 2006; Huntington et al. 2006; Huntington and Rao 2006] that use the Pseudospectral methods. All the techniques used to obtain the proposed tetrahedron constellation [Carpenter et al. 2003] are known and can be easily implemented for this problem.

In the deployment from the circular orbit to the elliptical orbit, the difference in the true anomaly angle between the satellites in the circular orbit must be less than 0.5° to obtain a minimum value in the separation distance between any pair of satellites at the final apogee point of the transfer maneuver. After the final Hohmann maneuver is performed, the satellites will reach the apogee point at the same time.

After the transfer maneuver is finished, the digital linear quadratic regulator is used to finally correct the drifts between the three pairs of satellites. It is shown that the satellites have a very small consumption of energy in which the mass inside of the satellites will not be changing rapidly. The satellite in the out-of-plane motion will require a higher thrust consumption to obtain the final tetrahedron constellation.

In conclusion, this work contributes, for the first time, a different solution for the deployment and station-keeping of the NASA Benchmark Tetrahedron Constellation when Hohmann transfer maneuvers and a digital linear quadratic regulator are combined to obtain the desired formation. Using both techniques, a small consumption of fuel is obtained for the deployment procedure of the proposed tetrahedron constellation.

References

[Bainum et al. 2005] P. M. Bainum, A. Strong, Z. Tan, and P. A. Capó-Lugo, “Techniques for deploying elliptically orbiting constellations in along-track formation”, *Acta Astronaut.* **57**:9 (2005), 685–697.

- [Battin 1999] R. H. Battin, *An introduction to the mathematics and methods of astrodynamics*, Rev. ed., Chapter 10, pp. 471–514, AIAA, Reston, VA, 1999.
- [Capó-Lugo and Bainum 2005] P. A. Capó-Lugo and P. M. Bainum, “Strategy for satisfying distance constraints for the NASA benchmark tetrahedron constellation”, pp. 775–793 in *Space flight mechanics 2005: proceedings of the AAS/AIAA Space Flight Mechanics Conference* (Copper Mountain, CO, 2005), vol. 1, edited by D. A. Vallado et al., Advances in the Astronautical Sciences **120**, American Astronautical Society, San Diego, CA, 2005. Paper #AAS 05-153.
- [Capó-Lugo and Bainum 2006a] P. A. Capó-Lugo and P. M. Bainum, “[Digital LQR control scheme to maintain the separation distance of the NASA benchmark tetrahedron constellation](#)”, in *AIAA/AAS Astrodynamics Specialist Conference and Exhibit* (Keystone, CO, 2006), AIAA, Reston, VA, 2006. Paper #AIAA 2006-6014. Reprinted in *Acta Astronaut.* **65**:7–8 (2009), 1058–1067, DOI [10.1016/j.actaastro.2009.03.040](https://doi.org/10.1016/j.actaastro.2009.03.040).
- [Capó-Lugo and Bainum 2006b] P. A. Capó-Lugo and P. M. Bainum, “Implementation of the strategy for satisfying distance constraints for the NASA benchmark tetrahedron constellation”, pp. 1463–1482 in *Astrodynamics 2005: proceedings of the AAS/AIAA Astrodynamics Specialists Conference* (Lake Tahoe, CA, 2005), vol. 2, edited by B. G. Williams et al., Advances in the Astronautical Sciences **123**, American Astronautical Society, San Diego, CA, 2006. Paper #AAS 05-344.
- [Capó-Lugo and Bainum 2007] P. A. Capó-Lugo and P. M. Bainum, “[Active control schemes to satisfy separation distance constraints](#)”, *J. Guid. Control Dyn.* **30**:4 (2007), 1152–1156.
- [Carpenter et al. 2003] R. J. Carpenter, J. A. Leitner, D. C. Folta, and R. D. Burns, “[Benchmark problems for spacecraft formation flying missions](#)”, in *AIAA Guidance, Navigation, and Control Conference and Exhibit* (Austin, TX, 2003), AIAA, Reston, VA, 2003. Paper #AIAA 2003-5364.
- [Carter and Humi 1987] T. Carter and M. Humi, “[Fuel-optimal rendezvous near a point in general Keplerian orbit](#)”, *J. Guid. Control Dyn.* **10**:6 (1987), 567–573.
- [Dow et al. 2004] J. Dow, S. Matussi, M. Dow, Roberta, M. Schmidt, and M. Warhaut, “[The implementation of the cluster II constellation](#)”, *Acta Astronaut.* **54**:9 (2004), 657–669.
- [Huntington and Rao 2006] G. T. Huntington and A. V. Rao, “[Optimal reconfiguration of a tetrahedral formation via a Gauss pseudospectral method](#)”, pp. 1337–1358 in *Astrodynamics 2005: proceedings of the AAS/AIAA Astrodynamics Specialists Conference* (Lake Tahoe, CA, 2005), vol. 2, edited by B. G. Williams et al., Advances in the Astronautical Sciences **123**, American Astronautical Society, San Diego, CA, 2006. Paper #AAS 05-338.
- [Huntington et al. 2006] G. T. Huntington, D. A. Benson, and A. V. Rao, “[Post-optimality evaluation and analysis of a formation flying problem via a Gauss pseudospectral method](#)”, pp. 1359–1377 in *Astrodynamics 2005: proceedings of the AAS/AIAA Astrodynamics Specialists Conference* (Lake Tahoe, CA, 2005), vol. 2, edited by B. G. Williams et al., Advances in the Astronautical Sciences **123**, American Astronautical Society, San Diego, CA, 2006. Paper #AAS 05-339.
- [Lawden 1963] D. F. Lawden, *Optimal trajectories for space navigation*, Butterworths, London, 1963.
- [STK 2003] *Satellite tool kit software*, Version 5.0, Analytical Graphics, Malvern, PA, 2003.
- [Wertz and Larson 1999] J. R. Wertz and W. J. Larson (editors), *Space mission analysis and design*, 3rd ed., Space Technology Library **8**, Microcosm, El Segundo, CA, 1999.
- [Williams and Trivailo 2006] P. Williams and P. Trivailo, “Numerical approach designing and deploying satellite formations”, in *Proceedings of the 25th International Symposium on Space Technology and Science* (Kanazawa, 2006), Japan Society for Aeronautical and Space Sciences, Tokyo, 2006. Paper #2006-d-40.

Received 11 Mar 2008. Revised 13 May 2009. Accepted 17 May 2009.

PEDRO A. CAPÓ-LUGO: pcapo@howard.edu

Department of Mechanical Engineering, Howard University, 2300 Sixth Street, NW, Washington, DC 20059, United States
Current address: EV41, Guidance, Navigation and Control Systems Design and Analysis Branch,
NASA Marshall Space Flight Center, Huntsville, AL 35812, United States

PETER M. BAINUM: pbainum@fac.howard.edu

Department of Mechanical Engineering, Howard University, 2300 Sixth Street, NW, Washington, DC 20059, United States

EVOLUTIONARY CONTROL OF STRUCTURALLY DAMAGED STEEL BUILDINGS USING AN OPTIMAL STATE TRANSITION FORMULATION

THOMAS L. ATTARD AND ROBIN E. DANSBY

An evolutionary gain formulation is proposed for minimizing the performance damage index of steel buildings subjected to earthquake forces. The gain formulation herein is used to develop the evolutionary control law of a control algorithm applied to inelastic systems. The optimal evolutionary gain is subsequently used to control building damages by satisfying desired performance objectives per time step “as needed”. The performance objectives are defined for various “damage-safe” and elastic demands. When the structure responds in the post-yield (inelastic) state, the material is assumed to follow a kinematic rule for strain hardening, which consequently may redefine the performance objective window at each unload/reload response state (cyclic control).

A control nonlinear time-history analysis program, dubbed CONON, was developed to simulate the stress-strain responses of structural members and to compute the optimal control forces per time step. The minimization of the cost function is independent of weighing matrices, thus alleviating cumbersome calculations that also lack physical description. Instead, an iterative Riccati matrix is computed per time step and is used to generate the evolutionary gain for the system leading to an appropriate evolution of the state transition between time steps. The calculated control responses are compared to uncontrolled responses. The results are also compared using various methods of gain calculation by examining the force-deflection hysteresis plots, the strain energy dissipation in the structural members, and the member accelerations of a steel frame. The proposed optimal system shows an excellent capability to control the desired target responses and meet acceptable performance objectives.

1. Introduction

Performance-based structural engineering may be defined according to allowable damage performance levels (e.g., life safety or collapse prevention objectives [FEMA 2001]), or according to structural control theory. Control devices may be manufactured to utilize this latter control-based formulation to enable structures to respond elastically by providing damage-mitigation capability [Ohtori et al. 2004].

Structural control devices may be classified into three general categories: passive, active, and semiactive [Christenson and Emmons 2005]. Passive control is characterized by nonadaptive behavior. Such devices are typically designed for an expected earthquake and are unable to vary their resistance during a seismic event [Hart and Wong 2000]. Active and semiactive control devices, however, have the ability to adapt to the performance needs of a structure during an earthquake. Active control devices work by applying counterforces to reduce structural responses. Semiactive control devices require less power to operate [Christenson and Emmons 2005] and are able to apply resistive forces by effectively changing the stiffness and/ or damping in a structure thus reducing the structural responses.

Keywords: evolutionary structural dynamics, optimal control, evolutionary gain, plastic analysis, inelastic structures.

Passive base isolation and (passive) viscous damping as adopted by the Federal Emergency Management Association [FEMA 2001] and the International Building Code [IBC 2003] may provide viable and relatively inexpensive solutions toward mitigating seismic damages in buildings. However, certain long-period displacement pulses (having low frequencies) that have been associated with near-field or pulse-type ground motions [Makris 1997; Kelly 1999] in the direction of the fault-plane rupture have shown large damage-inducing ability. This is due to the large amount of energy contained in such ground motions that may be imparted to the structures through large velocity pulses [Howard et al. 2005; Zhang and Iwan 2002]. Recent simulated stationary (random) plastic analyses of single- and multi-degree of freedom buildings by [Attard and Mignolet 2005; Attard and Mignolet 2008] have verified this. The study revealed that structural damage did not exceed certain thresholds even under near-resonant conditions unless an increase in the amount of energy was supplied through the ground motion.

While the lateral force-resisting system in buildings may be significantly improved by implementing semiactive devices or various energy-dissipating devices, inherent difficulties could include time-delays and/ or the suddenness of the engaging/ disengaging behavior of these devices. [Nagarajaiah et al. 2000], and [Varadarajan and Nagarajaiah 2004] developed a semiactive device to transition smoothly thus avoiding high-frequency resonance. Variable damping devices have been developed and applied by [Symans and Reigles 2004] and [Madden et al. 2002] as part of a “hybrid” system that uses passive base isolation to avoid structural resonance and dissipate high-energy from near-field excitations. Magnetorheological (MR) fluid dampers [Gavin et al. 2003b; Gavin et al. 2003c; Gavin et al. 2003a] have been used in variable damping devices and also in combination with variable stiffness devices in smart base-isolated systems [Nagarajaiah et al. 2004; Nagarajaiah and Mao 2004] to continuously vary their stiffness and damping and remain in a low energy nonresonant state during an earthquake (through the feedback mechanism).

Control devices develop control forces using embedded control laws. Their effectiveness may be verified through benchmark testing [Ohtori et al. 2004; Reynolds and Christenson 2006] or through analytical software test beds [Caughey 1998]. Many control laws are developed assuming a linear elastic response of the structure throughout the duration of loading. However, a seismic event may cause a structure to yield and respond inelastically despite the use of a control device [Wong 2005a; Wong 2005b]. In another scenario, if the structure already contains some preexisting damage, a ground excitation, for example, may cause the damaged structural members to respond nonlinearly. Because a nonlinear response may produce a significantly different result than a linear approximation, it is important to develop a control algorithm that can accommodate the inelastic behavior of a structure [Ohtori et al. 2004]. Such control algorithms have been proposed by [Wong 2005a; Wong 2005b; Ohtori et al. 2004], and [Zhou et al. 2003]. The Predictive Optimal Linear Control (POLC) algorithm developed by [Wong 2005a; Wong 2005b] was later expanded to include inelastic structural responses using a force analogy method (FAM). This algorithm developed by Wong reduces the time delay associated with the controller unit by calculating the state space transition matrix used in the control law formulation only once rather than at each time step. This is accomplished by varying the structural displacement field rather than varying the stiffness. Because time delays can greatly reduce the efficiency of the control mechanism [Yang et al. 1990], cutting the computational time is one way to improve the overall system response. The study by [Wong 2005a; Wong 2005b] investigates the effectiveness of his algorithm in the control of inelastic structures. The algorithm was tested using various magnitudes of time delay and various control gains. The results showed that the algorithm was effective in controlling the response of various

inelastic structures, but decreased in efficiency with increased time delay due to the control force being applied out of phase with the structural displacement [Agrawal and Yang 2000].

The algorithm developed by [Ohtori et al. 2004] uses the Newmark-Beta method which is altered to accommodate a nonlinear structural system. The purpose of the study was to test the efficiency of a complete control mechanism (including structure, damper, controller, sensors, etc) using a benchmark problem, not to present a competitive design. Nonetheless, this control mechanism did offer slight to moderate improvements in the calculated structural drift and moderate to substantial improvements in the calculated floor accelerations. Further investigations of control strategies were performed by [Christenson and Emmons 2005], and [Reynolds and Christenson 2006]. Both employed a clipped-optimal H_2/LQR controller. The study performed by [Christenson and Emmons 2005] was an analytical investigation of the reliability of a semiactive control strategy. Results showed that the control strategy reduced the maximum damage to the structure compared to the uncontrolled system [Christenson and Emmons 2005]. The study performed by [Reynolds and Christenson 2006] was an experimental verification of an analytical benchmark problem. Experimental verification is important because it captures phenomena that analytical methods may not, such as higher mode effects, sensor noise, and interaction between the structure and damping device [Reynolds and Christenson 2006]. The results indicated that the control mechanism was able to control structural damage and accelerations for moderate ground motions with small amounts of nonlinear behavior but was limited when subjected to severe earthquakes that caused the structure to exhibit more significant nonlinear behavior.

The fuzzy control algorithm developed by [Zhou et al. 2003] for the control of inelastic buildings used an adaptation law to increase the robustness of the control device. The adaptation law was used to change the parameters, specifically for an MR damper. By controlling the stiffness and damping through the MR damper, the control device was able to vary its resistive force in real time to meet the current demands of the system. This enabled the control device to be effectively incorporated into buildings without prior knowledge of the building-damper interaction or the excitation it may encounter [Zhou et al. 2003].

In terms of reducing structural accelerations, the study performed by [Wong 2005a; Wong 2005b], which employed a similar control strategy (POLC expanded for inelastic structures with FAM), the acceleration response from the controlled system was higher than the response from the uncontrolled system. Investigations of active variable stiffness systems performed by [Yang et al. 1996] showed that while these types of systems are effective in minimizing interstory drifts, they may cause a significant increase in floor accelerations [Ribakov 2004].

The investigation performed herein uses the Predictive Optimal Linear Control algorithm for inelastic structures, but employs an evolutionary approach for calculating the gain in order to make the control device adaptive to the needs of the structural system in real time by meeting performance objectives at each time step. Convergence to the optimal gain value is achieved by satisfying performance objectives, which are predefined either by assuming a maximum allowable inelastic deflection, or by a maximum inelastic strain after yielding has occurred in a member, which is related to the amount of strain-energy being dissipated. The latter is more conscientious of the amount of damage that a structure may incur and also adapts to the inelasticity of the structure which is assumed to kinematically strain-harden in order to model the anisotropy experienced by the material during cyclic unloading/reloading. The investigation formulates an optimal linear control law using an evolutionary state-transition to meet various performance objectives at each time step in both elastic- and inelastic-responding structures.

Two control algorithms are developed in this study: The first is predicated on the absolute responses of the structure, and the second uses the changes in the responses per time step (“delta responses”). It is determined that the optimal control law solution used to reduce structural damages in terms of displacements, strain energy dissipation, and acceleration reduction needs to be formulated using the delta responses using strain-based performance objectives. The procedure is entirely automated in a program developed herein, CONON (for control nonlinear time-history analysis), which simulates the optimally controlled responses of earthquake-excited systems through a feedback mechanism and evolutionary gain.

2. Analysis of damaged systems

It is believed that the time-history responses of a controlled structure needs to be calculated using a controls solution that is capable of analyzing systems that may have already yielded or have been damaged. There are three justifications for developing an inelastic evolutionary control solution. The first reason is that if a structure contains preexisting damage, then an elastic-based controls solution may not provide accurate controllability during a subsequent external excitation because the structure had already been damaged (and become inelastic), and in doing so, had lost some of its original strain energy. Secondly, even if the structure shows no signs of exterior damage, not only may some internal damage exist, but a strong unexpected earthquake may excite the structure enough to cause it to respond inelastically (beyond its elastic yield limit) during loading. Thirdly, because there are physical limitations to using external damping mechanisms, inevitable time delays due to (a) gathering sensor information/ noise interferences, (b) control device reaction time, and (c) computational delays may significantly delay when a control force is applied and preclude the structure from responding quickly enough to behave elastically and thus resulting in damage. Further, it is shown that by forcing a system to yield by continuing to apply a control force even after a performance objective has been met during unloading enables the system to dissipate some energy input to the system via the control device or by the earthquake. This is shown herein to reduce large accelerations that would otherwise occur in the structure.

The formulated controls solution generates and applies control forces on an as-needed basis during an earthquake, as opposed to applying a force at each time step [Kim and Adeli 2004; Wong and Yang 2002]. Further, the gain formulation used in the proposed solution is optimally computed at each time step as opposed to using a single gain that is only calculated initially [Franklin et al. 2002]. Also, the performance objectives are defined as allowable inelastic demands – i.e., some acceptable level of damage is permitted. In this light, control solutions based on performance objectives defined using allowable post-yield displacements are compared to those based on allowable post-elastic strains. The latter, *strain-based*, approach assumes an evolving window of acceptable inelastic strains depending on the structure’s yield displacement during *each* cycle. Thus, the performance objective may be thought of as an allowable *moving* range of post-yield strains for each cycle of response.

By analyzing the control of inelastic systems, the control force may be larger than that used to control an elastic system since the damaged material would at this point provide inherently less resistance due to its already-damaged state and subsequent reduced stiffness. The large control force may result in large accelerations, which, as noted above, may then be controlled by forcing the system to yield after

unloading. In other words, additional control force may help the structure rehabilitate itself through its material hysteresis.

Controlling inelastic responses computationally prepares a controller for any potential damage that may occur. By prescribing a moving performance *window* in terms of allowable inelastic strains past yield (i.e., an allowable *range* of inelastic performances), then the control force may be significantly reduced, thus making the control device more cost-effective. The inelastic behavior itself may be defined according to the anisotropic nature of materials once they have been damaged, thus resulting in a kinematic strain hardening of the material [Wu 2005]. Therefore, the structure may experience large, yet *safe*, lateral deflections and more importantly safe inelastic strains during each cycle.

Displacement-based versus strain-based performance windows. The displacement-based performance-window is defined globally where the range of allowable lateral displacements in each member is fixed for each cycle and is measured with respect to the equilibrium position of the member (e.g., at the origin in Figure 1).

However, the inelastic strains (defined here as the post-elastic strain after yielding has occurred in a member on a given cycle) may fluctuate from cycle to cycle. Therefore, the strain-based performance window uses a moving range of inelastic strains per cycle whenever control is used, and in this sense, it may be defined as a local objective. This creates a flexible algorithm for controlling inelastic strains that controls the amount of strain energy that is dissipated, which subsequently helps to reduce the amount of permanent member damage.

In the strain-based control approach, the allowable inelastic strains are defined *per cycle* after a member has yielded. In Figure 1, the material is shown to kinematically strain harden with yield strain $1.0 \times \epsilon_{yield}$, which corresponds to a positive (right-side) lateral deflection of 1 in; the allowable performance objective is $0.5\epsilon_{yield}$ per cycle once the member has yielded; thus, the allowable right-side deflection is 1.5 in, and the allowable lateral deflection left of the origin is 0.5 in. This is illustrated by the solid line after yielding has occurred. In displacement-based control, however, the allowable lateral (global) deflection remains

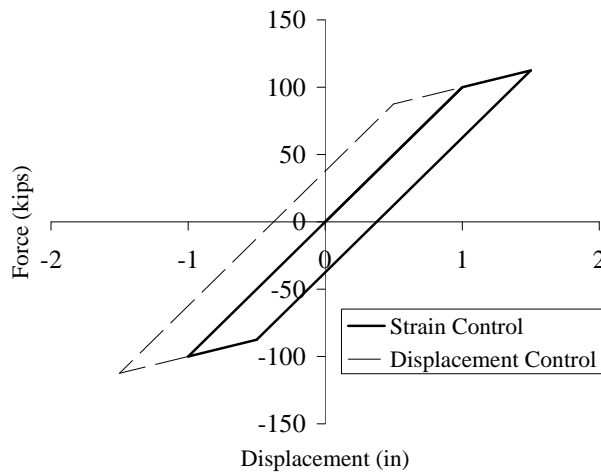


Figure 1. Illustration showing displacement control using a fixed performance window and strain control using a changing performance window.

fixed for any cycle and is independent of the hysteresis. In the [Figure 1](#) example, the fixed global range (displacement control) is ± 1.5 in (shown by the dotted lines). Ultimately, the strain-based approach enables a member to dissipate less energy per cycle, and, as it will be shown later, is a better strategy for controlling inelastic damage. Further, the strain-based methodology utilizes a kinematical strain hardening approach instead of an isotropic approach, where the former models the material anisotropy in damaged systems more accurately.

Displacement-based control. A displacement-based performance objective is described as a predefined allowable displacement measured from a member’s equilibrium, or undeformed, position; see [Figure 2a](#). The equation

$$\text{(displacement-based control)} \quad |x| > |x_{\text{perf}}| \tag{1}$$

gives the condition for applying displacement-based control, where x_{perf} is the performance objective (i.e., allowable displacement), and x is the calculated displacement that is measured at the tip of a member that has been subjected to cyclic loading; x is measured relative to the undeformed position of the member defined at the $F = 0$ axis (lateral force to the member) in [Figure 2a](#).

By using this fixed-window approach to control displacements, the control of inelastic strains, which are cyclic-dependent, is not addressed. In other words, inelastic strains are calculated based on each new yield position of a member (and are not measured relative to the original undeformed position of the member). For a given cycle, each yield position may be different from a previous yield position and depends on the unloading/ reloading displacement (x_{unload}) for that cycle. The inelastic strain on the i -th half-cycle is proportional to the displacements (relative to the equilibrium position) as shown by (1):

$$\varepsilon_i \propto |x_{\text{unload}}| - 2|x_{\text{yield}}| + |x_{\text{perf}}|, \tag{2}$$

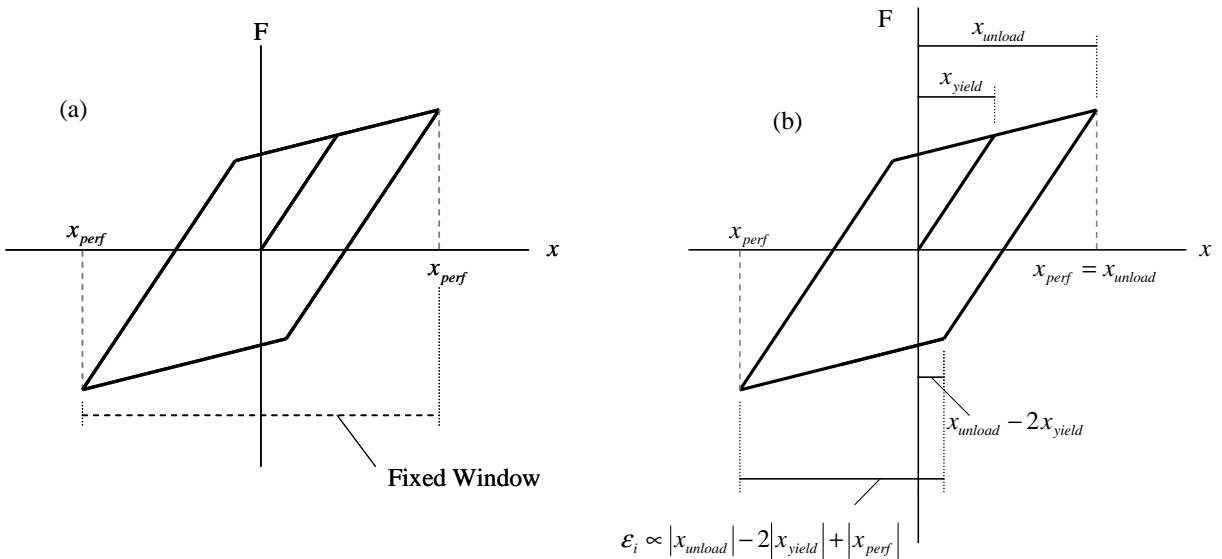


Figure 2. Displacement-based control (fixed window; left diagram) where control is called when $x = x_{\text{perf}}$ (ideal, no time-delays; right diagram).

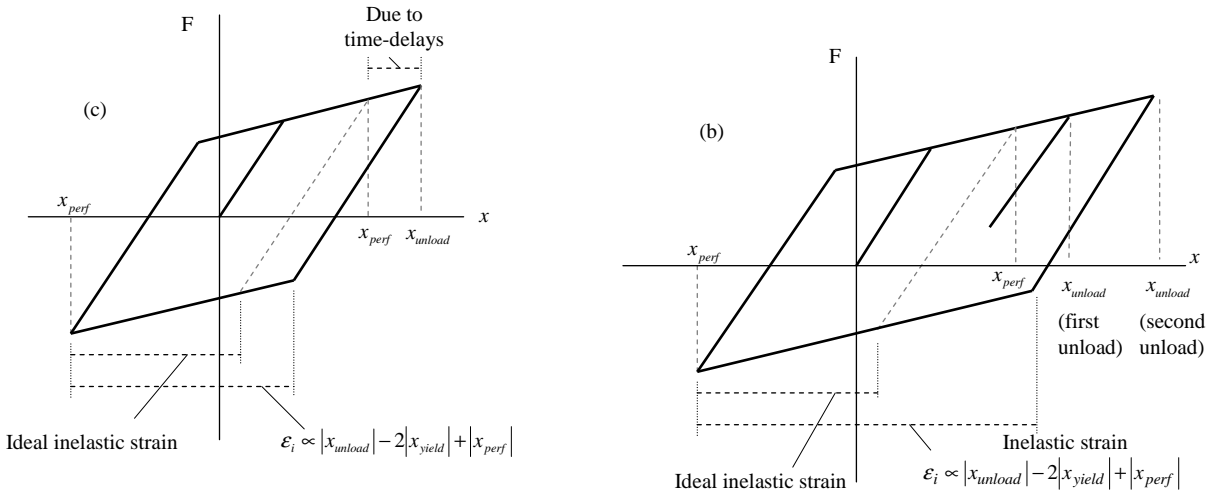


Figure 3. Displacement-based control where control is called when allowable inelastic strain is larger than the ideal inelastic strain due to (a) time delay; (b) same-side reyielding after load reversal.

where ϵ_i is the hysteretic half-cycle inelastic strain in the member, and x_{yield} is the displacement when a member had first yielded ($i = 1$). Figure 2b shows that $x_{unload} = x_{perf}$, which is an ideal scenario. In reality, however, sensor or controller limitations, including time-delays, result in the performance objective being exceeded before a control force is applied, where $|x| > |x_{perf}|$; see Figure 3a. Another possibility is that the control device is able to successfully unload the member (“first unload” in Figure 3b) and meet the desired performance objective, but instead of eventually yielding along this same direction, the member reverses direction and re-yields at the point of first unload (the member “remembers” this most recent unload point because of the presence of residual stresses that exist in damaged members.). The control device is then required to unload the member again (“second unload” in Figure 3b). However, this second control force is significantly larger than the previous force because of the increased level of damage and accumulated strain in the member, and because of the previous injection of control force into the system. This results in an energy surplus that the member was unable to initially dissipate (by having not yielded earlier in the direction of first unload). This has several adverse repercussions, including costly control devices (requiring larger force capacity) and large acceleration demands in damaged members. Hence, load reversals may be quite harmful to a control system’s capability to adequately control damaged systems; the issue is addressed later.

Strain-based control. Inelastic strain-based control enables a damaged member to dissipate less hysteretic energy than displacement-based control (Figure 1) by using a moving-window approach to satisfy performance objectives. A post-yield member displacement on each half-cycle, c , corresponds to an allowable post-yield strain measured from the point where the member yielded on that half-cycle, and not from the equilibrium position as in displacement-based control:

$$(strain-based control) \quad \epsilon_i \geq \epsilon_{perf}, \quad \text{where } \epsilon_{perf} \propto \hat{x}_{perf,c}. \tag{3}$$

Here $\varepsilon_{\text{perf}}$ is the allowable strain following each yielding event and is proportional to a corresponding allowable performance displacement $\hat{x}_{\text{perf},c}$. By using such a flexible performance-window, the control algorithm may accurately converge to the desired performance objectives while remaining stable and also reducing member accelerations. Figure 4 illustrates the same scenarios as Figures 2 and 3 using strain-based control where the inelastic strain remains the same as the ideal inelastic strain. The illustrations show that strain-based control may limit the amount of inelastic strain that a member experiences, which would in turn limit the amount of strain energy that is dissipated and control member damage.

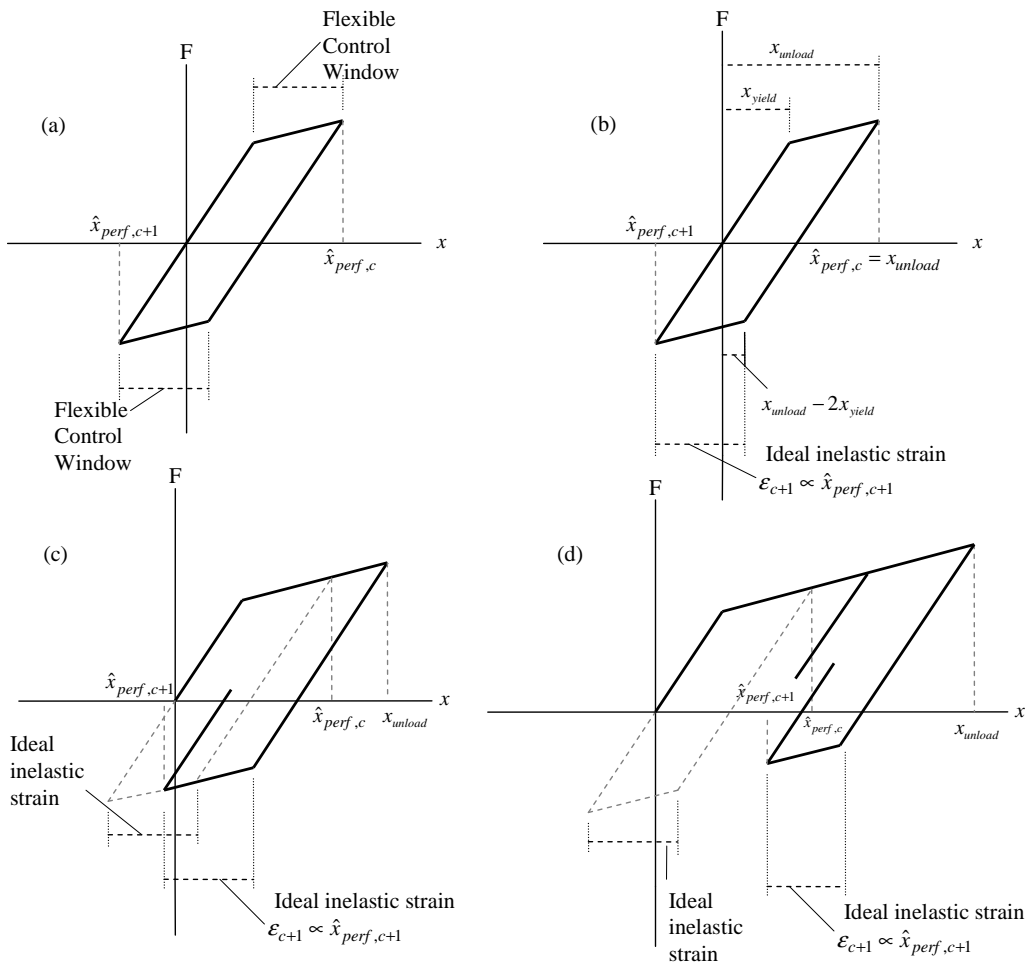


Figure 4. (a) Strain-based control (moving window) where control is called when: (b) $x = \hat{x}_{\text{perf},c}$ (allowable inelastic strain = ideal strain, no time-delays); (c) allowable inelastic strain equals the ideal inelastic strain even in the presence of time delay; and (d) allowable inelastic strain equals the ideal inelastic strain even after same-side reyielding occurs after load reversal.

Rehabilitative control: forcing members to yield. Note that in order to facilitate all further discussions, the performance objective will not be distinguished between x_{perf} (displacement-based) and $\hat{x}_{perf,c}$ (strain-based); instead, x_{perf} will be commonly used. When a performance objective is exceeded (displacement x_{k+1} in Figure 5a), the “control_unload” routine is called in CONON to attempt to unload the member on the subsequent time step. If the algorithm is unsuccessful in unloading the member (possibly because of the control-induced energy that had already been residing in the system), then the algorithm proceeds to the next time step and calculates a new control force to again attempt to unload the member. This enables the material to dissipate any residual (control) energy that may have been present, thus making the member more receptive to the new imposed control. Figure 5a illustrates the application of an unloading

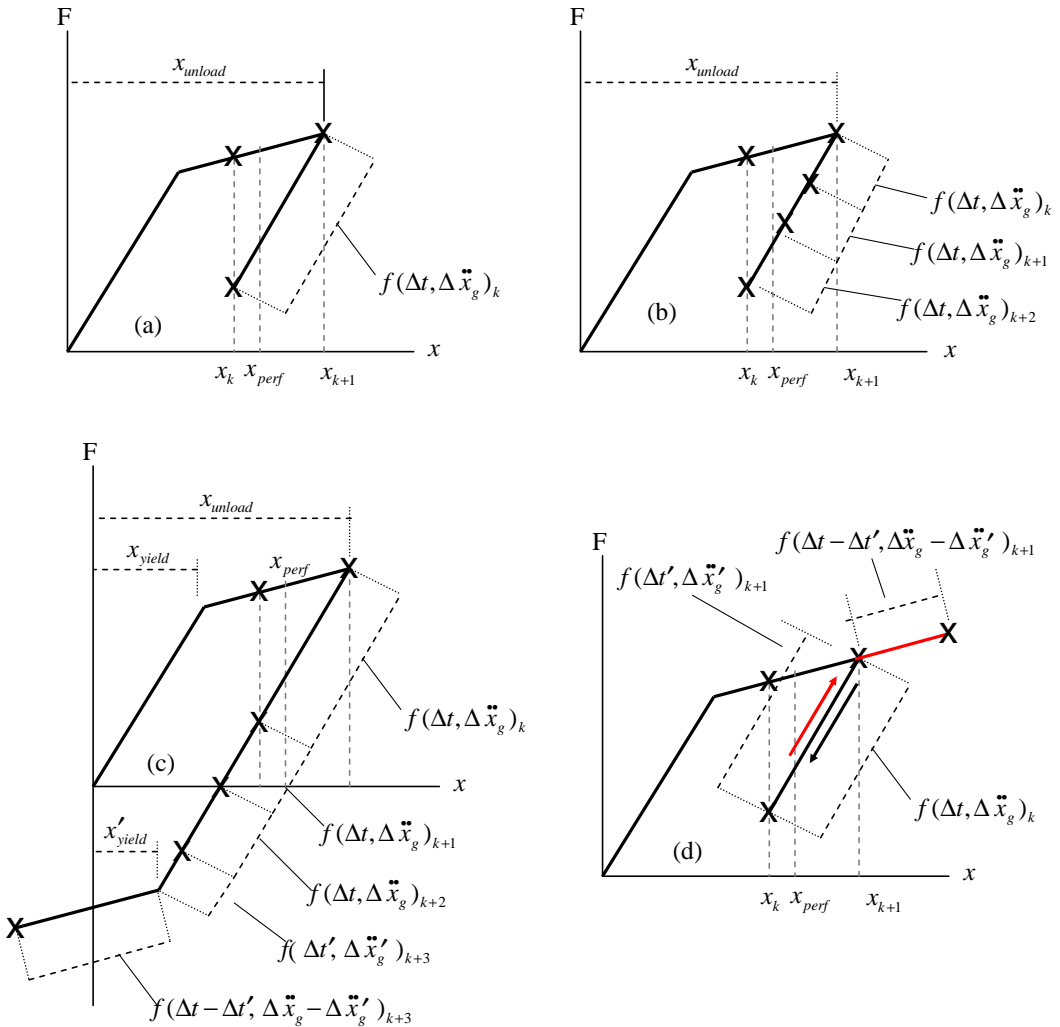


Figure 5. Controlled unloading of a member: (a) meeting the performance objective in a single time step after the member is unloaded; (b) meeting the performance objective in multiple time steps; (c) rehabilitating a member by forcing it to yield; (d) same-side reyielding after the performance objective has been satisfied.

control force over time step, Δt ; the control algorithm will deactivate at the end of Δt if the performance objective is satisfied. However, if the member unloads but does not satisfy the performance objective on step k , then a new control force is calculated that is applied on the ensuing time step ($k + 1$) until the objective is finally satisfied, for example on time step ($k + 2$) as in [Figure 5b](#).

As discussed in the preceding subsection (page 860), there are times when a performance objective may be satisfied, yet the control algorithm commands additional force to be supplied to continue unloading the member until it yields; see [Figure 5c](#) (time step $k + 3$). The reason for this is to prevent same-side reyielding that would have otherwise induced additional strain hardening in the member; same-side reyielding is defined as a reversal in the member displacement and subsequent reyielding on the same-side that had originally unloaded; see [Figure 5d](#). Thus, the forced yielding rehabilitates the structure by allowing it to dissipate any surplus energy it may have absorbed earlier. This helps reduce the velocity and acceleration of the member and maintains a stable system [[Attard et al. 2009](#)]. The time step over which the member is being forced to yield is iterated (see [Figure 5c](#), time step $k + 3$) until the necessary state-space transition matrix, S_s , and control force help the member yield. A new control force is then applied over the remainder of the time step ($\Delta t - \Delta t'$) using the appropriate reduction in the member stiffness.

3. Optimal inelastic control for already-damaged structures

The control law herein is used to formulate an optimal, evolutionary gain and subsequent control force for the purpose of reducing demands that may have exceeded prescribed performance objectives. The solution is formulated in state-space. The energy-based cost function is minimized, and structural demands may be controlled *per time step*. In this sense, the control device responds to each response in real-time and employs a new gain formulation at each time step only *as-needed* for the purpose of generating an appropriate counteracting force. This approach may be used in lieu of a constant or predetermined gain formulation that is otherwise used throughout the response time history in calculating a continual resistive control force. However, when a control device adds energy (either from an evolutionary gain or a constant gain basis) into a damaged (inelastic) member, there needs to be a mechanism in place to dissipate this additional energy since the damaged member has less resistance (i.e., less of its original strain energy). Without such a mechanism, the control force may even be counterproductive and result in increased damage and instability in the member response.

The algorithm in CONON is developed using an optimal linear centralized approach that is based on linear quadratic theory [[Franklin et al. 2002](#)]. The evolutionary gain is calculated by adapting the Riccati matrix per time step, where the damaged member may either be rehabilitated (see above), or where smaller quantities of control energy are formulated and utilized per time step in the calculation of the control force (discussed later). An allowable response window is used to represent the amount of tolerable material damage in a structural member. The allowable window may remain either fixed (displacement-based control) or flexible (strain-based control), where the latter accounts for the material anisotropy in damaged members caused by the realignment of the material's molecular structure.

The equation of motion for an multi-DOF shear-frame excited by horizontal base ground accelerations, $\ddot{x}_g(t)$, is given by

$$M\ddot{x}(t) + C\dot{x}(t) + Kx(t) = -M\ddot{x}_g(t) - F_R(t) + Df_c(t). \quad (4)$$

The location vector of the control devices having control force $f_c(t)$ is given as \mathbf{D} . The mass and damping matrices are defined as \mathbf{M} and \mathbf{C} , respectively. The displacement vector relative to the ground is defined as $\mathbf{x}(t)$. The elastic stiffness is defined as \mathbf{K} , which is a linear nonhysteretic spring that provides the only restoring force to the frame until yielding occurs in the j -th member at which point the nonhysteretic spring force remains constant, and $x_j(t) = x_{\text{yield},j}$, where $x_j(t)$ is a component of $\mathbf{x}(t)$. The hysteretic restoring force, \mathbf{F}_R , which includes the post-yield deflection, appears in those members that have started to yield (i.e., $x_j(t) > x_{\text{yield},j}$).

$$F_R(t) = \sum_{i=1}^{\text{plex}} \alpha_{ij} K x_{ie,ij}(t), \tag{5}$$

where the proportionality factor, α_{ij} , in (5) is the ratio of the inelastic stiffness to the elastic stiffness of the j -th member in the shear-frame. The term *plex* is the number of plastic excursions that the j -th member may ultimately experience during a given half-hysteretic cycle, where i represents the state of damage in the j -th member. The separation of the elastic and inelastic stiffness components in (4) facilitates the proposed inelastic control. The inelastic displacements, $x_{ie,ij}$, in (5) may be expressed as

$$x_{ie,ij}(t) = \begin{cases} x_{\text{tot},j}(t) - x_{\text{yield},j} - \sum_{m=1}^{i-1} x_{ie,mj}(t) & \text{if } i \geq 2, \\ x_{\text{tot},j}(t) - x_{\text{yield},j} & \text{if } i = 1. \end{cases} \tag{6}$$

The displacement $x_{\text{tot},j}(t)$ is calculated relative to when the now-yielded member started to unload or reload on any given half-cycle. The degradation of the stiffness is developed by introducing a nonlinear kinematic strain hardening in the material, where on a given half-cycle, a member will reyield at a displacement equal to the most recent unloading displacement minus twice the initial yield displacement [Ragab and Bayoumi 1999]. This permits each hysteresis loop to close and merge with each preceding loop [Lemaitre and Chaboche 1990]. Additionally, the same set of α_{ij} factors are used in calculating the degraded member stiffness starting with each half-cycle. Finally, the most recent member stiffness immediately before unloading is “remembered” to account for any residual stresses in the event that a load reversal occurs and the member reyields.

Damaged (inelastic) members have less restoring force capability than undamaged (elastic) members, thus requiring larger control forces that result in high manufacturing costs. In order to minimize the requisite control force, an optimal Riccati matrix and a new (or evolutionary) gain are used during *each* necessary time step to produce an optimal control force that will help satisfy elastic or inelastic performance objectives. The procedure is entirely automated in CONON. The control force is calculated using an optimal linear closed-loop control algorithm which relies on the velocity and displacement of the structure. The control law may be expressed as

$$f_c(t) = f_{c1}(x(t)) + f_{c2}(\dot{x}(t)), \tag{7}$$

where $f_c(t)$ is the applied control force, and f_{c1} and f_{c2} are functions that govern the participation of the structure’s displacement and velocity in the calculation of the control force. The objective is to determine the forms of f_{c1} and f_{c2} that will produce a control force to satisfy the desired performance objectives. Therefore, the cost function J_k in (8) is minimized subject to the constraint of the state-space response,

z_{k+1} , where

$$J_k = \int_{t_k}^{t_k+\Delta t} \frac{1}{2} (z_k^T(t) \mathbf{Q} z_k(t) + f_{c,k}^T(t) \mathbf{R} f_{c,k}(t)) dt. \tag{8}$$

The Riccati matrix is determined iteratively and is used to relate the current state-space response of the member, z_k , to a Lagrange multiplier, where the latter is used to find an expression for z_{k+1} in terms of z_k and which also leads to the calculation of the control law of $f_{c,k}$ (where k is the time step over which the control force is calculated). The cost function, J_k , is minimized per k -th time step over the time step interval, Δt , and \mathbf{Q} and \mathbf{R} are weighing matrices that affect the controlled responses and applied control force, respectively. The state-space response vector (for DOF degrees of freedom) is expressed as

$$z(t) = \begin{Bmatrix} x(t) \\ \dot{x}(t) \end{Bmatrix}_{(2 \text{ DOF}) \times 1} \tag{9}$$

and after multiplying through with \mathbf{M}^{-1} , we may express (4) in state-space form as

$$\dot{z}(t) = \mathbf{A}z(t) + \mathbf{H}\ddot{x}_g(t) + \sum_{i=1}^{\text{plex}} \mathbf{F}_{c,ie} x_{ie,ij}(t) + \mathbf{B}f_c(t), \tag{10}$$

where we have introduced the following matrices:

$$\mathbf{A} = \begin{bmatrix} \mathbf{0} & \mathbf{I} \\ -\mathbf{M}^{-1}\mathbf{K} & -\mathbf{M}^{-1}\mathbf{C} \end{bmatrix}_{(2 \text{ DOF}) \times (2 \text{ DOF})} \quad \mathbf{H} = \begin{Bmatrix} \mathbf{0} \\ -\mathbf{I} \end{Bmatrix}_{(2 \text{ DOF}) \times 1} \tag{11}$$

$$\mathbf{F}_{c,ie} = \begin{Bmatrix} \mathbf{0} \\ -\alpha_{ij}\mathbf{M}^{-1}\mathbf{K} \end{Bmatrix}_{(2 \text{ DOF}) \times 1} \quad \mathbf{B} = \begin{Bmatrix} \mathbf{0} \\ \mathbf{M}^{-1}\mathbf{D} \end{Bmatrix}_{(2 \text{ DOF}) \times 1} \tag{12}$$

Here \mathbf{I} is the identity matrix, $\mathbf{0}$ is a zero vector, \mathbf{H} is a location vector of the excited DOFs under action of the ground accelerations, \mathbf{B} is the location vector of the control forces, and $\mathbf{F}_{c,ie}$ characterizes the inelastic state of the members using α_{ij} . The minimization of the cost function in (8) is a recursive procedure that may be made on any necessary time step over which a performance objective has been exceeded, thus leading to the calculation of the state-space response z_{k+1} on time step $k + 1$:

$$z_{k+1} = \mathbf{S}_{s,k+1}z_k + \mathbf{G}\mathbf{B}^{-1}\mathbf{H}\ddot{x}_{g,k}(t) + \mathbf{G}\mathbf{B}^{-1} \sum_{i=1}^{\text{plex}} \mathbf{F}_{c,ie} x_{ie,i}(t), \tag{13}$$

where

$$\mathbf{G} = \mathbf{A}^{-1}(e^{\mathbf{A}\Delta t} - \mathbf{I})\mathbf{B} \tag{14}$$

and

$$\mathbf{S}_{s,k+1} = \mathbf{I}e^{\mathbf{A}\Delta t} + \mathbf{G}[\Gamma_{k+1}^{\text{ev}}]. \tag{15}$$

The evolution of the state-space transition matrix, \mathbf{S}_s , is a function of the gain (expressed by Γ_{k+1}^{ev} , the evolutionary gain matrix), and transitions the response from time step k to step $k+1$, while enabling z_{k+1} to converge to the predefined performance objective z_{perf} . The evolutionary gain matrix, Γ_{k+1}^{ev} , is a function of the Riccati matrix, \mathbf{P}_{k+1} , which is calculated iteratively so that $\mathbf{P}_{k+1} \sim \mathbf{P}_k$:

$$\mathbf{P}_{k+1} = \mathbf{Q} + (e^{\mathbf{A}\Delta t})^T \mathbf{P}_k (\mathbf{I} + \mathbf{G}\mathbf{R}^{-1}\mathbf{G}^T \mathbf{P}_k)^{-1} e^{\mathbf{A}\Delta t}. \tag{16}$$

The evolutionary gain may be expressed as

$$\Gamma_{k+1}^{\text{ev}} = -(\mathbf{G}^T \mathbf{P}_{k+1} \mathbf{G} + \mathbf{R})^{-1} \mathbf{G}^T \mathbf{P}_{k+1} e^{A\Delta t} \quad (17)$$

and the control force as

$$f_{c,k+1} = [\Gamma_{k+1}^{\text{ev}}] z_k. \quad (18)$$

The minimization of the total state-space response, $z(t)$, over the entire time history may finally be expressed as

$$J = \sum_{k=1}^{\text{TimeCount}} \int_{t_k}^{t_k+\Delta t} \frac{1}{2} (z_k^T(t) \mathbf{Q} z_k^T(t) + f_{c,k}^T(t) \mathbf{R} f_{c,k}^T(t)) dt, \quad (19)$$

where TimeCount is the number of time steps in CONON's numerical simulation algorithm.

4. Control force methodology: absolute-Z approach versus delta-Z approach

Two methods are used to calculate an optimal control force, $f_{c,k+1}$. In the first, the gain is used in conjunction with the absolute displacement of the structure while the second approach employs the gain in conjunction with the absolute value of the difference between the exceeded displacement (x_{k+1}) and x_{perf} , where x_{perf} and \dot{x}_{perf} are the performance objectives for displacement and velocity, respectively. The former approach is referred to herein as the absolute-Z approach, and we will refer to the latter as the *delta-Z approach*. The absolute-Z approach uses the state-space response in (9) to minimize the cost function in (19) over the time history. In the delta-Z approach, Equations (8) and (9) are modified to include difference (or "delta") components, Δz_k , on each time step:

$$J_k = \int_{t_k}^{t_k+\Delta t} \frac{1}{2} (\Delta z_k^T(t) \mathbf{Q} \Delta z_k(t) + f_{c,k}^T(t) \mathbf{R} f_{c,k}(t)) dt, \quad (20)$$

where

$$\Delta z_k = \begin{Bmatrix} |x_k - x_{\text{perf}}| \\ |\dot{x}_k - \dot{x}_{\text{perf}}| \end{Bmatrix}. \quad (21)$$

It is assumed that \dot{x}_{perf} is zero after applying the control force

$$f_{c,k+1} = [\Gamma_{k+1}^{\text{ev}}] \Delta z_k. \quad (22)$$

If, after calculating $f_{c,k+1}$ and solving for z_{k+1} in (13) via the minimization of (8), it is found that $x_{k+1} \neq x_{\text{perf}}$, then a new control force $f_{c,k+1,n}$ is calculated on that same time step $k+1$, where n represents the iteration number on time step $k+1$. The iteration continues until the performance objective is satisfied using the same value of \mathbf{P}_{k+1} ; see (16), during that time step. New \mathbf{Q}_n and \mathbf{R}_n values are calculated on the n -th iteration by multiplying previous \mathbf{Q}_{n-1} and \mathbf{R}_{n-1} by scale factors, $\beta_{x,k+1,n}$, $\beta_{\dot{x},k+1,n}$, and $\gamma_{k+1,n}$. This results in a new $\Gamma_{k+1,n}^{\text{ev}}$, which is used to calculate a new force $f_{c,k+1,n}$ in (22). The factors $\beta_{x,k+1,n}$,

$\beta_{\dot{x},k+1,n}$, and $\gamma_{k+1,n}$ are determined using the displacement $x_{k+1,n-1}$:

$$\left. \begin{aligned} \beta_{x,k+1,n} &= \frac{|x_{k+1,n-1} - x_{\text{perf}}|}{x_{\text{perf}}} \beta_{x,k+1,n-1} \\ \beta_{\dot{x},k+1,n} &= \frac{|x_{k+1,n-1} - x_{\text{perf}}|}{x_{\text{perf}}} \beta_{\dot{x},k+1,n-1} \\ \gamma_{k+1,n} &= \frac{|x_{k+1,n-1} - x_{\text{perf}}|}{x_{\text{perf}}} \gamma_{k+1,n-1} \end{aligned} \right\} \text{ for } n \geq 2, \quad (23)$$

where $x_{k+1,1}$ may be calculated using (13) and (9). Initially, \mathbf{Q} and \mathbf{R} (see [Hart and Wong 2000] and [Conner 2003]) are defined as

$$\mathbf{Q} = \begin{bmatrix} \mathbf{K} & \mathbf{0} \\ \mathbf{0} & \mathbf{M} \end{bmatrix}, \quad \mathbf{R} = [\mathbf{I}]. \quad (24)$$

The scale factors are applied over each iteration; the parameter $\beta_{x,k+1,n}$ multiplies \mathbf{K} , $\beta_{\dot{x},k+1,n}$ multiplies \mathbf{M} , and $\gamma_{k+1,n}$ multiplies \mathbf{R} . The evolution of $\Gamma_{k+1,n}^{\text{ev}}$ occurs iteratively on each time step whenever the performance objective has been exceeded. This forces the damaged (inelastic) members to unload without significantly overshooting the prescribed objective – either for an allowable displacement (displacement-based control) or allowable inelastic strain (strain-based control). In addition, the velocity and acceleration demands are reduced because \dot{x}_{perf} is assumed to be 0. In a “constant” gain formulation, \mathbf{Q} and \mathbf{R} remain constant, which may hinder the inelastic structure from unloading even after the performance objective has been exceeded. Further, a constant gain may potentially infuse a structure with too much energy and make it unstable [Attard and Dansby 2008].

There are three advantages to using the delta- Z approach over the absolute- Z approach and thereby working with smaller demands, $x_k - x_{\text{perf}}$:

- (1) The control device needs to dissipate smaller quantities of energy during each time step and therefore generate smaller control forces that result in smaller device costs.
- (2) The convergence algorithm in CONON for meeting the performance objectives remains consistently stable.
- (3) The velocity and acceleration responses of the structure are significantly reduced.

Since the control algorithm uses a delta state response vector, Δz_k , as input — see (21) — the solution (i.e., the output) to (13) is also in “delta” form and is calculated as Δz_{k+1} in (25).

$$\Delta z_{k+1} = S_{s,k+1}(\Delta z_k) + GB^{-1}H\ddot{x}_{g,k}(t) + GB^{-1} \sum_{i=1}^{\text{plex}} F_{c,ie} x_{ie,i}(t). \quad (25)$$

To convert Δz_{k+1} to the new state response (i.e., to the new delta displacement and velocity), Δz_{k+1} is added to z_{perf} , which results in the new state response

$$z_{k+1} = \Delta z_{k+1} + z_{\text{perf}}. \quad (26)$$

The error between x_{k+1} and the performance displacement, x_{perf} , on the $(k + 1)$ -th time step is

$$\text{err}_{k+1} = \frac{|\Delta x_{k+1}|}{|x_{\text{perf}}|}, \quad (27)$$

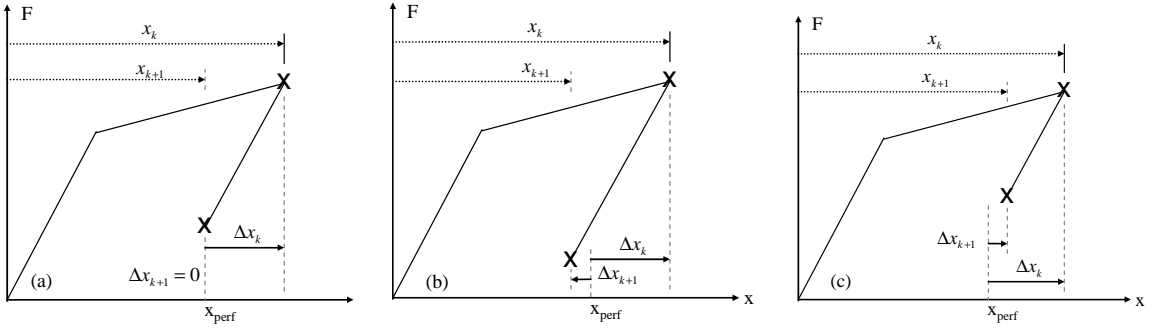
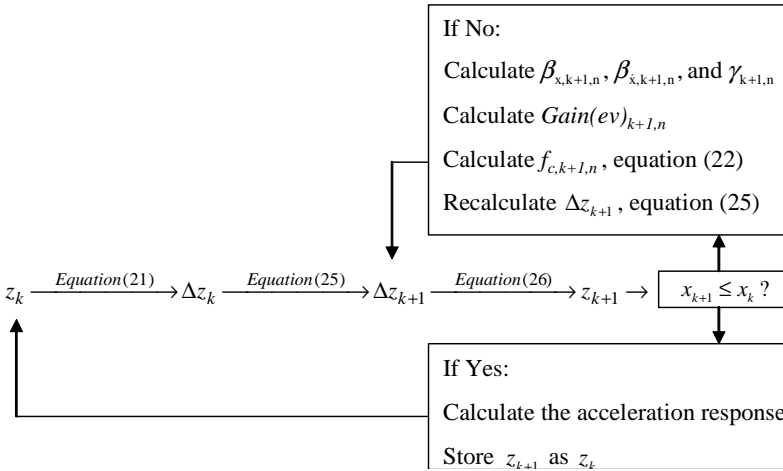


Figure 6. Illustration of the delta-Z approach: Δx_{k+1} is measured from the performance objective, or x_{perf} with (a) $\Delta x_{k+1} = 0$, where the performance objective is satisfied exactly, (b) $\Delta x_{k+1} < 0$, where the performance objective is over-shot, and (c) $\Delta x_{k+1} > 0$, where the performance objective is under met and not satisfied.

where

$$\Delta x_{k+1} = x_{k+1} - x_{\text{perf}}. \tag{28}$$

If err_{k+1} does not exceed a predefined error, the performance objective was satisfied on time step $(k + 1)$; see Figure 6a. However, if $|x_{k+1}| < |x_{\text{perf}}|$, the performance objective was met and exceeded (over-shooting), and the algorithm proceeds to the next time step; see Figure 6b. $|x_{k+1}| > |x_{\text{perf}}|$, the target displacement was not met; see Figure 6c. In this last case, a control force is calculated again using (22), and the process repeats until the predefined error is not exceeded. This flowchart below illustrates the delta-z approach:



5. Numerical examples

In the following examples, CONON used the state-space formulation discussed above when it was necessary to simulate the gain evolution and control responses (i.e., when the performance-objective had been exceeded). During all other time steps (when control was not necessary), the response time histories were marched by the Newmark Beta scheme assuming a linear change in the acceleration between time

section	W12×50 (W310×74)
mass m	0.5 kips-s ² /in (87.5 kN-s ² /m)
modulus E	29000 ksi (200 GPa)
length L	12 ft (3.66 m)
σ_{yield}	36 ksi (248 MPa)

Table 1. Single-DOF properties of the benchmark system.

steps. In either case, the time steps (Δt) were separated 0.02 seconds apart until the final time of the input earthquake starting from zero initial conditions. The properties of the single-DOF benchmark system used in the following examples are shown in Table 1. The analyses assumed rock-like ground conditions and 5% damping. The benchmark structure is modeled using two 3.65 m (12 ft) columns having total elastic stiffness of 160.8 kN/cm and an elastic natural frequency of 2.15 Hz (for initially fixed-fixed connections). The structural responses were simulated using the first 20 seconds of the El Centro ground acceleration record (S00E component) of the 1940 Imperial Valley Earthquake. In the cases where the calculated displacement at the tip of each column was not permitted to exceed the yield limit (e.g., to safeguard against potential time-delays), the prescribed performance objective was calculated as a percentage (under 100%) of the yield deflection, x_{yield} (which equaled 0.705 in), and the predefined error was taken as 0.1%; see (27). When the displacement exceeded x_{yield} , the post-yield stiffness degradation in each member was calculated using $\alpha_{11} = 0.18$ [Attard 2005] in (5) and (12); and a value of 1 was used for the constant plex in (5).

The W12 × 50 sections are assumed to kinematically strain harden, which accounts for the material anisotropy when the members unload/reload as shown in the main graph of Figure 7. The elastic (ε^e)

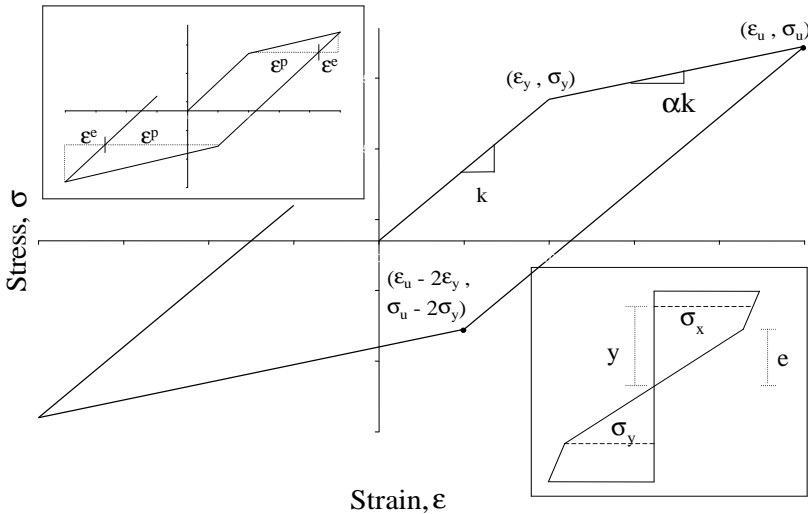


Figure 7. Model of kinematic strain hardening (anisotropic hardening). The insets show the elastic and plastic strain components (upper left) and through-thickness stress distribution (lower right).

and plastic (ϵ^p) strain components are shown in the inset graph on the top left, and the bilinear stress function (σ_x) used herein to calculate the post-yield stresses in the members once their cross-sections have yielded is calculated according to (29), where y is the depth to σ_x , and e is the elastic depth in the through-thickness of the cross-section; this is shown in the graph at the bottom right of the figure.

Embedding in CONON the model described by Figure 7 and the equation

$$\sigma_x = \sigma_y + \sigma_y \alpha_1 \left(\frac{y}{e} - 1 \right) \quad \text{for } y \geq e. \tag{29}$$

we obtain the benchmark responses of the single-DOF system (using no control) shown in Figure 8.

Constant gain. Two ways of applying a constant gain were investigated. First, a constant gain was applied in an always-on condition every other time step ($2x \Delta t$, or every 0.04 seconds) to build a conservative time delay into the response simulation. Secondly, a constant gain was applied after the performance objective had been exceeded, thus enabling control to be used in an as-needed condition.

Always-on condition. In a simulation (noted as case 1) of the single-DOF system (see Table 1) using the always-on condition, the following scale factors were determined using the absolute-Z approach

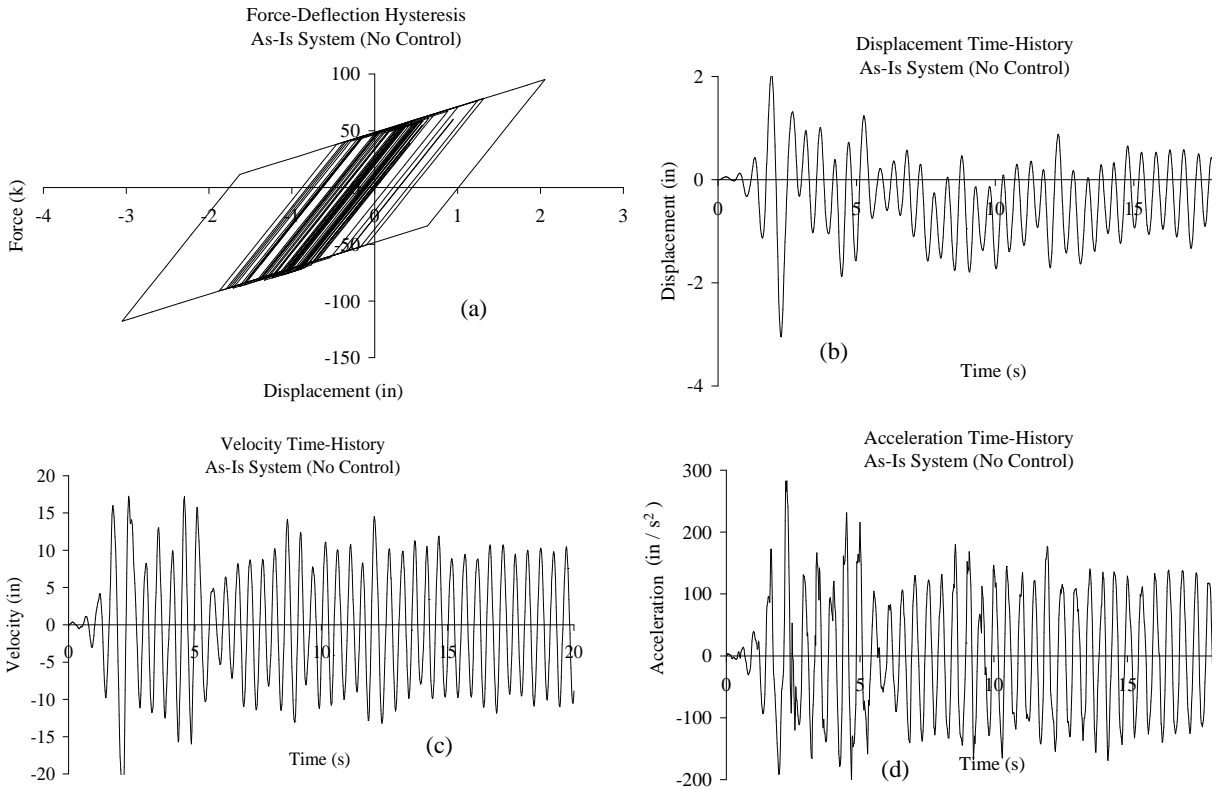


Figure 8. Benchmark shear-frame simulation (as-is system using no control): (a) force-displacement hysteresis; (b) displacement time histories; (c) velocity time histories; (d) acceleration time histories.

assuming a performance objective of 0 in measured at the tip of the column on the top story: $\beta_x = 0.32768$, $\beta_{\dot{x}} = 0.0032768$, and $\gamma = 3.2 \times 10^{-6}$. These values were calculated by minimizing J in (19) in individual time-history simulations of the El Centro earthquake, where the least square error of the demands was minimized over several simulations. The subsequently calculated optimal matrices \mathbf{Q} and \mathbf{R} were then used to control the single-DOF displacements, which remained elastic, during the earthquake using a constant gain in an always-on condition. The maximum calculated acceleration, 0.77 g's, was actually larger than the uncontrolled maximum acceleration, which was 0.73 g's, and the maximum control force that was required was 210 kips. By using an optimal always-on constant-gain control condition with a 0 in performance objective, the member displacements, while elastic, were not insignificant not to mention the relatively significant member accelerations that were found. The study implies the obvious limitations of using a constant gain approach to control.

In a case 2 simulation, the same parameters were used but using a delta-Z approach, where the system again responded elastically but incurred a maximum acceleration of 2.46 g's and a maximum control force of 495 kips at 2.3 seconds. The maximum displacement occurred one time step earlier at 2.28 seconds, which explains the large velocity and acceleration in response to the application of the preceding large control force. An as-needed condition was again assumed, and in this case, the system responded elastically only when the performance objective was defined not larger than 10% of yield, or 0.074 inches. This further illustrates the overall inefficiency of a constant gain formulation.

In a case 3 simulation, a more arbitrary selection of the scale factors in (23), where $\beta_x = 0.001$, $\beta_{\dot{x}} = 0.00001$, and $\gamma = 0.01$, shows the limitations of constant gain. In this case, the gain is applied in the always-on state using the absolute-Z approach. The performance objective is again defined as 0 in and is measured at the top story of the steel frame. After simulating the response for two cycles, the hysteresis showed that the control algorithm was unable to continue restraining the system, which became unstable with uncontrollable increases in the member displacements.

In a case 4 simulation, the delta-Z approach was used to calculate a maximum single-DOF acceleration of 0.49 g's and a maximum control force of only 0.8 kips although the displacements are once again not insignificant considering that a 0i performance objective was prescribed. The results (again using constant gain) for this last case are shown in Figure 9, which illustrates a significant reduction in the acceleration time histories compared to the uncontrolled system's accelerations.

Evolutionary gain. The four simulation cases above emphasize the importance of needing an alternative to a constant gain approach. The proposed evolutionary gain formulation is shown to desensitize the member responses to the weighing matrices while adequately controlling displacements (where little error is tolerated). The following six control scenarios were simulated using CONON:

1. absolute-Z approach, displacement-based, not forced to yield
2. absolute-Z approach, displacement-based, forced to yield
3. absolute-Z approach, strain-based, not forced to yield
4. absolute-Z approach, strain-based, forced to yield
5. delta-Z approach, displacement-based, not forced to yield
6. delta-Z approach, strain-based, not forced to yield

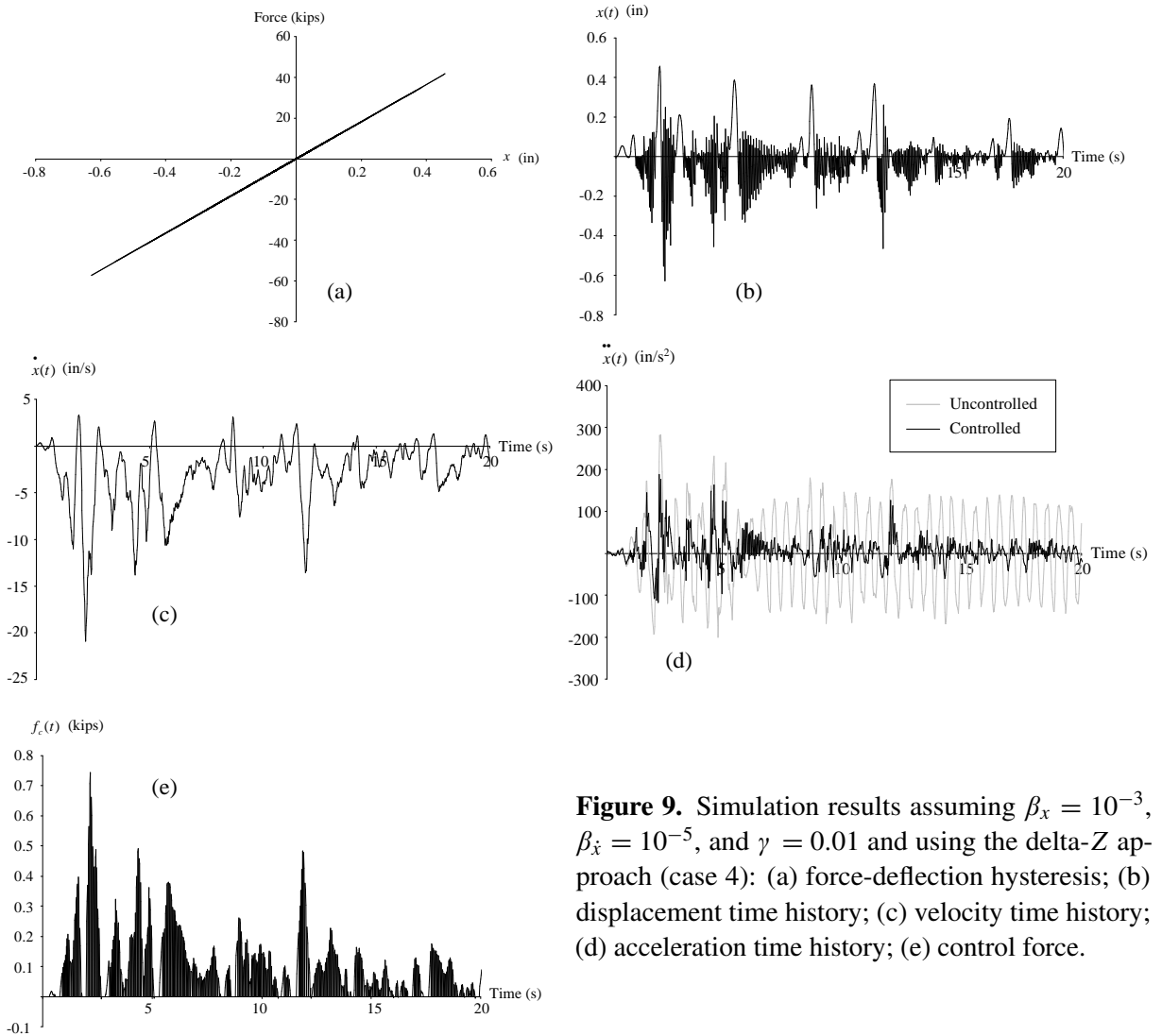


Figure 9. Simulation results assuming $\beta_x = 10^{-3}$, $\beta_{\dot{x}} = 10^{-5}$, and $\gamma = 0.01$ and using the delta-Z approach (case 4): (a) force-deflection hysteresis; (b) displacement time history; (c) velocity time history; (d) acceleration time history; (e) control force.

In each case, the gain may be varied at necessary time steps in order to satisfy the performance objectives of the single-DOF system.

In the delta-Z approach, it was found that forcing the system to yield was not necessary because of the small quantities used to calculate the control forces; see (21). As such, the responses remained easily controllable without needing to force additional energy to be dissipated through member yielding, where same-side reyielding was not an issue.

Always-on condition. An evolutionary gain was calculated every other time step depending on the current state of the system. The results are shown in Figure 10 using the absolute-Z approach.

The force-deflection hysteresis in Figure 10a shows that when control remains in an always-on state, the system responded elastically — at about 20% of the yield displacement. The controlled displacements were also significantly reduced compared to the uncontrolled displacement, as is seen from the time

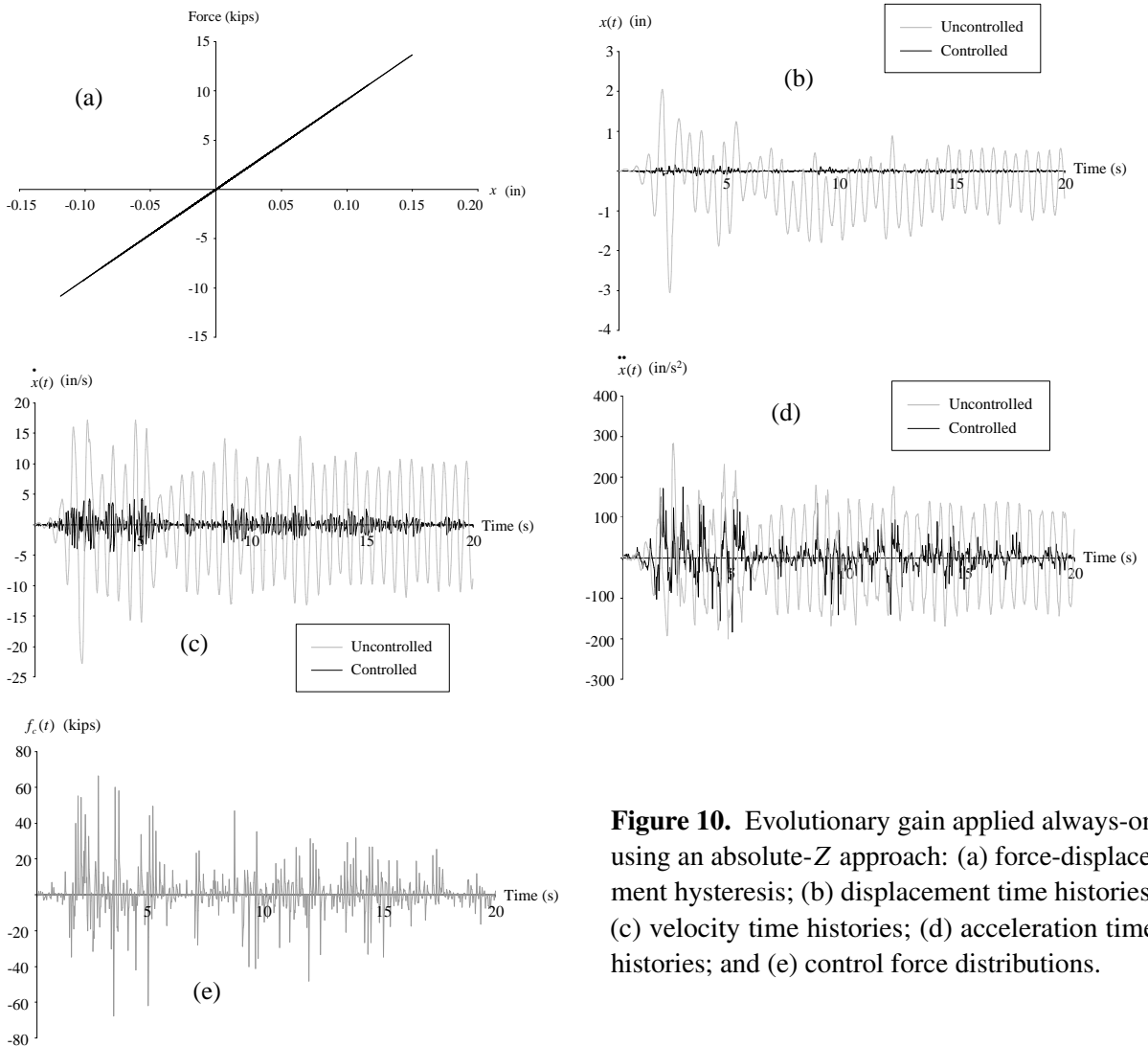


Figure 10. Evolutionary gain applied always-on using an absolute- Z approach: (a) force-displacement hysteresis; (b) displacement time histories; (c) velocity time histories; (d) acceleration time histories; and (e) control force distributions.

histories in Figure 10b. The velocity and acceleration time histories, shown in Figures 10c,d, were also smaller, and the maximum calculated control force, shown in Figure 10e, was 59 kips. If to compare these responses to those calculated in case 1 above (absolute- Z approach, always-on state) which had used a constant gain formulation, the evolutionary-controlled displacements are smaller, the accelerations are smaller (0.48 g's versus 0.77 g's), and the control force is significantly less (59 kips versus 210 kips). By varying the gain, the spikes observed in the velocity and acceleration responses of the constant gain system were alleviated since the infused earthquake energy was being dissipated from the structure in an optimal sense with respect to the exact necessary amount of gain.

The results using the delta- Z approach are virtually identical to those using the absolute- Z approach, where the responses are smaller than those of the uncontrolled system, and smaller than those using a constant gain approach (see case 2 above).

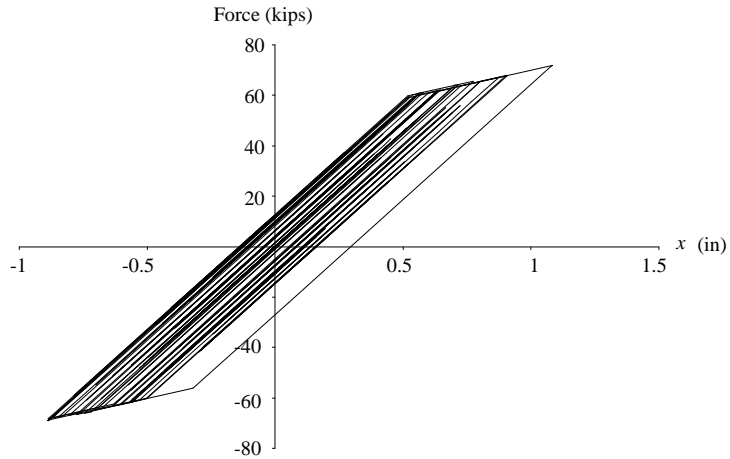


Figure 11. Force-deflection hysteresis using an evolutionary gain, and a performance objective of 50% of deflection at yield. Note that the response becomes inelastic.

As-needed condition. It was next desired to apply a control force only when needed, i.e., when the calculated displacement exceeded the allowable prescribed displacement. First, an elastic performance objective was defined - in this case, 50% of the yield deflection, or 0.352 in. The force-deflection hysteresis in Figure 11 used the absolute-Z approach and reveals that even with an elastic performance objective well below the yield deflection, the structure may still respond inelastically due to the inherent time-delay in the controller. In this case, a maximum deflection of 1.06 in was calculated, which exceeded the target displacement (50% of yield) by more than 3 times. As previously noted, the control of inelastic structures is an important consideration because of time delays, possible preexisting damages that may have altered the material constituency (e.g., the stress-strain curve), and because of unexpected earthquakes.

Next, focusing only on inelastic performance objectives, the differences between displacement-based control and strain-based control and the advantages of using the delta-Z approach over the absolute-Z approach are examined. In the strain-based control case, less energy is generally dissipated per cycle through the material hysteresis (see Figure 1), which helps preserve the structural member’s resistance and prevent further damage. Table 2 lists two evolutionary gain investigations consisting of displacement-based and strain-based performance objectives for inelastic control.

performance objective	displacement-based		strain-based	
	% of first yield	allowable deflection (in)	post-yield strain	post-yield deflection (in)
Investigation 1	125	$1.25 \times 0.704 = 0.881$	$0.25 \epsilon_{\text{yield}}$	0.176 (= 0.881 – 0.704)
Investigation 2	375	$3.75 \times 0.704 = 2.642$	$2.75 \epsilon_{\text{yield}}$	1.937 (= 2.642 – 0.704)

Table 2. Performance-objective criteria for two evolutionary-gain investigations.

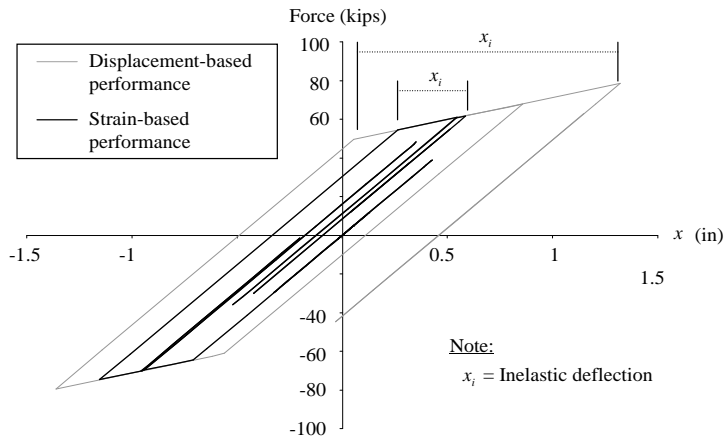


Figure 12. Hysteresis responses comparing inelastic control using displacement-based versus strain-based performance objectives.

Investigation 1. A strain-based performance objective helps minimize structural damage by controlling the amount of strain-energy that a member dissipates. The force-displacement hysteresis in this investigation is shown in Figure 12, which compares the simulated responses after 2.8 seconds using a strain-based performance objective to those of a displacement-based performance objective. The former enables the member to experience less inelastic displacement (and less strain energy dissipation) and consequently less structural damage.

Figure 13 shows the system responses using a displacement-based performance objective, without forcing the system to yield.

Referring to the force-deflection hysteresis in Figure 13a, the controlled structure's maximum deflection is less than that of the uncontrolled structure; however, if the amount of damage is a direct measure of the amount of dissipated strain energy, which is indicative of cyclic member behavior, then the controlled system dissipates nearly 3.6 times the strain energy of the uncontrolled system. Further, in this first investigation, the acceleration time histories reveal that the maximum acceleration for the controlled structure is about 10 times larger than those of the uncontrolled structure and is unacceptable.

However, by forcing the system to yield after the performance objective is met, the energy that is put into the system by the controller is reduced, and the controlled response remains stable. Figure 14a shows that when the system is forced to yield, the maximum displacement decreases, and more importantly, the strain energy dissipation reduces by 20% compared to the uncontrolled system and reduces by about 78% compared to the controlled system when it is not forced to yield. Therefore, forcing the system to yield ultimately precludes the system from reyielding on the same-side, which means that less energy is input into the system by the controller whereby the system remains stable and remains easier to control. As a result, not only is the overall damage reduced, but smaller control forces are also required (Figure 14b), since response reversals (same-side reyielding) necessitate larger control forces in order to meet performance objectives.

Figure 15 shows the system's response when using a strain-based performance objective compared against the uncontrolled responses. The force deflection hysteresis (Figure 15a) shows a significant

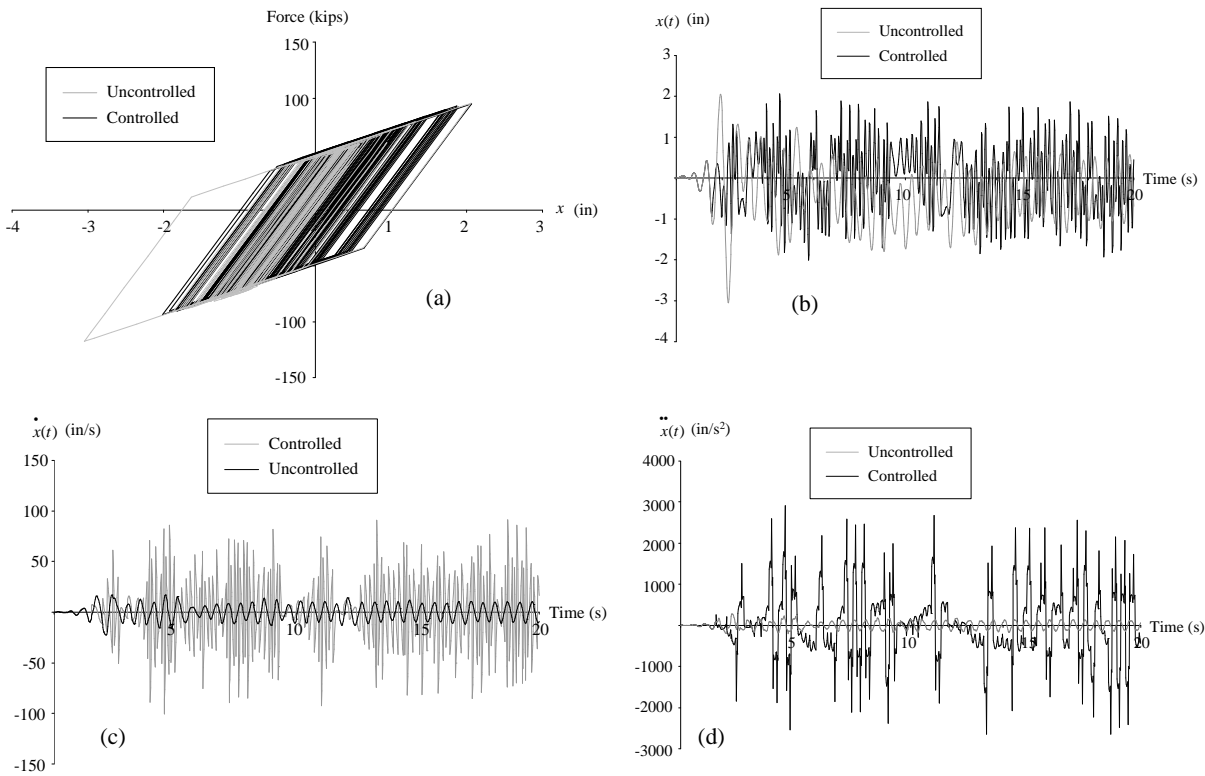


Figure 13. Responses using an evolutionary gain and the absolute- Z approach, with a displacement-based performance objective of 125% of the yield deflection (0.8805 in): (a) force-displacement hysteresis; (b) displacement time history; (c) velocity time history; and (d) acceleration time history.

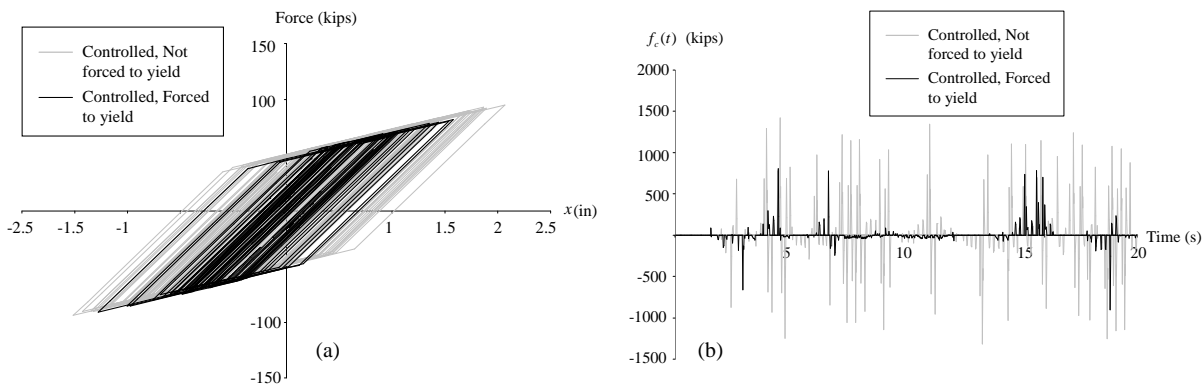


Figure 14. Evolutionary gain and the absolute- Z method, with a displacement-based performance objective of 125% of the yield deflection and forcing the system to yield: (a) force-deflection curve; (b) control force time history.

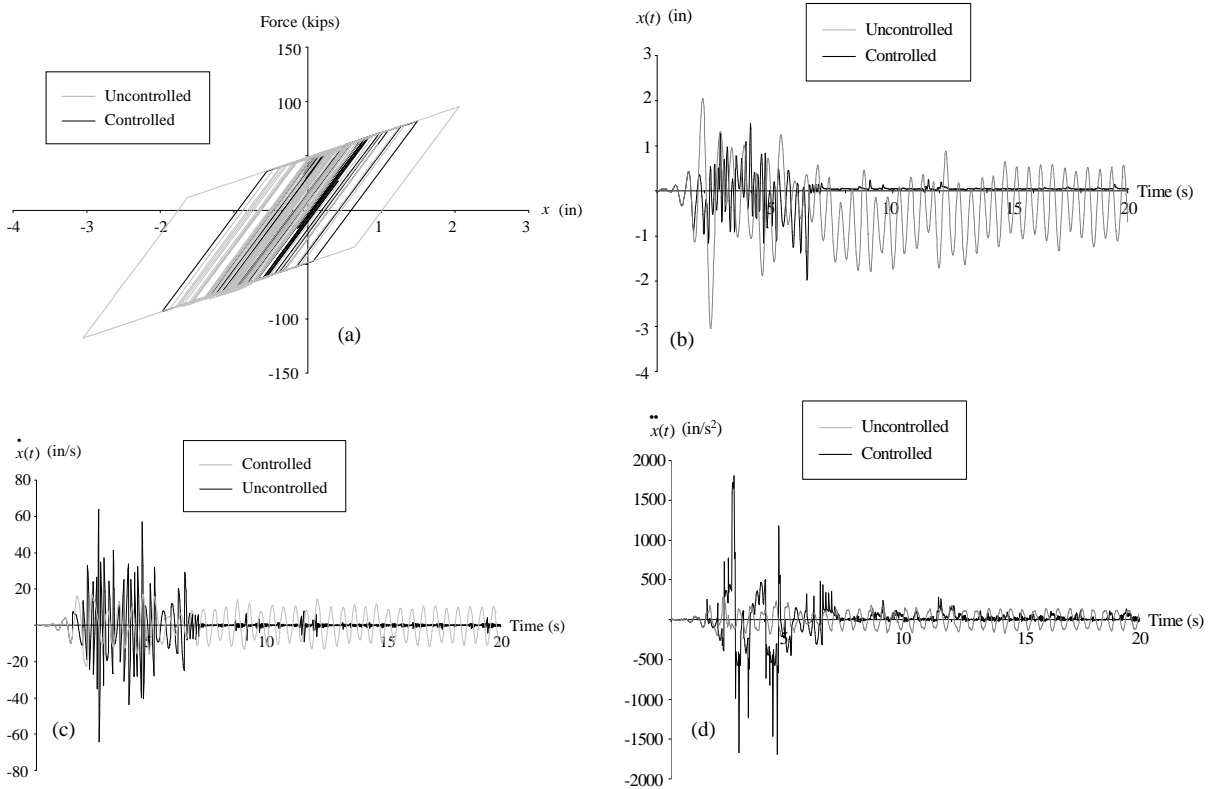


Figure 15. Responses using an evolutionary gain and the absolute- Z approach, with a strain-based performance objective of 125% of the yield deflection (0.8805 in): (a) force-displacement hysteresis; (b) displacement time history; (c) velocity time history; (d) acceleration time history.

reduction in deflection in addition to the amount of strain energy being dissipated, which is calculated as 71% less for this controlled system than for the uncontrolled system. Although the system produces dramatic improvement in the prevention of structural damage compared to the control system that uses the displacement-based performance objective (Figure 13), the velocity and acceleration time histories are greater than those for the uncontrolled system in the first few seconds of the response but are smaller for the majority of the response history; see Figures 15c,d.

Figures 16a–e show the responses using a strain-based performance objective and forcing the system to yield. Figure 16a shows the force-deflection hysteresis of the forced- and not forced-to yield responses, where the former are visibly smaller. The strain energy dissipation when forcing the system to yield dramatically reduces the amount of damage, if measured in terms of the dissipated strain energy, wherein strain energy decreases by 95% compared to the uncontrolled system and by 82% when compared to the system that is not forced to yield. Examining the time histories (parts b–e of Figure 16), it is again apparent that forcing the system to yield decreases the velocity and acceleration, and decreases the amount of control force required to manage the system. A comparison of Figures 13a, 14a, 15a, and 16a shows that

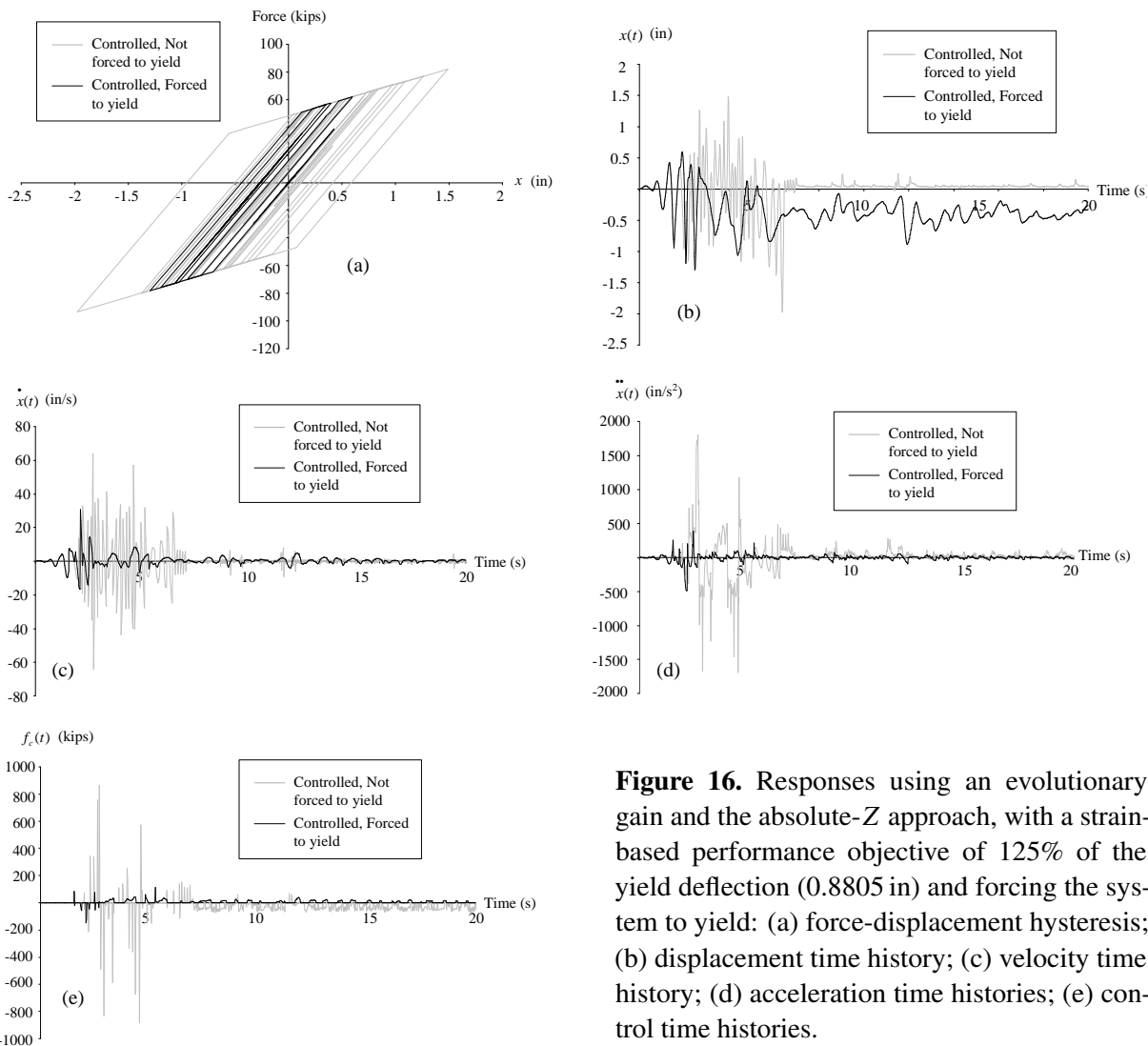


Figure 16. Responses using an evolutionary gain and the absolute- Z approach, with a strain-based performance objective of 125% of the yield deflection (0.8805 in) and forcing the system to yield: (a) force-displacement hysteresis; (b) displacement time history; (c) velocity time history; (d) acceleration time histories; (e) control time histories.

for the absolute- Z approach, the most optimal control solution for minimizing inelastic damage includes using a strain-based performance objective where the system is forced to yield in the as-needed condition and using an evolutionary gain formulation.

Figure 17 shows the responses using a delta- Z approach and a displacement-based performance objective. In Figure 17a we see the force-deflection hysteresis versus that of the uncontrolled system, where the controlled system does not even complete a full hysteresis loop during the tested duration of the earthquake. This implies that there is no same-side reyielding and results in strain energy dissipation that is 99% less than that of the uncontrolled system. The time histories in the remaining parts of Figure 17 reveal that the velocity and acceleration are also reduced, where the maximum acceleration is 34% less than that of the uncontrolled system. The magnitude of the control force (Figure 17e) is only 58 kips, but it is applied more frequently than in the displacement-based cases. This implies that smaller, more

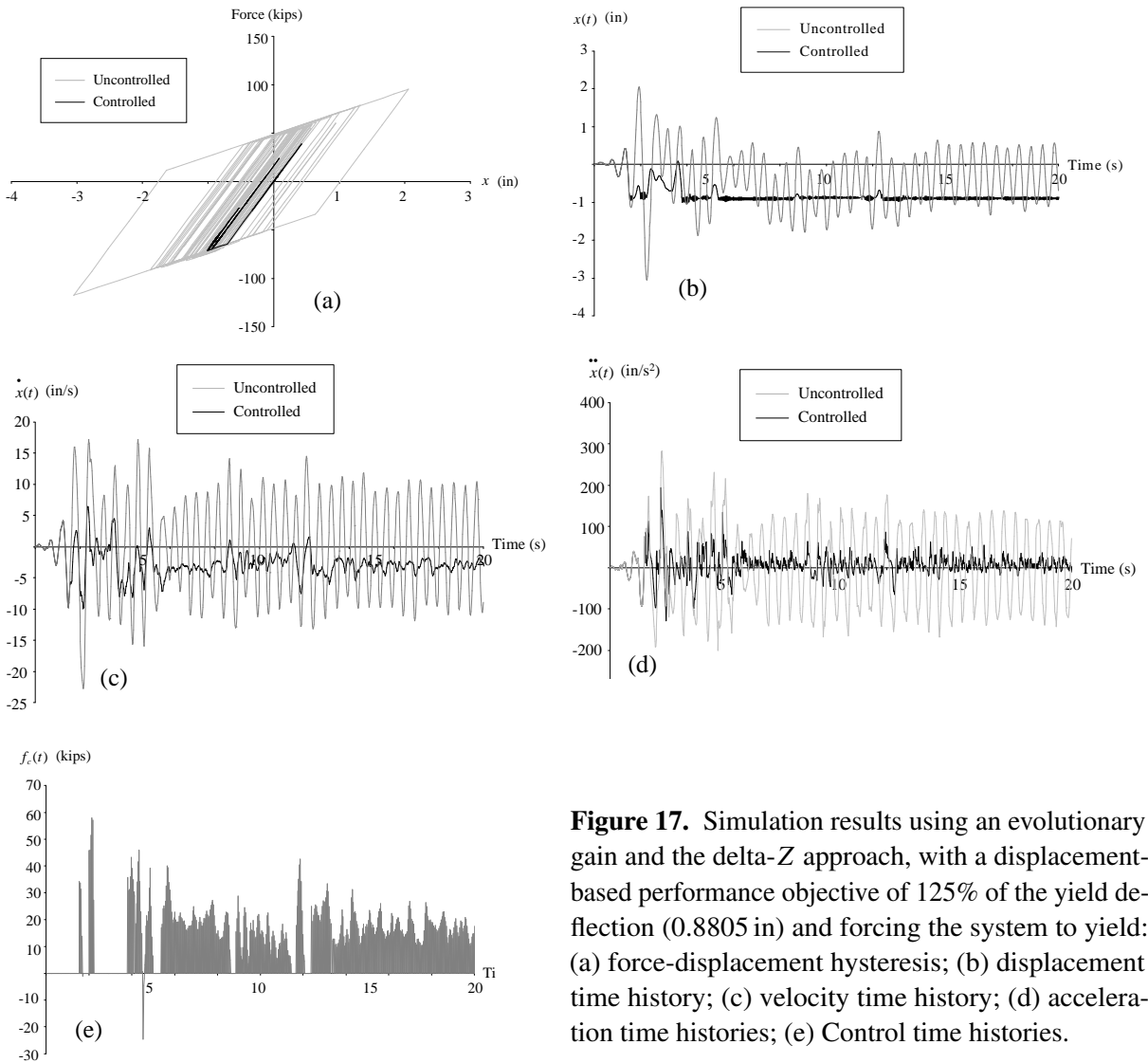


Figure 17. Simulation results using an evolutionary gain and the delta-Z approach, with a displacement-based performance objective of 125% of the yield deflection (0.8805 in) and forcing the system to yield: (a) force-displacement hysteresis; (b) displacement time history; (c) velocity time history; (d) acceleration time histories; (e) Control time histories.

cost-effective devices may be used to control the system using this method of control, but physically, they may be required to apply new control forces at each time step.

Using a strain-based performance objective, the force-deflection hysteresis is nearly the same as that in Figure 17a. Further, the dissipated strain energy is nearly identical for both the displacement-based and strain-based systems, as are the velocity and acceleration time histories, and as is the control force time-history, which has a maximum of 60 kips in this case. Therefore, it is evident that the selection of the performance objective (strain-based versus displacement-based), has virtually no influence when using the delta-Z approach since, as mentioned earlier, that small quantities of energy are utilized in the cost function minimization due to the delta formulation; see (21).

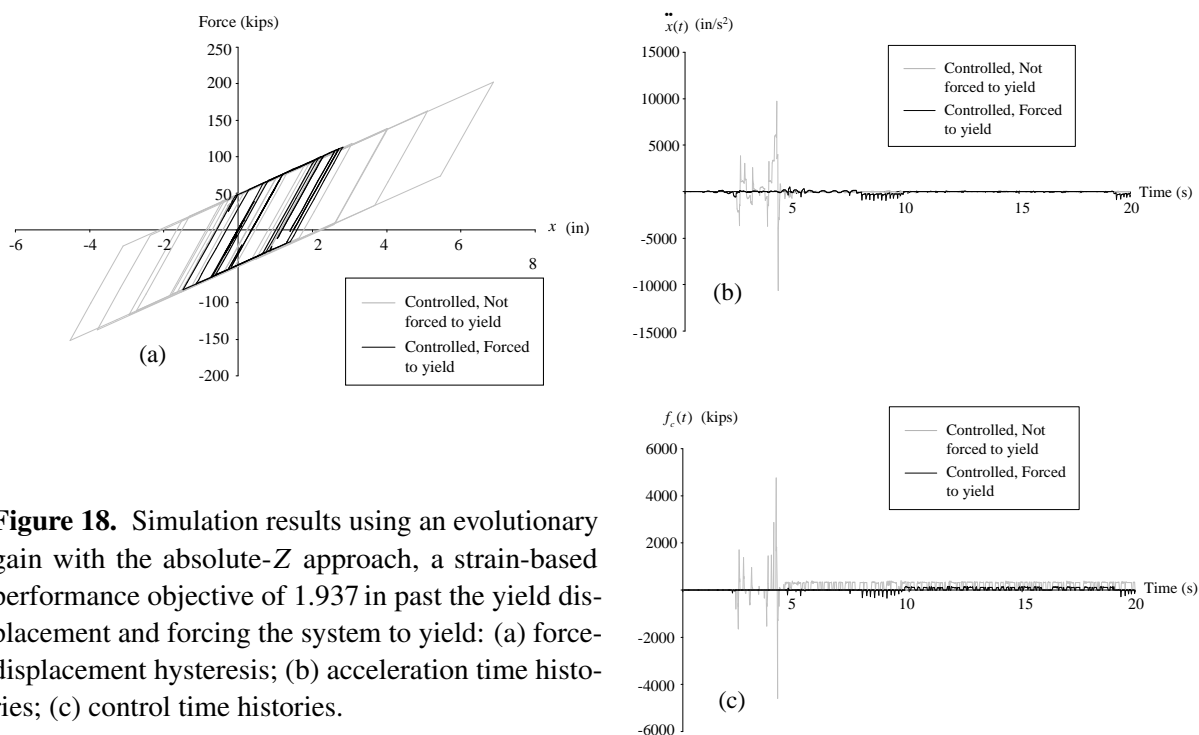


Figure 18. Simulation results using an evolutionary gain with the absolute- Z approach, a strain-based performance objective of 1.937 in past the yield displacement and forcing the system to yield: (a) force-displacement hysteresis; (b) acceleration time histories; (c) control time histories.

Investigation 2. The next investigation allows significantly more damage to occur in members; that is, a lower performance objective is demanded. Figure 18a shows the force-deflection hysteresis when the absolute- Z approach is applied to a system that is forced to yield and used in conjunction with a strain-based performance objective (set to 375% of the first-yield displacement in Investigation 2, or 1.937 inches past yield; see Table 2). The results are favorable; we see a considerable decrease in the size of the hysteresis loops when the system is forced to yield (as opposed to not being forced to yield) and a maximum displacement of 2.55 in. The maximum displacement of the uncontrolled system was 3.05 in. (Figure 8a) and the resulting strain energy dissipation is 46% less than that of the uncontrolled system. However, the maximum acceleration (Figure 18b) was 2.46 g 's, which was approximately 10% of the maximum acceleration in the unforced system, but still 3.37 times the maximum acceleration seen in Figure 8d (page 871) for the uncontrolled system. Figure 18c compares the control force time histories of the forced and unforced systems, where the former is clearly favorable.

The delta- Z approach was then applied to a not-forced-to-yield system in an effort to reduce the necessary control force and subsequent energy input to the single-DOF system so that responses may be minimized while the responses remained stable; Figure 19 shows the results for both the displacement-based system (left column) and the strain-based system (right column). The delta- Z approach significantly reduced the number of cycles in the force-deflection hysteresis (top row of Figure 19) compared to that of the uncontrolled system (Figure 8a), resulting in a 79% decrease (displacement-based) and a 84% decrease (strain-based) in the dissipated strain energy. The maximum accelerations (middle row of Figure 19) were found to be 0.84 g 's and 0.65 g 's for the displacement-based and strain-based systems, respectively, whereas the uncontrolled system's maximum acceleration was 0.73 g 's (Figure 8d). The

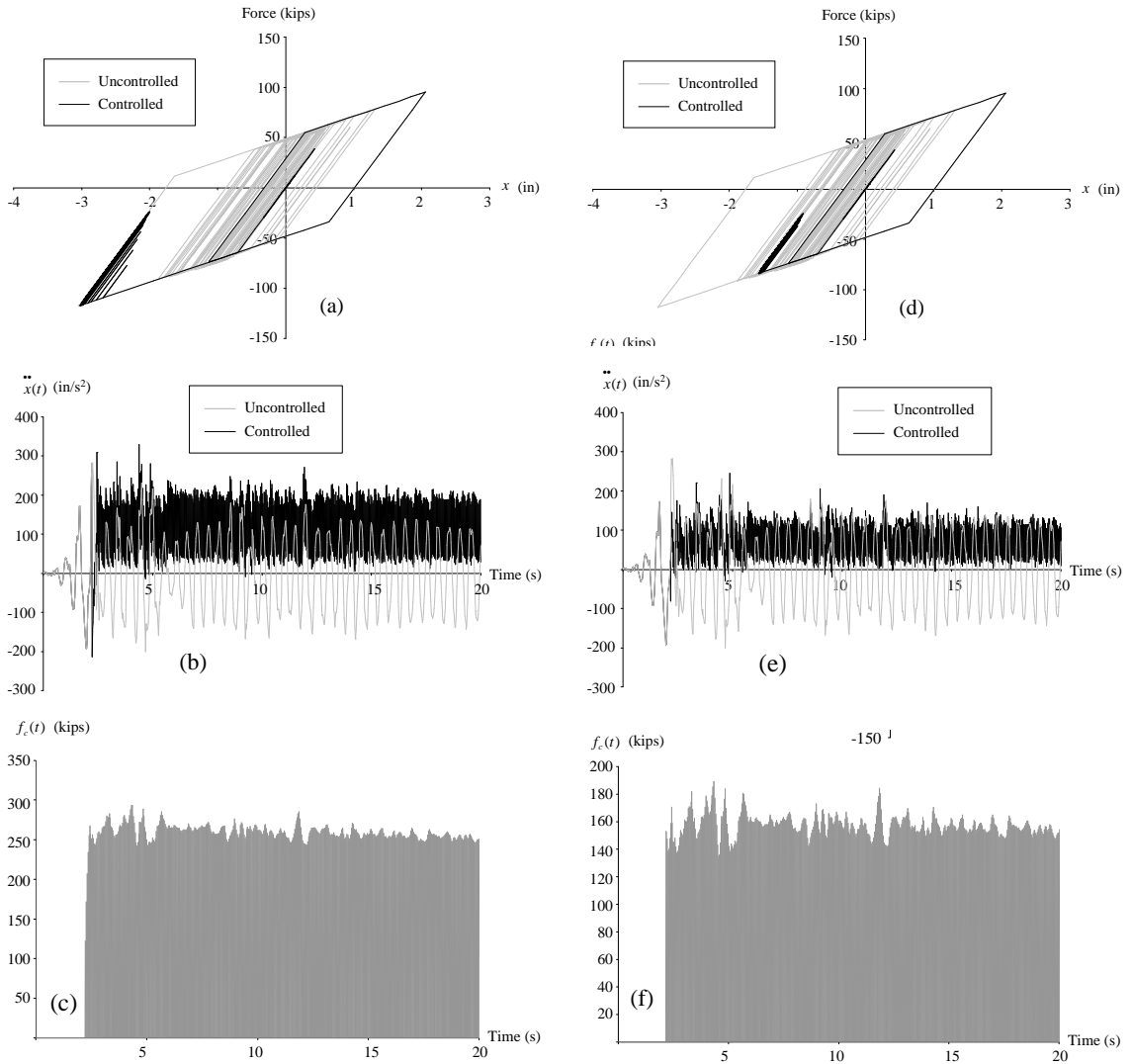


Figure 19. Left column: force-deflection hysteresis, acceleration, and control force obtained using evolutionary gain as part of the delta- Z approach with a displacement-based performance objective of 375% of the yield deflection, or 2.64 in. Right column: corresponding quantities obtained with a strain-based performance objective consisting of a post-yield strain of 2.75 times $\varepsilon_{\text{yield}}$, or a post-yield deflection of 1.94 in.

abrupt changes in the accelerations after 2.4 seconds were caused by the sudden application of control forces after 2.38 seconds — this in response to the system trying to reverse its direction after 2.38 seconds, as shown by the same-side reyielding of the force-displacement hysteresis in quadrant 3 in both cases.

The bottom row of Figure 19 shows the control force distributions for the displacement-based and strain-based systems; the maximum control forces are 298 kips and 190 kips, respectively. A comparison

Conditions	Experiment 1				Experiment 2			
	change in strain energy dissipation	maximum structure acceleration (in/s ²)	change in maximum acceleration	maximum control force	change in strain energy dissipation	maximum structure acceleration (in/s ²)	change in maximum acceleration	maximum control force
A D N	264%	3000	900%	1500	2536%	8000	2567%	3500
A D Y	-20%	2000	567%	800	25%	800	167%	450
A S N	-71%	1800	500%	900	207%	10000	3233%	5000
A S Y	-95%	500	67%	100	-46%	950	217%	350
Δ D N	-99%	200	-33%	60	-76%	325	8%	300
Δ S N	-99%	200	-33%	60	-84%	250	-17%	190

Table 3. Summary of evolutionary gain results for controlling inelastic damage, with percent changes relative to the uncontrolled situation. The first code under “Conditions” indicates the approach (absolute-Z or delta-Z), the second the type of performance objective (displacement-based or strain-based), and the third whether or not the member is forced to yield. The best results are highlighted.

of the two indicates that the latter is clearly capable of controlling already-damaged systems while reducing accelerations using a moderate level of control force.

Summary of as-needed approaches for inelastic control. A summary of the two investigations is shown in Table 3 using the six combination of conditions listed on page 872. In each investigation, the delta-Z approach proved to be more capable of controlling the amount of strain energy being dissipated (and henceforth limit the amount of permanent damage) in the members and reduce the accelerations than the absolute-Z approach.

Table 3 shows that by utilizing a strain-based performance objective, the delta-Z approach provides the optimal evolutionary control strategy where there is 99% reduction in structural damage and a 33% reduction in the maximum acceleration compared to the uncontrolled system in Investigation 1 while requiring a maximum control force of only 60 kips. In Investigation 2, which employed a lower performance objective (hence more allowable damage — damage of 2.75 times the yield response), there was an 84% decrease in damage and a 17% decrease in the maximum acceleration, with a still-moderate control force of 190 kips.

6. Conclusions

A linear optimal control solution for controlling inelastic and elastic systems using an evolutionary gain and a state-space transition formulation is presented. Control forces may be generated and applied during each time step in order to satisfy required performance objectives, which may be defined either globally

with respect to the original equilibrium position of the member, or locally with respect to the current yield position of the member during each cyclic response. The elastic and inelastic response components of the simulated responses are separated based on the discretized plastic excursions of the degrading system. A kinematically strain-hardening assumption is used to define the hysteresis of the material as it unloads, re-yields, and reloads. A computer program, CONON (for control nonlinear time-history analysis) was developed herein to simulate and control the inelastic responses in shear frames using the proposed evolutionary gain approach. The code uses an efficient subroutine to expeditiously converge to the desired performance objectives. It was found that the procedure was able to adequately converge to the desired performance objectives for an earthquake excitation using a minimal amount of control force while alleviating the dependence on weighing matrices that might inconsistently satisfy or not satisfy performance objectives and result in excessive and costly output control forces.

Further, the delta- Z approach used in conjunction with a strain-based performance objective was found to be the optimal solution in effectively mitigating damage (measured in terms of strain energy dissipation), which was reduced by at least 84%, and in effectively reducing the overall maximum acceleration by at least 17%. In addition, the delta- Z approach also required the smallest amount of control force, which indicated that developing such an optimal evolutionary controller may also present the cheapest solution. Nonetheless, the absolute- Z approach was also able to effectively reduce the strain energy dissipation in the two investigations when used in conjunction with a strain-based performance objective and when the system was forced to yield.

References

- [Agrawal and Yang 2000] A. K. Agrawal and J. N. Yang, “[Compensation of time-delay for control of civil engineering structures](#)”, *Earthquake Eng. Struct. Dyn.* **29**:1 (2000), 37–62.
- [Attard 2005] T. L. Attard, “[Post-yield material nonlinearity: optimal homogeneous shear-frame sections and hysteretic behavior](#)”, *Int. J. Solids Struct.* **42**:21–22 (2005), 5656–5668.
- [Attard and Dansby 2008] T. L. Attard and R. E. Dansby, “Evolutionary control of damaged systems using a rehabilitative algorithm”, in *Tenth Pan American Congress of Applied Mechanics (PACAM X)* (Cancún, 2008), vol. 12, edited by T. L. Attard, 2008. To appear.
- [Attard and Mignolet 2005] T. L. Attard and M. P. Mignolet, “[Evolutionary model for random plastic analyses of shear-frame buildings using a detailed degradation model](#)”, pp. 533–540 in *Safety and reliability of engineering systems and structures: proceedings of the 9th International Conference on Structural Safety and Reliability (ICOSSAR 2005)* (Rome, 2005), edited by G. Augusti et al., Millpress, Rotterdam, 2005.
- [Attard and Mignolet 2008] T. L. Attard and M. P. Mignolet, “[Random plastic analysis using a constitutive model to predict the evolutionary stress-related responses and time passages to failure](#)”, *J. Eng. Mech. (ASCE)* **134**:10 (2008), 881–891.
- [Attard et al. 2009] T. L. Attard, R. E. Dansby, and M. Marusic, “Optimal nonlinear structural damage control for kinematically strain hardened systems using an evolutionary state transition”, in *Computational structural dynamics and earthquake engineering, COMPDYN 2007* (Rethymno, 2007), edited by M. Papadrakakis et al., Structures and Infrastructures **2**, Taylor and Francis, London, 2009.
- [Caughey 1998] T. K. Caughey, “[The benchmark problem](#)”, *Earthquake Eng. Struct. Dyn.* **27**:11 (1998), 1125.
- [Christenson and Emmons 2005] R. E. Christenson and A. T. Emmons, “[Semiactive structural control of a nonlinear building model: considering reliability](#)”, in *Metropolis and beyond: proceedings of the 2005 Structures Congress and the 2005 Forensic Engineering Symposium* (New York, 2005), ASCE, Reston, VA, 2005.
- [Conner 2003] J. J. Conner, *Introduction to structural motion control*, Prentice Hall, Upper Saddle River, NJ, 2003.

- [FEMA 2001] “The 2000 NEHRP recommended provisions for seismic regulations for new buildings and other structures, 1: Provisions”, FEMA Report 368, Building Seismic Safety Council/Federal Emergency Management Agency, Washington, DC, 2001, Available at <http://www.bssconline.org/NEHRP2000/comments/provisions>.
- [Franklin et al. 2002] G. F. Franklin, J. D. Powell, and A. Emami-Naeini, *Feedback control of dynamic systems*, Prentice Hall, Upper Saddle River, NJ, 2002.
- [Gavin et al. 2003a] H. P. Gavin, C. Alhan, and N. Oka, “Fault tolerance of semiactive seismic isolation”, *J. Struct. Eng. (ASCE)* **129**:7 (2003), 922–932.
- [Gavin et al. 2003b] H. P. Gavin, P. Phule, and A. Jones, “Design optimization of MR devices and materials”, in *Proceedings of the 3rd World Conference on Structural Control (3WCSC)* (Como, 2002), edited by F. Casciati, Wiley, Chichester, 2003.
- [Gavin et al. 2003c] H. P. Gavin, J. Thurston, A. Singer, H. Fujitani, and C. Minowa, “Effects of damper force ranges and ground motion pulse periods on the performance of semi-active isolation systems”, pp. 79–85 in *Problems involving thermal hydraulics, liquid sloshing, and extreme loads on structures* (Cleveland, OH, 2003), edited by F. J. Moody et al., PVP **454**, ASME, New York, 2003. Paper No. PVP2003-1819.
- [Hart and Wong 2000] G. C. Hart and K. K. F. Wong, *Structural dynamics for structural engineers*, Wiley, New York, 2000.
- [Howard et al. 2005] J. K. Howard, C. A. Tracy, and R. G. Burns, “Comparing observed and predicted directivity in near-source ground motion”, *Earthquake Spectra* **21**:4 (2005), 1063–1092.
- [IBC 2003] *International building code*, International Code Council, Country Club Hills, IL, 2003.
- [Kelly 1999] J. M. Kelly, “The role of damping in seismic isolation”, *Earthquake Eng. Struct. Dyn.* **28**:1 (1999), 3–20.
- [Kim and Adeli 2004] H. Kim and H. Adeli, “Hybrid feedback-least square algorithm for structural control”, *J. Struct. Eng. (ASCE)* **130**:1 (2004), 120–127.
- [Lemaitre and Chaboche 1990] J. Lemaitre and J. L. Chaboche, *Mechanics of solid materials*, Cambridge University Press, Cambridge, 1990.
- [Madden et al. 2002] G. J. Madden, M. D. Symans, and N. Wongprasert, “Experimental verification of seismic response of building frame with adaptive sliding base-isolation system”, *J. Struct. Eng. (ASCE)* **128**:8 (2002), 1037–1045.
- [Makris 1997] N. Makris, “Rigidity-plasticity-viscosity: can electrorheological dampers protect base-isolated structures from near-source ground motions?”, *Earthquake Eng. Struct. Dyn.* **26**:5 (1997), 571–591.
- [Nagarajaiah and Mao 2004] S. Nagarajaiah and Y. Mao, “Response of smart base isolated structures with independently variable stiffness and variable damping systems in near fault earthquakes”, in *Proceedings of the US-Korea Joint Seminar/Workshop on Smart Structures Technologies* (Seoul, 2004), edited by C.-B. Yun and L. A. Bergman, Techno-Press, Daejeon, 2004.
- [Nagarajaiah et al. 2000] S. Nagarajaiah, S. Sahasrabudhe, and R. Iyer, “Seismic response of sliding isolated bridges with smart dampers subjected to near source ground motions”, Chapter 1, Section 5, in *Advanced technology in structural engineering: Structures Congress 2000* (Philadelphia, 2000), edited by M. Elgaaly, ASCE, Reston, VA, 2000.
- [Nagarajaiah et al. 2004] S. Nagarajaiah, A. Agrawal, and E. Sonmez, “Response of SDOF systems with variable stiffness and damping systems to pulse type of excitations”, in *Proceedings of the 3rd International Conference on Earthquake Engineering (3ICEE): new frontier and research transformation* (Nanjing, 2004), edited by W. Liu et al., China Water Power Press, Beijing, 2004.
- [Ohtori et al. 2004] Y. Ohtori, R. E. Christenson, B. F. Spencer, Jr., and S. J. Dyke, “Benchmark control problems for seismically excited nonlinear buildings”, *J. Eng. Mech. (ASCE)* **130**:4 (2004), 366–385.
- [Ragab and Bayoumi 1999] A. Ragab and S. E. Bayoumi, *Engineering solid mechanics: fundamentals and applications*, CRC Press, Boca Raton, FL, 1999.
- [Reynolds and Christenson 2006] W. E. Reynolds and R. E. Christenson, “Bench-scale nonlinear test structure for structural control research”, *Eng. Struct.* **28**:8 (2006), 1182–1189.
- [Ribakov 2004] Y. Ribakov, “Semi-active predictive control of non-linear structures with controlled stiffness devices and friction dampers”, *Struct. Des. Tall Spec. Build.* **13**:2 (2004), 165–178.
- [Symans and Reigles 2004] M. D. Symans and D. G. Reigles, “Supervisory fuzzy logic control of smart seismic isolation systems”, in *Building on the past, securing the future: proceedings of the 2004 Structures Congress* (Nashville, TN, 2004), edited by G. E. Blandford, ASCE, Reston, VA, 2004.

- [Varadarajan and Nagarajaiah 2004] N. Varadarajan and S. Nagarajaiah, “Wind response control of building with variable stiffness tuned mass damper using empirical mode decomposition/Hilbert transform”, *J. Eng. Mech. (ASCE)* **130**:4 (2004), 451–458.
- [Wong 2005a] K. K. F. Wong, “Predictive optimal linear control of elastic structures during earthquake, I”, *J. Eng. Mech. (ASCE)* **131**:2 (2005), 131–141.
- [Wong 2005b] K. K. F. Wong, “Predictive optimal linear control of inelastic structures during earthquake, II”, *J. Eng. Mech. (ASCE)* **131**:2 (2005), 142–152.
- [Wong and Yang 2002] K. K. F. Wong and R. Yang, “Earthquake response and energy evaluation of inelastic structures”, *J. Eng. Mech. (ASCE)* **128**:3 (2002), 308–317.
- [Wu 2005] H. C. Wu, *Continuum mechanics and plasticity*, Chapman and Hall/CRC Press, Boca Raton, FL, 2005.
- [Yang et al. 1990] J. N. Yang, A. Akbarpour, and G. Askar, “Effect of time delay on control of seismic-excited buildings”, *J. Struct. Eng. (ASCE)* **116**:10 (1990), 2801–2814.
- [Yang et al. 1996] J. N. Yang, J. C. Wu, and Z. Li, “Control of seismic-excited buildings using active variable stiffness systems”, *Eng. Struct.* **18**:8 (1996), 589–596.
- [Zhang and Iwan 2002] Y. Zhang and W. D. Iwan, “Active interaction control of tall buildings subjected to near-field ground motions”, *J. Struct. Eng. (ASCE)* **128**:1 (2002), 69–79.
- [Zhou et al. 2003] L. Zhou, C.-C. Chang, and L.-X. Wang, “Adaptive fuzzy control for nonlinear building-magnetorheological damper system”, *J. Struct. Eng. (ASCE)* **129**:7 (2003), 905–913.

Received 19 Jan 2009. Revised 16 May 2009. Accepted 16 May 2009.

THOMAS L. ATTARD: tattard@utk.edu

Department of Civil and Environmental Engineering, The University of Tennessee, 113 Perkins Hall, Knoxville, TN 37996-2010, United States

ROBIN E. DANSBY: rdansby@csufresno.edu

California State University, Fresno, Department of Civil and Geomatics Engineering, M/S EE94, 2320 E. San Ramon Avenue, Fresno, CA 93740-8030, United States

EFFECTIVE ELASTIC PROPERTIES OF NANOTUBE REINFORCED COMPOSITES WITH SLIGHTLY WEAKENED INTERFACES

MILTON ESTEVA AND POL D. SPANOS

In this paper a micromechanics approach is presented for determining the effective elastic properties of single-walled carbon nanotube (SWCNT) reinforced composites, while accounting for imperfect bonding in the matrix-inclusion interface. For this purpose, a linear spring layer of vanishing thickness is introduced to represent the interface. Furthermore, the well known Mori–Tanaka (MT) method, in conjunction with the Eshelby’s tensor, is modified to determine the effective elastic properties. The inclusions are considered to be either perfectly aligned infinite long cylinders or aligned ellipsoidal inclusions with a given aspect ratio; cases of perfect alignment or of randomly oriented fibers are treated. The numerical results show that the interface weakening influences the nanocomposite properties significantly only for high values of SWCNT volume fraction. Since most of the currently conducted experiments involve composites which contain small volume fractions, it is thus reasonable based on the findings of this paper to assume perfect bonding for low nanotube volumetric contents.

1. Introduction

Since the discovery of carbon nanotubes [Iijima 1991], single-walled CNTs have attracted increasing scientific interest because of their exceptional mechanical, electrical, and thermal properties. Experimental and theoretical results have shown that the Young’s moduli of SWCNTs are approximately 1 TPa depending on diameter size and chirality [Popov et al. 2000; Yakobson et al. 1996; Pipes et al. 2003; Saether et al. 2003]. Despite these properties, several researchers have reported experiments with modest improvement in the strength and stiffness of polymer nanocomposites (PNC) [Qian et al. 2002; Ajayan et al. 2000]. On the other hand, some others have obtained a substantial increase in the effective properties as shown in Table 1 on the next page. Researchers claim that alignment, dispersion, geometry, and load transfer properties are parameters that could significantly affect the final properties of PNCs [Chen and Tao 2006; Namilae and Chandra 2005].

Several techniques for modeling PNCs have been reported in the open literature. Frankland et al. [2003] have used molecular dynamics (MD) to obtain stress-strain curves of SWCNTs embedded in a polyethylene matrix; the interface has been simulated by nonbonding van der Waals interactions using the Lennard-Jones potential. Odegard et al. [2003] has presented an equivalent-continuum method to obtain an effective continuum fiber that includes interface interaction. Seidel and Lagoudas [2006] have obtained effective continuum fiber properties using a composite cylinder micromechanics approach that can be applied to SWCNT or multiwalled carbon nanotubes (MWCNT). They have used these properties

Keywords: nanocomposites, carbon nanotubes, modeling, imperfect bonding, Mori–Tanaka.

The financial support provided by the Air Force Research Laboratory Clarkson Aerospace Inc. to Rice University is gratefully acknowledged.

Composite	Young's modulus (GPa)	Tensile strength (MPa)	Elongation (%)	NT Orientation
Neat epoxy	$2.02 \pm .078$	83 ± 3.3	6.5 ± 0.17	—
Epoxy + 1 wt.% Bucky Pearl SWNT	$2.12 \pm .093$	80 ± 4.1	5.8 ± 0.33	random
Epoxy + 1 wt.% functionalized	$2.65 \pm .125$	104 ± 3.7	8.5 ± 0.72	random
Epoxy + 4 wt.% functionalized	$3.4 \pm .253$	102 ± 5.4	5.5 ± 0.21	random
TPU	7.7 ± 1	12.4 ± 4.5	852 ± 130	—
TPU + 0.5 wt.% SWNT	14.5 ± 3.4	13.3 ± 4	709 ± 160	aligned

Table 1. Some experimental mechanical properties of polymer nanocomposites. See [Zhu et al. 2004] for the first four rows and [Chen and Tao 2006] for the last two.

with the self consistent (SC), MT and finite element method (FEM) to determine the effective properties for aligned and randomly oriented perfectly bonded inclusions. In that work, an attempt to account for imperfect bonding has been made by using interphase regions involving a multilayer composite cylinder approach requiring the specification of elastic properties and thickness for the interphase layer. Song and Youn [2006] have investigated the effective properties using the asymptotic expansion homogenization method where again perfect interfacial bonding has been assumed. Liu and Chen [2003] have implemented a three dimensional representative volume element (RVE) and have used FEM to obtain effective mechanical properties; in this work perfect bonding between matrix and inclusion has also been assumed. Li and Chou [2003] have adopted a structural mechanics approach to obtain effective properties of cylindrical nanocomposites RVEs in which they have used nonlinear trusses to simulate nonbonding interactions along the interface. Namielae and Chandra [2005] have also discussed the problem of nonperfect bonding. They have developed a multiscale model introducing a constitutive behavior to the interface by means of cohesive zone models. They have used MD to obtain traction-displacement relations and have then implemented them in a numerical scheme using two dimensional axisymmetric FEM and cohesive zone elements for the interface. Despite this sophisticated model, final effective properties strongly depend on RVE dimensions for finite nanotube lengths.

In this paper, a micromechanics model for determining the effective properties of PNCs is presented. The model accounts for imperfect bonding between the matrix and the fiber. For this purpose, a spring layer of finite stiffness but of negligible thickness is introduced in the inclusion model. The layer produces continuous interfacial tractions but discontinuous displacements. The introduction of imperfect interfaces necessitates modified expressions for the Eshelby tensor [1957], which is used in conjunction with the MT method for composites [Qiu and Weng 1990]. In this modified MT approach, the properties of the fiber are derived using a composite cylinder concept [Seidel and Lagoudas 2006]. Results are presented for composites with infinite cylinders and ellipsoidal shape fibers which are either aligned or randomly oriented in the matrix.

2. The original Mori–Tanaka concept

Recently, the original MT approach has been used by several authors to estimate the mechanical properties of nanocomposites [Odegard et al. 2003; Seidel and Lagoudas 2006]. Specifically, interest has

been focused on the calculation of the effective elastic properties of a two phase composite where the inclusion phase is either aligned or randomly oriented. In this section, a review of the derivation of the MT equations is presented first towards accounting for the effect of imperfect bonding between the matrix and the inclusion; obviously this is done towards facilitating the elucidation of the herein adopted procedure, without claiming conceptual novelty.

Assume that the analyzed composite comprises two phases. The matrix is considered to be isotropic and linearly elastic with stiffness tensor L_0 and volume fraction c_0 . Strictly speaking, the stiffness matrix relates the strains with the stresses they produce by the generalized Hooke's law

$$\sigma_{ij} = L_{ijkl}\varepsilon_{kl}.$$

In a similar way, the inclusion phase is assumed to have ellipsoidal shape and its material is considered to be transversely isotropic with stiffness tensor L_1 and volume fraction c_1 . Throughout this section explicit tensor notation will be omitted for clarity unless needed.

Consider the two configurations shown in [Figure 1](#). These represent the composite material and the comparison material where the properties of the later are those of the matrix. If displacements are specified at the boundary to produce a uniform strain in both materials (ε_a), the average stress of the composite ($\bar{\sigma}$) and that in the comparison material ($\bar{\sigma}_0$) are $\bar{\sigma} = L\varepsilon_a$ and $\bar{\sigma}_0 = L_0\varepsilon_a$, where L is the effective stiffness tensor of the composite and an overscore represents volume average.

The presence of the inclusions causes the strain field in the matrix to be nonuniform. Thus, the average strain in the matrix is in this case represented by the equation $\bar{\varepsilon}_0 = \varepsilon_a + \bar{\varepsilon}_0^{pt}$. The same change happens to the inclusion phase; the strain is perturbed from that of the matrix and is quantified as

$$\bar{\varepsilon}_1 = \bar{\varepsilon}_0 + \varepsilon_1^{pt}. \quad (1)$$

Using the equivalent inclusion method developed in [[Eshelby 1957](#)], a relation between the inhomogeneous inclusion problem ([Figure 1](#), left) and the homogeneous inclusion problem ([Figure 1](#), right) can be pursued. In other words, the properties of the inclusion can be related to the properties of the matrix by the equation

$$\bar{\sigma}_1 = L_1\bar{\varepsilon}_1 = L_0(\bar{\varepsilon}_1 - \varepsilon^*), \quad (2)$$

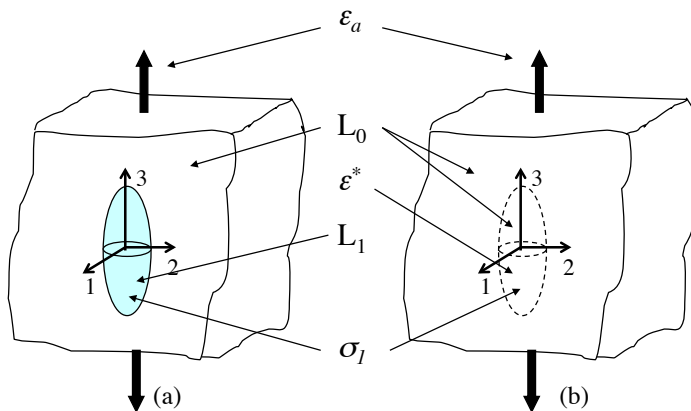


Figure 1. Eshelby's equivalent inclusion problem.

where ε^* is the inclusion eigenstrain. Eshelby [1957] demonstrated that this eigenstrain is related to the inclusion perturbation strain by the equation

$$\varepsilon_1^{pt} = \mathbf{S}\varepsilon^*, \quad (3)$$

where the tensor \mathbf{S} is well known as the Eshelby's tensor; expressions for cylindrical and ellipsoidal inclusions used herein can be found in references such as [Qiu and Weng 1990; Nemat-Nasser and Hori 1998].

Next, solving for ε^* in (2). The expression for the eigenstrain in terms of the average strain in the inclusion is found to be

$$\varepsilon^* = -\mathbf{L}_0^{-1}(\mathbf{L}_1 - \mathbf{L}_0)\bar{\varepsilon}_1. \quad (4)$$

Substituting (4) into (1) and making use of (3), the dilute strain concentration tensor \mathbf{A}^{dil} is found. This tensor relates the average strain in the inclusion with the average strain in the matrix and is given by

$$\bar{\varepsilon}_1 = \mathbf{A}^{\text{dil}}\bar{\varepsilon}_0 = [\mathbf{I} + \mathbf{S}\mathbf{L}_0^{-1}(\mathbf{L}_1 - \mathbf{L}_0)]^{-1}\bar{\varepsilon}_0, \quad (5)$$

where \mathbf{I} is the fourth-order identity tensor.

The relationship between the fiber and matrix strain averages and the overall strain average (ε_a) can be established by the use of the total volume average. That is,

$$c_0\bar{\varepsilon}_0 + c_1\bar{\varepsilon}_1 = \varepsilon_a. \quad (6)$$

By substituting (5) into (6), the strain concentration tensor of the matrix (\mathbf{A}_0) is obtained. This quantity relates the applied strain with the average strain in the matrix by the equation

$$\bar{\varepsilon}_0 = \mathbf{A}_0\varepsilon_a = [c_0\mathbf{I} + c_1\mathbf{A}^{\text{dil}}]^{-1}\varepsilon_a. \quad (7)$$

To derive the expression for the effective elastic moduli, the key assumption in the MT method is introduced. That is, when identical particles are introduced in the composite, the average strain in the inclusion is related to the average strain in the matrix by the dilute strain concentration tensor

$$\bar{\varepsilon}_1 = \mathbf{A}^{\text{dil}}\bar{\varepsilon}_0. \quad (8)$$

This means, that to account for inclusion interaction, the applied strain that each inclusion feels is the average strain in the matrix. Substituting (7) into (8), the nondilute strain concentration tensor is obtained (\mathbf{A}^{ndil}). This tensor relates the applied strain to the average strain in the inclusion by the equation

$$\bar{\varepsilon}_1 = \mathbf{A}^{\text{ndil}}\varepsilon_a = \mathbf{A}^{\text{dil}}\mathbf{A}_0\varepsilon_a. \quad (9)$$

Finally, to find the overall effective stiffness tensor for aligned inclusions, a similar expression as in (6) is used but for the case of stresses this is

$$\bar{\sigma} = c_0\bar{\sigma}_0 + c_1\bar{\sigma}_1 = \mathbf{L}\varepsilon_a, \quad (10)$$

where substitution of Hooke's law in (10) gives

$$\bar{\sigma} = c_0\mathbf{L}_0\bar{\varepsilon}_0 + c_1\mathbf{L}_1\bar{\varepsilon}_1 = \mathbf{L}\varepsilon_a.$$

Solving for L and using (7) and (9), the final expression for the effective stiffness tensor of the MT estimate is obtained as

$$L = (c_0 L_0 + c_1 L_1 A^{\text{dil}})(c_0 I + c_1 A^{\text{dil}})^{-1}. \quad (11)$$

This is the equation to implement the MT method for an aligned two phase composite.

It is also of interest to derive a MT estimate when the inclusions are randomly oriented inside the matrix. To this aim, the effective composite stiffness tensor will be determined using the orientational average of the pertinent properties. The difference between the aligned and the randomly oriented inclusions lies in that for the latter case the relation (6) becomes

$$c_0 \bar{\varepsilon}_0 + c_1 \{A^{\text{dil}} \bar{\varepsilon}_0\} = (c_0 I + c_1 \{A^{\text{dil}}\}) \bar{\varepsilon}_0 = \varepsilon_a, \quad (12)$$

where the brackets $\{\cdot\}$ designate the average over all possible orientations [Qiu and Weng 1990]. Similarly, (10) becomes

$$\bar{\sigma} = c_0 L_0 \bar{\varepsilon}_0 + c_1 \{L_1 \bar{\varepsilon}_1\} = (c_0 L_0 + c_1 \{L_1 A^{\text{dil}}\}) \bar{\varepsilon}_0 = L \varepsilon_a. \quad (13)$$

Finally, combining (12) and (13), the expression for the MT estimate for the case of randomly oriented inclusions is obtained as

$$L = (c_0 L_0 + c_1 \{L_1 A^{\text{dil}}\})(c_0 I + c_1 \{A^{\text{dil}}\})^{-1}, \quad (14)$$

which is similar to the expression for the case of aligned inclusions, except for those appropriate averaged quantities. Clearly, the MT approach can be used as a tool for deriving an effective stiffness tensor for the composite material. Specific studies regarding the MT method have been previously presented [Qiu and Weng 1990; Tucker and Liang 1999; Schjødt-Thomsen and Pyrz 2001; Benveniste 1987; Wang and Pyrz 2004].

3. Mori–Tanaka approach for composites with slightly weakened interfaces

In a model developed by Qu [1993] in conjunction with generic composite materials mechanics, imperfection in the interface can be introduced by using a layer of insignificant thickness in which tractions remain continuous and displacements become discontinuous. The equations that model the interfacial traction continuity and the displacement jump (Δu_i) at the interface can be written as

$$\Delta \sigma_{ij} n_j \equiv [\sigma_{ij}(S^+) - \sigma_{ij}(S^-)] n_j = 0, \quad (15)$$

and

$$\Delta u_i \equiv [u_i(S^+) - u_i(S^-)] = \eta_{ij} \sigma_{jk} n_k \quad (16)$$

respectively. In (15) and (16), S and n represent the interface and its unit outward normal vector, respectively. The terms $u(S^+)$ and $u(S^-)$ are the values of the displacements when approaching from outside and inside of the inclusion respectively. The second order tensor, η_{ij} , accounts for the compliance of the spring layer. It is obvious that when the tensor η_{ij} tends to zero (infinite stiffness), the displacement jump is zero and continuity in displacements are recovered. This tensor is chosen to be symmetric and positive definite and can be expressed in the form

$$\eta_{ij} = \alpha \delta_{ij} + (\beta - \alpha) n_i n_j, \quad (17)$$

where n_i is the normal outward vector and δ_{ij} is the Kronecker delta.

It is important to address the physical meaning of the parameters α and β . To define these terms more completely, an example is presented. Consider a two dimensional plane where a horizontal surface divides the matrix and the inclusion material (see Figure 2). The unit outward normal vector n is pointing in the vertical direction. Performing summation over dummy indexes in (16), the displacement jumps in direction 1 and 2 are

$$\begin{aligned} \Delta u_1 &= \eta_{11}\sigma_{11}n_1 + \eta_{11}\sigma_{12}n_2 + \eta_{12}\sigma_{21}n_1 + \eta_{12}\sigma_{22}n_2, \\ \Delta u_2 &= \eta_{21}\sigma_{11}n_1 + \eta_{21}\sigma_{12}n_2 + \eta_{22}\sigma_{21}n_1 + \eta_{22}\sigma_{22}n_2. \end{aligned} \tag{18}$$

Because the outward normal vector is in the vertical direction, $n_1 = 0$ and $n_2 = 1$. Using these values, (18) reduces to

$$\Delta u_1 = \eta_{11}\sigma_{12}n_2 + \eta_{12}\sigma_{22}n_2, \quad \Delta u_2 = \eta_{21}\sigma_{12}n_2 + \eta_{22}\sigma_{22}n_2. \tag{19}$$

In a similar manner and also making use of the Kronecker delta properties, (17) is used to generate the four required elements in (19). That is,

$$\begin{aligned} \eta_{11} &= \alpha\delta_{11} + (\beta - \alpha)n_1n_1 = \alpha, & \eta_{12} &= \alpha\delta_{12} + (\beta - \alpha)n_1n_2 = 0, \\ \eta_{21} &= \alpha\delta_{21} + (\beta - \alpha)n_2n_1 = 0, & \eta_{22} &= \alpha\delta_{22} + (\beta - \alpha)n_2n_2 = \beta. \end{aligned} \tag{20}$$

Substituting (20) into (19), the displacement jumps in direction 1 and 2 are

$$\Delta u_1 = \alpha\sigma_{12} = \alpha\tau, \quad \Delta u_2 = \beta\sigma_{22} = \beta\sigma. \tag{21}$$

It is clear in (21) that α and β are parameters that represent the compliance in the tangential and normal directions respectively as shown in Figure 2. Furthermore, setting the parameter β to zero (infinite stiffness in the normal direction) prevents material interpenetration.

After introducing the imperfect interface into the equivalent inclusion method, Qu found a modified expression for the Eshelby’s tensor, for the case of ellipsoidal inclusions with slightly weakened interfaces. The new expression is written as

$$\bar{S}_{ijkl}^M = S_{ijkl} + (I_{ijpq} - S_{ijpq})H_{pqrs}L_{rsmn}(I_{mnkl} - S_{mnkl}), \tag{22}$$

where S_{ijkl} is the original Eshelby’s tensor and L_{ijkl} is the matrix stiffness tensor. The second term in the right hand side of (22) is produced due to the introduction of the weakened interface, where the tensor

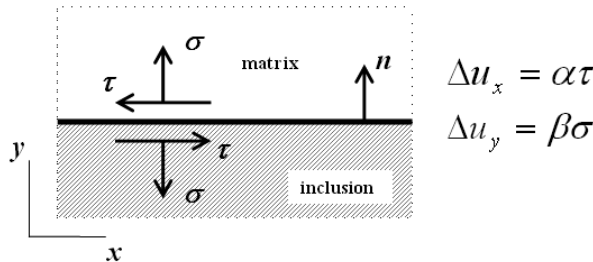


Figure 2. Physical meaning of parameters α and β in the compliance tensor η_{ij} .

\mathbf{H} is given by the equation

$$H_{ijkl} = \alpha P_{ijkl} + (\beta - \alpha) Q_{ijkl};$$

expressions for tensor \mathbf{P} and \mathbf{Q} are given in the [Appendix](#).

Once the modified Eshelby's tensor has been included in the analysis, the modified MT estimate is introduced. Following the same procedure to find (11) and using the result in [Qu 1993] for the average strains, the expression for the modified MT estimate for a two phase aligned composite is obtained as

$$\mathbf{L} = (c_o \mathbf{L}_o + c_1 \mathbf{L}_1 \mathbf{A}^{\text{dil}}) (c_o \mathbf{I} + c_1 [\mathbf{A}^{\text{dil}} + \mathbf{H} \mathbf{L}_1 \mathbf{A}^{\text{dil}}])^{-1}, \quad (23)$$

where

$$\mathbf{A}^{\text{dil}} = [\mathbf{I} + \bar{\mathbf{S}}^M \mathbf{L}_0^{-1} (\mathbf{L}_1 - \mathbf{L}_0)]^{-1}. \quad (24)$$

In all this new expressions, if the parameters α and β are set to zero, the tensor \mathbf{H} vanishes and equations (22), (23), and (24) reduce to the original MT expression shown in (11). It is worth mentioning that the expression for the effective elastic properties in (23) is length dependent, in contrast to the original MT which is aspect ratio dependent.

When the inclusions are randomly oriented inside the matrix, determination of the effective elastic properties can be obtained following the same procedure as in (14). Using the result found in [Qu 1993] for the total average strain, the MT expression with slightly weakened interfaces for the case of randomly oriented inclusions is

$$\mathbf{L} = (c_o \mathbf{L}_o + c_1 \{\mathbf{L}_1 \mathbf{A}^{\text{dil}}\}) (c_o \mathbf{I} + c_1 \{\mathbf{A}^{\text{dil}}\} + c_1 \{\mathbf{H} \mathbf{L}_1 \mathbf{A}^{\text{dil}}\})^{-1}. \quad (25)$$

Likewise, if the parameters α and β are set to zero, the tensor \mathbf{H} vanishes and (25) reduce to the original MT expression shown in (14). Similar studies have been reported for the case of inclusions with specific shape and material properties [Benveniste and Aboudi 1984; Benveniste 1985; Hashin 1991].

4. Implementation of the Mori–Tanaka estimate

As stated in the previous sections, to obtain effective elastic properties by means of the MT method it is necessary to use fourth-order tensor operations. To avoid the complexity that this task involves, the notation originally developed in [Walpole 1981] and used later in [Qiu and Weng 1990; Wang and Pyrz 2004] will be used. In this notation, a general symmetric fourth-order tensor can be represented by the equation

$$\mathbf{L} = (2k, l, l', n, 2m, 2p), \quad (26)$$

where the quantities k, l, l', n, m and p are related to the fourth-order tensor elements by the equation

$$k = \frac{1}{2}(L_{2222} + L_{2233}), \quad l = L_{1122}, \quad l' = L_{2211}, \quad n = L_{1111}, \quad m = \frac{1}{2}(L_{2222} - L_{2233}), \quad p = L_{1212},$$

in which for the case of a transversely isotropic stiffness tensor, the quantities l and l' are identical. An isotropic stiffness tensor can also be represented using this notation and the aforementioned quantities are defined as

$$k = K + \frac{1}{3}\mu, \quad l = l' = K - \frac{2}{3}\mu, \quad n = K + \frac{4}{3}\mu, \quad m = p = \mu, \quad (27)$$

where K and μ are the bulk modulus and the shear modulus, respectively. Thus, whenever a fourth-order tensor is expressed using this notation, algebraic operations of this kind of tensor can be easily performed.

The expression for the MT estimate requires the use of tensor inner products. The computation of the inner product of the two tensors $\mathbf{A} = (c, g, h, d, e, f)$ and $\mathbf{B} = (c', g', h', d', e', f')$ is given by the equation

$$\mathbf{AB} = (cc' + 2hg', gc' + dg', hd' + ch', dd' + 2gh', ee', ff'). \tag{28}$$

Besides inner products, tensor inversion is also required by the MT estimate. The inverse operation of tensor \mathbf{A} , denoted by \mathbf{A}^{-1} , satisfies the equation

$$\mathbf{AA}^{-1} = \mathbf{I}, \tag{29}$$

where \mathbf{I} is the identity tensor. If this tensor is expressed as $\mathbf{I} = (1, 0, 0, 1, 1, 1)$, it follows from (28) and (29) that

$$\mathbf{A}^{-1} = \left(\frac{d}{cd - 2gh}, -\frac{g}{cd - 2gh}, -\frac{h}{cd - 2gh}, \frac{c}{cd - 2gh}, \frac{1}{e}, \frac{1}{f} \right).$$

As shown in (14), when the inclusions in the composite are randomly oriented within the matrix, certain quantities require to be averaged over all possible directions. The result of this operation is a naturally isotropic tensor. Only two properties are required to fully define the tensor. For the case of tensor \mathbf{L} in (26), the isotropic bulk and shear modulus are calculated as

$$K = \frac{1}{9}[4k + 2(l + l') + n], \quad \mu = \frac{1}{15}[k - (l + l') + n + 6(m + p)].$$

Once these two quantities are obtained, one can form the new isotropic tensor by using the expressions in (27).

5. Estimation of nanocomposite effective elastic properties

The modified MT method is applied herein to obtain the effective elastic properties of the composite. Fiber and matrix material properties (for all cases in this paper) are identical to those shown in Table 2.

The work done in [Namilae and Chandra 2005] was used to obtain reasonable values for the parameter α , they used molecular dynamics to perform a fiber pull out test. Three values for the parameter α are chosen for all cases in this section (0, 0.01, and 0.05 nm/GPa) and β is set to zero to prevent material interpenetration. In this section, computations of composites with aligned inclusions and those with randomly oriented fibers are presented.

Matrix: EPON 862	
$E = 2.026$	$\nu = 0.3$
Effective carbon nanotubes	
$E_{11} = 704$ GPa	$\nu_{12} = 0.14$
$E_{22} = 345$ GPa	$\nu_{23} = 0.37$
$\mu_{12} = 227$ GPa	$\phi = 1.7$ nm

Table 2. Input data for effective properties computations. From [Seidel and Lagoudas 2006].

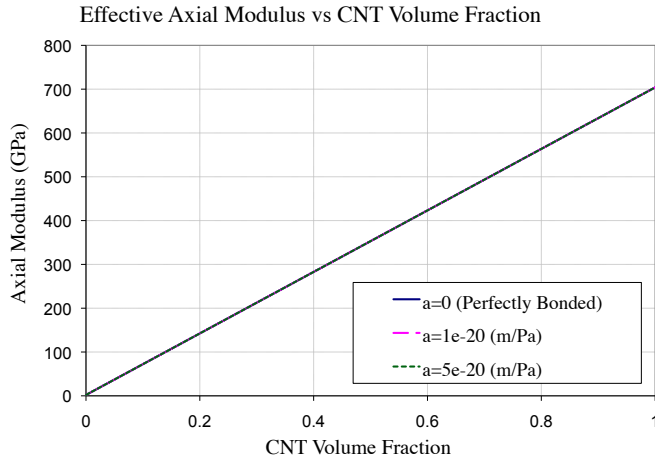


Figure 3. Effective axial modulus for composites with cylindrical inclusions.

Aligned SWCNT composites. It is known that for the case of isotropic matrices and aligned transversely isotropic inclusions, the resulting overall properties are also transversely isotropic. Five independent elastic properties fully describe the behavior of this type of materials. The modified MT method is applied and the computations assume aligned infinitely long nanotubes. The results shown in Figure 3 are for the effective axial modulus. No effect of weakened interfaces is observed as expected and the behavior is that of the rule of mixtures.

Figure 4 shows how interface properties impact the transverse modulus; it is slightly affected for almost the entire range of volume fractions but it is significantly reduced for values greater than 0.8. For the axial and transverse shear moduli similar behavior is found (see Figure 5). An important result of introducing imperfect interfaces in the model is that composite properties do not converge to nanotube

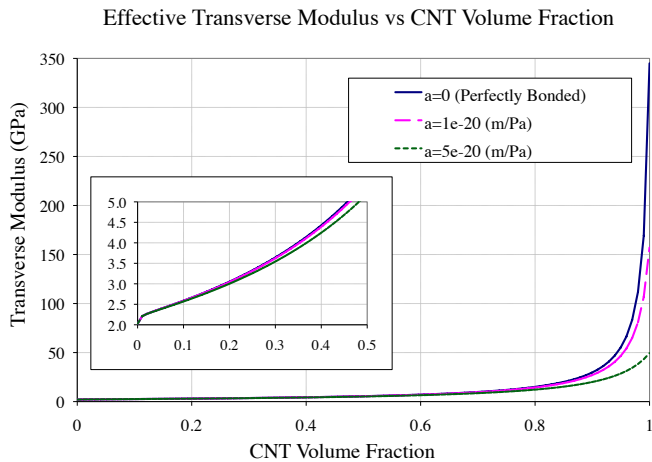


Figure 4. Dependence of transverse modulus on parameter α for composites with cylindrical inclusions, $d = 1.7$ nm.

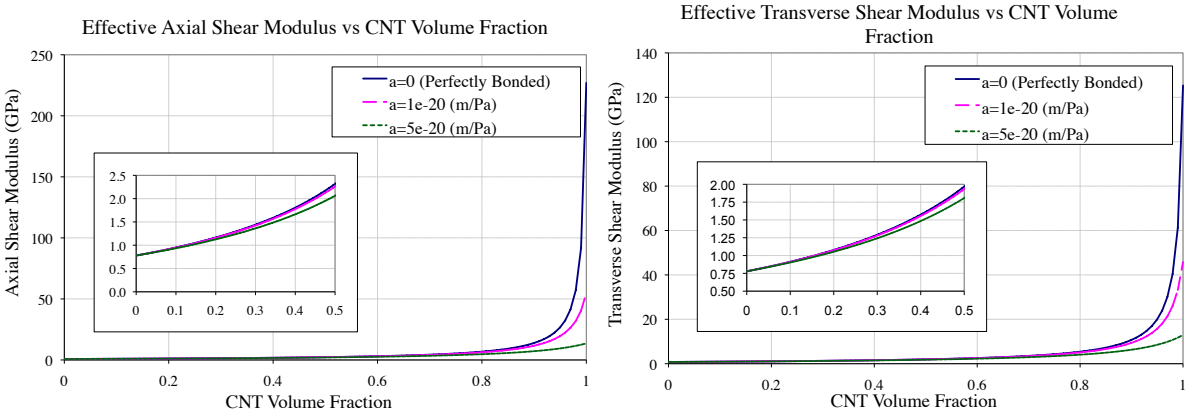


Figure 5. Effective axial (left) and transversal (right) shear moduli versus parameter α for composites with cylindrical inclusions, $d = 1.7$ nm.

properties when the volume fraction approaches 1, as can be seen in [Figure 4](#) and [Figure 5](#). This can be expected as the fiber material is no longer homogeneous; it is affected by the presence of the negligible layer with displacement discontinuities.

Another important aspect of the effective nanocomposite properties computation is to study the impact of inclusion aspect ratio (length/diameter) when the fibers are not considered infinitely long. Calculations of this type of composite can be conducted using the modified Eshelby’s tensor for ellipsoidal inclusions. Expressions for the computation of required tensors are shown in the [Appendix](#), in which numerical integration is used due to the complex terms generated. [Figure 6](#) captures the impact of the parameter α on the calculation of the axial and transverse effective modulus. These results are for the specific case of a nanotube diameter of 1.7 nm and an aspect ratio of 50. Similarly to the case of infinitely long nanotubes, the transverse modulus is affected more than the axial modulus by the presence of imperfect

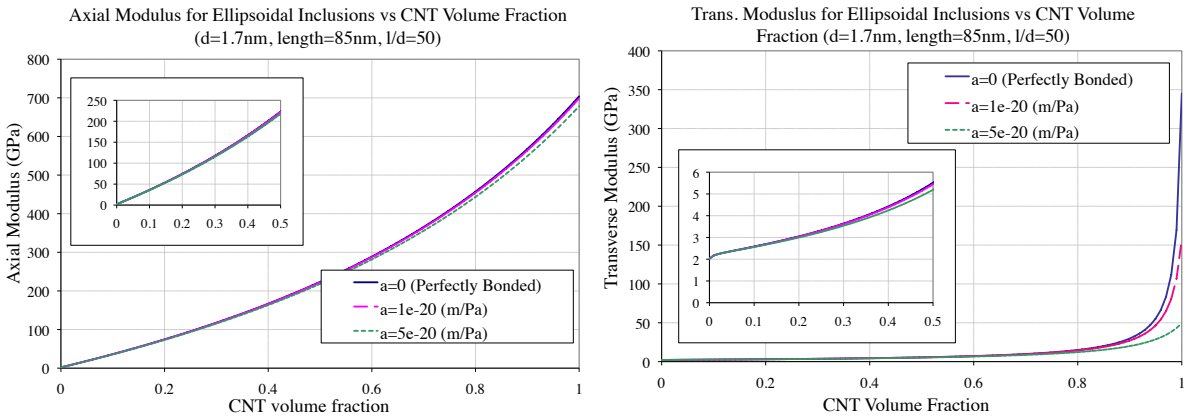


Figure 6. Effective axial (left) and transverse (right) moduli versus parameter α for composites with ellipsoidal inclusions, $d = 1.7$ nm, length=85 nm.

bonding. And, in this case, aspect ratio starts to slightly affect the axial modulus as it does not follow the rule of mixtures anymore.

Randomly oriented SWCNT composites. Next, the properties of SWCNT composites with randomly oriented cylindrical and ellipsoidal fibers are calculated assuming nanotubes have good dispersion in the matrix. The final elastic properties for both types of inclusions are fully isotropic because they are obtained from an average over all possible orientations [Qiu and Weng 1990]. Figure 7 shows the effective modulus of randomly oriented infinitely long cylinders and ellipsoids respectively. They both have the same type of behavior, but the effective properties predicted for the ellipsoidal inclusions are less than those for the cylindrical inclusions due to the aspect ratio dependence. The impact of introducing imperfect bonding is still more evident for high volume fractions (more than 0.6) as noted in Figure 7. Finally, Figure 8 provides the result on the effect of aspect ratio and volume fraction in the effective properties of nanocomposites with ellipsoidal randomly oriented inclusions and slightly weakened interfaces ($\alpha = 0.05$ nm/GPa). As expected, for high values of aspect ratio (more than 200) the behavior of cylindrical inclusions is reached but for values less than 200, effective modulus is highly affected.

6. Concluding remarks

The effect of introducing imperfect bonding in the calculation of PNC effective properties has been studied in this paper. Effective properties have been computed using a modified MT method to include the effect of the weakened interface. The properties of the effective fiber have been obtained by a composite cylinder method [Seidel and Lagoudas 2006]. Furthermore, three different configurations for the fibers have been considered. First, nanotubes were treated as aligned infinitely long cylinders where bonding imperfection affects only the transverse properties of the composite for high volume fractions values. Second, the nanotubes were treated as ellipsoidal fibers with a given aspect ratio. In this case, both the axial and the transverse properties were affected by the aspect ratio. Once more, the weakened interface became important only for high volume fraction values. Lastly, the cylindrical and the ellipsoidal fibers

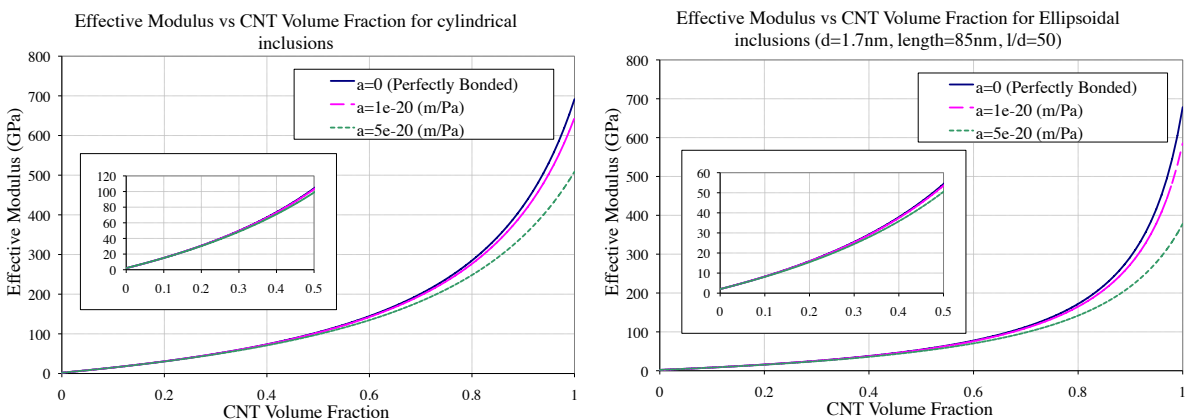


Figure 7. Effective modulus dependence on parameter α for composites with either cylindrical (a) or ellipsoidal (b) randomly oriented inclusions.

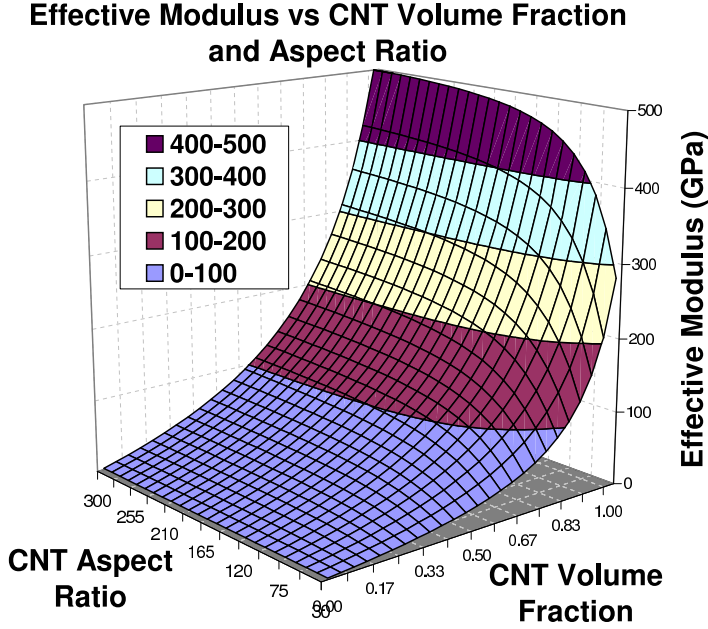


Figure 8. Effective modulus versus CNT volume fraction and aspect ratio for ellipsoidal inclusions with $\alpha = 0.05$ nm/GPa.

were treated as randomly oriented fibers. For the cylindrical fibers, the effective properties did not follow the rule of mixtures as in the aligned case, and the weakened interface became significant only at high volume fractions.

All of the numerical results reported have shown that interfacial weakening influences the effective nanocomposite properties significantly for high values of SWCNT volume fractions. Since most of the currently conducted experiments involve composites which contain small volume fractions, it is reasonable to assume perfect bonding for low nanotube volumetric contents. Nonetheless, the developed procedure is applicable for assessing the interfacial weakening effect for an arbitrary volume fraction.

The H tensor

The tensor H needed to compute the modified MT estimate can be written as follows with axis 1 as the symmetry axis

$$H_{ijkl} = \alpha P_{ijkl} + (\beta - \alpha) Q_{ijkl},$$

where the components of tensors P and Q depend on the inclusion shape and can be obtained using the following expressions:

For ellipsoids

$$P_{ijkl} = \frac{3}{16\pi} \int_0^\pi \left[\int_0^{2\pi} (\delta_{ik}\hat{n}_j\hat{n}_l + \delta_{jk}\hat{n}_i\hat{n}_l + \delta_{il}\hat{n}_k\hat{n}_j + \delta_{jl}\hat{n}_k\hat{n}_i)n^{-1}d\theta \right] \sin\phi d\phi,$$

$$Q_{ijkl} = \frac{3}{4\pi} \int_0^\pi \left[\int_0^{2\pi} \hat{n}_i\hat{n}_j\hat{n}_k\hat{n}_ln^{-3}d\theta \right] \sin\phi d\phi, \quad n = \sqrt{\hat{n}_i\hat{n}_i},$$

$$\hat{n} = \left(\frac{\cos\phi}{a_1}, \frac{\sin\phi\cos\theta}{a_2}, \frac{\sin\phi\sin\theta}{a_3} \right)^T.$$

For cylinders ($a_2 = a_3 = a$ and $a_1 \rightarrow \infty$) so

$$P_{2222} = P_{3333} = 4P_{3131} = 4P_{2121} = 2P_{2323} = \frac{3\pi}{8a},$$

$$Q_{2222} = Q_{3333} = 3Q_{2233} = 3Q_{3322} = 3Q_{2323} = \frac{9\pi}{32a},$$

with all others being 0.

References

- [Ajayan et al. 2000] P. M. Ajayan, L. S. Schadler, C. Giannaris, and A. Rubio, “Single-walled carbon nanotube-polymer composites: strength and weakness”, *Adv. Mater.* **12**:10 (2000), 750–753.
- [Benveniste 1985] Y. Benveniste, “The effective mechanical behaviour of composite materials with imperfect contact between the constituents”, *Mech. Mater.* **4**:2 (1985), 197–208.
- [Benveniste 1987] Y. Benveniste, “A new approach to the application of Mori–Tanaka’s theory in composite materials”, *Mech. Mater.* **6**:2 (1987), 147–157.
- [Benveniste and Aboudi 1984] Y. Benveniste and J. Aboudi, “A continuum model for fiber reinforced materials with debonding”, *Int. J. Solids Struct.* **20**:11–12 (1984), 935–951.
- [Chen and Tao 2006] W. Chen and X. Tao, “Production and characterization of polymer nanocomposite with aligned single wall carbon nanotubes”, *Appl. Surf. Sci.* **252**:10 (2006), 3547–3552.
- [Eshelby 1957] J. D. Eshelby, “The determination of the elastic field of an ellipsoidal inclusion, and related problems”, *Proc. R. Soc. Lond. A* **241**:1226 (1957), 376–396.
- [Frankland et al. 2003] S. J. V. Frankland, V. M. Harik, G. M. Odegard, D. W. Brenner, and T. S. Gates, “The stress-strain behavior of polymer-nanotube composites from molecular dynamics simulation”, *Compos. Sci. Technol.* **63**:11 (2003), 1655–1661.
- [Hashin 1991] Z. Hashin, “Thermoelastic properties of particulate composites with imperfect interface”, *J. Mech. Phys. Solids* **39**:6 (1991), 745–762.
- [Iijima 1991] S. Iijima, “Helical microtubules of graphitic carbon”, *Nature* **354** (1991), 56–58.
- [Li and Chou 2003] C. Li and T.-W. Chou, “Multiscale modeling of carbon nanotube reinforced polymer composites”, *J. Nanosci. Nanotechnol.* **3**:5 (2003), 423–430.
- [Liu and Chen 2003] Y. J. Liu and X. L. Chen, “Evaluations of the effective material properties of carbon nanotube-based composites using a nanoscale representative volume element”, *Mech. Mater.* **35**:1–2 (2003), 69–81.
- [Namilae and Chandra 2005] S. Namilae and N. Chandra, “Multiscale model to study the effect of interfaces in carbon nanotube-based composites”, *J. Eng. Mater. Technol. (ASME)* **127**:2 (2005), 222–232.
- [Nemat-Nasser and Hori 1998] S. Nemat-Nasser and M. Hori, *Micromechanics: overall properties of heterogeneous materials*, 2nd rev. ed., North Holland, Amsterdam, 1998.

- [Odegard et al. 2003] G. M. Odegard, T. S. Gates, K. E. Wise, C. Park, and E. J. Siochi, “Constitutive modeling of nanotube-reinforced polymer composites”, *Compos. Sci. Technol.* **63**:11 (2003), 1671–1687.
- [Pipes et al. 2003] R. B. Pipes, S. J. V. Frankland, P. Hubert, and E. Saether, “Self-consistent properties of carbon nanotubes and hexagonal arrays as composite reinforcements”, *Compos. Sci. Technol.* **63**:10 (2003), 1349–1358.
- [Popov et al. 2000] V. N. Popov, V. E. Van Doren, and M. Balkanski, “Elastic properties of crystals of single-walled carbon nanotubes”, *Solid State Comm.* **114**:7 (2000), 395–399.
- [Qian et al. 2002] D. Qian, G. J. Wagner, W. K. Liu, M.-F. Yu, and R. S. Ruoff, “Mechanics of carbon nanotubes”, *Appl. Mech. Rev. (ASME)* **55**:6 (2002), 495–533.
- [Qiu and Weng 1990] Y. P. Qiu and G. J. Weng, “On the application of Mori–Tanaka’s theory involving transversely isotropic spheroidal inclusions”, *Int. J. Eng. Sci.* **28**:11 (1990), 1121–1137.
- [Qu 1993] J. Qu, “The effect of slightly weakened interfaces on the overall elastic properties of composite materials”, *Mech. Mater.* **14**:4 (1993), 269–281.
- [Saether et al. 2003] E. Saether, S. J. V. Frankland, and R. B. Pipes, “Transverse mechanical properties of single-walled carbon nanotube crystals, I: Determination of elastic moduli”, *Compos. Sci. Technol.* **63**:11 (2003), 1543–1550.
- [Schjødt-Thomsen and Pyrz 2001] J. Schjødt-Thomsen and R. Pyrz, “The Mori–Tanaka stiffness tensor: diagonal symmetry, complex fibre orientations and non-dilute volume fractions”, *Mech. Mater.* **33**:10 (2001), 531–544.
- [Seidel and Lagoudas 2006] G. D. Seidel and D. C. Lagoudas, “Micromechanical analysis of the effective elastic properties of carbon nanotube reinforced composites”, *Mech. Mater.* **38**:8–10 (2006), 884–907.
- [Song and Youn 2006] Y. S. Song and J. R. Youn, “Modeling of effective elastic properties for polymer based carbon nanotube composites”, *Polymer* **47**:5 (2006), 1741–1748.
- [Tucker and Liang 1999] C. L. Tucker, III and E. Liang, “Stiffness predictions for unidirectional short-fiber composites: review and evaluation”, *Compos. Sci. Technol.* **59**:5 (1999), 655–671.
- [Walpole 1981] L. J. Walpole, “Elastic behavior of composite materials: theoretical foundations”, *Adv. Appl. Mech.* **21** (1981), 169–242.
- [Wang and Pyrz 2004] J. Wang and R. Pyrz, “Prediction of the overall moduli of layered silicate-reinforced nanocomposites, I: Basic theory and formulas”, *Compos. Sci. Technol.* **64**:7–8 (2004), 925–934.
- [Yakobson et al. 1996] B. I. Yakobson, C. J. Brabec, and J. Bernholc, “Nanomechanics of carbon tubes: instabilities beyond linear response”, *Phys. Rev. Lett.* **76**:14 (1996), 2511–2514.
- [Zhu et al. 2004] J. Zhu, H. Peng, F. Rodriguez-Macias, J. L. Margrave, V. N. Khabashesku, A. M. Imam, K. Lozano, and E. V. Barrera, “Reinforcing epoxy polymer composites through covalent integration of functionalized nanotubes”, *Adv. Funct. Mater.* **14**:7 (2004), 643–648.

Received 17 Apr 2008. Revised 16 May 2009. Accepted 17 May 2009.

MILTON ESTEVA: mesteva@rice.edu

Rice University, Department of Mechanical Engineering and Material Science - MS 321, PO Box 1892, Houston, TX 77521-1892, United States

POL D. SPANOS: spanos@rice.edu

Rice University, Department of Mechanical Engineering and Material Science - MS 321, PO Box 1892, Houston, TX 77521-1892, United States

CONTINUUM MECHANICS MODELS OF FRACTAL POROUS MEDIA: INTEGRAL RELATIONS AND EXTREMUM PRINCIPLES

MARTIN OSTOJA-STARZEWSKI

This paper continues the extension of continuum mechanics and thermodynamics to fractal porous media which are specified by a mass (or spatial) fractal dimension D , a surface fractal dimension d , and a resolution length-scale R . The focus is on a theory based on dimensional regularization, in which D is also the order of fractional integrals employed to state global balance laws. Thus, we first generalize the main integral theorems of continuum mechanics to fractal media: Stokes, Reynolds, and Helmholtz–Żórawski. Then, we review balance equations and recently obtained extensions of several subfields of continuum mechanics to fractal media. This is followed by derivations of extremum and variational principles of elasticity and Hamilton’s principle for fractal porous materials. In all the cases, we derive relations which depend explicitly on D , d and R , and which, upon setting $D = 3$ and $d = 2$, reduce to the conventional forms of governing equations for continuous media with Euclidean geometries.

1. Background and motivation

The term fractal was coined by Benoît Mandelbrot in 1975 [Mandelbrot 1982] to denote an object that is “broken” or “fractured” in space and/or time. Basically, a fractal object can be subdivided in parts, each of which is in a deterministic or stochastic sense a reduced-size copy of the whole; this is the famous self-similarity property (1). In general, a fractal also has these features: (2) fine structure at arbitrarily small scales; (3) too irregular to be easily described in traditional Euclidean geometric language; (4) Hausdorff dimension greater than the topological dimension; (5) a simple and recursive definition.¹

Thus, “mathematical fractals” appear similar at all levels of magnification, and, roughly speaking, they are infinitely complex. Focusing on fractals in space, as opposed to those in time (signals, processes), many natural and man-made objects approximate fractals to a degree: coastlines, porous media, cracks, turbulent flows, clouds, mountains, lightning bolts, brains, snow flakes, melting ice (and other systems at phase transitions). The list is very long, and hence book titles like *Fractals Everywhere* [Barnsley 1993]. Mathematical fractals provide appropriate models for many media for some finite range of length scales, with lower and upper cutoffs.

Concerning materials with fractal geometries, since the late eighties a lot of research has been carried out primarily in condensed matter physics [Feder 1988]. That work has been focused on physics — explaining physical phenomena and properties for materials whose fractal (non-Euclidean) geometry plays a key role. However, a field theory, an analogue of continuum physics and mechanics, has sorely been lacking. Some progress in that respect has recently been made by mathematicians [Kigami 2002;

Keywords: fractal, prefractal, continuum mechanics, thermomechanics, extremum principles.

¹Self-similarity does not suffice to characterize fractals: a straight line is formally self-similar but has no other fractal characteristics. On the other hand, space-filling curves such as the Hilbert curve do not satisfy (4).

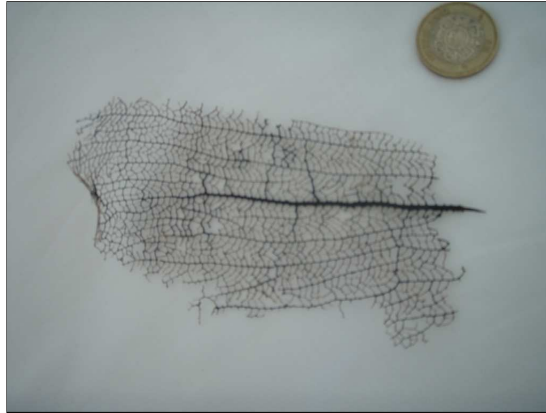


Figure 1. This fern, found on the seashore in Cancún, Mexico, just before PACAM X (January 2008), represents an example of a prefractal. A coin is shown for reference.

Strichartz 2006; Epstein and Śniatycki 2006; Epstein and Adee 2008], who began to look at classical problems, like Laplace’s or heat equation, on fractal (albeit nonrandom) sets. This approach, in fact very technical from the mathematical analysis standpoint, only begins to offer an avenue to tackle simple initial-boundary value (IBV) problems.

A very different step in the direction of a field theory and IBV problems has recently been taken by Tarasov [2005a, 2005b, 2005c]. He developed continuum-type equations of conservation of mass, linear and angular momenta, and energy for fractals, and, on that basis studied several fluid mechanics and wave problems. The beauty and power of Tarasov’s approach relies on a generalization of the Green–Gauss theorem to fractal objects through fractional integrals in Euclidean space, see Section 2.2 below. Another advantage of this approach is that it admits upper and lower cutoffs of fractal scaling, so that one effectively deals with a physical “prefractal”, like the one in Figure 1, rather than a purely mathematical fractal lacking cutoffs. It is in that sense that fractals are meant here. In principle, one can then map a mechanics problem of a fractal [which is described by its mass (D) and surface (d) fractal dimensions plus the spatial resolution (R)] onto a problem in Euclidean space in which this fractal is embedded, while having to deal with coefficients explicitly involving D , d and R . Clearly, this has very interesting ramifications for formulating continuum-type mechanics of fractal media, which need to be further explored. The great promise stems from the fact that the conventional requirement of continuum mechanics, the separation of scales, can be removed, yet the partial differential equations may still be employed.

Working in the outlined setting, in this paper we examine the integral theorems of continuum mechanics in the setting of fractal media: Stokes, Reynolds, and Helmholtz–Żórawski. In fact, the second of these leads us to modify Tarasov’s fractional material derivative back to a conventional material derivative. As a result, the balance laws of mass, linear momentum, energy as well as the second law of thermodynamics take simpler forms than using Tarasov’s interpretation. We also list generalizations of: the Clausius–Duhem inequality, the linear thermoelasticity, the Maxwell–Betti reciprocity, the Hill condition and energy principles, and the averaged equations of turbulence in fractal porous media [Ostoj-Starzewski 2007a, 2007b, 2008a]. This is followed by derivations of extremum and variational principles

of elasticity and the Hamilton's principle for fractal porous materials. In all the cases, we obtain relations which depend explicitly on D , d and R , and which, upon setting $D = 3$ and $d = 2$, reduce to conventional (well known) forms of governing equations for continuous media with Euclidean geometries.

2. Continuum mechanics in the setting of fractal media

Integral theorems. We consider fractal porous media in which mass obeys a power law relation

$$m(R) = kR^D, \quad D < 3, \quad (2-1)$$

where R is a box size (or a sphere radius, effectively a length scale of measurement), D is a fractal dimension of mass (based on, say, the box-counting method), and k is a proportionality constant. Equation (2-1) implies that the conventional equation giving mass in a three-dimensional region W (of volume V and boundary ∂W)

$$m(W) = \int_W \rho(r) d^3r \quad (2-2)$$

has to be generalized to

$$m_{3d}(W) = \frac{2^{3-D}\Gamma(3/2)}{\Gamma(D/2)} \int_W \rho(r)|r - r_0|^{D-3} d^3r. \quad (2-3)$$

That is, the fractal medium with a noninteger mass dimension D is described using a fractional integral of order D . This interpretation of the fractal (intrinsically discontinuous) medium as a continuum — in the vein of *dimensional regularization* of quantum mechanics [Collins 1984] and involving a Riesz fractional form — is based on a reformulation of the Green–Gauss (or divergence) Theorem

$$\int_{\partial W} f_k n_k dA_d = \int_W c_3^{-1}(D, R) \nabla_k (c_2(d, R) f_k) dV_D, \quad (2-4)$$

where f_k is a vector field (in subscript notation) and

$$dA_d = c_2(d, R) dA_2 dV_D = c_3(D, R) dV_3. \quad (2-5)$$

Here dA_2 and dV_3 are, respectively, the conventional infinitesimal elements of surface and volume in Euclidean space, while dA_d and dV_D are the corresponding elements of a fractal's surface and volume. Note that the left-hand side in (2-4) is a fractional integral, equal to a conventional integral $\int_{\partial W} c_2(d, R) f_k n_k dA_2$, while the right-hand side is a fractional integral, equal to a conventional integral $\int_W \text{div}(c_2(d, R) f_k) dV_3$. Thus, we can rewrite (2-4) as

$$\int_{\partial W} c_2(d, R) f_k n_k dA_2 = \int_W \nabla_k (c_2(d, R) f_k) dV_3, \quad (2-6)$$

and, in fact, extend this theorem to the setting with a jump $[f_k]$ on a surface S across W :

$$\int_{\partial W} c_2(d, R) f_k n_k dA_2 = \int_{W-S} \nabla_k (c_2(d, R) f_k) dV_3 + \int_S c_2(d, R) [f_k] n_k dA_2. \quad (2-7)$$

The proof of (2-7) follows the same lines as that in conventional continuum mechanics; dividing the body W into two parts separated by S , applying the Green–Gauss theorem to each part while accounting for

the jump from either side, and combining both results. From (2-7) one obtains a special form, sometimes simply called the Green’s (or gradient) Theorem,

$$\int_{\partial W} c_2(d, R) f n_k dA_2 = \int_{W-S} \nabla_k(c_2(d, R) f) dV_3 + \int_S c_2(d, R) [f] n_k dA_2. \tag{2-8}$$

While (2-4) was derived by Tarasov [2005b], the following form of the Reynolds (transport) Theorem was adopted in an *ad hoc* fashion without a derivation:

$$\frac{d}{dt} \int_W P(x, t) dV_D = \int_W \frac{\partial}{\partial t} P dV_D + \int_{\partial W} P v_k dA_d. \tag{2-9}$$

Effectively, (2-4) and (2-9) have led Tarasov to introduce these conventional forms of two key differential operators of continuum mechanics:

$$\begin{aligned} \nabla_k^D f &= c_3^{-1}(D, R) \frac{\partial}{\partial x_k} [c_2(d, R) f] \equiv c_3^{-1}(D, R) \nabla_k [c_2(d, R) f] \left(\frac{d}{dt}\right)_D f \\ &= \frac{\partial f}{\partial t} + c(D, d, R) v_k \frac{\partial f}{\partial x_k}, \end{aligned} \tag{2-10}$$

where

$$\begin{aligned} c(D, d, R) &= |\mathbf{R}|^{d+1-D} \frac{2^{D-d-1} \Gamma(D/2)}{\Gamma(3/2) \Gamma(d/2)} = c_3^{-1}(D, R) c_2(d, R), \\ c_2(d, R) &= |\mathbf{R}|^{d-2} \frac{2^{2-d}}{\Gamma(d/2)}, \quad c_3(D, R) = |\mathbf{R}|^{D-3} \frac{2^{3-D} \Gamma(3/2)}{\Gamma(D/2)}. \end{aligned} \tag{2-11}$$

Now, proceeding in the same vein as with (2-7), we obtain an extension of the Stokes (curl) Theorem

$$\int_{\partial W} \mathbf{n} \times \mathbf{f} dA_d = \int_W c_3^{-1}(D, R) \mathbf{curl}[c_2(d, R) \mathbf{f}] dV_D. \tag{2-12}$$

To clarify, this involved the steps

$$\begin{aligned} \int_{\partial W} e_{ijk} n_j f_k dA_d &= \int_{\partial W} e_{ijk} n_j f_k c_2(d, R) dA_2 = \int_W [e_{ijk} f_k c_2(d, R)]_{,j} dV_3 \\ &= \int_W c_3^{-1}(D, R) [c_2(d, R) e_{ijk} f_k]_{,j} dV_D. \end{aligned} \tag{2-13}$$

This procedure may now be extended to derive the Reynolds (transport) Theorem for fractal media. Similar to the case of nonfractal media, but focusing on a region W of mass fractal dimension D and bounded by a surface of another fractal dimension d , in the following steps we obtain the time rate of change of an integral involving a spatially distributed quantity f :

$$\begin{aligned} \frac{d}{dt} \int_W f(x, t) dV_D &= \frac{d}{dt} \int_W f J dV_D^0 = \int_W \frac{d}{dt} [f J] dV_D^0 = \int_W [\dot{f} J + P \dot{J}] dV_D^0 \\ &= \int_W [\dot{f} J + f v_{k,k} J] dV_D^0 = \int_W [\dot{f} + f v_{k,k}] dV \\ &= \int_W \left(\frac{\partial}{\partial t} f + f_{,k} v_k + f v_{k,k} \right) dV_D = \int_W \left(\frac{\partial}{\partial t} f + (f v_k)_{,k} \right) dV_D. \end{aligned} \tag{2-14}$$

Here dV_D^0 refers to the volume of a fractal object in the reference configuration, while J denotes a Jacobian of motion defined in terms of material coordinates. Two observations are relevant at this point:

- (i) The final result cannot be written as a sum of a volume integral and a surface integral, the way it is done in (2-9). Nor is it possible to write $\frac{d}{dt} \int_W f(x, t) dV_D$ as $\int_W \frac{\partial}{\partial t} f dV_3 + \int_{\partial W} f v_k dA_2$.
- (ii) The third line in (2-14) dictates the conventional material derivative

$$\frac{df}{dt} = \frac{\partial f}{\partial t} + v_k \frac{\partial f}{\partial x_k}. \quad (2-15)$$

This is in contrast to $(d/dt)_D = \partial f/\partial t + c(D, d, R)v_k f_{,k}$, with $c(D, d, R) = c_3^{-1}(D, R)c_2(d, R)$, of Tarasov's equation (2-9). In consequence, in all previous results in mechanics of fractal media, $(d/dt)_D$ is to be simply replaced by the conventional material derivative d/dt , which leads to certain simplifications.

Proceeding in a similar way for the time rate of change of a surface integral involving a quantity Q distributed over a surface ∂W , we find

$$\begin{aligned} \frac{d}{dt} \int_{\partial W} Q(x, t) n_p dA_d &= \int_{\partial W} \dot{Q}(x, t) n_p dA_d + \int_{\partial W} Q(x, t) \frac{d}{dt} (n_p dA_d) \\ &= \int_{\partial W} \dot{Q}(x, t) c_2 n_p dA_2 + \int_{\partial W} Q(x, t) (n_p v_{k,k} - n_k v_{k,p}) c_2 dA_2 \\ &= \int_{\partial W} ([\dot{Q}(x, t) + v_{k,k} Q(x, t)] \delta_{pq} - Q(x, t) v_{q,p}) n_q c_2 dA_2 \\ &= \int_{\partial W} ([\dot{Q}(x, t) + v_{k,k} Q(x, t)] \delta_{pq} - Q(x, t) v_{q,p}) n_q dA_d. \end{aligned} \quad (2-16)$$

This implies that the fractal structure of the medium does not affect the essential conclusion of the Helmholtz-Żórawski lemma.

Balance equations. The results above lead to modified balance equations of fractal media [Tarasov 2005a, 2005b; Ostoja-Starzewski 2007a]:

- the fractional equation of continuity,

$$\dot{\rho} = -\rho \nabla_k^D v_k; \quad (2-17)$$

- the fractional equation of balance of density of momentum,

$$\rho \dot{v}_k = \rho f_k + \nabla_k^D \sigma_{kl}; \quad (2-18)$$

- the fractional equation of balance of density of energy,

$$\rho \dot{u} = \sigma_{kl} d_{kl} - \nabla_i^D q_i; \quad (2-19)$$

- the Clausius-Duhem inequality,

$$\sigma_{ij}^{(d)} d_{ij} + \beta_{ij}^{(d)} \dot{a}_{ij} - \frac{\theta_{,k} q_k}{\theta} \geq 0. \quad (2-20)$$

Here σ_{kl} is the Cauchy stress (symmetric according to the balance of angular momentum, employed just like in nonfractal media), $\sigma_{ij}^{(d)}$ and $\beta_{ij}^{(d)}$ are the dissipative stresses, while α_{ij} are the internal parameters in the vein of thermomechanics with internal variables [Ziegler 1983]. One may argue, however, that a complex microstructure of many fractal media, such as exemplified by lattices involving bending moment interactions (see [Limat 1988], for instance), would imply micropolar effects. This subject will require a separate treatment.

3. Some previous results

For completeness, we list several recently obtained generalizations of conventional continuum mechanics results to the setting of fractal media. See [Ostoja-Starzewski 2007a, 2007b, 2008a] for details.

(i) The equation of Fourier-type heat conduction,

$$\rho c_p \dot{\theta} = \frac{\partial}{\partial x_i} \left(k_{ij} \frac{\partial \theta}{\partial x_j} \right), \quad (3-1)$$

is generalized for fractal media to (with k being the thermal conductivity)

$$\rho c_p \dot{\theta} = \nabla_i^D \left(k_{ij} \frac{\partial \theta}{\partial x_j} \right). \quad (3-2)$$

(ii) The Duhamel equation of linear thermoelasticity,

$$\rho c_p \dot{\theta} = -(3\lambda + 2\mu)\alpha\theta_0 \dot{\varepsilon}_{(1)} + \frac{\partial}{\partial x_i} \left(k_{ij} \frac{\partial \theta}{\partial x_j} \right),$$

is generalized for fractal media to

$$\rho c_p \dot{\theta} = -(3\lambda + 2\mu)\alpha\theta_0 \dot{\varepsilon}_{(1)} + \nabla_i^D \left(k_{ij} \frac{\partial \theta}{\partial x_j} \right).$$

Here λ and μ are the Lamé coefficients, α is the coefficient of thermal expansion and the subscript (1) indicates the first basic invariant of strain.

(iii) The Maxwell–Betti reciprocity relation of linear elasticity,

$$\int_{\partial W} t_i^* u_i dA_2 = \int_{\partial W} t_i u_i^* dA_2. \quad (3-3)$$

is generalized for fractal media to

$$\int_{\partial W} t_i^* u_i dA_d = \int_{\partial W} t_i u_i^* dA_d. \quad (3-4)$$

(iv) The Hill condition, which in the classical case reads

$$\overline{\sigma_{ij} \varepsilon_{ij}} = \overline{\sigma_{ij} \bar{\varepsilon}_{ij}}, \quad (3-5)$$

for a fractal medium becomes

$$\overline{c(D, d, R) \sigma_{ij} \varepsilon_{ij}} = \overline{\sigma_{ij} \bar{\varepsilon}_{ij}}. \quad (3-6)$$

(v) The local form of the balance of linear momentum of a turbulent flow, accounting for fluctuations and after averaging is carried out,

$$\rho \left(\frac{d}{dt} \bar{v}_i + \bar{v}_{i,j} \bar{v}_j \right) = -\rho \overline{(v'_i v'_j)},_j + \rho f_k + \bar{\sigma}_{ij,j}, \quad (3-7)$$

is modified for a fractal porous medium to

$$\rho \left(\frac{d}{dt} \bar{v}_i + \bar{v}_{i,j} \bar{v}_j \right) = -\rho \nabla_j^D \overline{(v'_i v'_j)} + \rho f_k + \nabla_j^D \bar{\sigma}_{ij}. \quad (3-8)$$

This implies that the Reynolds stress σ_{ij}^* can no longer be simply written as $\sigma_{ij}^* - \rho \overline{(v'_i v'_j)}$, but it is a function of D , d , and R .

The same type of approach allows a generalization of a telegraph equation governing the propagation of second sound in a rigid conductor with fractal geometry [Ignaczak and Ostoja-Starzewski 2009].

4. Extremum and variational principles in elasticity

Statically admissible fields. Consider a *statically admissible field* denoted by $*$. We can then write

$$\int_{\partial W} (t_i^* - t_i) u_i dA_d = \int_{\partial W_i} (t_i^* - t_i) u_i dA_d. \quad (4-1)$$

On account of (2-4) and the fractional equation of static equilibrium of a body without a body force field — a special case of (2-18) — this becomes

$$\int_W c(D, d, R) (\sigma_{ij}^* - \sigma_{ij}) \varepsilon_{ij} dV_D. \quad (4-2)$$

Now, at every point in the fractal, strictly speaking prefractal, elastic body, just like in a nonfractal elastic body, this inequality holds

$$(\sigma_{ij}^* - \sigma_{ij}) \varepsilon_{ij} < \frac{1}{2} (\sigma_{ij}^* \varepsilon_{ij}^* - \sigma_{ij} \varepsilon_{ij}). \quad (4-3)$$

Thus, (4-1) is written as

$$\frac{1}{2} \int_W c(D, d, R) \sigma_{ij}^* \varepsilon_{ij}^* dV_D - \int_{\partial W_u} t_i^* u_i dA_d > \frac{1}{2} \int_W c(D, d, R) \sigma_{ij} \varepsilon_{ij} dV_D - \int_{\partial W_u} t_i u_i dA_d, \quad (4-4)$$

or, equivalently,

$$\frac{1}{2} \int_W c(D, d, R) \sigma_{ij}^* \varepsilon_{ij}^* dV_D - \int_{\partial W_u} t_i^* u_i dA_d > \frac{1}{2} \int_{\partial W_i} t_i u_i dA_d - \frac{1}{2} \int_{\partial W_u} t_i u_i dA_d. \quad (4-5)$$

On account of (2-5), (4-5) can be written as

$$\begin{aligned} \frac{1}{2} \int_W c_2(d, R) \sigma_{ij}^* \varepsilon_{ij}^* dV_3 - \int_{\partial W_u} c_2(d, R) t_i^* u_i dA_2 \\ > \frac{1}{2} \int_{\partial W_i} c_2(d, R) t_i u_i dA_2 - \frac{1}{2} \int_{\partial W_u} c_2(d, R) t_i u_i dA_2, \end{aligned} \quad (4-6)$$

which means that the expression on the left-hand side takes an absolute minimum value in the actual state.

Next, consider the expression

$$\int_W c(D, d, R)u^*(\sigma_{ij}^*)dV_D - \int_{\partial W_u} t_i^*u_i dA_d, \tag{4-7}$$

where u^* is the potential energy density, a functional of σ_{ij}^* , such that

$$\frac{\partial}{\partial \sigma_{ij}^*}u^*(\sigma_{ij}^*) = \varepsilon_{ij}^*. \tag{4-8}$$

We inquire when the expression (4-7) assumes a stationary value with respect to σ_{ij}^* satisfying the equilibrium condition. First, we can rewrite (4-7) as

$$\int_W c(D, d, R)U^*(\sigma_{ij}^*)dV_D - \int_{\partial W} t_i^*u_i dA_d + \int_{\partial W_t} t_i^*u_i dA_d, \tag{4-9}$$

which becomes

$$\int_W c(D, d, R)[u^*(\sigma_{ij}^*) - \sigma_{ij}\varepsilon_{ij}]dV_D + \int_{\partial W_t} t_i^*u_i dA_d. \tag{4-10}$$

Since $t_i^* = t_i$ on ∂W_t , this has a stationary value when

$$\frac{\partial}{\partial \sigma_{ij}^*}u^*(\sigma_{ij}^*) = \varepsilon_{ij}. \tag{4-11}$$

In view of (4-8), (4-7) has a stationary value when

$$\varepsilon_{ij}^* = \varepsilon_{ij}, \tag{4-12}$$

that is, in the actual state.

Kinematically admissible fields. Consider a kinematically admissible field denoted by $*$. We can then prove

$$\int_{\partial W_t} (u_i^* - u_i)t_i dA_d = \int_W c(D, d, R)(\varepsilon_{ij}^* - \varepsilon_{ij})\sigma_{ij} dV_D. \tag{4-13}$$

Now, at every point in the prefractal elastic body, just as in a nonfractal elastic body, we have

$$\frac{1}{2}(\sigma_{ij}^*\varepsilon_{ij}^* - \sigma_{ij}\varepsilon_{ij}) > (\varepsilon_{ij}^* - \varepsilon_{ij})\sigma_{ij}, \tag{4-14}$$

unless $\sigma_{ij}^* = \sigma_{ij}$, which leads to

$$\int_{\partial W_t} (u_i^* - u_i)t_i dA_d < \frac{1}{2} \int_W c(D, d, R)(\sigma_{ij}^*\varepsilon_{ij}^* - \sigma_{ij}\varepsilon_{ij}) dV_D \tag{4-15}$$

or

$$\int_{\partial W_t} (u_i^* - u_i)t_i dA_d - \frac{1}{2} \int_W c(D, d, R)\sigma_{ij}^*\varepsilon_{ij}^* dV_D < \int_{\partial W_t} u_i t_i dA_d - \frac{1}{2} \int_W c(D, d, R)\sigma_{ij}\varepsilon_{ij} dV_D. \tag{4-16}$$

Equivalently, we can write

$$\int_{\partial W_t} (u_i^* - u_i) t_i dA_d - \frac{1}{2} \int_W c(D, d, R) \sigma_{ij}^* \varepsilon_{ij}^* dV_D < \int_{\partial W_t} u_i t_i dA_d - \frac{1}{2} \int_W c(D, d, R) \sigma_{ij} \varepsilon_{ij} dV_D. \quad (4-17)$$

Again on account of (2-5), this can be restated in terms of conventional integrals in Euclidean space:

$$\int_{\partial W_t} c_2(d, R) (u_i^* - u_i) t_i dA_2 - \frac{1}{2} \int_W c_2(d, R) \sigma_{ij}^* \varepsilon_{ij}^* dV_3 < \int_{\partial W_t} c_2(d, R) u_i t_i dA_2 - \frac{1}{2} \int_W c_2(d, R) \sigma_{ij} \varepsilon_{ij} dV_3. \quad (4-18)$$

This means that the expression on the left-hand side takes an absolute maximum value in the actual state.

The relations derived above imply that one can apply the extremum principles of elasticity to fractal bodies, provided extra information is taken into account through D , d and R .

5. Hamilton's principle for a fractal continuum

Just as in continuum mechanics of conventional media (see [Reddy 1984], for example), we begin with the statement of work done on a fractal body at time t by the resultant force in moving through the virtual displacement

$$\int_W \mathbf{f} \cdot \delta \mathbf{u} dV_D + \int_{\partial W_t} \mathbf{t} \cdot \delta \mathbf{u} dA_d - \int_W c(D, d, R) \sigma : \delta \varepsilon dV_D \quad (5-1)$$

(or equivalently $\int_W f_i \delta u_i dV_D + \int_{\partial W_t} t_i \delta u_i dA_d - \int_W c(D, d, R) \sigma_{ij} \delta \varepsilon_{ij} dV_D$), where the third term is dictated by (2-4) and the variation satisfies the conditions

$$\delta \mathbf{u} = 0 \text{ on } \partial W_u \text{ for all } t, \quad \delta \mathbf{u}(\mathbf{x}, t_1) = \delta \mathbf{u}(\mathbf{x}, t_2) = 0 \text{ for all } \mathbf{x}. \quad (5-2)$$

At the same time, the work done by the inertia force $m\mathbf{a}$ in moving through the virtual displacement $\delta \mathbf{u}$ is given by

$$\int_W \rho \frac{\partial \mathbf{u}^2}{\partial t^2} \cdot \delta \mathbf{u} dV_D. \quad (5-3)$$

Now Newton's second law,

$$\mathbf{F} - m\mathbf{a} = \mathbf{0}, \quad (5-4)$$

dictates that

$$\int_{t_1}^{t_2} \left(\int_W \rho \frac{\partial u_i^2}{\partial t^2} \delta u_i dV_D - \left(\int_W f_i \delta u_i dV_D + \int_{\partial W_t} t_i \delta u_i dA_d - \int_W c(D, d, R) \sigma_{ij} \delta \varepsilon_{ij} dV_D \right) \right) dt = 0. \quad (5-5)$$

Upon integration of the first term by parts, this is transformed to a form of Hamilton's principle for a continuous medium (without a requirement of a conservative force system or elastic material behavior)

$$- \int_{t_1}^{t_2} \left(\int_W \rho \frac{\partial u_i}{\partial t} \frac{\partial \delta u_i}{\partial t} dV_D + \left(\int_W f_i \delta u_i dV_D + \int_{\partial W_t} t_i \delta u_i dA_d - \int_W c(D, d, R) \sigma_{ij} \delta \varepsilon_{ij} dV_D \right) \right) dt = 0. \quad (5-6)$$

In the special case of a conservative force system and an elastic body, a potential energy of external forces and a strain energy density (dual by a Legendre transformation to u^* of (4-11) and (4-12)) exist,

such that

$$\delta V = - \int_W f_i \delta u_i dV_D - \int_{\partial W_t} t_i \delta u_i dA_d, \quad \frac{\partial}{\partial \varepsilon_{ij}} u = \sigma_{ij}, \quad u = u(\varepsilon_{ij}). \quad (5-7)$$

Hence (5-6) becomes

$$\int_{t_1}^{t_2} L dt = 0, \quad L = K - \Pi, \quad (5-8)$$

where L is the Lagrangian and Π is the total potential energy.

Finally, proceeding similarly to classical continuum mechanics albeit within the calculus pertinent to fractional integrals, by using integration by parts, the Green–Gauss Theorem (2-4) and the conditions (5-7), leads to

$$\begin{aligned} 0 &= \delta \int_{t_1}^{t_2} L(u_k, \dot{u}_k) dt \\ &= \int_{t_1}^{t_2} \left\{ \int_W \left[\rho \frac{d}{dt} v_k - \rho f_k + \nabla_l^D \sigma_{kl} \right] \delta u_i dV_D + \int_{\partial W_t} (t_k - t_k^*) \delta u_i dA_d \right\}. \end{aligned} \quad (5-9)$$

Given that $\delta \mathbf{u}$ is arbitrary for $t \in (t_1, t_2)$ and $\mathbf{x} \in W$, as well as on ∂W_t , we find the Euler–Lagrange equations associated with L :

$$\rho \frac{d}{dt} v_k = \rho f_k + \nabla_l^D \sigma_{kl} \quad \text{in } W, \quad t_k - t_k^* = 0 \quad \text{on } \partial W. \quad (5-10)$$

In (5-10)₁ we recognize Equation (2-18). Further results, in the setting of elastic and inelastic materials, are given in [Ostoj-Starzewski 2009].

6. Conclusions

The continuum property is desired in providing mathematical descriptions of random heterogeneous microstructures in terms of homogenizing fields. While a number of methods have been developed over the past few decades to justify this in the setting of materials having Euclidean geometries for deterministic as well as random fields (see a review in [Ostoj-Starzewski 2008b]), in the case of fractal (i.e., almost everywhere nondifferentiable) media, novel methods outside classical continuum mechanics have to be employed. As a result, new forms of governing (partial differential) equations are derived where fractal dimensions and spatial resolution appear through explicit coefficients $c(D, d, R)$, $c_2(d, R)$ and $c_3(D, R)$. This indicates that very complex and multiscale materials of both elastic and inelastic type – which have so far been the domain of condensed matter physics, geophysics and biophysics – will soon be open to studies via initial-boundary value problems in the vein conventionally developed for smooth materials. This is made possible thanks to the approach initiated by Tarasov [2005a, 2005b, 2005c], and, in fact, allows one to deal with prefractal media which are commonly seen in nature.

The resulting field equations are more general than those of nonfractal media encountered in conventional continuum mechanics. In the latter case, $D = 3$, $d = 2$, whereby $c(D, d, R) = c_2(d, R) = c_3(D, R) = 1$, so that one recovers conventional forms of transport equations, balance equations and extremum principles of continuum mechanics. Thus, having to handle continuum mechanics of fractal

media implies that one has to deal with partial differential equations and/or extremum principles in which the coefficients $c(D, d, R)$, $c_2(d, R)$ and $c_3(D, R)$ pertinent to a given microstructure are present.

The approach developed in this paper has its limitations: (i) spatial homogeneity, which actually allows smoothing at some finite length scale corresponding to the upper cutoff of the prefractal, and (ii) use of the Riesz form of fractional integrals for fractals in higher dimensional case using one integral variable, the radial scalar r , thus restricting the problem to a spherically symmetric one [Roy 2007], which in turn implies local isotropy of material response. The second limitation is removed with the help of a product measure instead of a Riesz measure, and thereby also ensuring that the mechanical approach to continuum mechanics is consistent with the energetic approach [Ostoja-Starzewski and Li 2009]. In that paper we have also extended the fracture mechanics (in terms of the strain energy release rate approach) and the elastodynamic equations of a Timoshenko beam to materials described by fractional integrals involving D , d and R . That line of approach has then allowed us [Li and Ostoja-Starzewski 2009] to specify the geometry configuration of continua via “fractal metric” coefficients, and therefore grasp the local material anisotropy. This then allows development of wave equations in one-, two- and three-dimensional fractal media or micropolar continuum models.

References

- [Barnsley 1993] M. F. Barnsley, *Fractals everywhere*, Academic Press, Boston, 1993.
- [Collins 1984] J. C. Collins, *Renormalization: an introduction to renormalization, the renormalization group, and the operator-product expansion*, Cambridge University Press, Cambridge, 1984.
- [Epstein and Adeeb 2008] M. Epstein and S. M. Adeeb, “Fractal structural elements”, pp. 357–361 in *Tenth Pan American Congress of Applied Mechanics (PACAM X)* (Cancún, 2008), edited by T. L. Attard, 2008. To appear.
- [Epstein and Śniatycki 2006] M. Epstein and J. Śniatycki, “Fractal mechanics”, *Physica D* **220**:1 (2006), 54–68.
- [Feder 1988] J. Feder, *Fractals*, Plenum, New York, 1988.
- [Ignaczak and Ostoja-Starzewski 2009] J. Ignaczak and M. Ostoja-Starzewski, *Thermoelasticity with finite wave speeds*, Oxford University Press, Oxford, 2009. To appear.
- [Kigami 2002] J. Kigami, *Analysis on fractals*, Cambridge Tracts in Mathematics **143**, Cambridge University Press, Cambridge, 2002.
- [Li and Ostoja-Starzewski 2009] J. Li and M. Ostoja-Starzewski, “Fractal solids, product measures and fractional wave equations”, *Proc. R. Soc. Lond. A* **465**:2108 (2009), 2521–2536. In press.
- [Limat 1988] L. Limat, “Micropolar elastic percolation: the superelastic problem”, *Phys. Rev. B* **38**:10 (1988), 7219–7222.
- [Mandelbrot 1982] B. Mandelbrot, *The fractal geometry of nature*, W. H. Freeman, San Francisco, 1982.
- [Ostoja-Starzewski 2007a] M. Ostoja-Starzewski, “Towards thermomechanics of fractal media”, *Z. Angew. Math. Phys.* **58**:6 (2007), 1085–1096.
- [Ostoja-Starzewski 2007b] M. Ostoja-Starzewski, “Towards thermoelasticity of fractal media”, *J. Therm. Stresses* **30**:9–10 (2007), 889–896.
- [Ostoja-Starzewski 2008a] M. Ostoja-Starzewski, “On turbulence in fractal porous media”, *Z. Angew. Math. Phys.* **59**:6 (2008), 1111–1117.
- [Ostoja-Starzewski 2008b] M. Ostoja-Starzewski, *Microstructural randomness and scaling in mechanics of materials*, Chapman and Hall/CRC, Boca Raton, FL, 2008.
- [Ostoja-Starzewski 2009] M. Ostoja-Starzewski, “Extremum and variational principles for elastic and inelastic media with fractal geometries”, *Acta Mech.* **205**:1–4 (2009), 161–170.
- [Ostoja-Starzewski and Li 2009] M. Ostoja-Starzewski and J. Li, “Fractal materials, beams, and fracture mechanics”, *Z. Angew. Math. Phys.* (2009). In press.

- [Reddy 1984] J. N. Reddy, *Energy and variational methods in applied mechanics: with an introduction to the finite element method*, Wiley, New York, 1984.
- [Roy 2007] N. Roy, “On spherically symmetrical accretion in fractal media”, *Mon. Not. R. Astron. Soc.* **378**:1 (2007), L34–L38.
- [Strichartz 2006] R. S. Strichartz, *Differential equations on fractals: a tutorial*, Princeton University Press, Princeton, NJ, 2006.
- [Tarasov 2005a] V. E. Tarasov, “Continuous medium model for fractal media”, *Phys. Lett. A* **336**:2–3 (2005), 167–174.
- [Tarasov 2005b] V. E. Tarasov, “Fractional hydrodynamic equations for fractal media”, *Ann. Physics* **318**:2 (2005), 286–307.
- [Tarasov 2005c] V. E. Tarasov, “Wave equation for fractal solid string”, *Mod. Phys. Lett. B* **19**:15 (2005), 721–728.
- [Ziegler 1983] H. Ziegler, *An introduction to thermomechanics*, Rev. ed., North-Holland Series in Applied Mathematics and Mechanics **21**, North-Holland, Amsterdam, 1983.

Received 3 May 2008. Revised 23 Jan 2009. Accepted 17 May 2009.

MARTIN OSTOJA-STARZEWSKI: martinos@uiuc.edu

*Department of Mechanical Science and Engineering and Institute for Condensed Matter Theory,
University of Illinois at Urbana–Champaign, 1206 W. Green Street, Urbana, IL 61801-2906, United States*
<http://www.mechse.uiuc.edu/research/martinos/>

AN ENDOSCOPIC GRASPER WITH CORRUGATED PLATE-SHAPED TACTILE SENSORS

MOHAMMAD AMEEN QASAIMEH, MOHAMMADREZA RAMEZANIFARD AND JAVAD DARGAHI

One of the major weaknesses in current endoscopic surgery is the lack of tactile feedback. This paper reports on the design, finite element modeling, and experimental testing of a corrugated tactile sensor. The sensor, a miniaturized and modified form of our previously developed tactile sensor, consists of a $75\ \mu\text{m}$ plate-shaped silicon layer and a $25\ \mu\text{m}$ polyvinylidene fluoride (PVDF) film, patterned on both sides using photolithographic techniques to form three independent sensing elements. The sensor is 15 mm long, 7.5 mm wide, and approximately 3 mm thick, which could make it versatile enough for integration with current endoscopic and medical robotics manipulators. The silicon layer is micromachined in such a way that a U-channel is formed. When a force is applied on the tactile sensor, output voltages from the patterned PVDF-sensing elements are combined to obtain tactile information. Results show that the sensor exhibits high sensitivity and can measure small dynamic loads, comparable to a human pulse, as well as large grasping forces. In addition to measuring the magnitude and position of the applied load, the sensor can determine the modulus of elasticity of the grasped object.

1. Introduction

Over a decade ago, surgical procedures called minimally invasive surgery (MIS) were introduced. Though initially limited to specific kinds of operations, MIS has now become a standard and widely used surgical procedure, replacing most of the traditional open-surgery procedures [Tendick et al. 1998]. MIS has substantial benefits over traditional open surgeries, which require large incisions to allow the surgeon access to perform procedures at the operation site [Carrozza et al. 2003].

Tactile sensing is defined as the continuous sensing of variable contacting forces, such as the sensing ability of the human finger. One of the most exciting and rapidly emerging areas where tactile sensing is making a significant impact is in robotic surgery, primarily because soft tissue can only be properly recognized by evaluating its softness, viscosity, and elasticity properties [Rebello 2004]. In the decision-making process during surgery, one of the most highly evaluated procedures is palpation of tissues [Howe et al. 1995]. This is an essential step for any surgical process because palpation of the grasped tissue gives some ideas about its properties.

To perform MIS more effectively, the surgeon should be able to feel the tissue and sense the pressure of blood vessels and ducts during the surgical procedure [Howe et al. 1995; Rebello 2004]. This ability is imperative during manipulation tasks such as grasping internal organs, gentle load transfer during lifting, and suturing and removing tissues [Melzer et al. 1994]. Tactile sensors recommended for use during MIS procedures should be small, highly sensitive, have low manufacturing and integration costs, and should preferably be disposable [Carrozza et al. 2003; Rebello 2004; Qasaimeh et al. 2007]. Combining

Keywords: tactile sensor, endoscopic grasper, minimally invasive surgery, microfabricated sensor.

all of these features in MIS is one of the leading aspects of research with regard to the integration of microfabrication and microelectromechanical system (MEMS) technology in the field of tactile sensing and MIS. MEMS have both electrical and mechanical parts. The sensor, or actuator, fabricated using this technology, is micromachined to be relatively small in the macro world and includes microfabrications of both electrical and mechanical components on one common substrate. MEMS technology can be applied to the tactile-sensing field to produce tiny micro tactile sensors. These improved microfabricated tactile sensors have made great strides recently in the field of MIS, and many more promising improvements are in progress. Miniaturization of sensors improves dexterity and increases the sensing elements per unit area. These sensors can be mass produced, resulting in low unit costs.

Endoscopic and laparoscopic tools are widely used in MIS operations. Endoscope graspers should have teeth that are able to grasp slippery and soft tissues usually associated with endoscope operations [Rebello 2004]. A currently available commercial endoscopic tool for laboratory use is shown in Figure 1 (Snowden–Pencer Graspers SP90-3104 type).

Few publications exist that deal with tactile sensor design, especially for use in MIS. Some currently fabricated devices are able to find the force and compliance of sensed tissues but failed when it came to detecting embedded lumps, and were limited to a force range in the milligrams [Dargahi et al. 2000; 2005]. Finite element methods were applied in parallel development works [Tanimoto et al. 1998; Najarian et al. 2006], but none of the proposed designs had the ability to measure the position of the applied forces besides finding grasping forces. Narayanan et al. [2006] presented a tactile sensor for MIS operations, but the sensor is active only on the teeth regions; the other regions are inactive and unable to sense the properties of the contacting object. One of our developed sensors was presented in [Qasaimeh et al. 2007]. It was able to locate the applied force magnitude, pressure distributions on the organ, and embedded lumps; however, primary results indicate that the design is somewhat deficient in finding and detecting low-magnitude loads similar to the pulse in a blood vessel.

Based on our previous work [Qasaimeh et al. 2008a; 2008b; 2009], this paper presents a modified and miniaturized tactile sensor (15 mm long and 7.5 mm wide) which could be incorporated on the tip of MIS tools (such as an endoscopic tool or robotic manipulators). The presented sensor is able to measure the magnitude and position of grasping forces and is therefore could be potentially able to estimate any embedded lump or abnormality inside a grasped organ. In addition, the proposed sensor is able to detect low mechanical forces and hence can potentially detect the pulse in a blood vessel. Also, this sensor can estimate the softness of the object with which it comes into contact.

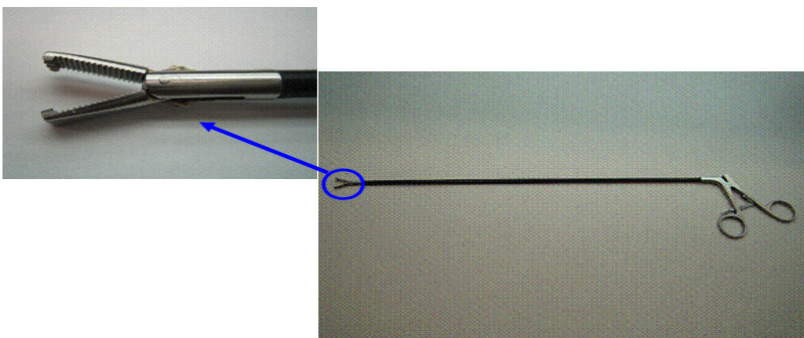


Figure 1. Commercial endoscopic graspers used for endoscopic surgeries (Snowden-Pencer SP90-3104).

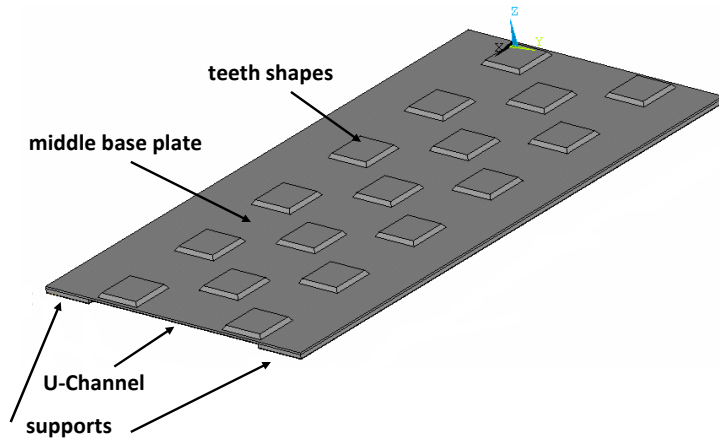


Figure 2. The silicon layer (first layer of the sensor assembly), comprising the teeth shape, the middle base plate, the U-channel, and the two supports.

2. Design and structure of the sensor

The proposed sensor is assembled using three layers. The first layer is micromachined from a silicon wafer. The second layer is the sensing element microfabricated by patterning a polyvinylidene fluoride (PVDF) film. Finally, the entire structure is supported by and attached to a substrate (third layer) of cage-shaped Plexiglas. The first layer is microfabricated to form the required teeth shapes of height $200\ \mu\text{m}$ on the top of a deformable base plate of thickness $75\ \mu\text{m}$. The base plate stands on two supports, $200\ \mu\text{m}$ in height, to form a U-shaped channel. All of these features are microfabricated in one step out of a single $475\ \mu\text{m}$ silicon layer. The designed teeth on the top are necessary for the purpose of grasping. The microfabricated silicon layer design is shown in [Figure 2](#), and a top view showing the teeth arrangements and dimensions is shown in [Figure 3](#). The middle base plate is designed to give a deformation under grasping action, and the supports hold the base plate to provide a suitable gap which is necessary for the plate deflection. The second layer within the sensor is microfabricated from PVDF film to create sensing elements — specifically, from metalized and poled piezoelectric PVDF film, $25\ \mu\text{m}$ thick [[Qasaimeh et al. 2008a](#)]. The third layer, or substrate, is machined out of Plexiglas to support the

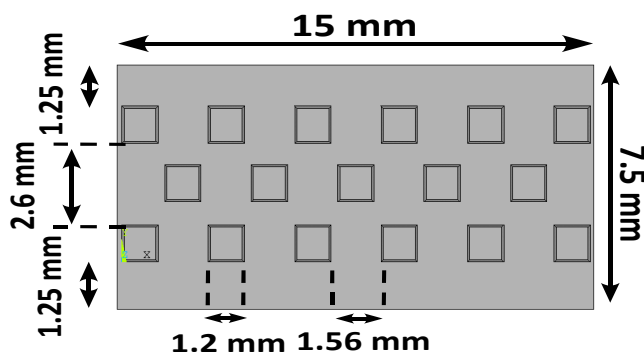


Figure 3. Top view of the sensor showing the teeth arrangement and dimensions. (The thickness is 3 mm.)

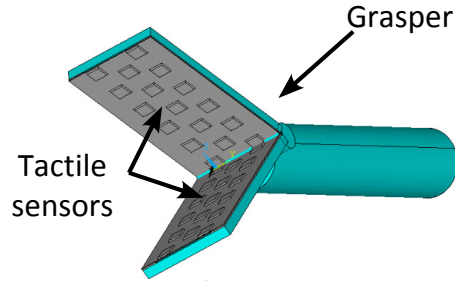


Figure 4. The proposed sensor after assembly and integration with an endoscopic MIS tool. A single sensor may be integrated with one jaw, or each jaw may be provided with its own sensor, allowing the combined signal to offer additional tactile information such as the depth of embedded lumps.

first two layers and hold them in place during tissue manipulation and operations such as handling, lifting and twisting. Plexiglas surrounds the first two layers on three sides (see Figures 10 and 11 on page 921) to protect the sensor assembly against shear forces associated with tissue manipulation. The integration between sensor and endoscopic grasper is schematically indicated in Figure 4.

The microfabricated prototype is 15 mm long and 7.5 mm wide. These dimensions are compatible with available commercial laparoscopic tools and could be easily integrated with them.

The silicon layer of the sensor base plate has a thickness of $75 \mu\text{m}$. This thickness was chosen to optimize the loading range of the grasping forces as well as to be sensitive to the small mechanical forces which are equivalent to the pulse in a blood vessel. Moreover, after a study of various tooth-like shapes, an irregular teeth arrangement was chosen (as shown in Figures 3 and 4). The orientations of the attached PVDF were investigated and the drawn direction (d_{31}) of the PVDF-sensing elements was chosen to be parallel with the sensor width (Y -direction) [Qasaimeh et al. 2008b]. This proposed sensor is the second generation of our previously invented sensor and is based on our continuing work [Qasaimeh et al. 2008b; 2009]. The design of the sensing element has been modified to eliminate any cross-talk between adjacent elements, and the supporting layer was customized to protect the sensor assembly under shear stresses (during surgical manipulations) and eliminate the contribution of these stresses to the output signal. The size was also reduced so the sensor can fit with current endoscopic tools and medical robotic manipulators.

3. Principle of the sensor

There are two sensing layers in different locations. The first is the sensing layer at the supports, which is sandwiched between the silicon supports and the Plexiglas supporting layer. The second is the middle sensing layer which is glued to the back of the base plate. The sensing layer at the supports has two functions: it determines the total grasping force magnitude, and it locates any concentric load application. The middle sensing layer determines the grasped tissue softness and detects low magnitude forces.

While grasping internal organs, a compression force is transferred to the PVDF layers at the supports via the silicon layer. These forces will actuate the PVDF layers to work on its thickness mode, resulting in an output voltage on the electrodes. For greater compression loads, the PVDF layer will be compressed more, resulting in a higher magnitude of voltage. Because the silicon layer has two supports, we can

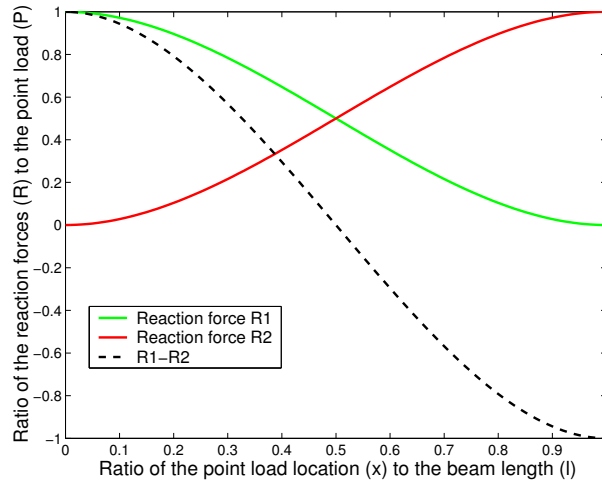


Figure 5. Reaction magnitudes as a function of the point load location. By comparing both quantities, the exact position of the applied point load can be estimated.

predict the applied load carried by these two supports using simple principles of mechanics. Depending on the pressure distributions and the concentric load location, the load will either be carried equally on both supports, or one of the supports will carry more than the other. For simplicity, a fixed-fixed simple beam with applied point load is considered. A point load P is applied at a distance x on the beam of length L . Two reactions, R_1 and R_2 , and two moments, M_1 and M_2 , appear at the fixed points of the beam. The magnitudes of both R_1 and R_2 are a function of x , and the summation of both is equal to the load magnitude P . Because the system is in static equilibrium, by equating to zero the sum of forces and the sum of moments, we obtain

$$R_1 = \frac{P(\ell^3 - 3\ell x^2 + 2x^3)}{\ell^3}, \quad R_2 = \frac{P(3\ell x^2 - 2x^3)}{\ell^3}.$$

By plotting both equations versus the point load location, the relation between each reaction magnitude and the point load location is shown clearly (see Figure 5). By comparing both curves (R_1 and R_2), the exact position of the applied point load can be estimated.

The voltage generated at each sensing element beneath its support will depend on position with a shape similar to the one in Figure 5. The amplitude of the variation has the functional form

$$V = F \frac{d}{A \times C},$$

where F is the magnitude of the reaction forces, d is the piezoelectric coefficient of the sensing element (PVDF) in compression mode, A is the surface area of the sensing element, and C is the capacitance of the sensing element.

The middle sensing layer is a PVDF layer working on its extensional mode. Deflection of the base silicon plate will cause the PVDF layer to stretch and supply an output voltage. This sensing layer is responsible for determining tissue softness and for finding and responding to any low magnitude loading comparable to the pulse in a blood vessel. The silicon layer deflection is related to the softness of the contacting tissue. In the case of grasping a soft tissue, the silicon will yield to a large deflection (because

the tissue itself does not resist the action of the distributed load and bend easily), in proportion to the large stretching of the PVDF layer, and produce a high voltage. On the other hand, in the case of grasping a hard tissue, the silicon layer will be only slightly deflected (because the tissue itself will resist the bending action due to its rigidity) with correspondingly less stretching of the PVDF giving rise to only a small voltage.

4. Sensor modeling

A complete physical model of the proposed sensor was modeled and analyzed using ANSYS 12 (see Figure 6 for a top view of the mesh). This model is used to determine the deformation of the sensor and the output voltage at the PVDF-sensing elements for different loading conditions. Silicon and Plexiglas layers were modeled using the SOLID45 element, which possesses plasticity, creep, swelling, stress stiffening, large deflection, and large strain capabilities for 3D modeling. The PVDF-sensing elements were modeled using the SOLID227 element.

The linearized constitutive equations solved by the software are $\{\sigma\}_{6 \times 1} = [C]_{6 \times 6} \{\epsilon\}_{6 \times 1}$ and $D_{6 \times 1} = [e]_{6 \times 6}^T \{\epsilon\}_{6 \times 1}$, where σ is the stress vector, ϵ the strain vector, C the elasticity matrix, and D the electric flux density vector. The piezoelectric matrix can be defined either in the $[e]$ form (piezoelectric stress matrix) or in the $[d]$ form (piezoelectric strain matrix), the two being related by $[e] = [C][d]$.

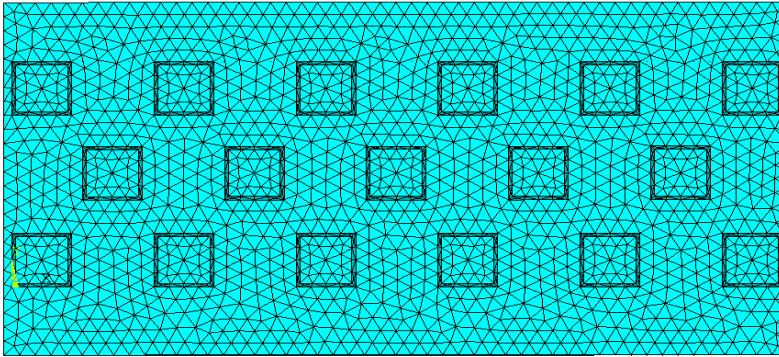


Figure 6. Top view of the meshed finite element model of the sensor.

5. Microfabrication and assembly

The silicon layer is microfabricated on both sides by employing anisotropic bulk etching using a tetramethylammonium hydroxide (TMAH) bath. The sensing elements are prepared by selectively etching each aluminum electrode covering the PVDF film on both sides. Each layer is prepared separately until the sensor is assembled.

Silicon microfabrications. The wafer is cleaned using deionized (DI) water and a nitrogen gun. It is then wet-oxidized in an oxidation furnace at 1100 °C for two hours to build a silicon oxide layer of almost 1.2 μm thickness. After oxidization, the silicon wafer is covered by a layer of Shipley S1813 positive photoresist (PR) by spin coating. It is then soft-baked on a hot plate at a temperature of 115 °C for about one minute. After preparing the dark field mask (which outlines the teeth shapes), the mask is

aligned to the flat edge of the wafer (100), using alignment marks, to have the $\{111\}$ silicon planes on the side walls of the silicon teeth. This is followed by exposure to ultraviolet light for fifteen seconds. The PR is then developed, using an appropriate PR developer, and subsequently the sample is hard-baked on a hot plate at a temperature of 115°C for one minute. After the careful alignments under the EVG mask aligner, the same procedure is repeated on the other surface of the silicon sample, using the second dark field mask which represents the supports. The next step is the wet-etching of the silicon oxide to form a hard mask for silicon bulk-etching. Oxide-etching begins by dipping the sample inside a buffered oxide etchant (HF) for a few minutes until the oxide-etching on the PR-free regions is complete. The remaining oxides act as the hard mask during the bulk silicon-etching process. The last step of the silicon layer microfabrication is the silicon bulk-etching inside a 25% TMAH bath. The sample is kept inside this bath for eleven hours to form teeth and supports with the desired heights and shapes. Finally, the remaining PR and silicon oxide is removed and the silicon sample is rinsed with DI water for a few minutes and dried using a nitrogen gun. The silicon microfabrication steps are shown in Figure 7.

PVDF fabrications. A sample of aluminum metalized PVDF film is prepared and cut with a rectangular shape and suitable dimensions. Care is taken that the drawn direction (d_{31}) of the PVDF strip is parallel with the width of the sample. The sample has dimensions $18 \times 8 \text{ mm}^2$, which is slightly wider and longer than the silicon sample to provide the necessary margins during assembly. The PVDF-sensing elements at both the middle and supports are microfabricated on single PVDF film. Therefore, both sides of the film are patterned to fabricate the PVDF-sensing elements at the middle and at the supports, and to ensure that all are electrically isolated from each other, thus eliminating cross-talk between elements.

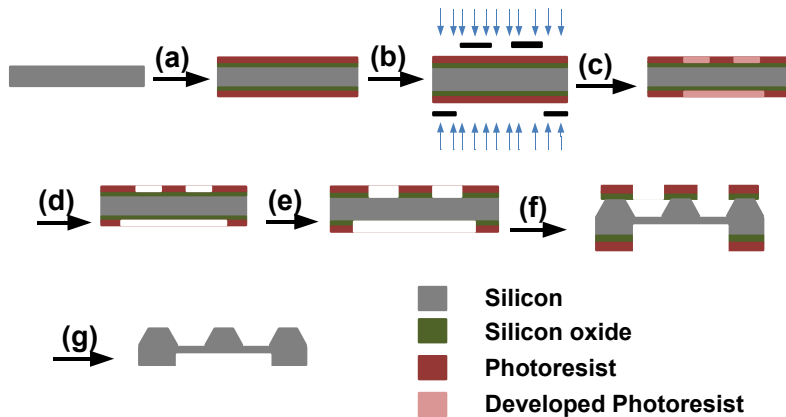


Figure 7. The silicon layer bulk etching process: (a) the silicon layer is thermally oxidized and photoresist is deposited on both surfaces; (b) the sample is soft-baked and then exposed to UV through different masks for each side; (c) the sample is hard-baked and then developed; (d) the developed photoresist is etched out; (e) unprotected silicon oxide is etched out; (f) unprotected silicon is etched out; (g) the remaining photoresist is removed, and then the silicon oxide is removed completely, resulting in the final microfabricated silicon layer.

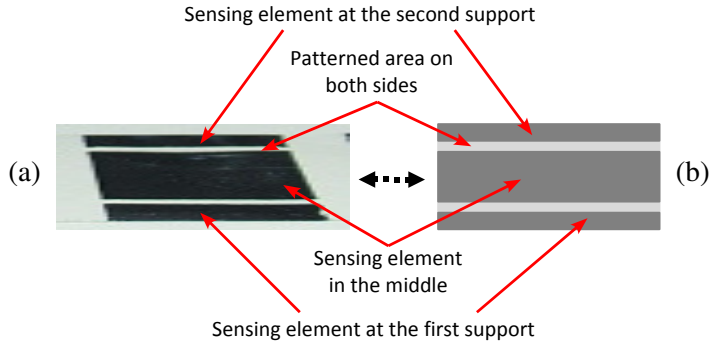


Figure 8. PVDF film and sensing elements: (a) the microfabricated PVDF sensing elements by patterning the PVDF film, and (b) designed PVDF sensing elements distribution on the PVDF film.

The three sensing elements are microfabricated using MEMS technology including the photolithography steps. The process starts with the PR deposition, and then the sample is soft-baked. After preparing the mask, the sample is exposed to UV light and the PR is hard-baked after developing. The same steps are then repeated for the other side of the sample after the care alignments under the EVG mask aligner. The aluminum cover is patterned using aluminum commercial etchant and then the remaining PR is removed. The patterned PVDF film, which includes the sensing elements, is shown in [Figure 8](#). Finally, working under stereomicroscope, each aluminum electrode at each PVDF-sensing element is connected to a copper electrode (which, in turn, is welded to a copper wire connected to the conditioning circuit to provide the sensor's output) using conductive silver epoxy (see [Figure 11](#) on the next page).

Layer assembly. First, the PVDF-sensing elements are glued to the microfabricated silicon layer. A nonconductive epoxy is distributed uniformly on the back of the middle silicon plate and on the bottom of both silicon supports as well. Afterwards, the PVDF sensing elements are aligned under a stereomicroscope to ensure their proper location. After that, as shown in [Figure 9](#), compression blocks are applied for 24 hours to compress the sensing elements to the silicon layer to ensure secure and uniform adhesion. Finally, the Plexiglas layer is integrated into the structure using the same procedure; see [Figure 10](#). The final assembled prototype sensor is shown in [Figure 11](#).

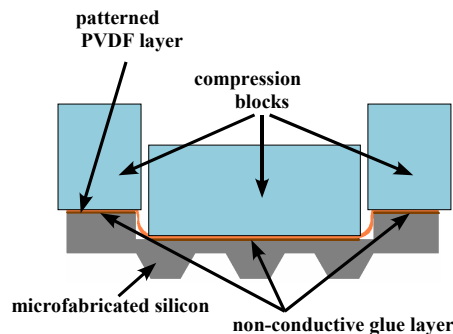


Figure 9. Assembly of the silicon and PVDF microfabricated sensor layers using non-conductive epoxy, with the application of compression blocks for 24 hours.

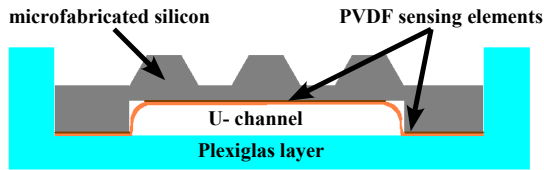


Figure 10. Final assembly of the sensor: the first two layers are fixed inside the Plexiglas cage with non-conductive epoxy, and compression is applied for 24 hours.

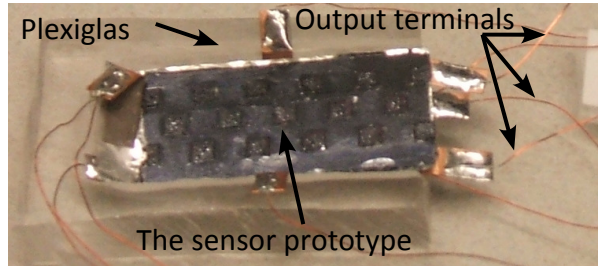


Figure 11. Photograph of the microfabricated prototype sensor.

6. Finite elements and experimental results

We now report and compare the simulation and experimental results. The experimental setup is shown in Figure 12. The sensor is fixed on an XYZ micropositioning stage and positioned under a cylindrical probe, which is driven by a vibration unit (Ling dynamic model V203) and used to apply a sinusoidal force of frequency 10 Hz, unless stated otherwise. The vibration unit is activated by a signal generator (Agilent 33220A).

The magnitude of the applied force is determined by a force transducer (KISTLER, Type 9712B50) inserted between the probe and the vibration unit. The force transducer output is connected to an amplifier which, in turn, is connected to a computer via the data acquisition card to monitor the applied load.

In the same way, the PVDF sensing elements are connected by wires to the charge amplifiers, which, in turn, are connected to a computer via the data acquisition card to measure output signals using the LabVIEW program.

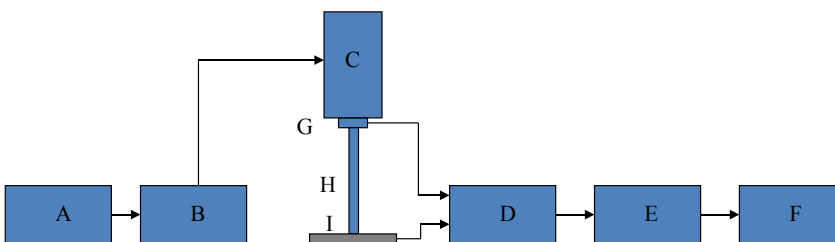


Figure 12. Experimental setup diagram: (A) signal generator, (B) power amplifier, (C) vibrator, (D) charge and voltage amplifiers, (E) A/D converter, (F) computer, (G) force transducer, (H) probe, and (I) the proposed sensor under test.

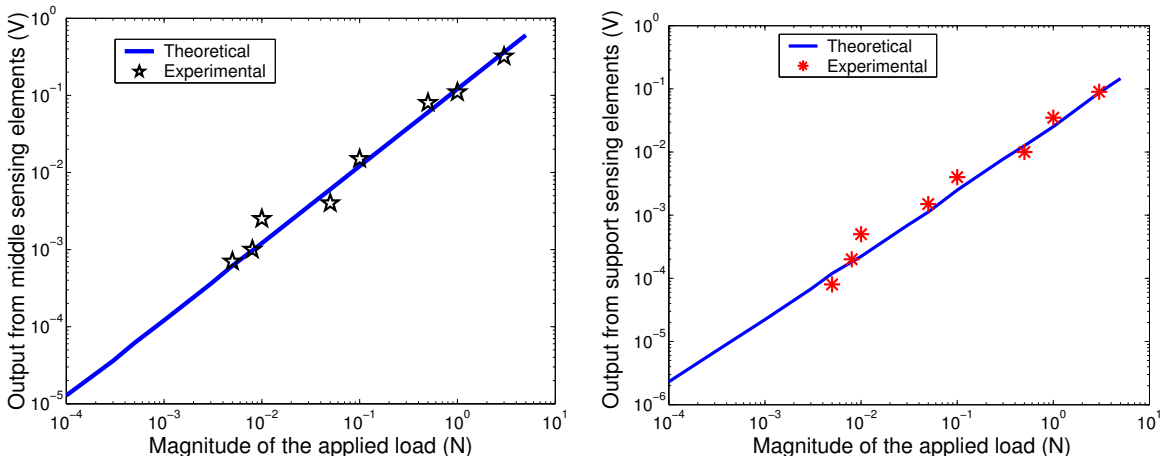


Figure 13. Left: calibration curve of the middle PVDF-sensing element. Right: calibration curve of each sensing element at the supports. For both curves, the experimental applied point loads ranged from 1 mN to 3 N and were always applied at the center of the sensor.

First, a point load is applied with a sharp head probe on the center point at the top of the sensor. This kind of loading is carried out in order to find a correlation between the output voltages in the PVDF-sensing elements with respect to the applied load magnitudes. Using this result, we obtained calibration curves for the sensor prototype, from which we can determine the grasping forces actually applied during surgery. The magnitudes of the forces applied ranged from 1 mN to 3 N. The output voltages with respect to the applied load magnitude at the PVDF-sensing elements are shown in Figure 13.

To detect the precise location of the applied point load, as when locating embedded lumps during surgery, a point load of 50 mN magnitude is applied on the silicon layer at different points. The point load was applied along the center line (which divides the length into two equal halves) of the silicon at different points in the Y -direction (crosswise). Output voltages from the middle PVDF-sensing element versus the 50 mN point load location are shown in Figure 14. To detect load location lengthwise, an array of sensing elements can be deployed along the sensor's length, as shown in [Qasaimeh et al. 2008b].

The output voltages versus the 50 mN point load location from the PVDF-sensing element at the first support (V_{S1}) and at the second support (V_{S2}) are shown in Figure 15. It can be seen from this figure that when a load is applied exactly onto the first support, the corresponding sensing element generates the maximum potential while the sensing element at the opposite support shows no output. Therefore, when the point of application moves away (along the Y -direction), the output voltage of the first support sensing element (V_{S1}) decreases and that of the second support (V_{S2}) increases. It is interesting to note that the difference between the output voltages of the pair of sensing elements at the supports (V_{S1} and V_{S2}) is linear with respect to the location of the applied concentric load. As a result, the location of applied load in the Y -direction can be calculated using this linear relationship.

Because the middle plate of silicon is thin ($75 \mu\text{m}$), it is therefore deformable under any action of forces. While contacting various tissues and objects, the plate will be deflected for small values if the tissue itself is hard. The reason for this is that hard tissue will resist bending under the load action. On

the other hand, where soft tissue is contacted, the plate will be deflected for larger values because soft tissue cannot resist bending as much as hard tissue can. When the plate deflects, the glued middle PVDF-sensing element at the back will be stretched and a voltage will be created. A larger deflection of the plate means that the PVDF layer will stretch even more, creating a correspondingly larger amount of voltage. Several simulations and experiments were carried out while considering different contacting objects with different moduli of elasticity. With a distributed load of 5 N applied to the top of a contacting object, theoretical and experimental results show that softer tissues cause a larger amount of created voltage, and harder contacting tissues cause a smaller amount of created voltage, as shown by the blue curve and red dots on Figure 16. In contrast, the output signals from the support sensing elements did not significantly

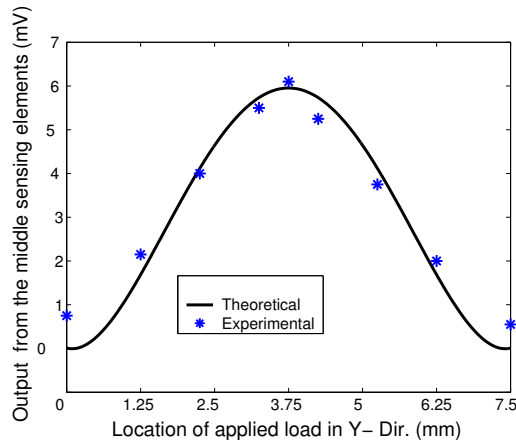


Figure 14. Output voltages from the middle sensing element versus the Y-location of the 50 mN point load. The maximum signal occurs when the force is applied exactly at the center of the sensor.

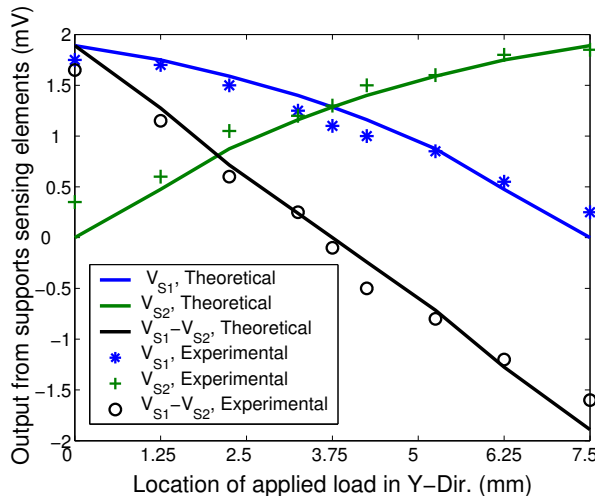


Figure 15. Output voltages from the first support sensing element ($V_{S1'}$) and the second support sensing element ($V_{S2'}$) versus the Y-location of the applied 50 mN point load.

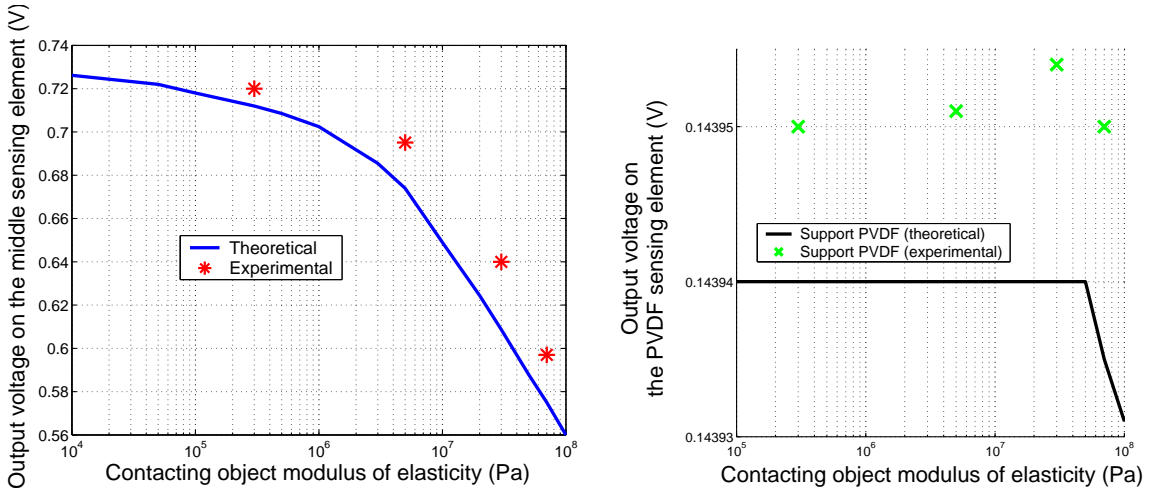


Figure 16. Theoretical and experimental values of the generated voltage on the sensing elements versus different modulus of elasticity of the contacting tissue, under application of a 5 N distributed uniform load. Left: middle sensing element. Right: support sensing element.

change with respect to the different contacting objects, as shown by the black curve and green dots in the same figure.

To test sensor response to an input comparable to the pulse of a blood vessel, a sinusoidal point load of 10 mN maximum amplitude and approximately 2 Hz frequency was applied at the middle of the sensor. The maximum response from the middle PVDF sensing element was found to be 2.2 mV, and the one from the support sensing elements, 0.3 mV. The output signals can be seen in Figure 17. In

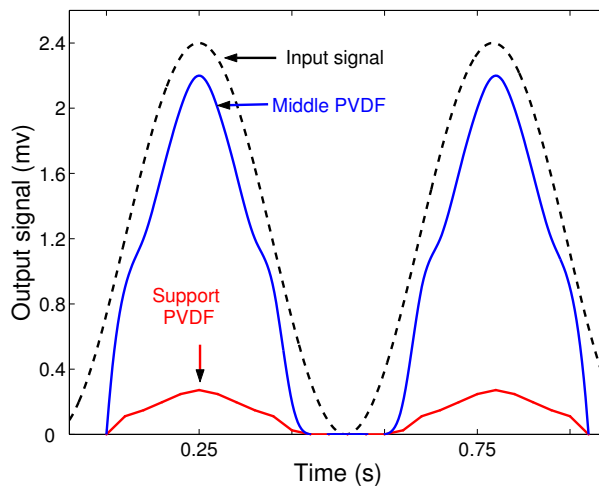


Figure 17. Experimental values of generated voltage on the support and middle sensing elements when a sinusoidal point load of amplitude 10 mN and frequency 2 Hz was applied on the middle of the sensor.

several experiments, we found that it is hard to see on the oscilloscope any response — especially from the support sensing elements — when the applied sinusoidal load is less than 1 mN (data not shown). As seen in the previous figure, the middle PVDF sensing element is more sensitive than the support sensing elements and can detect small dynamic loads comparable to the pulse of a blood vessel.

7. Discussion and conclusion

As shown in [Figure 13](#), linear relations exist between the output voltages from PVDF-sensing elements and the magnitude of the applied loads. The voltage appearing in the middle of the PVDF-sensing element is the most sensitive and can detect low-magnitude applied loads comparable to a blood vessel pulse, as shown in [Figure 17](#).

The summation of the two output voltages at the supports-sensing elements shows the total applied forces on the grasped object. As shown in [Figures 14 and 15](#), the precise location of any point load is detectable by comparing the output voltage values of the PVDF-sensing elements. The detection of any point load indicates the capability of the sensor to detect the presence of an embedded lump inside the grasped tissue. As shown in [Figure 16](#), the softness of the contacting object can be estimated using this novel plate design.

Differences between the theoretical and experimental results are due to many factors, one example of which is the electrical noise associated with the experimental setup. Another factor is the type of applied load. In theory, the applied load is a point force, but in experiments it is a sharp probe covering a small area. In addition, the contacting objects (tissues) used in the experiments are not ideal elastic objects; the known modulus of elasticity for each is not accurate and can even vary with different load applications. Also, the applied load in the simulations is static, but a low frequency dynamic sinusoidal load is applied in the experiments (peak-to-peak results were considered).

In conclusion, the potential sensor performance in relation to detecting grasping forces, embedded lumps, contacting tissues softness, and blood vessel pulse has been demonstrated. The sensor could be integrated with the commercial endoscopic tool for safer surgical procedures. Also, since it is micromachined, it could potentially be mass-produced with low unit cost, and be disposable.

However, improvements may need to be made before moving to the next stage of clinical test and use. One enhancement might be the use of an interface between the present sensor and graphical software, to display the contacting forces and tissue softness (as is being developed currently in our lab), or by integrating the sensor with a haptic interface to feel the contacting forces instead of monitoring them on a computer display. From the microfabrication point of view, direct deposition of PVDF on silicon chips as an alternative to gluing could make the sensor more precise. This might also help eliminate wiring to the PVDF sensing elements, leading to higher precision. Finally, proper packaging and protection is required for more effective functioning of the sensor.

References

- [Carrozza et al. 2003] M. C. Carrozza, P. Dario, and L. P. S. Jay, “[Micromechatronics in surgery](#)”, *Trans. Inst. Meas. Control* **25**:4 (2003), 309–327.
- [Dargahi et al. 2000] J. Dargahi, M. Parameswaran, and S. M. Payandeh, “[A micromachined piezoelectric tactile sensor for an endoscopic grasper: theory, fabrication and experiments](#)”, *IEEE/ASME J. Microelectromech. Sys.* **9**:3 (2000), 329–335.

- [Dargahi et al. 2005] J. Dargahi, S. Najarian, and K. Najarian, “Development and three-dimensional modelling of a biological-tissue grasper tool equipped with a tactile sensor”, *Can. J. Elect. Comput. Eng.* **30**:4 (2005), 225–230.
- [Howe et al. 1995] R. D. Howe, W. J. Peine, D. A. Kontarinis, and J. S. Son, “Remote palpation technology”, *IEEE Eng. Med. Biol. Mag.* **14**:3 (1995), 318–323.
- [Melzer et al. 1994] A. Melzer, G. Buess, and A. Cuschieri, “Instrumentation and allied technology for endoscopic surgery”, pp. 1–69 in *Operative manual of endoscopic surgery*, vol. 2, edited by A. Cuschieri et al., Springer, New York, 1994.
- [Najarian et al. 2006] S. Najarian, J. Dargahi, and X. Z. Zheng, “A novel method in measuring the stiffness of sensed objects with applications for biomedical robotic systems”, *Int. J. Med. Robot.* **2**:1 (2006), 84–90.
- [Narayanan et al. 2006] N. B. Narayanan, A. Bonakdar, J. Dargahi, M. Packirisamy, and R. Bhat, “Design and analysis of a micromachined piezoelectric sensor for measuring the viscoelastic properties of tissues in minimally invasive surgery”, *Smart Mater. Struct.* **15**:6 (2006), 1684–1690.
- [Qasaimeh et al. 2007] M. A. Qasaimeh, J. Dargahi, M. Kahrizi, and M. Packirisamy, “Design and analysis of tactile optical sensor for endovascular surgery”, pp. 67960J in *Photonics North 2007* (Ottawa, 2007), edited by J. C. Armitage, Proceedings of SPIE **6796**, SPIE, Bellingham, WA, 2007.
- [Qasaimeh et al. 2008a] M. A. Qasaimeh, J. Dargahi, M. Kahrizi, and S. Najarian, “Characterization of a multifunctional tactile sensor for use in endoscopic surgeries”, in *Tenth Pan American Congress of Applied Mechanics (PACAM X)* (Cancún, 2008), edited by T. L. Attard, 2008. To appear.
- [Qasaimeh et al. 2008b] M. A. Qasaimeh, S. Sokhanvar, J. Dargahi, and M. Kahrizi, “A micro-tactile sensor for *in situ* tissue characterization in minimally invasive surgery”, *Biomed. Microdevices* **10**:6 (2008), 823–837.
- [Qasaimeh et al. 2009] M. A. Qasaimeh, S. Sokhanvar, J. Dargahi, and M. Kahrizi, “PVDF-based microfabricated tactile sensor for minimally invasive surgery”, *IEEE/ASME J. Microelectromech. Sys.* **18**:1 (2009), 195–207.
- [Rebello 2004] K. J. Rebello, “Applications of MEMS in surgery”, *Proc. IEEE* **92**:1 (2004), 43–55.
- [Tanimoto et al. 1998] M. Tanimoto, F. Arai, T. Fukuda, H. Iwata, K. Itoigawa, Y. Gotoh, M. Hashimoto, and M. Negoro, “Micro force sensor for intravascular neurosurgery and in vivo experiment”, pp. 504–509 in *11th Annual International Workshop on Micro Electro Mechanical Systems (MEMS 98)* (Heidelberg, 1998), IEEE, New York, 1998.
- [Tendick et al. 1998] F. Tendick, S. S. Sastry, R. S. Fearing, and M. Cohn, “Applications of micromechatronics in minimally invasive surgery”, *IEEE/ASME Trans. Mechatron.* **3**:1 (1998), 34–42.

Received 12 May 2008. Revised 18 Apr 2009. Accepted 17 May 2009.

MOHAMMAD AMEEN QASAIMEH: mohammad.qasaimeh@mail.mcgill.ca

Biomedical Engineering Department, McGill University, 740 Dr. Penfield Avenue, Montreal, QC H3A 1A4, Canada

MOHAMMADREZA RAMEZANIFARD: m_ramez@encs.concordia.ca

Department of Mechanical and Industrial Engineering, Concordia University, 1455 De Maisonneuve Blvd. W, Montreal, QC H3G 1M8, Canada

JAVAD DARGAHI: dargahi@encs.concordia.ca

Department of Mechanical and Industrial Engineering, Concordia University, 1455 De Maisonneuve Blvd. W, Montreal, QC H3G 1M8, Canada

A NEW EARTHQUAKE-RESISTANT CONCRETE FRAME WITH FIBER-REINFORCED PLASTIC FABRICS AND SHIFTED PLASTIC HINGES

M. SAIID SAIIDI, ERIK REINHARDT AND FARAMARZ GORDANINEJAD

An innovative structural pier employing concrete, steel, and carbon fiber composite sheets was developed and implemented in a two-column bridge pier. The basic concept for the pier design is that the pier has preassigned plastic hinges in the columns. Outside the plastic hinges, the pier is to remain elastic. The innovative concept incorporated in the pier is that where plastic hinging and ductility is required, steel reinforcement is used as longitudinal reinforcement, and where elastic behavior is required, carbon-fiber-reinforced plastic (CFRP) sheets are used as longitudinal reinforcement. Confinement and shear capacity are provided for by fiber-reinforced polymer sheets at all locations. The pier is detailed so that the plastic hinges are shifted away from the column ends because shifted plastic hinges prevent damage from penetrating into the joint area and are easier to repair. A quarter-scale, two-column pier with square columns was designed and constructed based on the aforementioned concept. Ordinary concrete and mild steel were used in the pier. A unidirectional carbon composite was placed on the pier. The pier was studied using computer programs DRAIN 3-DX and RC-Shake and a shake table testing program was developed. The pier was subjected to successive runs of the 1994 Northridge–Sylmar record with increasing amplitudes until failure. The plastic hinges behaved as planned, and the failure occurred after the rupture of the CFRP confinement sheets at one of the plastic hinges. There was no apparent damage outside the plastic hinges. Extensive nonlinear analytical studies using multiple- and single-degree-of-freedom modes were conducted and the results were compared with the measured response. It was found that both models were generally capable of reproducing the experimental results.

1. Introduction

Applications of fiber-reinforced polymer (FRP) fabrics in civil infrastructure systems have been mainly in retrofits or repairs of substandard or damaged reinforced concrete structures [Teng et al. 2001]. FRP fabrics have rarely been used in new construction. In contrast, FRP members in the form of concrete filled tubes or FRP beams attached to concrete slabs have been investigated for use in new construction [Saiidi et al. 1994; Mirmiran et al. 2000]. The primary benefits of FRP materials are realized regardless of whether FRP fabrics or members are used. The high strength and ease of installation are generally the most important characteristics of FRPs. One characteristic of FRPs that could limit their application for certain uses is the lack of ductility in FRP fabrics and members when used by themselves. However, the linear behavior of FRP materials up to failure in combination with their high strength can be a feature that can be taken advantage of in structures where nonlinear behavior is not desired.

Current seismic design provisions for standard (noncritical) structural systems envision significant nonlinear deformations at preassigned locations in the structure. In building frames, the typical location for plastic hinges is at beam ends, whereas in bridges plastic hinges are expected at column ends. The

Keywords: bridges, carbon fiber, earthquake, nonlinear analysis, offset hinges, piers, shake table testing.

structure outside the plastic hinges is expected to remain elastic. This requirement can be satisfied by FRPs. The study presented here is aimed at developing and investigating a novel construction method for bridge piers in which FRP fabrics provide the primary longitudinal and transverse reinforcement in all segments of the pier except for the column plastic hinges where energy dissipation is expected. At the plastic hinges, conventional steel bars are used as longitudinal reinforcement and FRP fabrics are used as transverse reinforcement. An added feature of the proposed construction is the shifting of plastic hinges away from but close to the column ends, a concept that has been attempted in conventional reinforced concrete buildings but not bridges [Galunic et al. 1977; Abdel-Fattah and Wight 1987]. This article presents a summary of the concept, the design, construction, and shake table testing of a two-column pier utilizing this concept, measured data, and analytical studies of the new pier. Details of the study are presented in [Reinhardt et al. 2003].

2. Pier details

The proposed pier is a concrete structure with a very small amount of longitudinal and transverse steel reinforcement in all locations except for the column plastic hinges. Consistent with the practice of strong pier caps in bridge engineering, plastic hinging of the beams is precluded. In the column plastic hinges, longitudinal steel reinforcement is provided to dissipate the earthquake energy. However, confinement and shear capacity in the plastic hinges is provided by unidirectional FRP fabrics. The longitudinal and transverse reinforcement in the beam and the elastic portions of the columns are also provided by unidirectional FRP fabrics.

To evaluate the feasibility and seismic performance of the proposed structure, a two-column pier was constructed, reinforced with very low steel reinforcement ratios and carbon-fiber-reinforced plastic (CFRP) laminates, and tested to failure on a shake table. The test pier was a 1/4 scale model of a typical reinforced concrete bridge pier. Figure 1 shows the pier dimensions and the composite layout. The lines

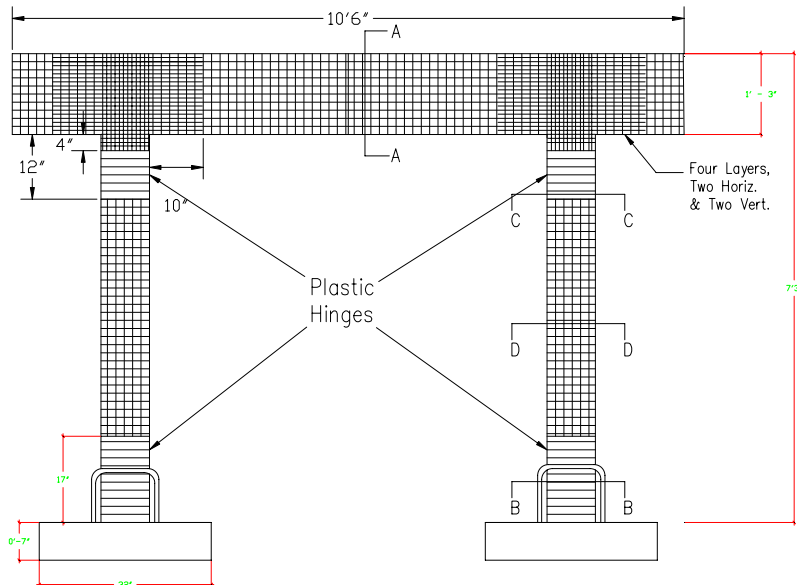


Figure 1. Dimensions of pier and arrangement of composites.

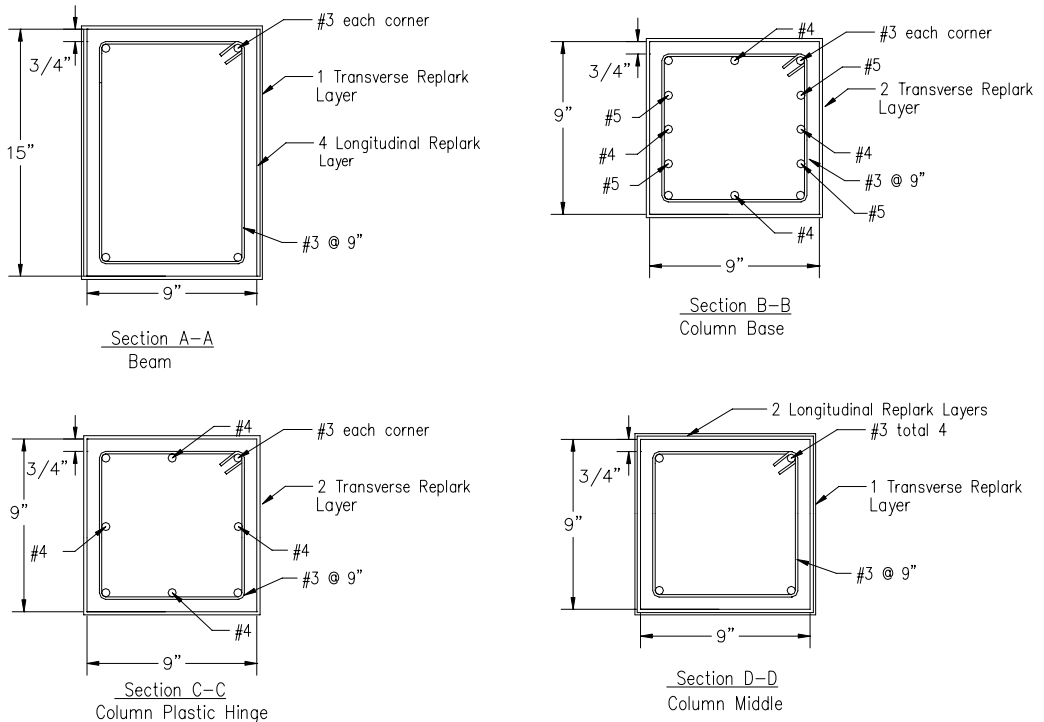


Figure 2. Pier section details and composite layout.

within the elements show the direction of the carbon fibers. [Figure 2](#) shows the bent cap and column cross-sections. The design criterion for the steel reinforcement outside the plastic hinges was for the concrete members to resist self weight. Other considerations were one bar at each corner and small diameter tie and stirrups at a spacing of approximately the minimum member cross sectional dimension.

Another feature of the proposed pier is that the plastic hinges are offset relative to the ends of the column. In a prototype, the shifting would facilitate repair and inspection of the plastic hinges after strong earthquakes. To shift the plastic hinges, a relatively high amount of steel was used at the column ends to ensure that they remained elastic (see [Section B-B](#) in [Figure 2](#)). Two horizontal and two vertical layers of CFRPs were provided on each side of the joints as shear reinforcement. The joint shear design was based on the ACI 352 provisions [[Mirmiran et al. 2000](#)].

Normal-weight concrete with a maximum aggregate size of 10 mm (3/8 in) was used. The target concrete compressive strength was 5 ksi (34 MPa), while the actual strengths were 6.26 ksi (42.8 MPa) in the columns and 5.29 ksi (36.1 MPa) in the bent cap on the day of testing. The concrete was air cured, and subsequently the surface of the concrete was prepared for laminate application. The specified grade of the steel reinforcement was 60. The measured yield stresses for the #3, #4, and #5 bars were, respectively, 66.3, 63.3, and 65.0 ksi (453, 432, and 444 MPa). The Mitsubishi CFRP product, Replark Type 30, was used. First the surface was ground using a disk grinder, then putty (supplied by the manufacturer of the composites) was applied to smooth out rough areas. Next, a layer of resin undercoat was applied followed by a layer of carbon fiber sheet. This was repeated as needed, and the process was completed by

application of a resin overcoat. Any air bubbles trapped beneath the laminate were repaired by injecting epoxy into the voids.

Per the manufacturer the lamina elastic modulus was 33,400 ksi (228 GPa) and its tensile strength was 493 ksi (3.365 GPa) in the fiber direction. One inch (25.4 mm) coupons were tested as part of the study. The measured lamina elastic modulus in the fiber direction was 38,400 ksi (262.3 GPa) and its tensile strength was 379.8 ksi (2.593 GPa). The measured lamina elastic modulus was 509.6 ksi (3.48 GPa) and its tensile strength was 1.76 ksi (12 MPa) perpendicular to the fiber direction.

Three configurations of the footings were used in the study: (1) as-built, flexible; (2) retrofitted, flexible; and (3) fixed. The first and second configurations were necessary for low-amplitude studies of the effect of footing flexibility in the linear range. The maximum longitudinal bar strains during that part of the study were kept below two-thirds of the measured steel yield strain. The results of the low-amplitude studies were presented elsewhere [Saiidi et al. 2002]. The subject of the present paper is the fixed footing configuration. The pier model was designated as B2SF for bent with 2 square columns and fixed footings. [Reinhardt et al. 2003] provides more details about the study.

3. Shake table tests

The test setup is shown in Figure 3. The footings were fixed to a 14.5 ft \times 15 ft (4.42 m \times 4.57 m) shake table using steel brackets and threaded bars. The bent was extensively instrumented with strain gages, displacement transducers (to measure displacements and curvatures), accelerometers, and a load cell (to measure lateral load applied to the specimen).

The target column axial load index (ALI, defined as the percent ratio of the axial load and the product of the gross area and the target concrete compressive strength) was 8%. The range of ALI in bridge columns is typically 5 to 10%. The uniform vertical load on the cap beam to produce an ALI of 8% was

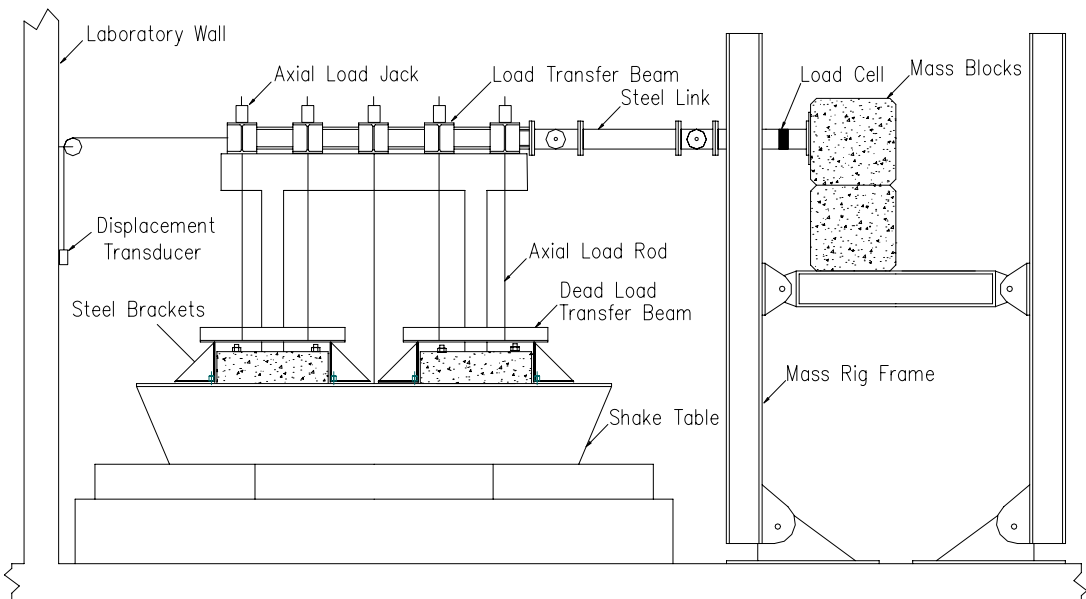


Figure 3. Shake table test setup for fixed-base model.

6.1 kip/ft (88.6 kN/m). The vertical loading was accomplished using five pairs of threaded bars running between the transfer beam and the footings each stressed to 6.4 kip (28.5 kN) using hydraulic rams (see [Figure 3](#)). A system of accumulators was attached to the rams to minimize axial load fluctuation caused by the extension of the threaded bars during earthquake simulations. To replicate the inertial effect of the gravity loads, a mass rig was used, which consisted of a pinned steel frame mechanism supporting concrete reaction blocks. The mass rig had an effective lateral inertial load of 64 kip (285 kN) and was connected to the loading frame by a pinned rectangular steel tube.

The earthquake history used to drive the shake table was the January 17, 1994 Northridge earthquake as measured at the Sylmar Hospital station. The peak ground acceleration of this record is 0.61 g. This record was chosen due to its being representative of typical earthquakes in the Western United States. Furthermore, preliminary analytical studies showed that this record would lead to high ductility demand thus allowing for ultimate behavior testing. Since the test specimen was a scaled model of the prototype column, the earthquake record time axis was scaled by a factor of 0.5 to create a response in the test specimen that would represent the prototype response. The pier was subjected to scaled versions of the Sylmar record in 13 simulations (runs), beginning with several preyield runs and continuing until pier failure. Intermittent low-amplitude quick release tests were conducted to measure the effective period and damping of the bent.

[Table 1](#) shows the target peak table accelerations (PTAs) for different runs. The fine increments in the first six runs were necessary for the evaluation of the footing flexibility effects reported in [[Saiidi et al. 2002](#)]. The peak target accelerations were 0.36 g and 0.24 g in the as-built and retrofitted footing configurations, respectively [[Saiidi et al. 2002](#)]. The actual peak accelerations were within 5% of the target values. The increment in run 12 was small because failure appeared to be imminent. However, it took an additional motion with a slightly higher PTA to cause the pier to fail. During the postyield runs the actual PTAs were within 10% of the target values.

Run number	Motion	Peak table acceleration (g)
1	0.1 × Sylmar	0.06
2	0.2 × Sylmar	0.12
3	0.3 × Sylmar	0.18
4	0.4 × Sylmar	0.24
5	0.5 × Sylmar	0.30
6	0.6 × Sylmar	0.36
7	0.8 × Sylmar	0.48
8	1.0 × Sylmar	0.60
9	1.25 × Sylmar	0.75
10	1.50 × Sylmar	0.90
11	1.75 × Sylmar	1.05
12	1.90 × Sylmar	1.14
13	2.00 × Sylmar	1.20

Table 1. Earthquake simulation protocol for B2SF.

4. Test results

The testing of the fixed footing configuration (3) was conducted after the pier had been subjected to low-amplitude motions. The maximum measured longitudinal bar strains for configurations (1) and (2) were 67% and 60% of the yield strains, respectively. The initial stiffness data indicated some softening due to minor cracking, but cracks were not visible and there were no signs of damage. The key response parameters that were evaluated to judge the performance of the pier were: observed damage, displacements, curvatures, and strains.

Observed damage. During the first two runs (see Table 1), no damage was visible. Under run 3 (with PTA of 0.18 g), horizontal cracks were seen in the transverse layer of composites at the bottom of the columns. In subsequent runs these cracks widened slightly and new thin horizontal cracks in the epoxy resin were visible. Multiple epoxy cracking noises could be heard in these runs. After run 11 (PTA of 1.05 g), a crack in the concrete at the right beam-column joint was noted. The bent appeared to be stable, but large and increasing movements were of concern. As a result the increment for the following run (run 12) was reduced. More cracking of the epoxy was noted during this run without any notable further damage. During the following run, with a peak acceleration of 1.2 g, a part of the confinement composite layer failed near the bottom of the right column in the plastic hinge region (see Figure 4). Also, the confinement composite jacket at the top of the right column delaminated from the concrete. Testing was terminated after this run due to the failure of the composite jacket and a drop in the lateral load capacity.

Lateral displacement response. Figure 5 shows the cumulative force-displacement hysteresis curve. The first few input motions resulted in mostly linear response. At larger PTAs, nonlinear loops were developed. Run 7 with a target PTA of 0.48 g led to a maximum lateral displacement of 1.1 in (28 mm) or

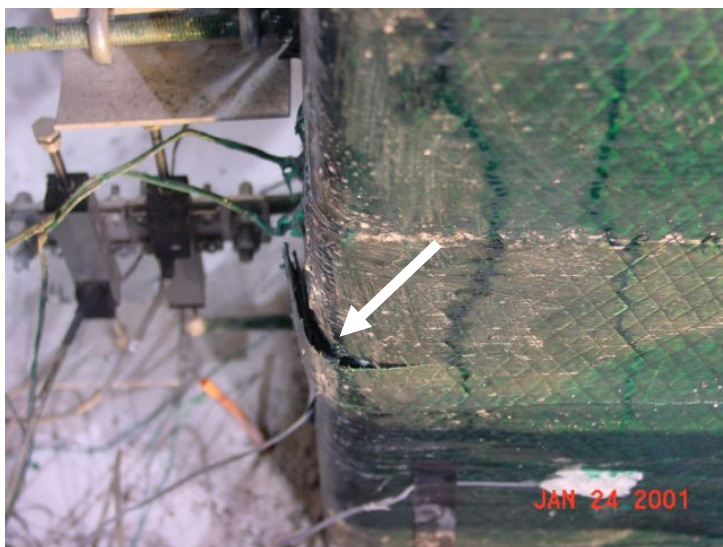


Figure 4. Ruptured jacket at bottom plastic hinge of right column.

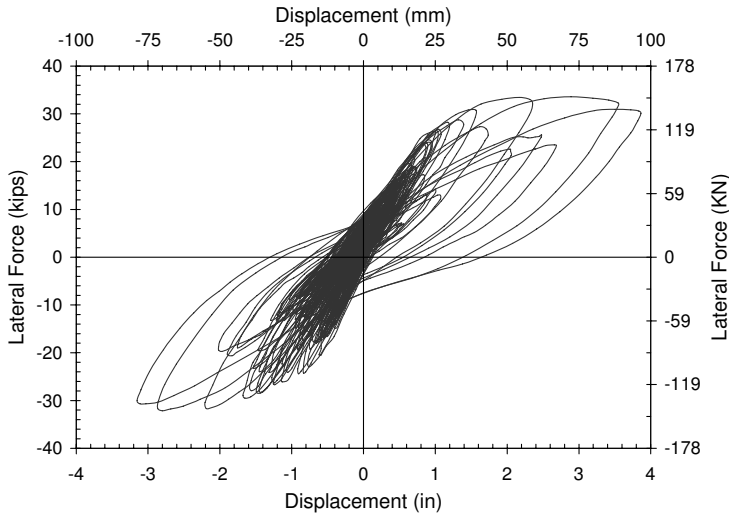


Figure 5. Cumulative measured force-displacement relationship.

approximately 1.5% drift. Subsequent runs led to relatively large-amplitude hysteresis loops and extensive nonlinear deformations. The hysteresis loops were relatively wide and indicative of large energy dissipation. The shifted plastic hinges were effective in providing the mechanism for energy dissipation and ductility.

The envelope of the measured force-displacement relationships for the primary direction of motion (the positive displacement range in Figure 5) is shown in Figure 6. It can be seen that stiffness reduced

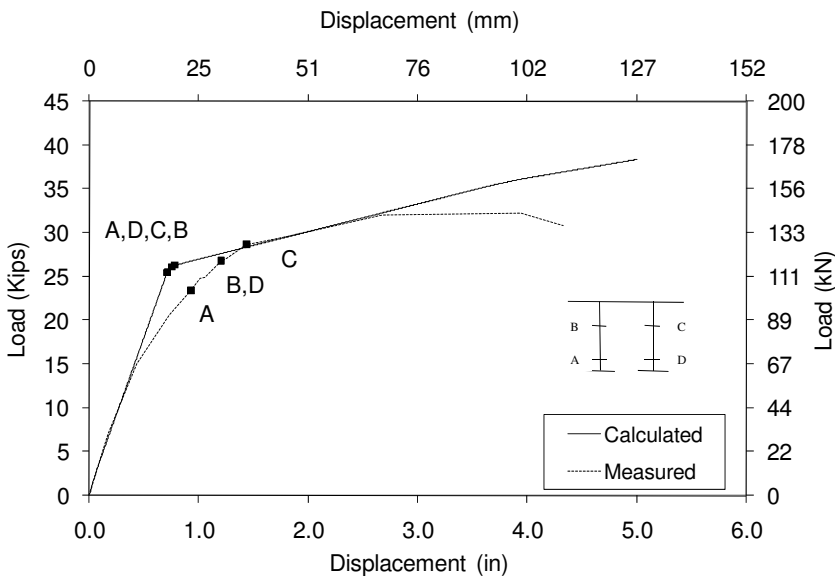


Figure 6. Force-displacement envelope: calculated values (upper curve) and measured ones (lower curve).

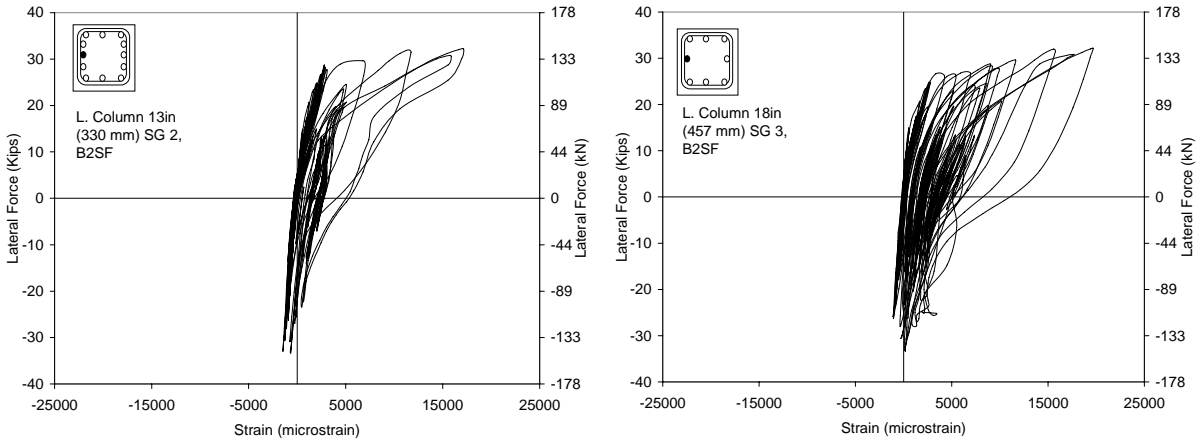


Figure 7. Force-strain relationship outside (left graph) and inside (right graph) the lower left column plastic hinge.

progressively with increasing level of acceleration, indicating gradual yielding at the hinges. Slight nonlinearity was observed in the first 7 runs, corresponding to displacements up to 1.05 in (26.7 mm). The source of the nonlinearity was primarily concrete deformation. The lateral load capacity did not change significantly during Runs 10–13, corresponding to displacements of 2.2 in (56 mm) to failure. During Run 13 when the FRP jacket failed the peak lateral force dropped by approximately 10%.

Based on an elastoplastic idealization of the measured envelope the measured effective yield displacement was 0.7 in (17.8 mm). At the first sign of failure the ductility capacity was 5.6, which exceeds the target ductility capacity of 4 or 5 used in practice. The drift capacity of the bent was 5.4%, which is also indicative of ample deformability of the proposed bent. The ductility and drift capacity of the proposed pier were close to the corresponding capacities of a conventional bridge bent with similar aspect ratio that was tested in a previous study [Moustafa et al. 2004] and labeled “B2CM” there.

Strains. The maximum strains in the column plastic hinge steel bars were approximately 20,000 microstrains at about 8 in (200 mm) below the bottom of bent cap and 8 in (200 mm) above top of footings. The peak strains in the column bars immediately below the bottom of the bent cap and immediately above the footings were less than these values demonstrating that the plastic hinges were indeed formed away from the ends as intended. Figure 7 shows sample strain data as a function of the pier lateral force for column bars outside and inside the plastic hinge near the bottom of the left column. Note some yielding of the longitudinal bars spread outside the plastic hinge. This is attributed to strain hardening of the bars inside the plastic hinge. Peak strains in the bent cap bars were approximately 3000 microstrains, indicating that the bent cap steel bars experienced limited yielding (the measured yield strain for the bars was 2190 microstrains).

The maximum measured strain on the transverse FRP layers on the column plastic hinges was approximately 4000 microstrains and was far less than the design strain of 10800 microstrains. As stated earlier, the transverse FRP layers eventually failed. However, there were no strain gages at the failure location and the actual strain could not be measured. The tensile strains in the longitudinal FRP layers

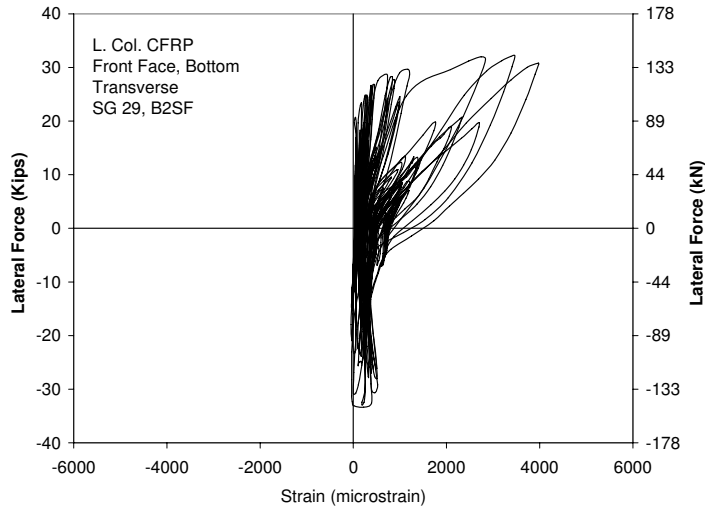


Figure 8. Force-transverse strain relationship on FRP at the lower left column plastic hinge.

parallel to the column axes were close to 4000 microstrains, well below the design strain of 10800 microstrains. Figure 8 shows a sample measured pier force-strain relationship for the transverse direction. The maximum strain in the composite layers on the bent cap parallel to the bent cap axis was less than 3000 microstrains, implying that the bent cap composite fabrics did not suffer any damage, as intended. Also, the maximum strain in the composite fabrics perpendicular to the bent cap, which were used for shear reinforcement, was approximately 1500 microstrains, meaning that the bent cap shear design was adequate. The maximum fabric strain in the joint region was close to 1000 microstrains. However, upon removal of the composite layer after the final shake table test, cracks were seen in the joint indicating that the joint design procedure may need to be reevaluated for possible increase in the number of fabric layers.

The composite fabrics were removed after the test to survey the damage locations and evaluate crack patterns. Horizontal cracks were noted at the plastic hinge region, which was to be expected because no vertical composite fibers were present in this area (see Figure 9). However, a number of shear cracks at approximately 40° to the horizontal were noted in the plastic hinges in the right column. These cracks are believed to have formed after the confinement CFRP ruptured. Shear cracks were also visible in the joint region, as shown in Figure 9, which suggests that additional CFRP layers may be necessary.

The composite layers in the bent cap and the portion of the columns in between plastic hinges did not delaminate, indicating that these regions remained elastic as was intended.

5. Analytical studies

The analytical studies consisted of nonlinear dynamic analysis of the test model using a multiple-degree-of-freedom (MDOF) and a single-degree-of-freedom (SDOF) model. The objective was to determine the adequacy of the modeling techniques used in detailed MDOF models and in simplified global SDOF models. More details of the analytical studies are presented in [Reinhardt et al. 2003].

MDOF modeling. The computer program DRAIN-3DX was used for the detailed representation of the test pier and for conducting nonlinear static and dynamic analyses of the test pier [Prakash et al. 1994]. Figure 10 shows the location of the nodes and elements in the analytical model. Linear beam-column elements were used outside the plastic hinges, and cracked section properties were used for the linear elements. A lumped plasticity moment rotation element was assigned to each plastic hinge. The hysteretic response of the plastic hinges was represented by the Takeda model. This model was developed to represent the cyclic response of reinforced concrete elements confined with steel reinforcement and accounts for the degradation of stiffness as cracking and yielding occurs. In the absence of a more specific model, it was assumed that the Takeda model is applicable to the plastic hinges in the test pier, even though the confinement in the test pier was provided by CFRP rather than steel reinforcement.

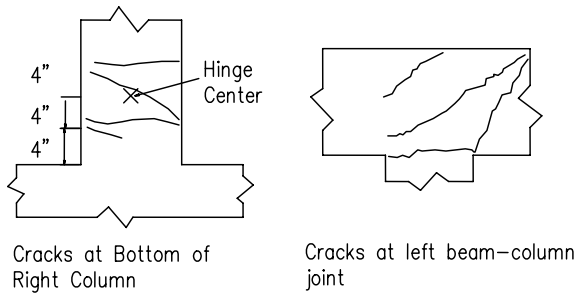


Figure 9. Postfailure crack patterns.

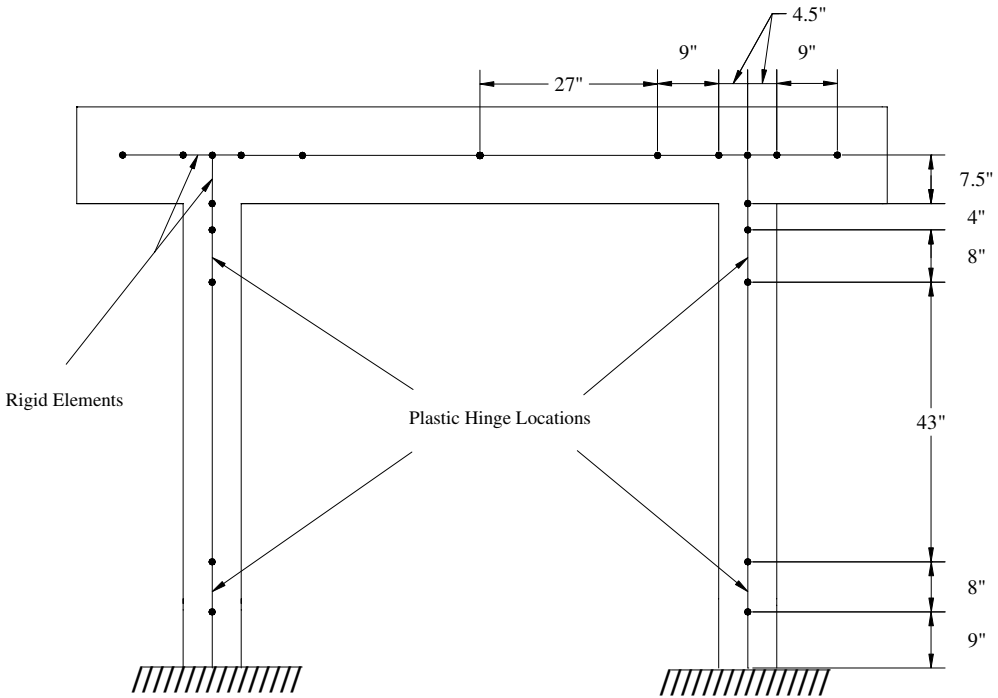


Figure 10. DRAIN-3DX model of the pier.

Results from MDOF analysis. The nonlinear static analysis of the test pier under lateral load was carried out under increasing displacements up a lateral drift ratio of 6%. Figure 6 shows the results of the analysis and comparison with experimental data. It is evident that the correlation between the measured and calculated curves was close. The initial stiffness values from the two curves were within 2% of each other. The calculated plastic hinging occurred at the same point marked A through D and presented a clear, sharp yield point. The measured longitudinal bar strains in the plastic hinges showed a more gradual yielding reflecting variation in the axial load between the two columns and perhaps material variability and slight deviation from the planned location of the bars. The postyielding slope of the calculated curves was close to the measured slope except at larger displacements. The difference is attributed to the fact that the analytical model did not include strength degradation effects, whereas in the actual pier there was some degradation of concrete strength at larger displacements. Altogether the correlation between the calculated and measured static lateral load analysis results was close and satisfactory.

To evaluate the performance of the dynamic analytical model in duplicating the measured results, the calculated and measured displacement histories for different shake table earthquake runs were compared. The actual shake table acceleration records were used in the analysis. The input record used in the analysis was the compilation of all the earthquake simulations that had been applied to the test model, spliced to ensure that the accumulated damaging effects of different earthquakes were accounted for. Intermittent free vibration tests of the pier were not included in the input motion because they are of very small amplitudes having negligible effect. The free vibration tests had shown that the effective damping ratio was 2%. However, the damping ratio typically assumed for reinforced concrete (RC) structures is 5%. The analysis of the pier was conducted for both 2% and 5% damping ratios and the results were compared with the measured displacement histories.

Figures 11 and 12 show sample results comparing the calculated and measured displacement histories for $1 \times$ Sylmar and $1.75 \times$ Sylmar motions, respectively. The former corresponds to a relatively small level of nonlinearity at 2% maximum drift and the other is associated with a relatively high nonlinearity at 4.4% maximum drift. A reasonably close agreement can be observed between the measured and calculated results for both damping ratios in both figures in terms of the waveforms and amplitudes. For both earthquakes the calculated results for 2% damping showed better correlation with the test data than the results with 5% damping did. The damping ratio of the test pier was lower than the ratio normally

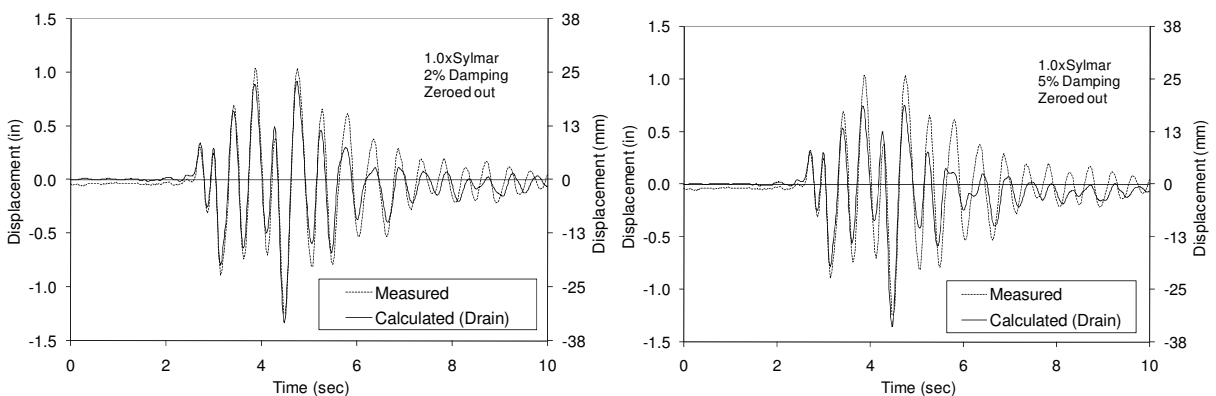


Figure 11. Measured and DRAIN-3DX results for 2% and 5% damping under $1 \times$ Sylmar.

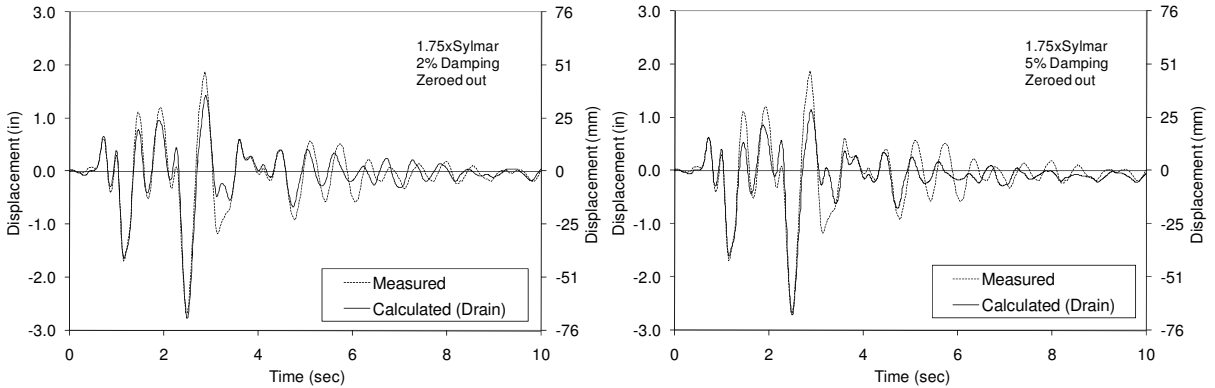


Figure 12. Measured and DRAIN-3DX results for 2% and 5% damping under $1.75 \times$ Sylmar.

attributed to RC structures because the test pier did not include any nonstructural members that usually add to the overall damping of structures. Under $1 \times$ Sylmar the calculated peak displacements were lower than the measured displacements by 6.9% and 8.4% for the 2% and 5% damping analyses, respectively. The differences for the $1.75 \times$ Sylmar motion were lower at 3.6% and 1.4% for the 2% and 5% damping analyses, respectively.

SDOF modeling. The SDOF idealization of the test pier was carried out using the program RC-Shake [Saïidi 1982]. This is a computer program that calculates the dynamic response of a structure modeled as a SDOF nonlinear system, considering both hysteretic and viscous damping, as well as the loading setup of the mass rig system used in shake table testing. A degrading stiffness hysteresis model, called Q-hyst, characterizes the nonlinear load-deformation response [Saïidi 1982]. The input to the program requires a bilinear load-displacement relationship. The calculated nonlinear static analysis results obtained from DRAIN-3DX were used for this purpose. Because Q-hyst operates on a bilinear force-displacement relationship, it assumes that the system is already cracked. As a result the results from RC-Shake do not represent the low-amplitude, uncracked response of the structure. The output of the program provides the force and displacement histories of the SDOF system.

Results from SDOF analysis. RC-Shake was used to analyze the pier subjected to the measured acceleration histories collected during shake table tests. The acceleration records for all the earthquake simulation runs were spliced and used in the analysis. Response histories were calculated for both 2% and 5% damping. The results for $1 \times$ Sylmar and $1.75 \times$ Sylmar are shown in the next two figures. Figure 13 shows that the correlation between the measured and calculated results was excellent. The results for the 2% damping ratio were slightly better in duplicating the amplitudes in the second half of the response indicating that the 5% damping ratio overestimated the actual viscous damping. Under $1 \times$ Sylmar the calculated peak displacements were lower than the measured displacements by 8.1% and 7.1% for the 2% and 5% damping analyses, respectively. Comparing Figures 13 and 11 reveals that the correlation between the RC-Shake results and the measured data was better than that between the DRAIN-3DX results and the measured displacements. The correlation between the calculated and measured results for $1.75 \times$ Sylmar was also close, although the peak displacements were overestimated by 26% and 13% for the 2% and 5% damping, respectively (see Figure 14). In Figure 14 it can be observed that the calculated

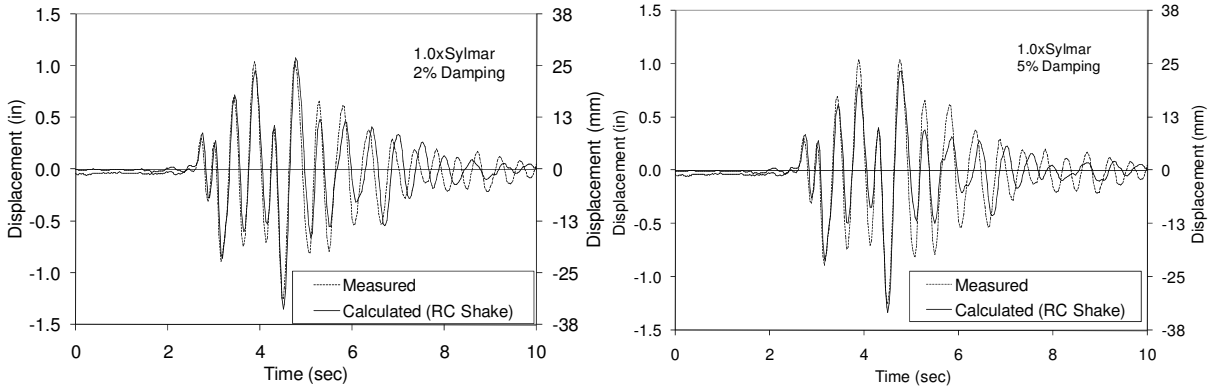


Figure 13. Measured and RC-shake results for 2% and 5% damping under $1 \times$ Sylmar.

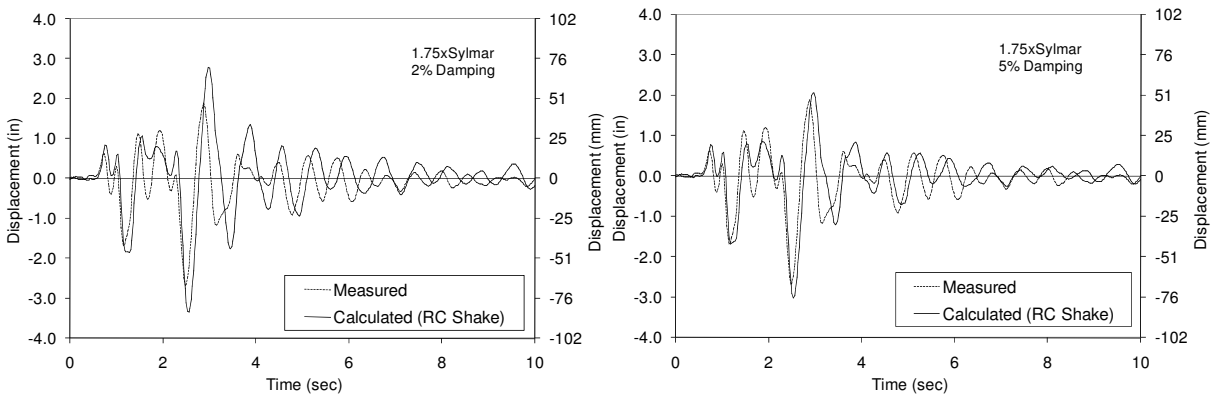


Figure 14. Measured and RC-shake results for 2% and 5% damping under $1.75 \times$ Sylmar.

results for the 5% damping correlated better with the measured data than those for the 2% damping did. Review of Figures 14 and 12 shows that the performance of the SDOF model was comparable to that of the MDOF model.

6. Conclusions

The exploratory study presented in this article showed the feasibility of using carbon fiber laminate in combination with concrete for eventual application in highway bridge piers in which durability is of concern, and where steel reinforcement congestion is a problem. The measured shake table test data indicated that the target behavior was achieved with respect to shifting of the plastic hinge locations, linear response of members outside the plastic hinges, and the effectiveness of CFRP fabrics in keeping the bent cap and the joints damage free.

Comparison of the analytical and experimental results indicates that familiar constitutive relationships may be used to estimate the strength of concrete-carbon fiber laminate sections. However it should be noted that the computations are somewhat more involved than conventional structural engineering analyses.

Both the MDOF and the SDOF nonlinear response history analytical models with stiffness degradation led to a reasonably close agreement with the test data particularly when 2% viscous damping ratio was used. For the relatively simple, two-column test pier in which the fundamental mode essentially controlled the response no particular improvement of the response was evident when the MDOF model was used instead of the SDOF model.

Acknowledgements. The study presented in this article was funded by the National Science Foundation Grant CMS 980080. The support is gratefully acknowledged. The assistance of Dr. Nathan Johnson and Dr. Patrick Laplace in the experimental phase of the study is appreciated.

References

- [Abdel-Fattah and Wight 1987] B. Abdel-Fattah and J. K. Wight, “Study of moving beam plastic hinging zones for earthquake-resistant design of reinforced concrete buildings”, *ACI Struct. J.* **84**:1 (1987), 31–39.
- [Galunic et al. 1977] B. Galunic, V. V. Bertero, and E. P. Popov, “An approach for improving seismic behavior of reinforced concrete interior joints”, Technical Report UCB/EERC-77/30, Earthquake Engineering Research Center, University of California, Berkeley, CA, 1977, Available at <http://nisee.berkeley.edu/elibrary/Text/81001486>.
- [Mirmiran et al. 2000] A. Mirmiran, M. Shahawy, C. El Khoury, and W. Naguib, “Large beam-column tests on concrete-filled composite tubes”, *ACI Struct. J.* **97**:2 (2000), 268–276.
- [Moustafa et al. 2004] K. Moustafa, D. Sanders, and M. Saiidi, “Impact of aspect ratio on two-column bent seismic performance”, Technical Report CCEER-04-3, Center for Civil Engineering Earthquake Research, Department of Civil Engineering, University of Nevada, Reno, NV, February 2004.
- [Prakash et al. 1994] V. Prakash, G. H. Powell, and S. D. Campbell, *DRAIN-3DX: base program description and user guide*, Version 1.10, Department of Civil Engineering, Univ. of California, Berkeley, CA, 1994, Available at <http://nisee.berkeley.edu/elibrary/Text/300016>.
- [Reinhardt et al. 2003] E. Reinhardt, M. Saiidi, and R. Siddharthan, “Seismic performance of a CFRP/concrete bridge bent on flexible footings”, Technical Report CCEER-03-4, Civil Engineering Department, University of Nevada, Reno, NV, August 2003.
- [Saiidi 1982] M. Saiidi, “Hysteresis models for reinforced concrete”, *J. Struct. Div. (ASCE)* **108**:5 (1982), 1077–1087.
- [Saiidi et al. 1994] M. Saiidi, F. Gordaninejad, and N. Wehbe, “Behavior of graphite/epoxy concrete composite beams”, *J. Struct. Eng. (ASCE)* **120**:10 (1994), 2958–2976.
- [Saiidi et al. 2002] M. Saiidi, B. Gopalakrishnan, and R. Siddharthan, “Shake table studies of effects of foundation flexibility on seismic demand in substandard bridge piers”, pp. 553–570 in *Innovations in design with emphasis on seismic, wind, and environmental loading: quality control and innovations in materials/hot-weather concreting* (Cancún, 2002), edited by V. M. Malhotra, ACI Special Publication **209**, American Concrete Institute, Farmington Hills, MI, 2002. Report No. SP-209-30.
- [Teng et al. 2001] J. G. Teng, J. F. Chen, S. T. Smith, and L. Lam, *FRP-strengthened RC structures*, Wiley, Chichester, 2001.

Received 8 Mar 2009. Revised 16 May 2009. Accepted 17 May 2009.

M. SAIID SAIIDI: saiidi@unr.edu

Department of Civil and Environmental Engineering, University of Nevada, Reno, NV 89557, United States

ERIK REINHARDT: ereinhardt22@yahoo.com

Halcrow-Yolles Structural Engineers, 5550 W Flamingo Road, Las Vegas, NV 89103, United States

FARAMARZ GORDANINEJAD: faramarz@unr.edu

Department of Mechanical Engineering (MS 312), University of Nevada, Reno, NV 89557, United States

NONLINEAR BENDING RESPONSE OF GIANT MAGNETOSTRICTIVE LAMINATED ACTUATORS IN MAGNETIC FIELDS

YASUhide SHINDO, FUMIO NARITA, KOTARO MORI AND TASUKU NAKAMURA

We report numerical and experimental investigations into the nonlinear bending behavior of magnetostrictive laminated actuators under magnetic fields. Magnetostrictive actuators were fabricated from thin layers of Terfenol-D and metal, and the magnetostriction of the devices was measured. A nonlinear finite element analysis was employed to evaluate the contribution of magnetic domain switching to the second-order magnetoelastic constants in the Terfenol-D layer. The effect of a magnetic field on the nonlinear deflection and internal stress of magnetostrictive laminated actuators is discussed.

1. Introduction

Smart materials, such as piezoelectric, magnetostrictive, and electrostrictive structures, are currently under intense investigation due to their ability to efficiently interconvert magnetic, electrical, and mechanical energies. Terfenol-D ($\text{Tb}_{0.3}\text{Dy}_{0.7}\text{Fe}_{1.9}$) is a highly magnetostrictive alloy of iron and the rare-earth metals [Moffett et al. 1991] terbium and dysprosium that stands out among smart materials in its ability to produce large actuation forces [Ryu et al. 2001]. An additional advantage of Terfenol-D over other smart materials is that it can be easily deposited onto nonmagnetic substrates. Recent work [Jia et al. 2006] has investigated applications of magnetostrictive materials as active actuators in layered bimorph structures. One limitation on the practical use of Terfenol-D is its nonlinear behavior [Wan et al. 2003]. Additionally, the tools available for modeling and design of magnetostrictive layered structures have not been sufficiently developed. To optimize the performance of magnetostrictive actuators, a detailed study into the nonlinear behavior of devices, especially under magnetic field driving, is necessary.

In this work, we report on the nonlinear bending behavior of magnetostrictive laminated actuators under magnetic fields in a combined numerical and experimental investigation. The fabricated magnetostrictive actuators consist of thin Terfenol-D and metal layers, and the magnetostriction of specimen devices was measured as a function of applied magnetic field strength. A nonlinear finite element analysis was also performed, and the contribution of magnetic domain switching to the second-order magnetoelastic constant in the Terfenol-D layer was evaluated. The effect of magnetic field strength on nonlinear deflection and internal stress for the magnetostrictive laminated actuators is examined.

Keywords: finite element method, material testing, giant magnetostrictive material, nonlinear bending.

This work was partially supported by the Grant-in-Aid for Exploratory Research from the Ministry of Education, Culture, Sports, Science and Technology, Japan.

2. Analysis

Basic equations. In the rectangular Cartesian coordinate system, x_1, x_2, x_3 , the equations for magnetoelastic materials are

$$\begin{aligned} \sigma_{ji,j} = 0, & \quad H_i = \phi_{,i}, & \quad \varepsilon_{ij} = s_{ijkl}\sigma_{kl} + d'_{kij}H_k, \\ B_{i,i} = 0, & \quad B_i = d'_{ikl}\sigma_{kl} + \mu_{ik}H_k, & \quad \varepsilon_{ij} = \frac{1}{2}(u_{j,i} + u_{i,j}), \end{aligned}$$

where σ_{ij} , B_i , ε_{ij} , and H_i are the stress tensor, magnetic induction vector, strain tensor, and magnetic field intensity vector; u_i and ϕ are the displacement and magnetic potential; and s_{ijkl} , d'_{kij} , and μ_{ij} are the elastic compliance, magnetoelastic constant and magnetic permittivity. A comma followed by an index denotes partial differentiation with respect to the space coordinate x_i . We invoke the summation convention for repeated tensor indices. Valid symmetry conditions for the material constants are

$$s_{ijkl} = s_{jikl} = s_{ijlk} = s_{klij}, \quad d'_{kij} = d'_{kji}, \quad \mu_{ij} = \mu_{ji}.$$

For Terfenol-D, the constitutive relations can be written as

$$\begin{aligned} \begin{Bmatrix} \varepsilon_1 \\ \varepsilon_2 \\ \varepsilon_3 \\ \varepsilon_4 \\ \varepsilon_5 \\ \varepsilon_6 \end{Bmatrix} &= \begin{bmatrix} s_{11} & s_{12} & s_{13} & 0 & 0 & 0 \\ s_{12} & s_{11} & s_{13} & 0 & 0 & 0 \\ s_{13} & s_{13} & s_{33} & 0 & 0 & 0 \\ 0 & 0 & 0 & s_{44} & 0 & 0 \\ 0 & 0 & 0 & 0 & s_{44} & 0 \\ 0 & 0 & 0 & 0 & 0 & s_{66} \end{bmatrix} \begin{Bmatrix} \sigma_1 \\ \sigma_2 \\ \sigma_3 \\ \sigma_4 \\ \sigma_5 \\ \sigma_6 \end{Bmatrix} + \begin{bmatrix} 0 & 0 & d'_{31} \\ 0 & 0 & d'_{31} \\ 0 & 0 & d'_{33} \\ 0 & d'_{15} & 0 \\ d'_{15} & 0 & 0 \\ 0 & 0 & 0 \end{bmatrix} \begin{Bmatrix} H_1 \\ H_2 \\ H_3 \end{Bmatrix}, \\ \begin{Bmatrix} D_1 \\ D_2 \\ D_3 \end{Bmatrix} &= \begin{bmatrix} 0 & 0 & 0 & 0 & d_{15} & 0 \\ 0 & 0 & 0 & d_{15} & 0 & 0 \\ d_{31} & d_{31} & d_{33} & 0 & 0 & 0 \end{bmatrix} \begin{Bmatrix} \sigma_1 \\ \sigma_2 \\ \sigma_3 \\ \sigma_4 \\ \sigma_5 \\ \sigma_6 \end{Bmatrix} + \begin{bmatrix} \mu_{11} & 0 & 0 \\ 0 & \mu_{11} & 0 \\ 0 & 0 & \mu_{33} \end{bmatrix} \begin{Bmatrix} H_1 \\ H_2 \\ H_3 \end{Bmatrix}, \end{aligned}$$

where

$$\begin{aligned} \sigma_1 = \sigma_{11}, & \quad \sigma_2 = \sigma_{22}, & \quad \sigma_3 = \sigma_{33} \\ \sigma_4 = \sigma_{23} = \sigma_{32}, & \quad \sigma_5 = \sigma_{31} = \sigma_{13}, & \quad \sigma_6 = \sigma_{12} = \sigma_{21}, \\ \varepsilon_1 = \varepsilon_{11}, & \quad \varepsilon_2 = \varepsilon_{22}, & \quad \varepsilon_3 = \varepsilon_{33}, \\ \varepsilon_4 = 2\varepsilon_{23} = 2\varepsilon_{32}, & \quad \varepsilon_5 = 2\varepsilon_{31} = 2\varepsilon_{13}, & \quad \varepsilon_6 = 2\varepsilon_{12} = 2\varepsilon_{21}, \\ s_{11} = s_{1111} = s_{2222}, & \quad s_{12} = s_{1122}, & \quad s_{13} = s_{1133} = s_{2233}, \\ s_{33} = s_{3333}, & \quad s_{44} = 4s_{2323} = 4s_{3131}, & \quad s_{66} = 4s_{1212} = 2(s_{11} - s_{12}), \\ d'_{15} = 2d'_{131} = 2d'_{223}, & \quad d'_{31} = d'_{311} = d'_{322}, & \quad d'_{33} = d'_{333}. \end{aligned}$$

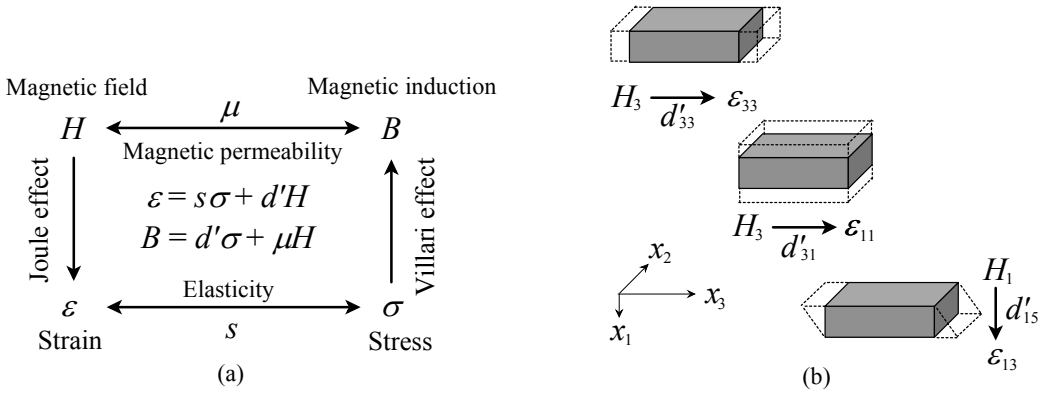


Figure 1. Magnetostrictive effect. (a) Mathematical relationships, (b) Various deformation modes.

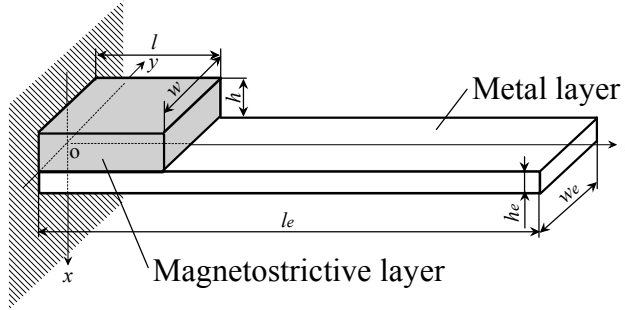


Figure 2. A magnetostrictive laminated actuator.

Figure 1(a) shows several physical effects related to the magnetostrictive effect [Yamamoto et al. 1999]. When a magnetic field is applied along the x_3 -direction (easy axis) of the magnetostrictive material, both the longitudinal (33) and transverse (31) magnetostrictive deformation modes are excited, as shown in Figure 1(b). When a magnetic field is applied along the x_1 -direction, the shear mode (15) is excited.

Finite element model. A magnetostrictive laminated plate is shown in Figure 2, in which a magnetostrictive layer of length l , width w , and thickness h is perfectly bonded on the top surface of a metal layer of length l_e , width $w_e = w$, and thickness h_e . The subscript e corresponds to the elastic layer. Dimensions $h(h_e)$, $w(w_e)$, and $l(l_e)$ are measured along the $x_1 = x$, $x_2 = y$, and $x_3 = z$ axis, respectively. The easy axis for magnetization of the magnetostrictive layer is the z -direction. The origin of the coordinate system is located at bottom left side of the magnetostrictive layer. The laminated plate is cantilevered, with $z = 0$ denoting the clamped end.

The laminated plate is subjected to a uniform magnetic field of magnetic induction $B_x = B_0$ or $B_z = B_0$. The constitutive relations of Terfenol-D layer are

$$\begin{aligned} \epsilon_{xx} &= s_{11}\sigma_{xx} + s_{12}\sigma_{yy} + s_{13}\sigma_{zz} + d'_{31}H_z, & \epsilon_{yz} &= (s_{44}/2)\sigma_{yz} + (d'_{15}/2)H_y, \\ \epsilon_{yy} &= s_{12}\sigma_{xx} + s_{11}\sigma_{yy} + s_{13}\sigma_{zz} + d'_{31}H_z, & \epsilon_{zx} &= (s_{44}/2)\sigma_{zx} + (d'_{15}/2)H_x, \\ \epsilon_{zz} &= s_{13}\sigma_{xx} + s_{13}\sigma_{yy} + s_{33}\sigma_{zz} + d'_{33}H_z, & \epsilon_{xy} &= (s_{66}/2)\sigma_{xy}, \\ B_x &= d'_{15}\sigma_{zx} + \mu_{11}H_x, & B_y &= d'_{15}\sigma_{yz} + \mu_{11}H_y, & B_z &= d'_{31}\sigma_{xx} + d'_{31}\sigma_{yy} + d'_{33}\sigma_{zz} + \mu_{33}H_z. \end{aligned}$$

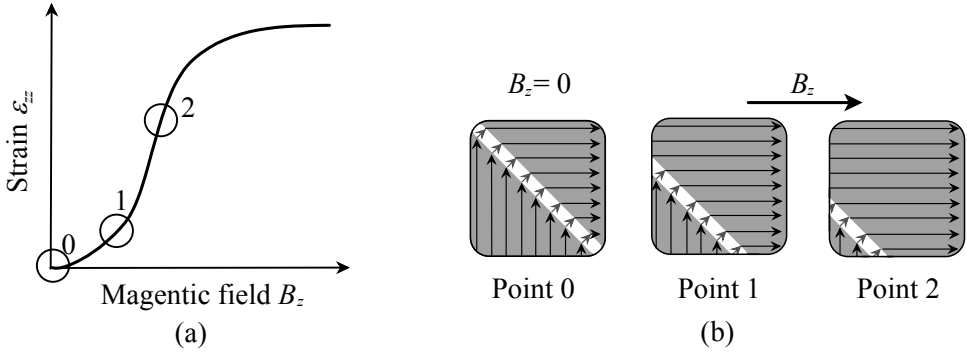


Figure 3. Schematic diagram of (a) strain versus magnetic field, and (b) domain structure.

Nonlinearity in the relationship between magnetostriction and magnetic field strength arises from movement of magnetic domain walls. The constants d'_{15} , d'_{31} , and d'_{33} for the Terfenol-D layer under $B_x = B_0$ become

$$d'_{15} = d_{15} + m_{15}H_x, \quad d'_{31} = d_{31}, \quad d'_{33} = d_{33}, \quad (1)$$

where d_{15} , d_{31} , d_{33} are the piezomagnetic constants and m_{15} is the second-order magnetoelastic constant. The constants d'_{15} , d'_{31} , and d'_{33} for the Terfenol-D layer under $B_z = B_0$ are

$$d'_{15} = d_{15}, \quad d'_{31} = d_{31}, \quad d'_{33} = d_{33} + m_{33}H_z, \quad (2)$$

where m_{33} is the second-order magnetoelastic constant. Figure 3 shows the relationship between magnetostriction (ϵ_{zz}) and magnetic field (B_z) strength along with the associated domain structure. A magnetic domain switching associated with 90° domain wall rotation gives rise to the nonlinear changes in magnetoelastic constants.

We performed finite element calculations to obtain the strain, deflection, and internal stresses for the magnetostrictive laminated plates. The equations describing magnetostrictive materials are mathematically equivalent to those describing piezoelectric materials [Tiersten 1969]. Therefore, coupled-field solid elements in ANSYS were used for the analysis. From (1) and (2) we see that the magnetoelastic constants d'_{15} , d'_{33} vary with the magnetic field due to domain wall movement. Making use of magnetic field-dependent material properties, the model calculated the nonlinear behavior.

Elastic stiffnesses ($\times 10^{-12} \text{m}^2/\text{N}$)					Piezo-magnetic constants ($\times 10^{-9} \text{m}/\text{A}$)			Magnetic permittivities ($\times 10^{-6} \text{H}/\text{m}$)	
s_{11}	s_{33}	s_{44}	s_{12}	s_{13}	d_{31}	d_{33}	d_{15}	μ_{11}	μ_{33}
17.9	17.9	26.3	-5.88	-5.88	-5.3	11	28	6.29	6.29

Table 1. Material properties of Terfenol-D.

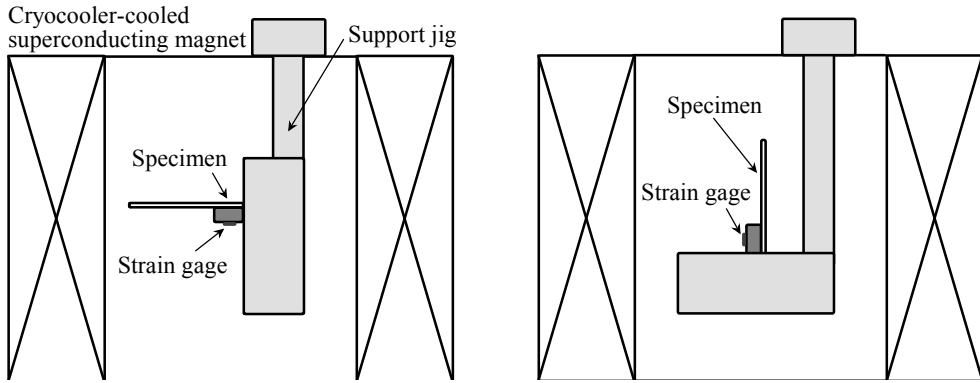


Figure 4. Experimental set-up of macroscopic strain measurement under magnetic fields normal (left) and parallel (right) to the easy axis. The magnetic field is in the vertical direction.

3. Experimental procedure

Magnetostrictive laminated actuators were prepared using Terfenol-D (ETREMA Products, Inc., USA) of $l = w = 10$ mm and SUS316 of $l_e = 40$ mm, $w_e = 10$ mm, and $h_e = 0.5$ mm. The thickness of Terfenol-D was $h = 1, 3,$ and 5 mm. Table 1 shows the material properties of Terfenol-D [Engdahl 2000; Nan et al. 2001]. The Young's modulus E and Poisson's ratio ν of SUS316 are $E = 189$ GPa and $\nu = 0.3$, respectively. We also consider the magnetostrictive laminated actuators (small size) using Terfenol-D of $l = w = 5$ mm and metal layer (SUS316, Cu or Al) of $l_e = 20$ mm, $w_e = 5$ mm, and $h_e = 0.5$ mm. The thickness of Terfenol-D is $h = 0.5$ mm. The Young's modulus E and Poisson's ratio ν of copper are $E = 130$ GPa and $\nu = 0.34$, while for aluminum they are $E = 70.3$ GPa and $\nu = 0.345$.

A strain gage was placed at the surface ($x = -h$, $y = 0$, $z = l/2$) of Terfenol-D. The magnetic field was then applied in the x - or z - direction, and the magnetostriction was evaluated. A cryocooler-cooled superconducting magnet with a 100 mm diameter working bore was used to create a static uniform magnetic field of magnetic induction B_0 . A schematic diagram of the experimental set-up used to measure the macroscopic strain is shown in Figure 4. The magnetic field is applied vertically with respect to the apparatus orientation shown in the figure.

4. Results and discussion

We first present results for the magnetostrictive laminated actuators using Terfenol-D ($l = w = 10$ mm) and SUS316 ($l_e = 40$ mm, $w_e = 10$ mm, $h_e = 0.5$ mm). Figure 5 shows the strain ε_{zz} at $x = -1$ mm, $y = 0$ mm, and $z = 5$ mm versus applied magnetic field $B_z = B_0$ for the magnetostrictive laminated actuator with $h = 1$ mm. Solid circles denote experimental data. The dashed line represents the values of strain predicted by the linear finite element analysis (FEA) and the solid line represents the strain after the second-order magnetoelastic constants have been considered. The constant $m_{33} = 1.4 \times 10^{-11}$ m²/A² is obtained, and agreement between nonlinear FEA and experiment is fair. Figure 6 shows similar results for the magnetostrictive laminated actuators with $h = 3$ and 5 mm, respectively. The constants m_{33} of

Terfenol-D layer with $h = 3$ and 5 mm are 4.4×10^{-12} and $1.1 \times 10^{-12} \text{ m}^2/\text{A}^2$, respectively. The second-order magnetoelastic constant m_{33} decreases as the thickness of the magnetostrictive layers increases.

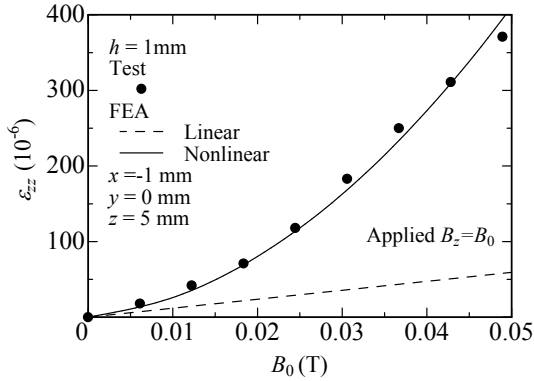


Figure 5. Strain versus magnetic field in the z -direction for $h = 1$ mm. Dashed line: values of strain predicted by the linear finite element analysis. Solid line: strain after second-order magnetoelastic constants have been considered.

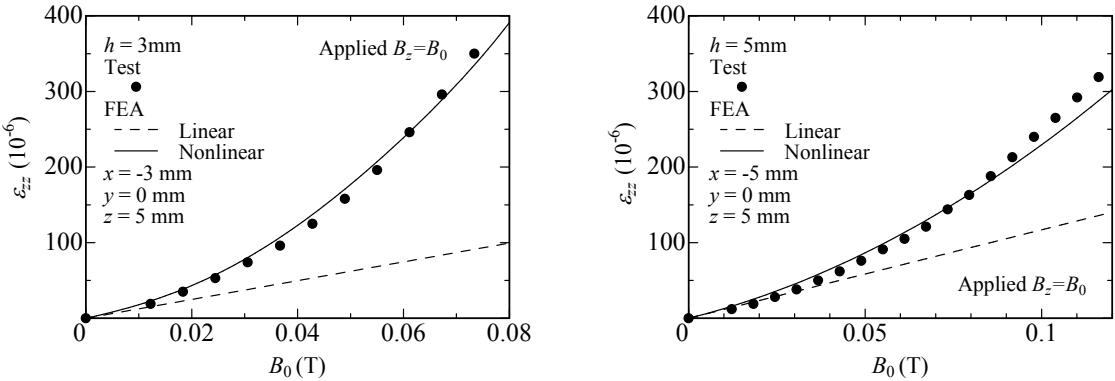


Figure 6. Strain versus magnetic field in the z -direction for $h = 3$ mm (left) and $h = 5$ mm (right).

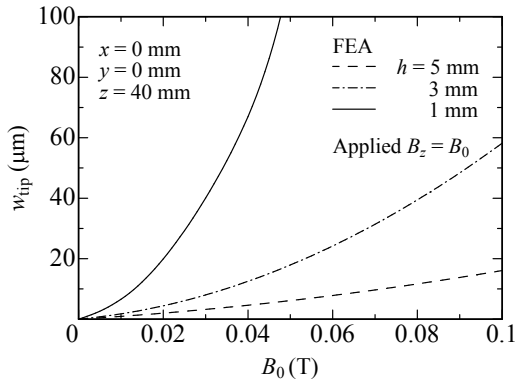


Figure 7. Tip deflection versus magnetic field in the z -direction for $h = 1, 3, 5$ mm.

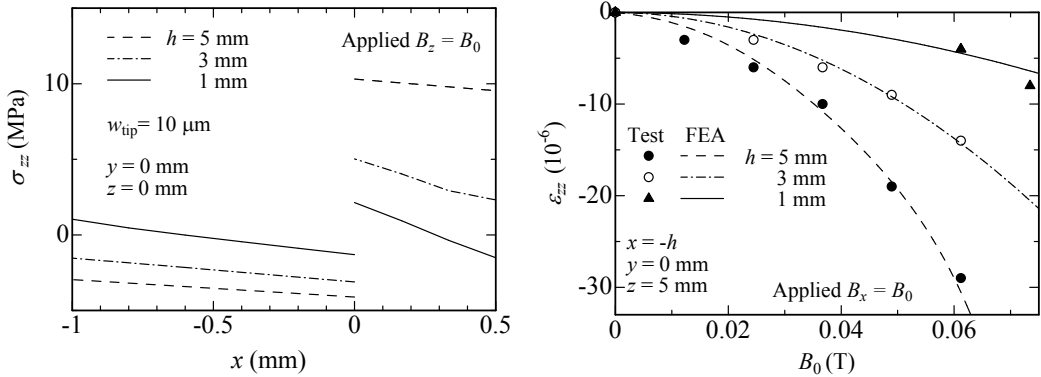


Figure 8. Left: normal stress distribution along the thickness direction at $y, z = 0$ for $h = 1, 3, 5$ mm. Right: Strain versus magnetic field in the x -direction for $h = 1, 3, 5$ mm.

Figure 7 shows the tip deflection w_{tip} at $x = 0$ mm, $y = 0$ mm, and $z = 40$ mm versus applied magnetic field $B_z = B_0$ for the magnetostrictive laminated actuators with $h = 1, 3,$ and 5 mm. A nonlinear relationship between tip deflection and magnetic field is observed. The tip deflection increases as the thickness of the magnetostrictive layers decreases.

The variations of normal stress σ_{zz} along the thickness direction are calculated for the magnetostrictive laminated actuators at a chosen point ($y = 0$ mm and $z = 0$ mm here), and the results are shown in Figure 8, left. All calculations were done at a fixed tip deflection of $10 \mu\text{m}$. The applied magnetic fields in the z -direction of the Terfenol-D layer under $w_{tip} = 10 \mu\text{m}$ are $0.074, 0.036, 0.014$ T for $h = 5, 3, 1$ mm, respectively. Some stress gaps are present at the interface between Terfenol-D and SUS316 layers, as is expected. At smaller Terfenol-D thickness, lower normal stress is found for the same deflection. Also, a $10 \mu\text{m}$ deflection is produced at lower magnetic field.

Figure 8, right, shows strain ϵ_{zz} at $x = -h$ mm, $y = 0$ mm and $z = 5$ mm as a function of applied magnetic field $B_x = B_0$ for the magnetostrictive laminated actuators with $h = 1, 3, 5$ mm. The constants m_{15} of Terfenol-D layer with $h = 1, 3,$ and 5 mm are $1.5 \times 10^{-10}, 9.3 \times 10^{-11},$ and $3.7 \times 10^{-11} \text{ m}^2/\text{A}^2$, respectively. The second-order magnetoelastic constant m_{15} decreases with an increase of the thickness of the magnetostrictive layers. By increasing the magnetostrictive layer thickness, the compressive strain of the Terfenol-D layer subjected to a magnetic field in the x -direction is raised. The tip deflection is also raised by increasing the thickness of the magnetostrictive layers (no figure shown), in contrast to the magnetostrictive laminated actuators subjected to a magnetic field in the z -direction. The tip deflection of the magnetostrictive laminated actuators under $B_z = B_0$ is much smaller than that under $B_x = B_0$.

Next, the bending behavior of the magnetostrictive laminated actuators (small size) using Terfenol-D ($l = w = 5$ mm, $h = 0.5$ mm) and a metal layer ($l_e = 20$ mm, $w_e = 5$ mm, $h_e = 0.5$ mm) is discussed. Figure 9, left, shows the plots of the strain ϵ_{zz} at $x = -0.5$ mm, $y = 0$ mm, and $z = 2.5$ mm against the applied magnetic field $B_z = B_0$ for the magnetostrictive laminated actuators of different elastic layers. Similar to the previous report [Jia et al. 2006], the second-order magnetoelastic constant depends on the elastic layers, and m_{33} of the Terfenol-D layer with SUS316, Cu, and Al are $9.9 \times 10^{-12}, 1.7 \times 10^{-11},$ and $7.4 \times 10^{-12} \text{ m}^2/\text{A}^2$, respectively. Figure 9, right, shows the corresponding tip deflection. The largest tip deflection is noted for the magnetostrictive laminated actuator with Cu. Figure 10 plots the variations

of normal stress σ_{xx} along the thickness direction at $y = 0$ mm and $z = 0$ mm for the magnetostrictive laminated actuators of different elastic layers under a fixed tip deflection of $10 \mu\text{m}$. The applied magnetic fields in the z -direction of the Terfenol-D layer under $w_{\text{tip}} = 10 \mu\text{m}$ are 0.029, 0.022, 0.030 T for the actuators with SUS316, Cu, and Al, respectively. The stress gap under a constant tip deflection depends on the elastic layers.

5. Conclusions

Three-dimensional finite element analysis, in which the nonlinearity of Terfenol-D (the effect of magnetic domain switching) is incorporated into the model, is presented for magnetostrictive laminated actuators. The magnetostriction is also evaluated. We demonstrate that the mathematical procedure for this analysis is straightforward, and yields accurate values for the strain, as a function of magnetic field strength, present in the magnetostrictive laminated actuators. We find that the second-order magnetoelastic constants depend on the magnetostrictive layer thickness and elastic substrates, and that when a magnetic field is applied in the length direction, the tip deflection increases and the internal stress decreases with decreasing magnetostrictive layer thickness.

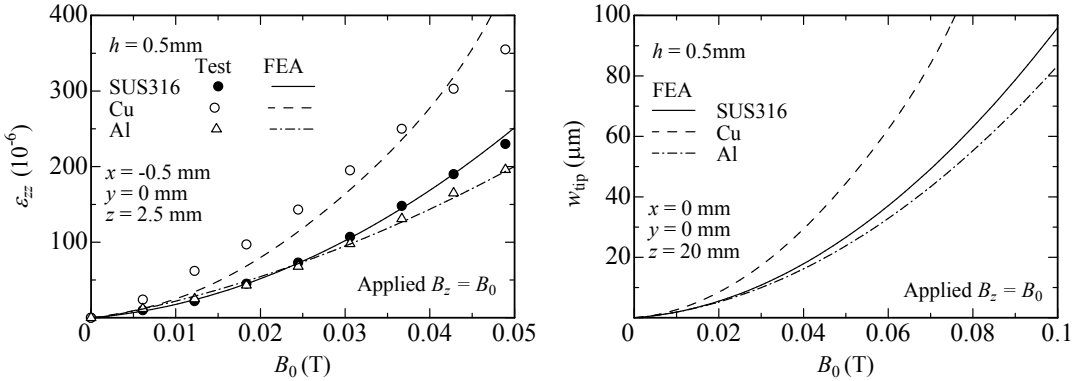


Figure 9. Strain (left) and tip deflection (right) versus magnetic field in the z -direction for different elastic layers.

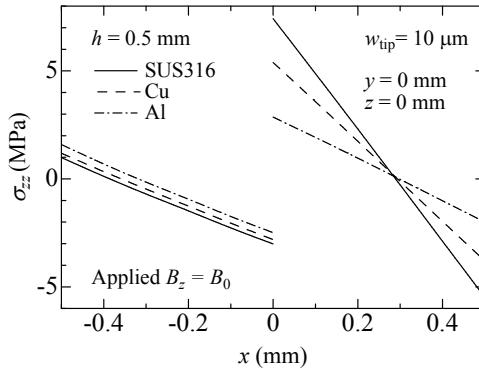


Figure 10. Normal stress distribution along the thickness direction at $y = 0$ and $z = 0$ mm for different elastic layers.

The present analysis can be applied to magnetostrictive laminated actuators with a wide range of magnetostrictive material and geometric properties. This study is also useful in designing magnetostrictive laminated devices and in reducing the problem of delamination that frequently occurs during service.

References

- [Engdahl 2000] G. Engdahl (editor), *Handbook of giant magnetostrictive materials*, Academic Press, San Diego, CA, 2000.
- [Jia et al. 2006] Z. Jia, W. Liu, Y. Zhang, F. Wang, and D. Guo, “A nonlinear magnetomechanical coupling model of giant magnetostrictive thin films at low magnetic fields”, *Sens. Actuators A Phys.* **128**:1 (2006), 158–164.
- [Moffett et al. 1991] M. B. Moffett, A. E. Clark, M. Wun-Fogle, J. Linberg, T. P. Teter, and E. A. McLaughlin, “Characterization of Terfenol-D for magnetostrictive transducers”, *J. Acoust. Soc. Am.* **89**:3 (1991), 1448–1455.
- [Nan et al. 2001] C. W. Nan, M. Li, and J. H. Huang, “Calculations of giant magnetoelectric effects in ferroic composites of rare-earth-iron alloys and ferroelectric polymers”, *Phys. Rev. B* **63**:14 (2001), #144415.
- [Ryu et al. 2001] J. Ryu, S. Priya, A. V. Carazo, K. Uchino, and H.-E. Kim, “Effect of the magnetostrictive layer on magneto-electric properties in lead zirconate titanate/Terfenol-D laminate composites”, *J. Am. Ceram. Soc.* **84**:12 (2001), 2905–2908.
- [Tiersten 1969] H. F. Tiersten, *Linear piezoelectric plate vibrations: elements of the linear theory of piezoelectricity and the vibrations of piezoelectric plates*, Plenum, New York, 1969.
- [Wan et al. 2003] Y. Wan, D. Fang, and K.-C. Hwang, “Non-linear constitutive relations for magnetostrictive materials”, *Int. J. Non-Linear Mech.* **38**:7 (2003), 1053–1065.
- [Yamamoto et al. 1999] Y. Yamamoto, H. Eda, and J. Shimizu, “Application of giant magnetostrictive materials to positioning actuators”, pp. 215–220 in *1999 IEEE/ASME International Conference on Advanced Intelligent Mechatronics proceedings : AIM '99* (Atlanta, GA, 1999), IEEE, Piscataway, NJ, 1999.

Received 8 Apr 2008. Revised 2 Dec 2008. Accepted 17 May 2009.

YASUhide SHINDO: shindo@material.tohoku.ac.jp

Tohoku University, Department of Materials Processing, Graduate School of Engineering, Aoba-ku, Sendai 980-8579, Japan

FUMIO NARITA: narita@material.tohoku.ac.jp

Tohoku University, Department of Materials Processing, Graduate School of Engineering, Aoba-ku, Sendai 980-8579, Japan

KOTARO MORI: A8TM5628@stu.material.tohoku.ac.jp

Tohoku University, Department of Materials Processing, Graduate School of Engineering, Aoba-ku, Sendai 980-8579, Japan

TASUKU NAKAMURA: Tohoku University, Department of Materials Processing, Graduate School of Engineering, Aoba-ku, Sendai 980-8579, Japan

A DISPERSIVE NONLOCAL MODEL FOR WAVE PROPAGATION IN PERIODIC COMPOSITES

JUAN MIGUEL VIVAR-PÉREZ, ULRICH GABBERT, HARALD BERGER,
REINALDO RODRÍGUEZ-RAMOS, JULIÁN BRAVO-CASTILLERO,
RAUL GUINOVART-DÍAZ AND FEDERICO J. SABINA

In this paper, the problem of wave propagation in periodic structured composites is studied, and a dispersive asymptotic method for the description of these dynamic processes is proposed. Assuming a single-frequency dependence of the solution for the one dimensional wave equation in a periodic composite material, higher-order terms in the asymptotic expansion for the displacement functions are studied. Nonuniformity is eliminated by finding a suitable regular asymptotic expansion for the perturbation frequency. Only two spatial scales are considered, and the equivalence of this method and the introduction of multiple slow temporal scales is shown, in good agreement with previous approaches. For a selection of boundary problems, analytic solutions are given and graphically illustrated. The problem of failures is also discussed, and some illustrative calculations are presented.

1. Introduction

Due to their importance in industry and their wide range of applications, many attempts have been made to describe the global behavior of composite materials. In elastodynamics, for example, if a traveling signal has scale comparable to the size of the material's heterogeneities, successive wave reflections and refractions take place at the interfaces. Significant wave dispersion then results, leading to distortions of the pulse shape and wave front.

The introduction of multiple scales and the methods of asymptotic homogenization [Bensoussan et al. 1978; Pobedria 1984; Bakhvalov and Panasenko 1989] has been helpful in treating a particularly important problem, the prediction of global or effective properties for composites which small-scale heterogeneities. Asymptotic analysis, as a powerful mathematical tool in dealing with problems involving small parameters, plays a fundamental role in bridging the small and large scales relevant to models of composite materials [Sánchez-Huber and Sánchez-Palencia 1992].

For a composite with periodic structure, these methods involve the dependence on two geometric scales through the expansion of the fields in powers of a small parameter ε , the ratio between the micro and macro scales. These techniques has been successful in providing effective quantities and methods

Keywords: composite materials, wave dispersion, asymptotics, homogenization, wave propagation, bilaminated composite, dynamic asymptotic homogenization.

This work was sponsored by DFG Graduiertenkolleg 828 "Micro-Macro Interactions in Structured Media and Particle Systems" and by CONACYT projects 101489 and 82474. The provisions of the Basic Sciences Program Project CITMA No. 9/2004 and the Department of Basic Science of the Monterrey Institute of Technology, Campus of México State are also acknowledged. The partial support of COIC-STIA-239-08, UNAM is recognized.

for the solution of partial differential equations for static problems in structures such as laminated, fiber-reinforced composites [Guinovart-Díaz et al. 2005], laminated piezocomposites [Castillero et al. 1998], and helical elastic and thermoelastic structures [Vivar-Pérez et al. 2005; 2006].

Approaches other than asymptotics are also available. Wang and Rokhlin [2002a; 2002b] developed a dynamic homogenization method based on Floquet wave theory for treating laminated composites in which the model was restricted to a *homogenization domain* consisting of frequencies and incident angles below certain critical values that depended on the composite. The problem of wave propagation in elastic fluid media with periodic structure is considered in [Santosa and Symes 1991] for cases in which the ratio between cell size and the shortest wavelength of the initial disturbance is small. Within this regime, an effective dispersive medium is obtained using the Bloch expansion. A similar analysis is made in [Sjöberg et al. 2005], in which the solutions to Maxwell's equations in periodic media are expanded in Bloch waves under the limiting condition that the unit cell is small compared to the wavelength.

The classical method of asymptotic homogenization describes the effect of wave dispersion by accounting for the influence of the first and second-order terms on the asymptotic expansion for relatively long wavelengths in fiber reinforced composites [Parnell and Abrahams 2006]. This approach fails when the observation time is relatively long or when the characteristic size of the perturbation is small, i.e., comparable to the representative volume element.

The classical method fails because of nonuniformity that results from the existence of unbounded higher-order terms in the asymptotic expansion. It was shown in [Fish and Chen 2001] that in an initial boundary value problem, whereas higher-order terms are capable of capturing dispersion effects, they introduce secular terms which grow unboundedly with time. Chen and Fish [2001] reported a recent attempt to solve this problem successfully by introducing one or more slow temporal scales, eliminating the problem of nonuniformity that could not be addressed by classical homogenization.

The main objective of this paper is to describe the dispersive behavior of periodic composites by means of time variable asymptotic rescaling, which is a necessary condition for the accurate description of a composite's global behavior. For this purpose, a reformulation of the problem is made in which the slow temporal scale is replaced by a single-frequency time-dependence, and an asymptotic expansion for the main frequencies is assumed to exist. This shows that the time rescaling needed to find the effective law of movement in composites is strongly frequency dependent. As an advantage, there is no need to study the selection of temporal scales, because the model only treats the fast spatial variable and yields closed form general expressions for the coefficients in the global model.

This treatment shows good agreement with the model presented in [Chen and Fish 2001]. We also present an analytical solution for the averaged problem for certain cases, including the situation in which a failure (defect due to the presence of fissures, voids, cracks, etc.) is present in the composite. Results for the asymptotic expansion of eigenfrequencies show that the range of validity of the method is restricted to low frequency wave propagation. The effective model is therefore not accurate for cases in which the initial disturbance has significant high frequency components. In asymptotic language, high frequencies are of order $O(1/\varepsilon)$, where ε is the ratio between the size of the periodic cell and characteristic length of the composite.

This work is the start of a study of wave propagation in composite materials with applications to damage detection and health monitoring for periodic laminated composites. The dispersive method is only considered here for one spatial dimension.

2. Statement of the problem

Our study reduces to a periodic laminated composite of length L , that is, a specimen consisting of a linear periodic repetition of a representative volume element (RVE) (or periodic cell) with characteristic length ε , [Figure 1](#). Our analysis is independent of the number of phases embedded in the RVE, although ε is required to be small compared to the composite length, $\varepsilon \ll L$.

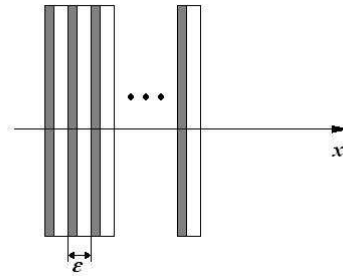


Figure 1. A laminated two-phase periodic composite.

The direction of wave propagation is assumed to be parallel to the x axes, normal to the lamination. If the laminate is considered to be isotropic, the elastodynamic equation is

$$(E_\varepsilon(x)u_x)_x - \rho_\varepsilon(x)u_{tt} = 0. \tag{2.1}$$

Here, $u = u(x, t)$ gives the longitudinal displacement from the equilibrium position at point x and time t , while $E_\varepsilon = E_\varepsilon(x)$ and $\rho_\varepsilon = \rho_\varepsilon(x)$ are the elastic modulus and the mass density at each position. The subscript ε stands for the thickness of the RVE (implying that E_ε and ρ_ε are periodic with period ε), and subscript x, t denote the respective partial derivatives.

If, for this laminated composite, we also consider a displacement $\mu(t)$ at one end $x = 0$, a load $F(t)$ at the other end $x = L$, an initial displacement $U(x)$ from the equilibrium position, and an initial velocity $V(x)$ at each point x , then the initial and boundary conditions for (2.1) are

$$u(0, t) = \mu(t), \quad E_\varepsilon(L)u_x(L, t) = F(t), \quad u(x, 0) = U(x), \quad u_t(x, 0) = V(x). \tag{2.2}$$

Finally, it is necessary to include the contact conditions between the faces of the laminate components. At such interfaces, the coupling conditions must be well determined. Here we will consider ideal contact conditions, where there is no discontinuity in displacement or traction at the interface. If we introduce the notation $\|f\|_\nu = \lim_{x \rightarrow \nu^+} f(x) - \lim_{x \rightarrow \nu^-} f(x)$, the ideal contact conditions are

$$\|u\|_\nu = 0, \quad \|E_\varepsilon u_x\|_\nu = 0, \tag{2.3}$$

for every point $x = \nu$ on the interface. Under these assumptions, we would like to obtain an effective homogeneous model with constant coefficients that can approximate the response of the heterogeneous material under study. This avoids the difficulties of treating rapid variation in the coefficients due to heterogeneities and, at the same time, gives information about the dispersive nature of the laminated composite. This is achieved by first considering a single arbitrary frequency-dependence and then applying asymptotic techniques for multiple scales, which allow us to find a regular asymptotic expansion for the single arbitrary frequency and the displacement function.

3. Frequency dependence and asymptotic analysis

Following the classical methods of separation of variables or Fourier’s method, a solution to (2.1) in the form $u(x, t) = X(x)T(t)$ is sought. After substitution of this product into (2.1), we obtain

$$\frac{(E_\varepsilon(x)X_x(x))_x}{\rho_\varepsilon(x)X(x)} = \frac{T_{tt}(t)}{T(t)} = -\omega_\varepsilon^2, \tag{3.1}$$

where ω_ε is the circular frequency of the longitudinal wave. This is equivalent to a pair of ordinary differential equations for $X(x)$ and $T(t)$ (Sturm–Liouville equations),

$$(E_\varepsilon X_x)_x + \omega_\varepsilon^2 \rho_\varepsilon X = 0, \quad T_{tt} + \omega_\varepsilon^2 T = 0. \tag{3.2}$$

$X(x)$ inherits the interface conditions given in (2.3):

$$\|X\|_v = 0, \quad \|E_\varepsilon X_x\|_v = 0. \tag{3.3}$$

Initial and boundary conditions can be derived from (2.2). Having assumed the periodicity conditions on $E_\varepsilon(x)$ and $\rho_\varepsilon(x)$ stated in the previous section, and considering that the size of the periodic cell ε is small compared to the characteristic length of the composite L , it is convenient to introduce the dependence on a new scale

$$\zeta = x/\varepsilon. \tag{3.4}$$

This is the “fast spatial scale”, widely used for asymptotic analysis in periodic structures [Bensoussan et al. 1978].

We can now express the elastic modulus as $E(\zeta) = E(x/\varepsilon) = E_\varepsilon(x)$ and the mass density as $\rho(\zeta) = \rho(x/\varepsilon) = \rho_\varepsilon(x)$. Note that $E(\zeta)$ and $\rho(\zeta)$ are 1-periodic (periodic with period 1), regardless of the value of ε , due to the periodic structure of the composite under consideration. The dependence of X on ζ , $X = X(x, \zeta)$, now yields, from (3.2)₁,

$$(E(\zeta)X_x(x, \zeta))_x + \omega_\varepsilon^2 \rho(\zeta)X(x, \zeta) = 0. \tag{3.5}$$

Taking regular asymptotic expansions of the principal frequency of the perturbation and $X(x, \zeta)$ gives¹

$$\omega_\varepsilon = \omega_0 + \varepsilon\omega_1 + \varepsilon^2\omega_2 + \dots = \sum_{n \geq 0} \varepsilon^n \omega_n, \tag{3.6}$$

$$X(x, \zeta) = X_0(x, \zeta) + \varepsilon X_1(x, \zeta) + \varepsilon^2 X_2(x, \zeta) + \dots = \sum_{n \geq 0} \varepsilon^n X_n(x, \zeta), \tag{3.7}$$

where ω_n are constant and X_n are 1-periodic with respect to the variable ζ . Introducing a comma notation for the derivative with respect to the variable indicated, $X_{,x} = \partial X/\partial x$, the chain rule and (3.4) give $X_x = \varepsilon^{-1}X_{,\zeta} + X_{,x}$. Then we have for $X(x, \zeta)$ and ω_ε :

$$(EX_x)_x = \frac{1}{\varepsilon^2}(EX_{,\zeta})_{,\zeta} + \frac{1}{\varepsilon} [(EX_{,\zeta})_{,x} + (EX_{,x})_{,\zeta}] + (EX_{,x})_{,x}, \tag{3.8}$$

$$\omega_\varepsilon^2 = \sum_{n \geq 0} \varepsilon^n a_n. \tag{3.9}$$

¹The equalities in (3.6) and (3.7) are defined in the asymptotic sense, and do not imply convergence of the series.

The numbers α_n are related to ω_n through the chain of equations:

$$\alpha_0 = \omega_0^2, \quad \alpha_1 = 2\omega_1\omega_0, \quad \alpha_2 = 2\omega_2\omega_0 + \omega_1^2, \quad \dots \quad \alpha_n = \sum_{k=0}^n \omega_k\omega_{n-k}. \tag{3.10}$$

With the aid of (3.8) and (3.9), it is possible to substitute the asymptotic expansions (3.6) and (3.7) into (3.5) and reorder the result by powers of ε ,

$$\sum_{n \geq -2} \varepsilon^n H_n(x, \xi) = 0. \tag{3.11}$$

The coefficients $H_n(x, \xi)$, for $n \geq -2$, are given by

$$H_{-2} = (EX_{0,\xi})_{,\xi}, \tag{3.12}$$

$$H_{-1} = (EX_{1,\xi})_{,\xi} + (EX_{0,\xi})_{,x} + (EX_{0,x})_{,\xi}, \tag{3.13}$$

⋮

$$H_n = (EX_{n+2,\xi})_{,\xi} + (EX_{n+1,\xi})_{,x} + (EX_{n+1,x})_{,\xi} + (EX_{n,x})_{,x} + \rho \sum_{k=0}^n \alpha_k X_{n-k}, \tag{3.14}$$

The asymptotic sum in (3.11) vanishes, yielding

$$H_n(x, \xi) = 0. \tag{3.15}$$

Bearing in mind (3.12)–(3.14), this constitutes a recurrent system of partial differential equations with unknown functions $X_n(x, \xi)$ in which the solutions X_n and X_{n+1} for the n -th and $(n+1)$ -th equations are inserted into the next $(n+2)$ -th equation. Once the functions X_n are found, they can be used in (3.7) to approximate $X(x, \xi)$. Observe that the numbers α_n must also be found. This is accomplished by imposing conditions of boundedness over the functions X_n discussed in the next section.

The substitution process for the asymptotic expansion (3.7) must be made in the expressions for the interface coupling conditions, (3.3), to find the conditions that X_n should satisfy at the interfaces:

$$\|X_0\|_v = 0, \quad \|EX_{0,\xi}\|_v = 0; \quad \|X_{n+1}\|_v = 0, \quad \|EX_{n+1,\xi} + EX_{n,x}\|_v = 0 \quad \text{for } n \geq 0. \tag{3.16}$$

4. Asymptotic homogenization up to $O(\varepsilon^0)$

In this section, we describe a method for solving the system resulting from imposing (3.15) onto (3.12)–(3.14), to find the approximating functions $X_n(x, \xi)$ and the numbers α_n for each power of ε in the asymptotic expansion for X and the square of the frequency ω_ε , respectively. For this purpose it will be helpful to state the following lemma.

Lemma 1. *Consider positive functions $E(\xi)$, $f(\xi)$, and $F(\xi)$, all periodic of period 1, defined over the interval $[0, 1]$, and continuously differentiable except, perhaps, at finitely many points $0 \leq v_1 < v_2 < \dots < v_m \leq 1$ where they might be discontinuous. The equation*

$$(Ev_{,\xi})_{,\xi} = f \tag{4.1}$$

in the function $v(\xi)$, defined for all points $\xi \in (0, 1)$ apart from the v_i and satisfying the conditions

$$\|v(\xi)\|_{v_i} = 0, \quad \|Ev_{,\xi} + F\|_{v_i} = 0, \tag{4.2}$$

has a 1-periodic solution, unique up to an additive constant, if and only if $\langle f \rangle = \sum_{i=1}^m \|F\|_{v_i}$, where

$$\langle \cdot \rangle = \int_0^1 d\zeta \tag{4.3}$$

is the averaging operator over the RVE.

A proof can be found in the first chapter of [Bensoussan et al. 1978].

Considering (3.15) for $n = -2$ leads to the equation, of order $O(\varepsilon^{-2})$,

$$(EX_{0,\zeta})_{,\zeta} = 0. \tag{4.4}$$

Here, X_0 is restricted to 1-periodicity conditions, $X_0(x, 0) = X_0(x, 1)$, and to the conditions given in (3.16)_{1,2}. Lemma 1 supports the conclusion that, since E is a positive function, the general solution for X_0 in (4.4) is

$$X_0(x, \zeta) = \hat{X}_0(x). \tag{4.5}$$

Having solved the equation for the order corresponding to $O(\varepsilon^{-2})$, the equation for next order $O(\varepsilon^{-1})$ is recalled by considering again (3.15), this time with $n = -1$,

$$(EX_{1,\zeta})_{,\zeta} + (EX_{0,\zeta})_{,x} + (EX_{0,x})_{,\zeta} = 0, \tag{4.6}$$

and the conditions (3.16)_{3,4} for $n = 0$,

$$\|X_1\|_v = 0, \quad \|EX_{1,\zeta} + EX_{0,x}\|_v = 0. \tag{4.7}$$

From (4.6) and the fact that X_0 does not depend on the fast variable ζ , it follows that

$$(EX_{1,\zeta})_{,\zeta} + E_{,\zeta} \hat{X}_{0,x} = 0. \tag{4.8}$$

Due to the linear nature of this equation, its general solution is a sum of two terms,

$$X_1(x, \zeta) = N_1(\zeta) \hat{X}_{0,x}(x) + \hat{X}_1(x). \tag{4.9}$$

Here, $\hat{X}_1(x)$ only depends on the slow scale x . By substituting (4.9) into (4.7)–(4.8), we find an expression for the 1-periodic function $N_1(\zeta)$,

$$(EN_{1,\zeta} + E)_{,\zeta} = 0, \tag{4.10}$$

and the continuity conditions

$$\|N_1\| = 0, \quad \|EN_{1,\zeta} + E\| = 0. \tag{4.11}$$

This is the *first local problem*. Lemma 1 guarantees the existence of the local function N_1 up to an additive constant. To avoid nonuniqueness, we will take N_1 so that $\langle N_1 \rangle = 0$.

Before solving for X_2 , which corresponds to the next order in the asymptotic expansion of X , we note that $N_1(\zeta)$ does not need to be found explicitly to obtain a homogenized model. (4.10) and (4.11)₂ imply that it is sufficient that $EN_{1,\zeta} + E = C$, where C is a constant that does not depend on ζ . The average $\langle N_{1,\zeta} \rangle = 0$ vanishes because N_1 is a 1-periodic continuous function. We have $N_{1,\zeta} + 1 = C/E(\zeta)$ and,

applying the averaging operator $\langle \cdot \rangle$ to both sides of the equality, we obtain $1 = C\langle 1/E \rangle$. Finally, the equality $C = \langle 1/E \rangle^{-1}$ holds, and consequently

$$EN_{1,\zeta} + E = \left\langle \frac{1}{E} \right\rangle^{-1} = \hat{E}. \tag{4.12}$$

For the analysis of the $O(\varepsilon^0)$ equation, consider (3.15) and (3.14), for $n = 0$,

$$(EX_{2,\zeta})_{,\zeta} + (EX_{1,\zeta})_{,x} + (EX_{1,x})_{,\zeta} + (EX_{0,x})_{,x} + \rho\omega_0^2 X_0 = 0. \tag{4.13}$$

Here, we substitute the expressions found for X_0 and X_1 into (4.5) and (4.9), respectively,

$$(EX_{2,\zeta})_{,\zeta} + [(EN_1)_{,\zeta} + EN_{1,\zeta} + E] \hat{X}_{0,xx} + E_{,\zeta} \hat{X}_{1,x} + \rho\omega_0^2 \hat{X}_0 = 0. \tag{4.14}$$

Averaging both sides of the equation over one period and considering that $EX_{2,\zeta}$ satisfies the condition (3.16)_{3,4} and is therefore a 1-periodic continuous function in ζ , we have

$$\langle EN_{1,\zeta} + E \rangle \hat{X}_{0,xx} + \omega_0^2 \langle \rho \rangle \hat{X}_0 = 0. \tag{4.15}$$

The coefficients $\langle EN_{1,\zeta} + E \rangle$ and $\langle \rho \rangle$ are the effective coefficients given in previous discussions of homogenization [Pobedria 1984; Bakhvalov and Panasenko 1989]. They are well known, and for one-dimensional periodic structured composites, they can be found explicitly. Finally, we write

$$\hat{E} \hat{X}_{0,xx} + \omega_0^2 \hat{\rho} \hat{X}_0 = 0, \tag{4.16}$$

where \hat{E} is given in (4.12) and $\hat{\rho} = \langle \rho \rangle$.

As we can see, (4.16) contains \hat{X}_0 by itself, and does not show dispersive wave propagation behavior in the composite. This result is obtained if we set $\varepsilon = 0$ in our model. In this case, the structure is effectively homogeneous and nondispersive if the component materials are nondispersive. Applying the normalization condition $\langle N_1 \rangle = 0$, dropping the approximation $\langle X \rangle \approx \hat{X}_0$, and applying the principle of superposition, we are led from (4.16) and (3.2)₂ with $\omega_\varepsilon \approx \omega_0$ to the averaged model for the function $\langle u \rangle = \hat{u}$,

$$\hat{E} \hat{u}_{,xx} - \hat{\rho} \hat{u}_{tt} = 0. \tag{4.17}$$

The classical method of asymptotic homogenization yields the same result, although this result is not expected if the wavelength is comparable to the size of the periodic cell. To describe the dispersive behavior, more terms must be considered in (3.15).

From (4.16), we have

$$\hat{X}_0 = -\frac{1}{\omega_0^2} \frac{\hat{E}}{\hat{\rho}} \hat{X}_{0,xx}, \tag{4.18}$$

which, in combination with (4.14), leads to

$$(EX_{2,\zeta})_{,x} + [(EN_1)_{,\zeta} + EN_{1,\zeta} + E - \frac{\rho}{\hat{\rho}} \langle EN_{1,\zeta} + E \rangle] \hat{X}_{0,xx} + E_{,\zeta} \hat{X}_{1,x} = 0. \tag{4.19}$$

Because this equation is linear, the general solution, X_2 , is

$$X_2(x, \zeta) = N_2(\zeta) \hat{X}_{0,xx} + N_1 \hat{X}_{1,x} + \hat{X}_2(x). \tag{4.20}$$

Analogously to previous cases, $\hat{X}_2(x)$ only depends on x , and $N_2(\xi)$ is the 1-periodic function called the second local function. This function yields a null average, $\langle N_2 \rangle = 0$, and must satisfy the *second local problem*,

$$(EN_{2,\xi} + EN_1)_{,\xi} + EN_{1,\xi} + E - \frac{\rho}{\hat{\rho}} \langle EN_{1,\xi} + E \rangle = 0, \tag{4.21}$$

with conditions

$$\|N_2\| = 0, \quad \|EN_{2,\xi} + EN_1\| = 0. \tag{4.22}$$

5. Higher-order homogenization

In this section, we continue with higher-order approximations in the asymptotic expansion, (3.11). The objective is to relate the terms of the asymptotic expansions of ω_ε and $X(x, \xi)$, given in (3.6) and (3.7), to the periodicity of the composite laminated structure.

From the equation corresponding to $O(\varepsilon)$, we have

$$(EX_{3,\xi})_{,\xi} + (EX_{2,\xi})_{,x} + (EX_{2,x})_{,\xi} + (EX_{1,x})_{,x} + \omega_0^2 \rho X_1 + 2\omega_1 \omega_0 \rho X_0 = 0. \tag{5.1}$$

Combining the formulas for X_0 , X_1 , and X_2 given in (4.5), (4.9), and (4.20), respectively, and taking $\hat{c}^2 = \hat{E}/\hat{\rho}$, we have

$$(EX_{3,\xi})_{,\xi} + [(EN_2)_{,\xi} + EN_{2,\xi} + EN_1 - \hat{c}^2 \rho N_1] \hat{X}_{0,xxx} + [(EN_1)_{,\xi} + EN_{1,\xi} + E] \hat{X}_{1,xx} + E_{,\xi} \hat{X}_{2,x} + \omega_0^2 \rho \hat{X}_1 + 2\omega_0 \omega_1 \rho \hat{X}_0 = 0. \tag{5.2}$$

Averaging this equation, and using (4.12), we have

$$\langle EN_{2,\xi} + EN_1 - \hat{c}^2 \rho N_1 \rangle \hat{X}_{0,xxx} + \hat{E} \hat{X}_{1,xx} + \omega_0^2 \hat{\rho} \hat{X}_1 + 2\omega_0 \omega_1 \hat{\rho} \hat{X}_0 = 0. \tag{5.3}$$

It can be shown that

$$\langle EN_{2,\xi} + EN_1 - \hat{c}^2 \rho N_1 \rangle = 0. \tag{5.4}$$

The functions N_1 and N_2 are continuous because they satisfy (4.11) and (4.22)₁. This is also true for the functions $EN_{1,\xi} + E$ and $EN_{2,\xi} + EN_1$ due to (4.11)₂ and (4.22)₂. Then,

$$\langle [N_2(EN_{1,\xi} + E) - N_1(EN_{2,\xi} + EN_1)]_{,\xi} \rangle = 0, \tag{5.5}$$

because the bracketed function is continuous and 1-periodic. Applying the rule for the derivation of the product, we have

$$\langle N_{2,\xi} (EN_{1,\xi} + E) - N_{1,\xi} (EN_{2,\xi} + EN_1) \rangle + \langle N_2(EN_{1,\xi} + E)_{,\xi} - N_1(EN_{2,\xi} + EN_1)_{,\xi} \rangle = 0. \tag{5.6}$$

Substituting the first and second local problems (4.10) and (4.21) yields

$$\langle N_{2,\xi} (EN_{1,\xi} + E) - N_{1,\xi} (EN_{2,\xi} + EN_1) + N_1(EN_{1,\xi} + E) - \hat{c}^2 \rho N_1 \rangle = 0. \tag{5.7}$$

Finally, after eliminating parentheses and reducing terms, we obtain (5.4). Therefore, from (5.3), we conclude that

$$\hat{E} \hat{X}_{1,xx} + \omega_0^2 \hat{\rho} \hat{X}_1 = -2\omega_0 \omega_1 \hat{\rho} \hat{X}_0. \tag{5.8}$$

This equation is a second-order ordinary differential equation in \hat{X}_1 with constant coefficients. The right-hand side satisfies the corresponding homogeneous second-order equation from (4.16). To obtain bounded solutions for (5.8), we must set $\omega_1 = 0$ because ω_0 and \hat{X}_0 are arbitrary. This yields

$$\hat{E} \hat{X}_{1,xx} + \omega_0^2 \hat{\rho} \hat{X}_1 = 0, \quad \omega_1 = 0. \tag{5.9}$$

Combining (5.9) and (5.2), we have

$$(EX_{3,\zeta})_{,\zeta} + [(EN_2)_{,\zeta} + EN_{2,\zeta} + EN_1 - \hat{c}^2 \rho N_1] \hat{X}_{0,xxx} + [(EN_1)_{,\zeta} + EN_{1,\zeta} + E - \hat{c}^2 \rho] \hat{X}_{1,xx} + E_{,\zeta} \hat{X}_{2,x} = 0. \tag{5.10}$$

The general solution, X_3 , to (5.10) is

$$X_3(x, \zeta) = N_3(\zeta) \hat{X}_{0,xxx} + N_2 \hat{X}_{1,xx} + N_1 \hat{X}_{2,x} + \hat{X}_3(x). \tag{5.11}$$

The third 1-periodic local function N_3 , for which $\langle N_3 \rangle = 0$, is the solution to the *third local problem*,

$$(EN_{3,\zeta} + EN_2)_{,\zeta} + EN_{2,\zeta} + EN_1 - \hat{c}^2 \rho N_1 = 0, \tag{5.12}$$

with continuity conditions

$$\|N_3\| = 0, \quad \|EN_{3,\zeta} + EN_2\| = 0, \tag{5.13}$$

obtained by substituting (5.11) and (4.20) into the ideal contact conditions given in (3.16)_{3,4} for $n = 2$. ω_1 does not change the result obtained thus far for ω_ε . Improvements on this value must be made at subsequent levels of approximation.

Continuing with the term of order $O(\varepsilon^2)$, we have

$$(EX_{4,\zeta})_{,\zeta} + (EX_{3,\zeta})_{,x} + (EX_{3,x})_{,\zeta} + (EX_{2,x})_{,x} + \omega_0^2 \rho X_2 + 2\omega_2 \omega_0 \rho X_0 = 0. \tag{5.14}$$

Substituting in (5.14) the values of X_2 and X_3 from (4.20) and (5.11), and the constraints (4.16) and (5.9)₁ satisfied by \hat{X}_0 and \hat{X}_1 , we get

$$(EX_{4,\zeta})_{,\zeta} + [(EN_3)_{,\zeta} + EN_{3,\zeta} + EN_2 - \hat{c}^2 \rho N_2] \hat{X}_{0,xxx} + [(EN_2)_{,\zeta} + EN_{2,\zeta} + EN_1 - \hat{c}^2 \rho N_1] \hat{X}_{1,xxx} + (EN_{1,\zeta} + E) \hat{X}_{2,xx} + \omega_0^2 \hat{\rho} \hat{X}_2 + 2\omega_2 \omega_0 \hat{\rho} \hat{X}_0 = 0. \tag{5.15}$$

Averaging over this last equality yields

$$\langle EN_{3,\zeta} + EN_2 - \hat{c}^2 \rho N_2 \rangle \hat{X}_{0,xxx} + \hat{E} \hat{X}_{2,xx} + \omega_0^2 \hat{\rho} \hat{X}_2 + 2\omega_2 \omega_0 \hat{\rho} \hat{X}_0 = 0. \tag{5.16}$$

Considering the second-order homogeneous equation (4.16), we have

$$\hat{X}_0 = -\frac{\hat{c}^2}{\omega_0^2} \hat{X}_{0,xx} = \frac{\hat{c}^4}{\omega_0^4} \hat{X}_{0,xxxx}. \tag{5.17}$$

Consequently, we can rewrite (5.16) as

$$\hat{E} \hat{X}_{2,xx} + \omega_0^2 \hat{\rho} \hat{X}_2 = -\left[\langle EN_{3,\zeta} + EN_2 - \hat{c}^2 \rho N_2 \rangle \frac{\omega_0^4}{\hat{c}^4} + 2\omega_2 \omega_0 \hat{\rho} \right] \hat{X}_0. \tag{5.18}$$

Once again, we have obtained a second-order differential equation, this time for the function \hat{X}_2 . Because \hat{X}_0 satisfies the corresponding second order homogeneous equation, the right-hand side of (5.18) does

also. To avoid unbounded solutions for \hat{X}_2 , we must select ω_2 so that the coefficient of \hat{X}_0 in the right-hand side is equal to zero:

$$\omega_2 = -\frac{\omega_0^3}{2\hat{c}^4\hat{\rho}}\langle EN_{3,\xi} + EN_2 - \hat{c}^2\rho N_2\rangle. \tag{5.19}$$

The equation for \hat{X}_2 is

$$\hat{E}\hat{X}_{2,xx} + \omega_0^2\hat{\rho}\hat{X}_2 = 0. \tag{5.20}$$

With this result, an averaged expression for (2.1), up to $O(\varepsilon^2)$, can be obtained. Combining

$$\hat{X} = \hat{X}_0 + \varepsilon\hat{X}_1 + \varepsilon^2\hat{X}_2 \tag{5.21}$$

and the normalization condition, $\langle N_n \rangle = 0$ for $n = 1, 2, \dots$, it can be seen that $\langle X \rangle \approx \hat{X}$, and we have

$$\hat{E}\hat{X}_{,xx} + \omega_0^2\hat{\rho}\hat{X} = 0. \tag{5.22}$$

If $u = X(x, \zeta)T(t)$, then $\hat{u} = \langle u \rangle = \langle X(x, \zeta)T(t) \rangle \approx \hat{X}T$, and

$$\hat{\rho}\hat{u}_{tt} = \hat{\rho}\hat{X}T_{tt} = -\hat{\rho}\omega_\varepsilon^2\hat{X}T, \tag{5.23}$$

considering (3.2)₂. Taking only the terms up to the second-order of approximation in the second equality of (5.23), we obtain

$$\begin{aligned} \hat{\rho}\omega_\varepsilon^2\hat{X}T &\approx \hat{\rho}(\omega_0 + \varepsilon^2\omega_2)^2\hat{X}T = \hat{\rho}\omega_0^2\hat{X}T + \varepsilon^2\hat{\rho}2\omega_0\omega_2\hat{X}T + \varepsilon^4\hat{\rho}\omega_2^2\hat{X}T \\ &= \hat{\rho}\omega_0^2\hat{X}T + \varepsilon^22\hat{\rho}\omega_2(\omega_0 + \varepsilon^22\omega_2)\hat{X}T - \varepsilon^4\hat{\rho}3\omega_2^2\hat{X}T \\ &= \hat{\rho}\omega_0^2\hat{X}T + \varepsilon^22\hat{\rho}\frac{\omega_2}{\omega_0}\omega_\varepsilon^2\hat{X}T - \varepsilon^4\hat{\rho}3\omega_2^2\hat{X}T. \end{aligned} \tag{5.24}$$

Neglecting terms of order $O(\varepsilon^4)$ and substituting the value for ω_2 from (5.19), this reduces to

$$\hat{\rho}\hat{X}T_{tt} = -\hat{\rho}\omega_0^2\hat{X}T - \varepsilon^2\frac{\omega_0^2}{\hat{c}^4}\kappa\omega_\varepsilon^2\hat{X}T, \tag{5.25}$$

where we have set $\kappa = \langle EN_{3,\xi} + EN_2 - \hat{c}^2\rho N_2 \rangle$. In view of (5.22) and (3.2)₂, we can substitute $\frac{\omega_0^2}{\hat{c}^2}\hat{X} = -\hat{X}_{xx}$ and $\omega_\varepsilon^2T = -T_{tt}$ to obtain

$$\hat{\rho}\hat{X}T_{tt} = \hat{E}\hat{X}_{xx}T - \frac{\varepsilon^2\kappa}{\hat{c}^2}\hat{X}_{xx}T_{tt}. \tag{5.26}$$

Finally, we have, for \hat{u} ,

$$\hat{\rho}\hat{u}_{tt} = \hat{E}\hat{u}_{xx} - \frac{\varepsilon^2\kappa}{\hat{c}^2}\hat{u}_{xxtt}. \tag{5.27}$$

Applying the principle of superposition, we find that this equation is valid for more general functions \hat{u} which are sums of stationary modes $\hat{u}(x, t) = \hat{X}(x)T(t)$ multiplied by a constant amplitude. This result demonstrates the dispersive nature of wave propagation in the composite under study.

One-dimensional homogenization yields a closed-form expression for κ , which depends on the coefficients in the original equation, $E(\zeta)$ and $\rho(\zeta)$. This procedure is presented in the [Appendix](#). If we define

$$R = \int_0^\zeta \left(\frac{\rho}{\hat{\rho}} - 1\right)ds, \quad B = \int_0^\zeta \left(\frac{\hat{E}}{E} - 1\right)ds, \tag{5.28}$$

then

$$\kappa = \hat{E} \left[\left\langle \left(\frac{\hat{E}}{E} R - B \right) \left(R - \left\langle \frac{\hat{E}}{E} R \right\rangle \right) \right\rangle + \left\langle \left(\frac{\rho}{\hat{\rho}} B - R \right) (B - \langle B \rangle) \right\rangle \right]. \tag{5.29}$$

If $E(\xi)\rho(\xi)$ is a constant, then $\kappa = 0$. Under such conditions, $\rho(\xi)/\hat{\rho} = \hat{E}/E(\xi)$, $R = B$, and

$$\kappa = \hat{E} \left[\left\langle 2 \left(\frac{\hat{E}}{E} - 1 \right) B^2 \right\rangle - \left\langle \left(\frac{\hat{E}}{E} + 1 \right) B \right\rangle \left\langle \left(\frac{\hat{E}}{E} - 1 \right) B \right\rangle \right]. \tag{5.30}$$

This expression vanishes if we consider $dB/d\xi = \hat{E}/E - 1$: indeed, this condition implies

$$\left\langle \left(\frac{\hat{E}}{E} - 1 \right) B^n \right\rangle = \frac{1}{n+1} \left\langle \frac{d}{d\xi} (B^{n+1}) \right\rangle = 0, \tag{5.31}$$

because B^n is a 1-periodic function. This fact can be used to verify that the quantity in brackets in (5.30) is zero. From a physical standpoint, this demonstrates that for constant acoustic impedance $E\rho$ in a periodic composite, dispersion is not observed in the global model because that would imply that $\kappa = 0$.

6. Arbitrary orders of approximation

The results obtained in the last section can be extended to arbitrary orders of approximation for the functions $X(x, \xi)$ and the angular frequency ω_ε . To achieve this goal, we require the following result.

Lemma 2. *For all $n \geq 0$, we have*

$$X_n(x, \xi) = \sum_{m=0}^n N_{n-m}(\xi) \frac{d^{n-m} \hat{X}_m}{dx^{n-m}}(x), \tag{6.1}$$

and the expressions for α_n become

$$\alpha_n = -\frac{1}{\hat{\rho}} \left(-\frac{\omega_0^2}{\hat{c}^2} \right)^{n/2+1} \left\langle EN_{n+1, \xi} + EN_n + \sum_{k=0}^{n/2-1} \alpha_{2k} \left(-\frac{\hat{c}^2}{\omega_0^2} \right)^{k+1} \rho N_{n-2k} \right\rangle, \tag{6.2}$$

for n even, or

$$\alpha_n = 0, \tag{6.3}$$

otherwise. By convention, we take $N_0 \equiv 1$, and d^0/dx^0 is the identity operator. The local functions N_n are 1-periodic, of null average, and must satisfy the recurrent set of local problems given by

$$(EN_{n+2, \xi} + EN_{n+1})_{, \xi} + EN_{n+1, \xi} + EN_n + \sum_{k=0}^{[n/2]} \alpha_{2k} \left(-\frac{\hat{c}^2}{\omega_0^2} \right)^{k+1} \rho N_{n-2k} = 0. \tag{6.4}$$

$[n/2]$ is the largest integer less than or equal to $n/2$, and the 1-periodic solution N_{n+2} to this equation is restricted to the continuity conditions

$$\|N_{n+2}\| = 0, \quad \|EN_{n+2, \xi} + EN_{n+1}\| = 0. \tag{6.5}$$

All functions \hat{X}_n satisfy the equation

$$\hat{c}^2 \hat{X}_{n, xx} + \omega_0^2 \hat{X}_n = 0. \tag{6.6}$$

Proof. (The reader may prefer to skip to the end of the proof, on page 964.) We proceed by induction. Suppose n_0 is even, (6.1)–(6.3) are valid for $n < n_0 + 2$, and (6.4)–(6.6) hold for every $n < n_0$. From the expression for the order $O(\varepsilon^{n_0})$, we have

$$(EX_{n_0+2,\zeta})_{,\zeta} + (EX_{n_0+1,\zeta})_{,x} + (EX_{n_0+1,x})_{,\zeta} + (EX_{n_0,x})_{,x} + \rho \sum_{k=0}^{n_0/2} \alpha_k X_{n_0-k} = 0. \tag{6.7}$$

A necessary and sufficient condition for the existence of a 1-periodic solution X_{n_0+2} for this equation is

$$\left\langle (EX_{n_0+1,x})_{,\zeta} + (EX_{n_0,x})_{,x} + \rho \sum_{k=0}^{n_0} \alpha_k X_{n_0-k} \right\rangle = 0. \tag{6.8}$$

Once the expressions for X_{n_0} and X_{n_0+1} from (6.3) are substituted into this equality, we have

$$\sum_{m=0}^{n_0-1} \left\langle EN_{n_0-m+1,\zeta} + EN_{n_0-m} + \sum_{k=0}^{\lfloor \frac{n_0-m}{2} \rfloor} \alpha_{2k} \left(-\frac{\hat{c}^2}{\omega_0^2}\right)^{k+1} \rho N_{n_0-m-2k} \right\rangle \frac{d^{n_0-m+2} \hat{X}_m}{dx^{n_0-m+2}} + \langle EN_{1,\zeta} + E \rangle \frac{d^2 \hat{X}_{n_0}}{dx^2} + \omega_0^2 \langle \rho \rangle \hat{X}_{n_0} = 0. \tag{6.9}$$

As long as (6.5)₁ is valid for $n < n_0$, we have

$$\left\langle EN_{n+1,\zeta} + EN_n + \sum_{k=0}^{\lfloor n/2 \rfloor} \alpha_{2k} \left(-\frac{\hat{c}^2}{\omega_0^2}\right)^{k+1} \rho N_{n-2k} \right\rangle = 0, \tag{6.10}$$

for $n < n_0$. All terms in the sum from $m = 0$ to $m = n_0 - 1$ in (6.9) vanish except for the one corresponding to $m = 0$, and (6.9) is equivalent to

$$\langle EN_{1,\zeta} + E \rangle \frac{d^2 \hat{X}_{n_0}}{dx^2} + \omega_0^2 \langle \rho \rangle \hat{X}_{n_0} = - \left\langle EN_{n_0+1,\zeta} + EN_{n_0} + \sum_{k=0}^{n_0/2} \alpha_{2k} \left(-\frac{\hat{c}^2}{\omega_0^2}\right)^{k+1} \rho N_{n_0-2k} \right\rangle \frac{d^{n_0+2} \hat{X}_0}{dx^{n_0+2}}. \tag{6.11}$$

At the same time, we have

$$\frac{d^{n_0+2} \hat{X}_0}{dx^{n_0+2}} = \left(-\frac{\omega_0^2}{\hat{c}^2}\right)^{n_0/2+1} \hat{X}_0. \tag{6.12}$$

(6.11) is a second-order differential equation, with constant coefficients, in the unknown functions \hat{X}_{n_0+1} . To obtain a bounded solution, we must set the right-hand side equal to zero because \hat{X}_0 satisfies the corresponding homogeneous equation. Then,

$$\left\langle EN_{n_0+1,\zeta} + EN_{n_0} + \sum_{k=0}^{n_0/2} \alpha_{2k} \left(-\frac{\hat{c}^2}{\omega_0^2}\right)^{k+1} \rho N_{n_0-2k} \right\rangle = 0, \tag{6.13}$$

and solving for α_{n_0} , we obtain precisely (6.2), for $n = n_0$, and for \hat{X}_{n_0} , we get (6.6). This yields

$$\hat{X}_{n_0} = -\frac{\hat{c}^2}{\omega_0^2} \frac{d^2 \hat{X}_{n_0}}{dx^2}. \tag{6.14}$$

We can use this fact and (6.2) to obtain, from (6.7)

$$(EX_{n_0+2,\zeta})_{,\zeta} + \sum_{m=0}^{n_0+1} \left[(EN_{n_0-m+1})_{,\zeta} + EN_{n_0-m+1,\zeta} + EN_{n_0-m} + \sum_{k=0}^{\lfloor \frac{n_0-m}{2} \rfloor} \alpha_{2k} \rho N_{n_0-m-2k} \right] \frac{d^{n_0-m+2} \hat{X}_m}{dx^{n_0-m+2}} = 0.$$

Because this equation is linear, the general solution X_{n_0+2} , for (6.15), is the expression given in (6.1) for $n = n_0 + 2$, where the local functions $N_{n_0+2}(\zeta)$ satisfy (6.4)–(6.5) when $n = n_0$.

Next, we consider the equation corresponding to the order $O(\varepsilon^{n_0+1})$:

$$(EX_{n_0+3,\zeta})_{,\zeta} + (EX_{n_0+2,\zeta})_{,x} + (EX_{n_0+2,x})_{,\zeta} + (EX_{n_0+1,x})_{,x} + \rho \sum_{k=0}^{n_0/2} \alpha_k X_{n_0-k+1} = 0. \tag{6.15}$$

If we average over a period, we have

$$\left\langle (EX_{n_0+2,x})_{,\zeta} + (EX_{n_0+1,x})_{,x} + \rho \sum_{k=0}^{n_0/2} \alpha_k X_{n_0-k+1} \right\rangle = 0. \tag{6.16}$$

Analogously to the previous case, this is equivalent to

$$\begin{aligned} \langle EN_{1,\zeta} + E \rangle \frac{d^2 \hat{X}_{n_0+1}}{dx^2} + \omega_0^2 \langle \rho \rangle \hat{X}_{n_0+1} = \\ - \left\langle EN_{n_0+2,\zeta} + EN_{n_0+1} + \sum_{k=0}^{n_0/2} \alpha_{2k} \left(-\frac{\hat{c}^2}{\omega_0^2} \right)^{k+1} \rho N_{n_0-2k+1} \right\rangle \frac{d^{n_0+3} \hat{X}_0}{dx^{n_0+3}} - \alpha_{n_0+1} \langle \rho \rangle \hat{X}_0. \end{aligned} \tag{6.17}$$

Here it can be proved that

$$\left\langle EN_{n_0+2,\zeta} + EN_{n_0+1} + \sum_{k=0}^{n_0/2} \alpha_{2k} \left(-\frac{\hat{c}^2}{\omega_0^2} \right)^{k+1} \rho N_{n_0-2k+1} \right\rangle = 0. \tag{6.18}$$

Consider, for that purpose, the identity

$$\left\langle \sum_{n=0}^{n_0+1} (-1)^n [N_{n_0-n+2}(EN_{n+1,\zeta} + EN_n)]_{,\zeta} \right\rangle = 0. \tag{6.19}$$

Applying here the rule for the derivative of the product, we arrive at

$$\left\langle \sum_{n=0}^{n_0+1} (-1)^n N_{n_0-n+2,\zeta} (EN_{n+1,\zeta} + EN_n) \right\rangle + \left\langle \sum_{n=0}^{n_0+1} (-1)^n N_{n_0-n+2} (EN_{n+1,\zeta} + EN_n)_{,\zeta} \right\rangle = 0. \tag{6.20}$$

We can substitute the expressions for the local problems in (6.4) into the second term of the left-hand side of (6.20) to obtain, after some algebra,

$$\begin{aligned} \left\langle \sum_{n=0}^{n_0+1} (-1)^n EN_{n_0-n+2,\zeta} N_{n+1,\zeta} \right\rangle + \langle EN_{n_0+2,\zeta} \rangle + \left\langle \sum_{n=1}^{n_0+1} (-1)^n EN_{n_0-n+2,\zeta} N_n \right\rangle \\ + \left\langle \sum_{n=1}^{n_0+1} (-1)^{n+1} EN_{n_0-n+2} N_{n,\zeta} \right\rangle + \langle EN_{n_0+1} \rangle + \left\langle \sum_{n=2}^{n_0+1} (-1)^{n+1} EN_{n_0-n+2} N_{n,\zeta} \right\rangle \\ + \left\langle \sum_{q=0}^{n_0/2} \alpha_{2q} \left(-\frac{\hat{c}}{\omega_0^2} \right)^{q+1} \rho N_{n_0-2q+1} \right\rangle + \left\langle \sum_{n=2}^{n_0+1} (-1)^{n+1} N_{n_0-n+2} \sum_{k=0}^{[n/2-1]} \alpha_{2k} \left(-\frac{\hat{c}}{\omega_0^2} \right)^{k+1} \rho N_{n-2k+1} \right\rangle = 0. \end{aligned} \tag{6.21}$$

The first term in this expression is equal to zero. To verify this, is sufficient to change the summation index to $n = n_0 - m + 1$. Recalling that n_0 is an even number, we have

$$\sum_{n=0}^{n_0+1} (-1)^n EN_{n_0-n+2,\zeta} N_{n+1,\zeta} = \sum_{n_0-m+1=0}^{n_0-m+1=n_0+1} (-1)^{n_0-m+1} EN_{m+1,\zeta} N_{n_0-m+2,\zeta} = - \sum_{m=0}^{n_0+1} (-1)^m EN_{m+1,\zeta} N_{n_0-m+2,\zeta},$$

That is, the sum is equal to its negative and hence vanishes. A similar procedure can be used to verify that the third and fourth terms in left-hand side of (6.21) cancel, the sixth and eighth terms are zero as well, and (6.21) gives (6.18). Finally, (6.17) reduces to

$$\left\langle EN_{1,\zeta} + E \right\rangle \frac{d^2 \hat{X}_{n_0+1}}{dx^2} + \omega_0^2 \langle \rho \rangle \hat{X}_{n_0+1} = -\alpha_{n_0+1} \langle \rho \rangle \hat{X}_0. \tag{6.22}$$

Here, we must take $\alpha_{n_0+1} = 0$ to obtain bounded solutions for the unknown \hat{X}_{n_0+1} in (6.22), consistent with (6.3), which is the goal of this proof. This leaves, for \hat{X}_{n_0+1} , the equation given in (6.6) for $n = n_0 + 1$. This can be used

to restate (6.15):

$$(EX_{n_0+3}, \zeta), \zeta + \sum_{m=0}^{n_0+2} \left[(EN_{n_0-m+2}), \zeta + EN_{n_0-m+2, \zeta} + EN_{n_0-m+1} + \sum_{k=0}^{\lfloor \frac{n_0-m+1}{2} \rfloor} \alpha_{2k} \rho N_{n_0-m-2k+1} \right] \frac{d^{n_0-m+3} \hat{X}_m}{dx^{n_0-m+3}} = 0. \tag{6.23}$$

Then, the general solution, X_{n_0+3} , to this equation is given by (6.1), for $n = n_0 + 3$, and by substitution it can be seen that the local function N_{n_0+3} must satisfy (6.4)–(6.5) for $n = n_0 + 1$ which is the goal of the proof.

Finally, the expressions for X_0 and X_1 become

$$X_0(x, \zeta) = \hat{X}_0(x), \quad X_1(x, \zeta) = N_1(\zeta) \frac{d\hat{X}_0}{dx}(x) + \hat{X}_1(x),$$

from Section 4. Combining this with the first local problem, (4.10)–(4.11), and the relation $\alpha_0 = \omega_0^2$ we conclude the proof for the lemma. □

The equality (6.1) gives the following asymptotic expansion for the function $X(x, \zeta)$,

$$X(x, \zeta) = \sum_{n \geq 0} \varepsilon^n \sum_{m=0}^n N_{n-m}(\zeta) \frac{d^{n-m} \hat{X}_m}{dx^{n-m}}(x). \tag{6.24}$$

As a consequence, if we take

$$\hat{X}(x) = \sum_{n \geq 0} \varepsilon^n \hat{X}_n(x), \tag{6.25}$$

then (6.24) and the normalization condition $\langle N_n \rangle = 0$ yield

$$X(x, \zeta) = \sum_{n \geq 0} \varepsilon^n N_n(\zeta) \frac{d^n \hat{X}}{dx^n}, \quad \langle X \rangle = \hat{X}, \quad \hat{E} \hat{X}_{xx} + \omega_0^2 \hat{\rho} \hat{X} = 0. \tag{6.26}$$

Because we now have an explicit expression for \hat{X} and have solved the local problems, X can be successfully approximated. The condition that $\alpha_n = 0$ if n is odd implies that $\omega_n = 0$ if n is odd, and

$$\omega_\varepsilon = \sum_{n \geq 0} \varepsilon^{2n} \omega_{2n}. \tag{6.27}$$

Note that all ω_{2n} satisfy the recurrence condition in (6.3) and can therefore be found for arbitrary n once ω_0 is obtained. Then, for the function $T(t)$,

$$T_{tt} + (\omega_0 + \varepsilon^2 \omega_2 + \varepsilon^4 \omega_4 + \dots)^2 T = 0. \tag{6.28}$$

This allows us to define \hat{u} . The boundary conditions allow calculation of the eigenfunctions $\hat{X}^{(n)}$ and the eigenfrequencies $\omega_0^{(n)}$ from (6.26). The formula (6.2) for α_n tell us that all quantities α_n and ω_n depend recurrently on ω_0 . Once ω_0 and the local functions N_n are determined up to a certain order, ω_n can be obtained which define a suitable approximation for ω_ε . Substituting ω_ε into the equation for $T(t)$ in (3.2)₂ and defining initial conditions, the functions $T^{(n)}(t)$ can be calculated to give $\hat{u} = \sum_n^\infty \hat{X}^{(n)} T^{(n)}$. This result will be described in the next section, in which an analytic solution for \hat{u} is obtained for select cases. It should be emphasized that the procedure followed so far is equivalent to the one introduce in the original problem, (2.1)–(2.2). This procedure depends on a rescaled temporal variable $\tau = (1 + \varepsilon r_1 + \varepsilon^2 r_2 + \dots)t$,

following the method of strained coordinates or the method of Linsted-Poincaré [Sánchez-Huber and Sánchez-Palencia 1992].

Note that $r_n = \omega_n/\omega_0$ depend on ω_0 . From (6.2) and (6.3), we can deduce a general expression for ω_ε that depends on ω_0 . Considering the expressions given in (3.10) and using induction, one obtains

$$\omega_\varepsilon = \omega_0 \left(1 - \varepsilon^2 \omega_0^2 \frac{K_1}{\hat{c}^2} + \dots + (-1)^n \varepsilon^{2n} \omega_0^{2n} \frac{K_n}{\hat{c}^{2n}} + \dots \right), \tag{6.29}$$

where K_n depend only on the local functions N_i , for $i = 1, 2, \dots, 2n + 1$, and the coefficients in the original equation.

7. Solution for the averaged model

We next consider wave propagation problems under various initial and boundary conditions. We present analytical solutions to the propagation equations and an explicit expression for the averaged model.

7A. Perturbation from the steady state. First, consider the one-dimensional problem of wave propagation given by (2.1), with boundary conditions given in (2.2)_{1,2}, with $\mu(t) = 0$ and $F(t) = 0$. The initial conditions are given by (2.2)_{3,4} with $U(x) = f(x)$ and $V(x) = 0$. This corresponds to an initial disturbance from the equilibrium position.

From (6.26) and the homogeneous boundary conditions introduced, we have the following equation and boundary conditions for \hat{X} :

$$\hat{E} \hat{X}_{,xx} + \omega_0^2 \hat{\rho} \hat{X} = 0, \quad \hat{X}(0) = 0, \quad \hat{X}_{,x}(L) = 0. \tag{7.1}$$

This is a second-order linear differential equation with constant coefficients, and the solution can be explicitly determined as $\hat{X}^{(n)}(x) = \sin(\omega_0^{(n)}/\hat{c})x$, where

$$\omega_0^{(n)} = \frac{(2n - 1)\pi \hat{c}}{2L}, \tag{7.2}$$

for $n = 1, 2, 3, \dots$, yielding

$$\hat{X}^{(n)}(x) = \sin \frac{(2n - 1)\pi x}{2L}. \tag{7.3}$$

Next, the functions $T^{(n)}(t)$, corresponding to each value of $\omega_0^{(n)}$, are solved as follows:

$$T_{tt}^{(n)} + (\omega_\varepsilon^{(n)})^2 T^{(n)} = 0, \quad T^{(n)}(0) = f^{(n)}, \quad T_t^{(n)}(0) = 0. \tag{7.4}$$

Here the $\omega_\varepsilon^{(n)}$, with $n = 1, 2, 3, \dots$, can be found from $\omega_0^{(n)}$ using (6.29), and the $f^{(n)}$ are the coefficients of the Fourier expansion of the initial condition $f(x)$, relative to the orthogonal basis $\hat{X}^{(n)}$:

$$f^{(n)} = \frac{\int_0^L f(x) \hat{X}^{(n)}(x) dx}{\int_0^L [\hat{X}^{(n)}(x)]^2 dx}. \tag{7.5}$$

The approximation for $\omega_\varepsilon^{(n)}$ is easily calculated to second order. Using the expression for ω_2 in (5.19) and the expansion for ω_ε in (6.29), we derive

$$\omega_{(2)}^{(n)} = \omega_0^{(n)} \left(1 - \frac{(\varepsilon \omega_0^{(n)})^2 K}{\hat{c}^2} \frac{K}{2} \right), \tag{7.6}$$

where $K = \kappa/\hat{E}$ is a material constant based on the parameter κ of (5.29). The $f^{(n)}$ are then given by

$$f^{(n)} = \frac{2}{L} \int_0^L f(x) \sin \frac{(2n-1)\pi x}{2L} dx, \tag{7.7}$$

for $n = 1, 2, 3, \dots$. The solution to (7.4) is given by $T_{(2)}^{(n)}(t) = f^{(n)} \cos \omega_{(2)}^{(n)}t$, where

$$T_{(2)}^{(n)}(t) = f^{(n)} \cos \frac{(2n-1)\pi \hat{c}}{2L} \left(1 - \left[\frac{\varepsilon(2n-1)\pi}{2L} \right]^2 \frac{K}{2} \right) t. \tag{7.8}$$

Having found the expressions for $\hat{X}^{(n)}$ and $T^{(n)}$, with $n = 1, 2, 3, \dots$, \hat{u} is given analytically as

$$\hat{u}(x, t) = \sum_{n=1}^{\infty} f^{(n)} \sin \frac{(2n-1)\pi x}{2L} \cos \frac{(2n-1)\pi \hat{c}}{2L} \left(1 - \left[\frac{\varepsilon(2n-1)\pi}{2L} \right]^2 \frac{K}{2} \right) t. \tag{7.9}$$

Note that the same analytical solution is obtained using the classical asymptotic homogenization method, setting $\varepsilon = 0$ in (7.9). The qualitative differences between our approach and the classical asymptotic homogenization approach become evident upon inspection of (7.9). The difference between these two approaches arises when $(\varepsilon(2n-1)\pi/(2L))^2(K/2)t$ is comparable to unity, that is, when t is of the order

$$\left(\frac{2L}{\varepsilon(2n-1)\pi} \right)^2 \frac{2}{K}.$$

7B. One moving boundary. Next, we evaluate the problem of wave propagation in (2.1) setting $F(t) = U(x) = V(x) = 0$ in (2.2). These conditions correspond to a regime of movement on one boundary with a free load on the other border, starting from the equilibrium position. For homogeneous boundary conditions, we consider the auxiliary function $v(x, t) = u(x, t) - \mu(t)$, which satisfies

$$(Ev_x)_x - \rho v_{tt} = \rho \mu''(t), \quad v(0, t) = 0, \quad v_x(L, t) = 0, \quad v(x, 0) = -\mu(0), \quad v_t(x, 0) = -\mu'(0).$$

The total derivative of μ is denoted by a prime. Following the procedure in the previous section, we find that $\omega_0^{(n)}$ and $\hat{X}^{(n)}$ are as in (7.2) and (7.3). Then,

$$T_{tt}^{(n)} + (\omega_\varepsilon^{(n)})^2 T^{(n)} = -\hat{k}^{(n)} \mu''(t), \quad T^{(n)}(0) = -\hat{k}^{(n)} \mu(0), \quad T_t^{(n)}(0) = -\hat{k}^{(n)} \mu'(0), \tag{7.10}$$

where

$$\hat{k}^{(n)} = \frac{\int_0^L \hat{X}^{(n)}(x) dx}{\int_0^L [\hat{X}^{(n)}(x)]^2 dx} = \frac{4}{(2n-1)\pi}. \tag{7.11}$$

This nonhomogeneous second-order equation with constant coefficients can be solved the theory of distributions; see [Schwartz 1966] for details. We obtain

$$T^{(n)}(t) = -\hat{k}^{(n)} \mu(t) + \omega_\varepsilon^{(n)} \hat{k}^{(n)} \int_0^t \mu(s) \sin \omega_\varepsilon^{(n)}(t-s) ds. \tag{7.12}$$

This gives an analytic expression for $\hat{v}(x, t) = \langle v \rangle$,

$$\hat{v}(x, t) = -\mu(t) + \sum_{n=1}^{\infty} \omega_\varepsilon^{(n)} \hat{k}^{(n)} \hat{X}^{(n)}(x) \int_0^t \mu(s) \sin \omega_\varepsilon^{(n)}(t-s) ds. \tag{7.13}$$

Considering approximations only up to the second power of ε , that is, $\omega_\varepsilon^{(n)} \approx \omega_{(2)}^{(n)}$, we get

$$\hat{u}(x, t) = \frac{2\hat{c}}{L} \sum_{n=1}^{\infty} \left[1 - \left(\frac{\varepsilon(2n-1)\pi}{2L} \right)^2 \frac{K}{2} \right] \sin \frac{(2n-1)\pi x}{2L} \times \int_0^t \mu(s) \sin \frac{(2n-1)\pi \hat{c}}{2L} \left[1 - \left(\frac{\varepsilon(2n-1)\pi}{2L} \right)^2 \frac{K}{2} \right] (t-s) ds. \quad (7.14)$$

7C. Modeling failures. Next we consider the problem described in Section 7B with the added presence of a failure in the composite at $x = \theta L$, where $0 < \theta < 1$. The failure will be described mathematically as a dimensionless spring at $x = \theta L$ in the domain $[0, L]$. In addition to satisfying (2.1) and the boundary and initial conditions given in Section 7B, $F(t) = U(x) = V(x) = 0$ in (2.2), the displacement functions must satisfy

$$q \|u\|_{x=\theta L} = E \frac{du}{dx} \Big|_{x=\theta L}, \quad \left\| E \frac{du}{dx} \right\|_{x=\theta L} = 0, \quad (7.15)$$

where q is the elastic coefficient for the dimensionless spring. In the limit as q approaches infinity, the right-hand side of (7.15) approaches zero (division by q), which corresponds to the case when no failure is present. When q approaches zero, the left-hand side of the equality approaches zero, which corresponds to the case when two faces at $x = \theta L$ are under free stress conditions, that is, the material consists of two separate pieces. The methodology used for the standard case is applied again, with the same auxiliary function $v(x, t) = u(x, t) - \mu(t)$. Thus, we are looking for an expression for \hat{X} , satisfying (7.1) and the conditions

$$\|\hat{X}\|_{x=\theta L} = \frac{\hat{E}}{q} \frac{d\hat{X}}{dx} \Big|_{x=\theta L}, \quad \left\| \frac{d\hat{X}}{dx} \right\|_{x=\theta L} = 0. \quad (7.16)$$

In this case, the function \hat{X} defined by

$$\hat{X}(x) = \begin{cases} A \sin(\omega_0 x / \hat{c}) & \text{for } 0 < x < \theta L, \\ B \cos(\omega_0(L-x) / \hat{c}) & \text{for } \theta L < x < L, \end{cases} \quad (7.17)$$

automatically satisfies the conditions (7.1). Substituting (7.17) into (7.16) and introducing the quantity $\phi = \omega_0 L / \hat{c}$ for convenience, we obtain a system of linear equations in A and B :

$$\begin{cases} B \cos((1-\theta)\phi) - A \left(\sin(\theta\phi) + \frac{\phi \hat{E}}{qL} \cos(\theta\phi) \right) = 0, \\ B \sin((1-\theta)\phi) - A \cos(\theta\phi) = 0. \end{cases} \quad (7.18)$$

The only solution is $A = 0$ and $B = 0$ unless the determinant vanishes, leading after simplification to the condition

$$\cos \phi - \frac{\hat{E}}{qL} \phi \cos \phi \theta \sin \phi (1-\theta) = 0. \quad (7.19)$$

Once the solutions $\varphi^{(n)}$ to this equation are found, we can take

$$\begin{aligned}
 A &= \sin \varphi^{(n)}(1 - \theta), & B &= \cos \varphi^{(n)}\theta & \text{if } \varphi^{(n)} &\neq \frac{2n - 1}{2}\pi, \\
 A &= 1, & B &= 1 & \text{if } \varphi^{(n)} &= \frac{2n - 1}{2}\pi,
 \end{aligned}$$

from which we finally determine the functions $\hat{X}^{(n)}$:

$$\hat{X}^{(n)}(x) = \begin{cases} \sin \varphi^{(n)}(1 - \theta) \sin \varphi^{(n)}x/L & \text{if } 0 < x/L < \theta, \\ \cos \varphi^{(n)}\theta \cos \varphi^{(n)}(1 - x/L) & \text{if } \theta < x/L < 1. \end{cases} \tag{7.20}$$

This expression holds if $\varphi^{(n)}$ is not a half-integer multiple of π ; otherwise $\hat{X}^{(n)}$ takes the form given in equation (7.3). The steps for finding $T^{(n)}$ are analogous to those in Section 7B. Since $T^{(n)}$ satisfies (7.10) we write it in the for (7.12). Again, for $\hat{k}^{(n)}$ we have

$$\hat{k}^{(n)} = \frac{\int_0^L \hat{X}^{(n)}(x) dx}{\int_0^L [\hat{X}^{(n)}(x)]^2 dx}. \tag{7.21}$$

This finally gives

$$\hat{k}^{(n)} = \frac{2}{\varphi^{(n)}} \frac{\sin \varphi^{(n)}(1 - \theta)}{\theta \sin^2 \varphi^{(n)}(1 - \theta) + (1 - \theta) \cos^2 \varphi^{(n)}\theta + (\hat{E}/qL) \sin^2 \varphi^{(n)}(1 - \theta) \cos^2 \varphi^{(n)}\theta}, \tag{7.22}$$

except when $\varphi^{(n)}$ is a half-integer multiple of π , in which case $\hat{k}^{(n)}$ is as in (7.11). The expression for $\hat{\delta}$ is exactly the same we found in (7.13), except that $\hat{X}^{(n)}$ and $\hat{k}^{(n)}$ have the values in (7.20) and (7.22). For ω_ε we have

$$\omega_\varepsilon^{(n)} \approx \omega_{(2)}^{(n)} = \frac{\hat{c}\varphi^{(n)}}{L} \left[1 - \left(\frac{\varepsilon\varphi^{(n)}}{L} \right)^2 \frac{K}{2} \right]. \tag{7.23}$$

We have now arrived at the final analytic expression for $\hat{u}(x, t)$,

$$\hat{u}(x, t) = 2 \frac{\hat{c}}{L} \sum_{n=1}^{\infty} r_n \left[1 - \left(\frac{\varepsilon\varphi^{(n)}}{L} \right)^2 \frac{K}{2} \right] \hat{X}_n(x) \int_0^t \mu(s) \sin \frac{\hat{c}\varphi^{(n)}}{L} \left[1 - \left(\frac{\varepsilon\varphi^{(n)}}{L} \right)^2 \frac{K}{2} \right] (t - s) ds, \tag{7.24}$$

where the r_n , for $n = 1, 2, \dots$, are given by

$$r_n = \begin{cases} \frac{\sin \varphi^{(n)}(1 - \theta)}{\theta \sin^2 \varphi^{(n)}(1 - \theta) + (1 - \theta) \cos^2 \varphi^{(n)}\theta + \frac{\hat{E}}{qL} \sin^2 \varphi^{(n)}(1 - \theta) \cos^2 \varphi^{(n)}\theta} & \text{if } \varphi^{(n)} \neq \frac{2n - 1}{2}\pi, \\ 1, & \text{if } \varphi^{(n)} = \frac{2n - 1}{2}\pi. \end{cases} \tag{7.25}$$

8. Numerical results

We performed several numerical computations in order to illustrate these results. For this purpose, we used the example of the composite described in [Chen and Fish 2001]. For all calculations, $L = 40$ m and $\varepsilon = 0.2$ m. The periodic cell is composed of two homogeneous materials with properties $E_1 = 120$ GPa, $E_2 = 6$ GPa, $\rho_1 = 8000$ kg/m³, and $\rho_2 = 3000$ kg/m³, distributed on the periodic cell with a volume ratio of $\nu = 0.5$. This gives $\hat{c} = (\hat{E}/\hat{\rho})^{1/2} = 1441.5$ m/s and $K = 0.03849$ m².

8A. Propagation of an initial disturbance. To verify the efficacy of the results obtained, we compared our formulation to the method proposed in [Chen and Fish 2001]. Consider the problem of an initial disturbance from the steady state with homogeneous boundary conditions at points $x = 0$ and $x = L$,

$$(E_\varepsilon u_x)_x - \rho_\varepsilon u_{tt} = 0, \quad u(0, t) = 0, \quad E_\varepsilon(L)u_x(L, t) = 0, \quad u(x, 0) = f(x), \quad u_t(x, 0) = 0.$$

The method proposed here yields an analytic solution for $\hat{u} = \langle u \rangle$ (to a second-order approximation), as described in Section 7A,

$$\hat{u}(x, t) = \sum_{n=0}^{\infty} f^{(n)} \sin \frac{(2n-1)\pi x}{2L} \cos \left[\frac{(2n-1)\pi \hat{c}}{2L} \left(1 - \left[\frac{(2n-1)\pi \varepsilon}{2L} \right]^2 \frac{K}{2} \right) t \right], \quad (8.1)$$

where

$$f^{(n)} = \frac{2}{L} \int_0^L f(x) \sin \frac{2n-1}{2} \frac{\pi x}{L} dx, \quad K = \frac{\kappa}{\hat{E}} = \frac{1}{\hat{E}} \langle EN_{3,\xi} + EN_2 - \hat{c}^2 \rho N_2 \rangle.$$

To reproduce the conditions given in [Chen and Fish 2001], we worked with following class of initial disturbances:

$$f(x) = \frac{f_0}{\delta^8} (x - (x_0 - \delta))^4 (x - (x_0 + \delta))^4 (1 - H(x - x_0 - \delta))(1 - H(x_0 - \delta - x)), \quad (8.2)$$

where $H(x)$ is the Heaviside step function, and f_0 , δ , and x_0 are the magnitude, half-width, and center coordinate of the pulse. For calculations, we only considered pulses of magnitude $f_0 = 1$ centered at $x_0 = 20$ m with different values for the half-width $\delta = 1.4$ m, $\delta = 0.8$ m, and $\delta = 0.6$ m, illustrated in Figure 2. These values were selected to evaluate the effect of the typical width of the disturbance and the size of the RVE.

The results of the comparison are shown in Figure 3. They agree well with those given in [Chen and Fish 2001] and corroborate the conclusion that asymptotic homogenization does not give good results if the characteristic size of the initial perturbation is comparable to the size of the periodic cell. According to the method of Chen and Fish, this discrepancy can be seen for long observation times. Our model demonstrates that this discrepancy should appear if the length traveled by the initial perturbation is

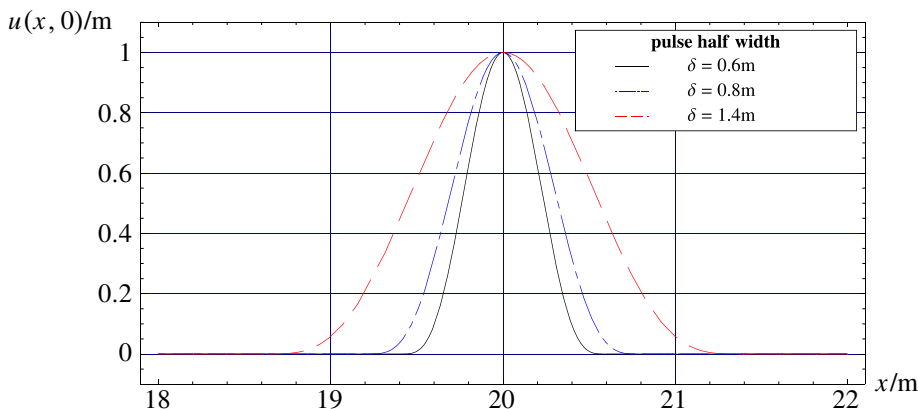


Figure 2. Shape and position of the initial pulses used for numerical illustration.

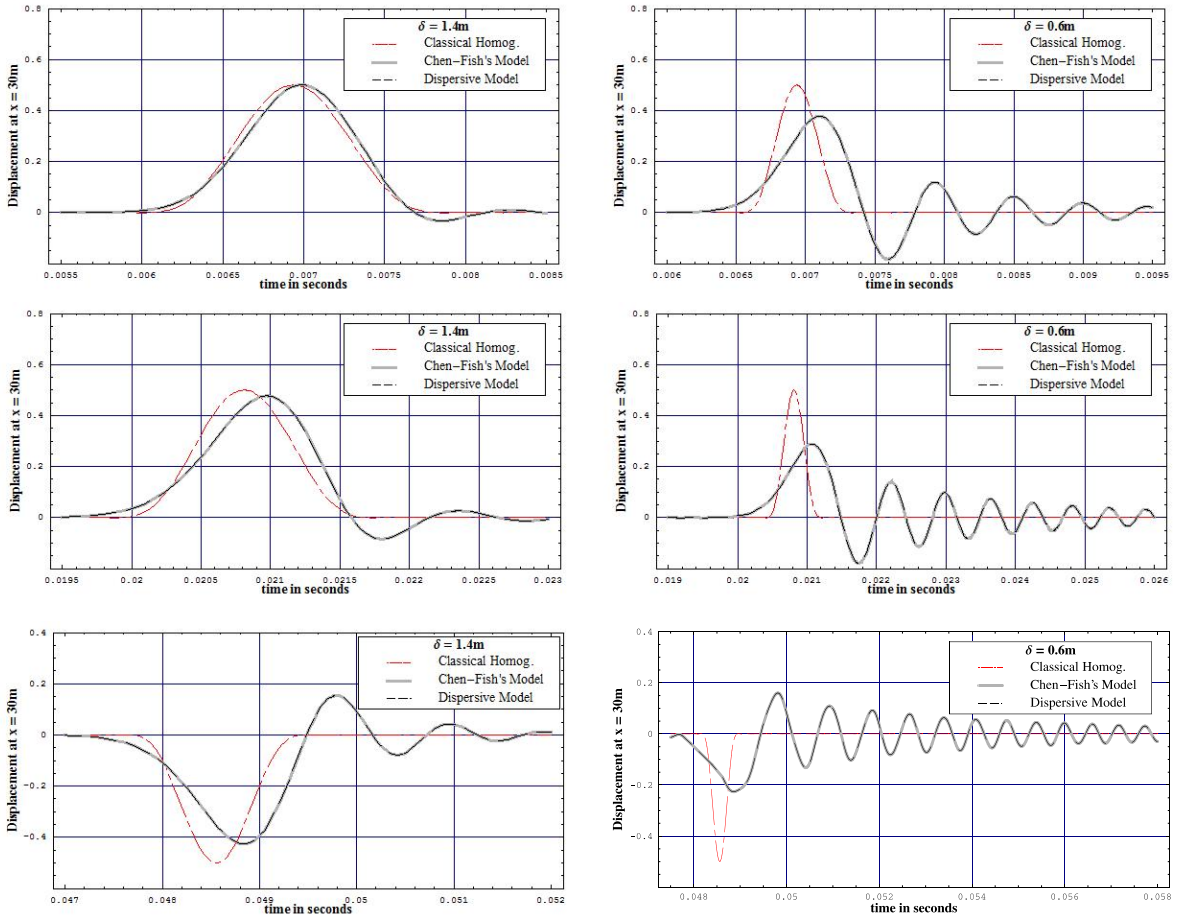


Figure 3. Value of the solution at $x = 30$ m for $\delta = 1.4$ m (left column) and for $\delta = 0.6$ m (right column) as a function of time.

relatively large (of order $O(1/\varepsilon)$). In the left column of the figure, it is apparent that classical asymptotic homogenization can be applied provided that the distance traveled by the wave front is not too large. The same is not true when the width of the perturbation is 4 times the size of the periodic cell and the distance traveled is larger than 20 m, as shown in the right column.

8B. Traveling pulse. We next illustrate the results of the proposed method by describing the behavior of a traveling pulse under the dispersion effect induced by the heterogeneous periodic structure of the composite material. We consider the case of a pulse applied to one end, $x = 0$, with free load conditions on the other end, $x = L$. If the process starts from static equilibrium, the problem is described by

$$(E_\varepsilon u_x)_x - \rho_\varepsilon u_t t = 0, \quad u(0, t) = \mu(t), \quad E_\varepsilon(L)u_x(L, t) = 0, \quad u(x, 0) = 0, \quad u_t(x, 0) = 0. \quad (8.3)$$

The proposed method gives the following analytic solution (up to second order) for $\hat{u} = \langle u \rangle$, as seen in [Section 7B](#):

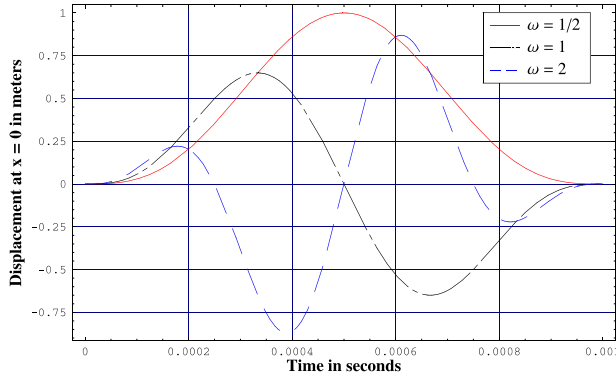


Figure 4. Different pulses used for numerical illustration.

$$\hat{u}(x, t) = \frac{2\hat{c}}{L} \sum_{n=1}^{\infty} \left[1 - \left(\frac{\varepsilon(2n-1)\pi}{2L} \right)^2 \frac{K}{2} \right] \sin \frac{(2n-1)\pi x}{2L} \times \int_0^t \mu(s) \sin \frac{(2n-1)\pi \hat{c}}{2L} \left[1 - \left(\frac{\varepsilon(2n-1)\pi}{2L} \right)^2 \frac{K}{2} \right] (t-s) ds. \quad (8.4)$$

The following type of pulses will be considered:

$$\mu(t) = \frac{A}{2} \left(1 - \cos \frac{2\pi t}{d} \right) \sin \frac{2\pi \omega t}{d} H \left(1 - \frac{t^2}{d^2} \right), \quad (8.5)$$

where $H(x)$ is the Heaviside step function, and A , d , and ω are the magnitude, duration, and number of oscillations. The shapes of these pulses for $A = 1$ m, $d = 0.001$ s, and $\omega = \frac{1}{2}, 1, 2$ are illustrated in Figure 4. For numerical experimentation we considered only these values of A , d and ω .

The results for $\omega = \frac{1}{2}$ are shown in Figure 5, left. The pulse shapes as a function of t are indicated by a dashed line for the classical asymptotic homogenization and by a solid line for the dispersive model. A decrease of the pulse amplitude due to the dispersion effect and wiggles behind the wave front predicted by the dispersive model are apparent. For greater distances traveled by the pulse, the dispersive effect becomes more pronounced. At larger values of ω , the effect appears earlier, at smaller distances. The explanation for this is that for larger values of ω the characteristic size of pulse shape variation becomes

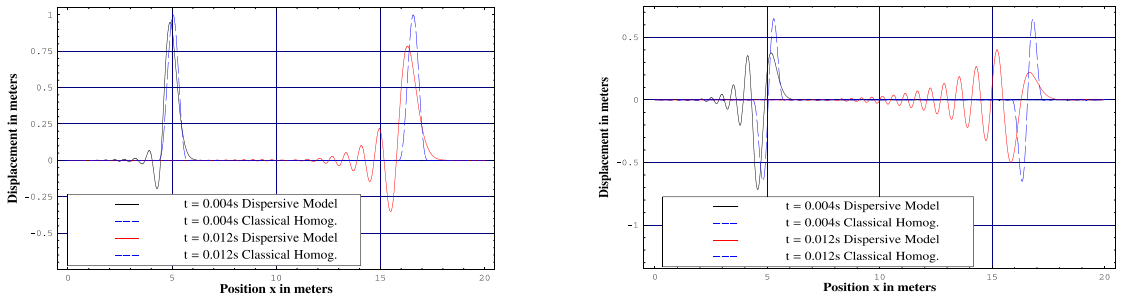


Figure 5. Prediction of the evolution of the pulse shape for $\omega = \frac{1}{2}$ (left) and $\omega = 1$ (right), and for times $t = 0.004$ s and $t = 0.012$ s, using standard asymptotic homogenization (dashed line) and the proposed dispersive model (solid line).

smaller and approaches the size of the periodic cell, producing more reflections and refractions at the interfaces separating component materials. This effect is also observed in Figure 5, right, for the evolution of the pulse shape when $\omega = 1$.

8C. Interaction with failures. Next we consider numerical descriptions of the behavior of a traveling pulse when a failure in the periodic structure composite is present. A failure in the material is modeled by a dimensionless spring with elasticity constant q . The boundary conditions and equation of motion describing wave propagation under these assumptions are given in (8.3). The failure is accounted for mathematically by including conditions (7.15) on the displacements functions $u(x, t)$ at a point θL , $0 < \theta < 1$, belonging to the interval $[0, L]$.

Using the proposed method as in Section 7C, the expression for $\hat{u} = \langle u \rangle$ becomes

$$\hat{u}(x, t) = 2 \frac{\hat{c}}{L} \sum_{n=1}^{\infty} r_n \left[1 - \left(\frac{\varepsilon \varphi^{(n)}}{L} \right)^2 \frac{K}{2} \right] \hat{X}_n(x) \int_0^t \mu(s) \sin \frac{\hat{c} \varphi^{(n)}}{L} \left[1 - \left(\frac{\varepsilon \varphi^{(n)}}{L} \right)^2 \frac{K}{2} \right] (t-s) ds, \quad (8.6)$$

where K and $\hat{c} = (\hat{E}/\hat{\rho})^{1/2}$ are material constants, the $\varphi^{(n)}$, for $n = 1, 2, \dots$, are the roots of

$$\cos \varphi - \frac{\hat{E}}{qL} \varphi \cos \varphi \theta \sin \varphi (1 - \theta) = 0, \quad (8.7)$$

the values of r_n are given in (7.25), and the functions \hat{X}_n , in this case, are piecewise defined as in (7.20) for $\varphi^{(n)} \neq (n - \frac{1}{2})\pi$, and

$$\hat{X}_n(x) = \sin \frac{(2n-1)\pi x}{2L} \quad \text{for } \varphi^{(n)} = (n - \frac{1}{2})\pi.$$

We will work with the same type of pulses as in (8.5), again with $A = 1$ m, $d = 0.001$ s and $\omega = \frac{1}{2}, 1$.

The n -th root $\varphi^{(n)}$ of (8.7) lies in the interval $(0, \pi/2]$ for $n = 1$ and in $((2n-3)\pi/2, (2n-1)\pi/2]$ for $n > 1$. A variant of Newton’s method was used to find the roots numerically. Figure 6 shows the

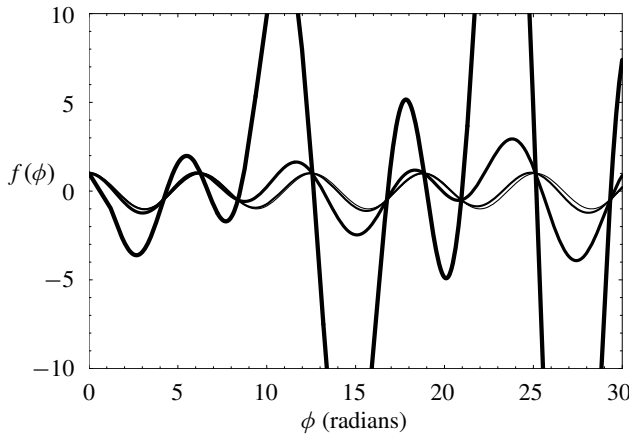


Figure 6. Plots of the function $f(\varphi) = \cos \varphi - (\hat{E}/qL)\varphi \cos \varphi \theta \sin \varphi (1 - \theta)$ against φ over the interval $[0, 9\pi]$ for $\theta = 1/4$ and different choices of q . Thicker lines and wider variations correspond to low q ; in order, $q = 2 \times 10^8$ N/m² ($\hat{E}/qL = 1.429$), 2×10^9 N/m² (0.143), 2×10^{10} N/m² (0.014), and ∞ (0).

distribution of roots on the real axis for $f(\varphi) = \cos \varphi - (\hat{E}/qL)\varphi \cos \varphi \theta \sin \varphi (1 - \theta)$, $\theta = \frac{1}{4}$, and several values of q . Solutions to (8.7) are given by the intersections of $f(\varphi)$ with the φ -axis.

Once the quantities $\varphi^{(n)}$ and the roots of (8.7) are found, (8.6) can be evaluated. presented in the following examples. The results are illustrated in Figures 7 and 8 for $\omega = \frac{1}{2}$ and $\omega = 1$, and $q = 2 \cdot 10^8 \text{ N/m}^3$, $q = 2 \cdot 10^9 \text{ N/m}^3$, and $q = 2 \cdot 10^{10} \text{ N/m}^3$. We also set $\theta = \frac{1}{4}$; that is, the failure occurs at $x = 10 \text{ m}$.

The pulse shapes for different values of t are shown for the classical asymptotic homogenization (dashed line) and for the dispersive model (solid line). In these figures, the evolution of the pulse shape after reaching the point of failure $x = 10 \text{ m}$ is illustrated for two values of the constant q (recall that low q means severe debonding). For $q = 2 \cdot 10^8 \text{ N/m}^3$, the reflection of the pulse at the point of failure is almost complete for both cases. In contrast, for the larger value $q = 2 \cdot 10^{10} \text{ N/m}^3$, the pulse splits and two traveling perturbations emanate from the point of failure, instead of one. Also, in contrast to the classical

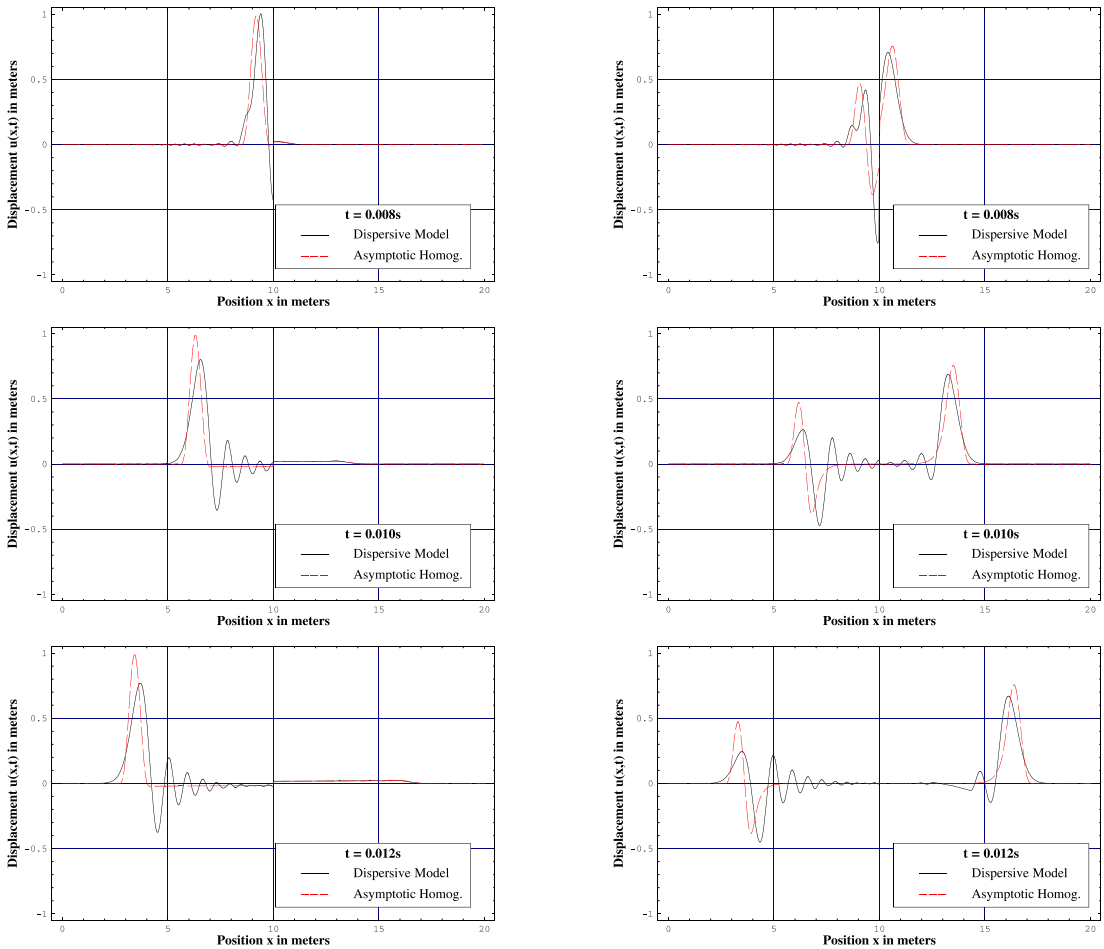


Figure 7. Prediction of the evolution of the pulse shape for $\omega = \frac{1}{2}$ and $q = 2 \cdot 10^8 \text{ N/m}^3$ (left) or $q = 2 \cdot 10^{10} \text{ N/m}^3$ (right), at times $t = 0.008 \text{ s}$, $t = 0.010 \text{ s}$ and $t = 0.012 \text{ s}$ after the pulse reaches the point of failure, $x = 10 \text{ m}$, using standard asymptotic homogenization (dashed line) and the proposed dispersive model (solid line).

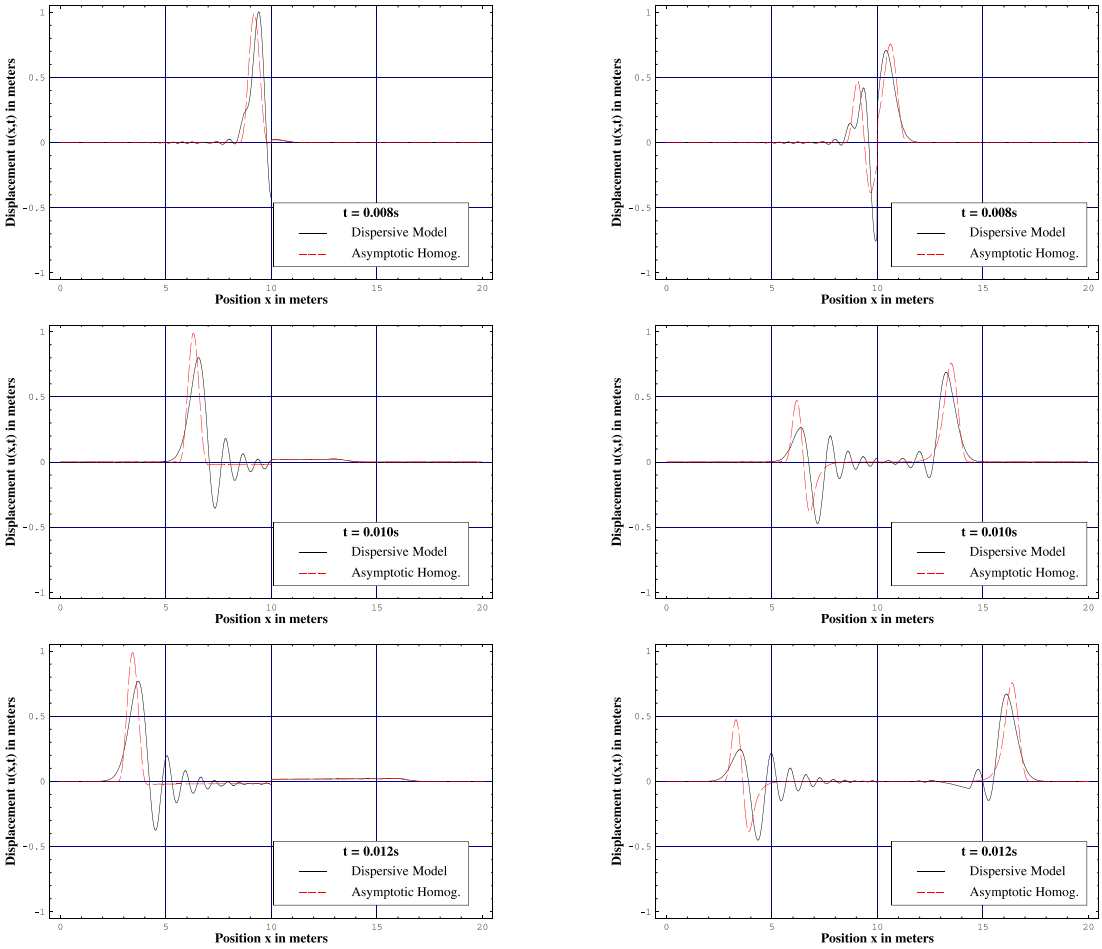


Figure 8. Prediction of the evolution of the pulse shape for $\omega = 1$ and $q = 2 \cdot 10^8 \text{ N/m}^3$ (left) or $q = 2 \cdot 10^{10} \text{ N/m}^3$ (right), at times $t = 0.008 \text{ s}$, $t = 0.010 \text{ s}$ and $t = 0.012 \text{ s}$ after the pulse reaches the point of failure, $x = 10 \text{ m}$, using standard asymptotic homogenization (dashed line) and the proposed dispersive model (solid line).

asymptotic homogenization, the pulse shape described by the dispersive model becomes distorted. Thus the dynamical responses, translated by the reflected and transmitted perturbations after interaction with the failure, are different for each approach, and more noticeably so for larger ω .

Conclusions

In this work, an asymptotic model for describing wave propagation in periodic composites was proposed. In this approach, the heterogeneous nature of the composite introduces a perturbation in the principal frequencies relative to the homogenized problem. As a result, no new temporal scales need be considered. Instead, a regular asymptotic expansion for the eigenfrequencies is obtained from the condition of boundedness for the solution. The results are graphically illustrated for different types of boundary problems. The model is asymptotically valid for low frequency wave propagation.

This approach describes the dispersion effects in periodic composites, and we have discussed the differences between this model and the classical asymptotic homogenization. This model provides a starting point for the study of frequency perturbations in laminated composites when the angle of incidence is not perpendicular to the laminates, and the periodicity take place at small scales.

Appendix: Closed form expression of κ

We present the calculation of the constant $\kappa = \langle EN_{3,\xi} + EN_2 - \hat{c}^2 \rho N_2 \rangle$. First, (4.12) is solved to find

$$\frac{dN_1}{d\xi} = \frac{\hat{E}}{E} - 1, \tag{A.1}$$

and consequently,

$$N_1 = B - \langle B \rangle, \tag{A.2}$$

where B is given in (5.28). Considering the second local problem described in (4.21) and (4.12), we have $(EN_{2,\xi} + EN_1)_{,\xi} = \hat{E}(\rho/\hat{\rho} - 1)$. Because N_1 has a null average, it can be deduced that

$$EN_{2,\xi} + EN_1 = \hat{E} \left(R - \left\langle \frac{\hat{E}}{E} R \right\rangle \right), \tag{A.3}$$

and R is given in (5.28). Substituting the formula for N_1 gives

$$N_{2,\xi} = \frac{\hat{E}}{E} \left(R - \left\langle \frac{\hat{E}}{E} R \right\rangle \right) - B + \langle B \rangle. \tag{A.4}$$

Now, the equation (5.12) of the third local problem is multiplied by N_1 and averaged over the period to obtain

$$\langle N_1 (EN_{3,\xi} + EN_2)_{,\xi} \rangle = - \langle N_1 (EN_{2,\xi} + EN_1 - \hat{c}^2 \rho N_1) \rangle. \tag{A.5}$$

Integrating the left-hand side by parts and using (A.1) and the equality $\langle N_2 \rangle = 0$, we find that

$$\langle N_1 (EN_{3,\xi} + EN_2)_{,\xi} \rangle = - \langle N_{1,\xi} (EN_{3,\xi} + EN_2) \rangle = - \left\langle \left(\frac{\hat{E}}{E} - 1 \right) (EN_{3,\xi} + EN_2) \right\rangle = \langle EN_{3,\xi} + EN_2 \rangle.$$

On the other hand, $-\langle \rho \hat{c}^2 N_2 \rangle = -\hat{E} \left\langle \frac{\rho}{\hat{\rho}} N_2 \right\rangle = \hat{E} \left\langle R \frac{dN_2}{d\xi} \right\rangle$. Together with (A.5), this leads to

$$\langle EN_{3,\xi} + EN_2 - \hat{c}^2 \rho N_2 \rangle = \left\langle \hat{E} R \frac{dN_2}{d\xi} - N_1 (EN_{2,\xi} + EN_1 - \hat{c}^2 \rho N_1) \right\rangle. \tag{A.6}$$

Substituting equations (A.2) and (A.3), we obtain (5.29).

References

- [Bakhvalov and Panasenko 1989] N. Bakhvalov and G. Panasenko, *Homogenisation: averaging processes in periodic media*, Kluwer, Dordrecht, 1989.
- [Bensoussan et al. 1978] A. Bensoussan, G. C. Papanicolaou, and J. L. Lions, *Asymptotic analysis for periodic structures*, North Holland, Amsterdam, 1978.
- [Castillero et al. 1998] J. B. Castillero, J. A. Otero, R. R. Ramos, and A. Bourgeat, “Asymptotic homogenization of laminated piezocomposite materials”, *Int. J. Solids Struct.* **35**:5–6 (1998), 527–541.

- [Chen and Fish 2001] W. Chen and J. Fish, “A dispersive model for wave propagation in periodic heterogeneous media based on homogenization with multiple spatial and temporal scales”, *J. Appl. Mech. (ASME)* **68**:2 (2001), 153–161.
- [Fish and Chen 2001] J. Fish and W. Chen, “Higher-order homogenization of initial/boundary-value problem”, *J. Eng. Mech. (ASCE)* **127**:12 (2001), 1223–1230.
- [Guinovart-Díaz et al. 2005] R. Guinovart-Díaz, R. Rodríguez-Ramos, J. Bravo-Castillero, F. J. Sabina, and G. A. Maugin, “Closed-form thermoelastic moduli of a periodic three-phase fiber-reinforced composite”, *J. Therm. Stresses* **28**:10 (2005), 1067–1093.
- [Parnell and Abrahams 2006] W. J. Parnell and I. D. Abrahams, “Dynamic homogenization in periodic fibre reinforced media: quasi-static limit for SH waves”, *Wave Motion* **43**:6 (2006), 474–498.
- [Pobedria 1984] B. E. Pobedria, *Mechanics of composite materials*, Moscow State University Press, Moscow, 1984.
- [Sánchez-Huber and Sánchez-Palencia 1992] J. Sánchez-Huber and E. Sánchez-Palencia, *Introduction aux méthodes asymptotiques et à l’homogénéisation*, Masson, Paris, 1992.
- [Santosa and Symes 1991] F. Santosa and W. W. Symes, “A dispersive effective medium for wave propagation in periodic composites”, *SIAM J. Appl. Math.* **51**:4 (1991), 984–1005.
- [Schwartz 1966] L. Schwartz, *Mathematics for the physical sciences*, Hermann, Paris, 1966.
- [Sjöberg et al. 2005] D. Sjöberg, C. Engström, G. Kristensson, D. J. N. Wall, and N. Wellander, “A Floquet–Bloch decomposition of Maxwell’s equations applied to homogenization”, *Multiscale Model. Simul.* **4**:1 (2005), 149–171.
- [Vivar-Pérez et al. 2005] J. Vivar-Pérez, J. Bravo-Castillero, R. Rodríguez-Ramos, and M. Ostoja-Starzewski, “Homogenization of a micro-periodic helix”, *Philos. Mag.* **85**:33-35 (2005), 4201–4212.
- [Vivar-Pérez et al. 2006] J. Vivar-Pérez, J. Bravo-Castillero, R. Rodríguez-Ramos, and M. Ostoja-Starzewski, “Homogenization of a micro-periodic helix with parabolic or hyperbolic heat conduction”, *J. Therm. Stresses* **29**:5 (2006), 467–483.
- [Wang and Rokhlin 2002a] L. Wang and S. I. Rokhlin, “Floquet wave homogenization of periodic anisotropic media”, *J. Acoust. Soc. Am.* **112**:1 (2002), 38–45.
- [Wang and Rokhlin 2002b] L. Wang and S. I. Rokhlin, “Floquet wave ultrasonic method for determination of single ply moduli in multidirectional composites”, *J. Acoust. Soc. Am.* **112**:3 (2002), 916–924.

Received 8 Mar 2009. Accepted 17 May 2009.

JUAN MIGUEL VIVAR-PÉREZ: jm@matcom.uh.cu

Facultad de Matemática y Computación, Universidad de La Habana, San Lázaro esq. L, Vedado, Habana 4, CP 10400, Cuba

ULRICH GABBERT: ulrich.gabbert@mb.uni-magdeburg.de

Facultät für Maschinbau, Otto-von-Guericke Universität, Universitätsplatz 2, 39106 Magdeburg, Germany

HARALD BERGER: harald.berger@mb.uni-magdeburg.de

Facultät für Maschinbau, Otto-von-Guericke Universität, Universitätsplatz 2, 39106 Magdeburg, Germany

REINALDO RODRÍGUEZ-RAMOS: reinaldo@matcom.uh.cu

Facultad de Matemática y Computación, Universidad de La Habana, San Lázaro esq. L, Vedado, Habana 4, CP 10400, Cuba

JULIÁN BRAVO-CASTILLERO: jbravo@matcom.uh.cu

Facultad de Matemática y Computación, Universidad de La Habana, San Lázaro esq. L, Vedado, Habana 4, CP 10400, Cuba

RAUL GUINOVART-DÍAZ: guino@matcom.uh.cu

Facultad de Matemática y Computación, Universidad de La Habana, San Lázaro esq. L, Vedado, Habana 4, CP 10400, Cuba

FEDERICO J. SABINA: fjs@mym.iimas.unam.mx

Instituto de Investigaciones en Matemáticas Aplicadas y en Sistemas, Universidad Nacional Autónoma de México, Apartado Postal 20-726, Delegación de Álvaro Obregón, 01000 México, DF, Mexico

A COCHLEAR MODEL USING THE TIME-AVERAGED LAGRANGIAN AND THE PUSH-PULL MECHANISM IN THE ORGAN OF CORTI

YONGJIN YOON, SUNIL PURIA AND CHARLES R. STEELE

In our previous work, the basilar membrane velocity V_{BM} for a gerbil cochlea was calculated and compared with physiological measurements. The calculated V_{BM} showed excessive phase excursion and, in the active case, a best-frequency place shift of approximately two fifths of an octave higher. Here we introduce a refined model that uses the time-averaged Lagrangian for the conservative system to resolve the phase excursion issues. To improve the overestimated best-frequency place found in the previous feed-forward active model, we implement in the new model a *push-pull mechanism* from the outer hair cells and phalangeal process. Using this new model, the V_{BM} for the gerbil cochlea was calculated and compared with animal measurements. The results show excellent agreement for mapping the location of the maximum response to frequency, while the agreement for the response at a fixed point as a function of frequency is excellent for the amplitude and good for the phase.

A list of symbols can be found on page 985.

1. Introduction

The cochlea of the inner ear transforms the input sound into output neural excitation. The basic model consists of a long, straight box of fluid with a flat lengthwise partition. The spiral coiling of the cochlea is neglected, as it has been shown to have little effect on the model response [Loh 1983; Steele and Zais 1985]. The partition has an elastic portion called the *basilar membrane* (BM). Generally, this membrane is narrow and thick, and therefore stiff, at the input end, where it connects with stapes, and wide and thin, and consequently flexible, at the far end, the apex. From a sinusoidal pressure input, a traveling fluid-elastic wave is generated on the BM.

For a fixed frequency of input, experiments show a traveling wave on the BM that builds to a peak at a certain point and then rapidly decays as it moves further. The location of the peak depends on frequency; thus each point has a “best frequency” (BF) that causes the maximum amplitude of the BM response. In the actual cochlea, a sensory epithelium, called the organ of Corti, is attached to the BM. The organ of Corti contains the sensory hair cells, which respond to the BM motion and initiate neural excitation. However, three rows of outer hair cells (OHC) are piezoelectric and most likely provide an amplification of the wave for low input amplitude; this is known as the *active mechanism*. Because of the geometry of the outer hair cells, a feed-forward approximation can be used in the cochlear model. Two-dimensional [Geisler and Sang 1995] and three-dimensional models with the active feed-forward mechanism have been employed [Steele et al. 1993; Lim and Steele 2002; Yoon et al. 2007].

Keywords: cochlear active model, basilar membrane velocity, outer hair cell, push-pull mechanism, gerbil.
Work supported by the NIDCD of the National Institutes of Health through grant no. R01-DC007910.

In the present work, we improve on this previous feed-forward active model with further consideration of the actual geometry. For the low amplitude of sound intensity, there is significant energy feedback that enhances the wave. Located on the elastic region is the organ of Corti, which contains the sensory hair cells in an interesting arrangement of structural elements. A possible explanation for the form is derived from an analysis of the effect of the electromotile (piezoelectric) expansion and contraction of the outer hair cells which is known as OHC motility. This motility causes a positive spatial “feed-forward” of force on the basilar membrane (the “push”) as well as a negative “feed-backward” of force (the “pull”) from the phalangeal process. These push and pull mechanism work together to provide a two order of magnitude increase in the amplitude of the wave for the short wavelengths, but cancel each other out for the long wavelengths. Thus, the significant enhancement occurs in a narrow band of spatial wavelengths, without the need for special filtering or tuning. The calculations for the simple box model of the cochlea with the push-pull mechanism and the “time-averaged Lagrangian” method [Steele and Taber 1979] yield results very similar to gerbil measurements [Ren and Nuttall 2001].

2. Mathematical methods

Passive cochlear model. The physical cochlea is modeled as a straight-tapered fluid-filled chamber with rigid walls. The chamber is divided longitudinally by the flexible orthotropic plate into two equal rectangular ducts, which represent the *scala vestibuli* and *scala tympani*. The two fluid ducts are joined at the apical end of the chamber by a hole, representing the *helicotrema*. The flexible plate represents the pectinate zone of the basilar membrane, which bends under the motion of the fluid driven by the stapes motion. A schematic drawing of the model is shown in Figure 1.

The equations of the system are formulated in the frequency domain. Harmonic excitation is applied at the stapes and the steady-state response of the system is considered. The equation for wave propagation in the passive model is obtained by equating the time-averaged kinetic and potential energies of the conservative system. The detailed derivations and features for the passive mechanics were described in [Steele and Taber 1979]. Briefly, the three-dimensional fluid equations are integrated over the cross section to obtain the relation between volume flow and fluid pressure, using a Fourier series expansion.

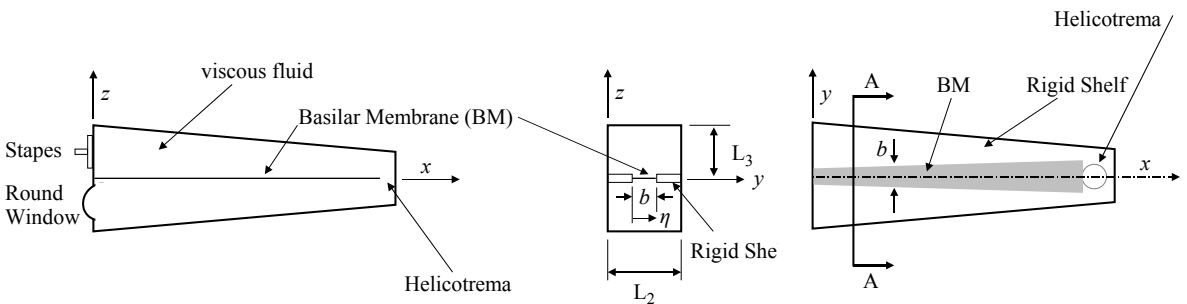


Figure 1. Geometric layout of the passive cochlear model: from left to right, side view, cross section (A-A), and top view. Distances are parameterized in cartesian coordinates, x representing the distance from the stapes, y the distance across the scala width, and z the height above the partition.

The time-averaged kinetic energy of the fluid (T_f) and of the elastic basilar membrane (T_p) are then obtained, as is the time-averaged potential energy of the plate (V_p). By equating the time-averaged kinetic and potential energies of the system, the eikonal equation is obtained, which can be written as

$$L = T_f + T_p - V_p = F(n, \omega)W(x)^2 \left(\int_0^b \eta^2(\xi) d\xi \right) = 0. \tag{1}$$

This gives the phase relation for the active case, $F(n, \omega) = 0$, where b is the BM width, n is the wavenumber, and ω is the frequency. Here, L is the time-averaged Lagrangian density of the system, $W(x)$ the amplitude of the wave envelope, and $\eta(\xi) = \sin(\pi \xi / b)$ the shape function for simply-supported edges; the coordinate ξ has its origin at one edge of the BM.

Active cochlear model: push-pull mechanism. For the push-pull active model, the arrangement of the organ of Corti is indicated in Figure 2. If the OHCs expand, the Deiters rod at the horizontal distance $x + \Delta x_1$ will be pushed down by the OHC with the apex at x , and pulled up by the phalangeal process connected to the OHC with the apex at $x + \Delta x_2$. The force in an OHC is proportional to the shear force on the cilia at the apex, which is approximately equal to the total force acting on the BM. This push-pull mechanism is quantified by writing the total force on the BM as

$$F_{PZ} = 2F_{BM}^f + F_{BM}^c. \tag{2}$$

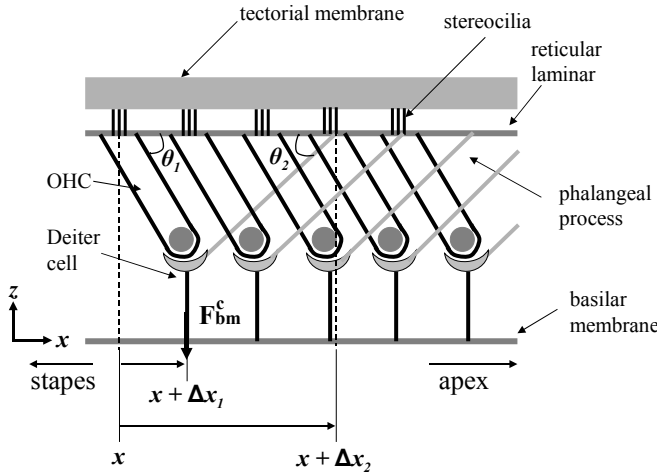


Figure 2. Schematic longitudinal view of the organ of Corti, showing the tilt of the outer hair cells. For one hair cell with apex at the distance x , the base is at $x + \Delta x_1$; the phalangeal process connected at the base attaches to the upper surface at $x + \Delta x_2$; the OHC angle is θ_1 ; and θ_2 is the angle of the phalangeal process angle with the reticular lamina. The force on the BM through the Deiters rod is F_{BM}^c , which consists of the downward push from an expansion of the hair cell at x and an upward pull through the phalangeal process from an expansion of the hair cell at $x + \Delta x_2$.

in which F_{BM}^C is the force due to the OHCs, and F_{BM}^f is the force due to the fluid on one side. The force acting through the Deiters rod at $x + \Delta x_1$ is

$$F_{BM}^C(x + \Delta x_1) = \alpha_1(2F_{BM}^f(x) + F_{BM}^C(x)) - \alpha_2(2F_{BM}^f(x + \Delta x_2) + F_{BM}^C(x + \Delta x_2)), \tag{3}$$

in which the gains from the push and the pull are α_1 and α_2 , respectively, while Δx_1 is the longitudinal distance between the apex and the base of the OHC, which depends on the length l_{OHC} of the OHC and its angle θ_1 with respect to the longitudinal direction to the reticular lamina (see [Figure 2](#)):

$$\Delta x_1 = l_{OHC} \cos \theta_1. \tag{4}$$

Moreover $\Delta x_2 - \Delta x_1$ is the longitudinal distance between the base and the apex of the phalangeal process, which depends on the length l_p of the phalangeal process and its angle θ_2 with respect to the longitudinal direction of the reticular lamina:

$$\Delta x_2 - \Delta x_1 = l_p \cos \theta_2. \tag{5}$$

Based on the geometric relationship between OHC and phalangeal process, l_p can be expressed as

$$l_p = l_{OHC} \frac{\sin \theta_1}{\sin \theta_2}. \tag{6}$$

By (5) and (6), $\Delta x_2 - \Delta x_1$ can be reduced without l_p :

$$\Delta x_2 - \Delta x_1 = l_{OHC} \sin \theta_1 \cot \theta_2. \tag{7}$$

From the phase integral, (3) reduces to

$$F_{BM}^C e^{in\Delta x_1} = \alpha_1(2F_{BM}^f + F_{BM}^C) - \alpha_2(2F_{BM}^f + F_{BM}^C) e^{in\Delta x_2}. \tag{8}$$

The force from the OHC motility is related to the fluid force:

$$F_{BM}^C = \frac{2(\alpha_1\Gamma_1 - \alpha_2\Gamma_2)F_{BM}^f}{1 - \alpha_1\Gamma_1 + \alpha_2\Gamma_2}, \tag{9}$$

where

$$\Gamma_1 = e^{-in\Delta x_1} \quad \text{and} \quad \Gamma_2 = e^{in(\Delta x_2 - \Delta x_1)}.$$

Therefore, the total force on the BM from (2) is

$$F_{PZ} = 2 \left(1 + \frac{(\alpha_1\Gamma_1 - \alpha_2\Gamma_2)}{(1 - \alpha_1\Gamma_1 + \alpha_2\Gamma_2)} \right) F_{BM}^f = \frac{2F_{BM}^f}{1 - \alpha_1\Gamma_1 + \alpha_2\Gamma_2}. \tag{10}$$

Matching the force to the displacement of the fluid and the OHC to the BM stiffness yields the eikonal (dispersion) relation of the active model. We consider a positive value of α_2 to be a negative feedback effect of the phalangeal processes. Because of the flexibility of the upper surface consisting of the tectorial membrane and the reticular lamina in [Figure 2](#), the upward and downward forces tend to cancel each other, so that $\alpha_1 = \alpha_2$. Then, for the long wavelength, i.e., the small values of the wave number n , the push-pull effect in (2) are negligible, while for very short wavelengths, the fluid viscosity dominates. Thus, the push-pull is effective only in a band of wavelengths. It is assumed that OHC force production does not roll off with frequency and thus α_1 and α_2 are constant with frequency. Although this is controversial,

there is evidence that suggests that OHCs can generate forces for frequencies up to 50 kHz [Rabbitt 2008].

Wave propagation of BM plate. An energy approach is used involving variational calculus which is applied to the time-averaged Lagrangian density L of the system Equation (1). Independent variation of n and $W(x)$ yields the Euler–Lagrange equations

$$\frac{\partial L}{\partial W} = 2F(n, \omega)W(x) \left(\int_0^b \eta^2(\xi) d\xi \right) = 0, \quad (11)$$

$$\frac{d}{dx} \frac{\partial L}{\partial n} = \frac{d}{dx} \left[\frac{\partial F(n, \omega)}{\partial n} W^2(x) \left(\int_0^b \eta^2(\xi) d\xi \right) \right] = 0. \quad (12)$$

The eikonal equation is obtained using (11):

$$F(n, \omega) = 0. \quad (13)$$

The amplitude function, $W(x)$, which is the solution of the transport equation (12), is expressed as

$$W(x) = C \left(\frac{\partial F(n, \omega)}{\partial n} b \right)^{-1/2}, \quad (14)$$

where C is a constant determined from the boundary condition.

Hamilton’s principle is valid only for a conservative system; however, nonconservative terms can be added to the Lagrange equations of motion. Thus, we extend Equation (11) and (12) to the push-pull active model to obtain the eikonal and transport equation.

Ratio of the BM velocity to the stapes velocity. For a given harmonic excitation frequency ω , the eikonal equations for the passive and active case are solved to give the wavenumber (n) by using Newton–Raphson iterative scheme for each cross section along the cochlear duct. Once n is determined, the ratio of the BM velocity V_{BM} to the stapes velocity V_{st} is obtained. With the stapes motion defined as positive outward, the ratio at $x = x^*$ is

$$\left(\frac{V_{BM}}{V_{st}} \right)_{x=x^*} = \frac{2nA_{st}}{b_{x=0}} \left[\frac{(b \partial F(n, \omega) / \partial n)_{x=0}}{(b \partial F(n, \omega) / \partial n)_{x=x^*}} \right] \exp\left(\frac{\pi}{2} - \int n dx \right), \quad (15)$$

where A_{st} is the stapes foot-plate area.

Modification for nonconservative system. An extension of the time-averaged Lagrangian method to nonconservative systems is given in [Jimenez and Whitham 1976], in which the adjoint is considered. An alternate approach is to consider the reciprocity principle. For a linear elastic system, consider two independent solutions, denoted by superscript ⁽¹⁾ and ⁽²⁾. The stress from (2) multiplied by the displacement of (1) subtracted from the stress from (1) multiplied by the displacement from (2), integrated over the entire surface, must be zero. In standard notation this is

$$\int \mathbf{n} \cdot (\boldsymbol{\sigma}^{(1)} \cdot \mathbf{u}^{(2)} - \boldsymbol{\sigma}^{(2)} \cdot \mathbf{u}^{(1)}) d\Sigma = 0. \quad (16)$$

This depends on the symmetry of the tensor of elastic constants. The symmetry is preserved when dealing with viscoelastic materials, including a viscous fluid, and working in the frequency domain, for which

the coefficients are complex-valued. For a tube such as the cochlea, in which no work is done on the side walls, the integral over one end is the negative of that over the other end. Since the sign change is due to the change in the direction \mathbf{n} , the integral itself must be constant with the distance along the tube. So one solution is taken with a positive exponential,

$$(\sigma^{(1)}, \mathbf{u}^{(1)}) \rightarrow \exp \int \lambda dx, \tag{17}$$

while the other is taken with a negative exponential,

$$(\sigma^{(2)}, \mathbf{u}^{(2)}) \rightarrow \exp \int -\lambda dx. \tag{18}$$

One is a backward traveling wave, exponentially increasing, while the other is a forward traveling wave, exponentially decreasing. For a conservative system, the condition (16) yields the same result for the transport condition as (14). For a dissipative system with fluid viscosity, we find little difference, since the wave number changes little. In addition, Equation (16) can be used for the case of feedback, when the system is no longer self-adjoint. In this case the second solution in (16) must be taken as a solution of the adjoint problem. Again we find little effect on the solutions for the cochlea, so (14) remains a good approximation.

3. Results and discussion

The cochlear model is used to calculate the response of a gerbil cochlea. The material property values in Table 1 were taken from [Smith 1968; Lim 1980; Steele et al. 1995; Karavitaki 2002], and the dimensions in Table 2 from anatomical measurements for the gerbil cochlea [Sokolich et al. 1976; Greenwood 1990; Dannhof et al. 1991; Cohen et al. 1992; Edge et al. 1998; Thorne et al. 1999; Naidu and Mountain 2007].

The model is meshed into 1200 sections along the 12 mm length of the cochlea. Forty terms are used in the Fourier expansion across the width of the fluid duct. Calculation with eighty terms for the Fourier expansion shows no difference with forty terms. Running on an Intel Pentium IX (3.40 GHz) processor, the average time taken for a single harmonic excitation calculation is about one second. This method provides a fast and efficient solution compared to a full-scale finite element model. Note that the computation time indicated by [Parthasarathi et al. 2000] is measured in hours of computing time for the linear solution for a single frequency.

The results include the BF-to-place map and the BM velocity frequency response. The modeling results for the gerbil cochlea are compared with recent *in vivo* experiment measurements in the cochlea.

scala fluid	basilar membrane	outer hair cell
$\rho_f = 1.0 \times 10^3 \text{ kg/m}^3$ $\mu = 0.7 \times 10^{-3} \text{ Pa s}$	$\rho_p = 1.0 \times 10^3 \text{ kg/m}^3$ $E_{11} = 1.0 \times 10^{-3} \text{ GPa}$ $E_{22} = 1.0 \text{ GPa}$ $E_{12} = 0.0 \text{ GPa}$ $\nu = 0.5$	$\theta_1 = 85^\circ$ $\theta_2 = 25^\circ$ $\alpha_1 = 0.14$ $\alpha_2 = 0.14$

Table 1. Gross properties in cochlear model.

x (mm)	b (mm)	h (mm)	f	L_2, L_3 (mm)	l_{OHC} (μm)
0		0.0210	0.030	1.000	25.0
1.5		0.0175		0.707	
2.9	0.162			0.387	
3.5		0.0131			
5.0				0.316	
5.9		0.0088			
7.2	0.190	0.0073		0.282	
8.4					
9.0		0.0055		0.316	
10.2	0.205	0.0044			
12.0		0.0031	0.007	0.245	65.0

Table 2. Property variations in gerbil cochlear model. Notation: b : width of plate; h : plate thickness; h_f : BM fluid thickness; L_2, L_3 : width and height of fluid chamber; l_{OHC} : length of outer hair cell length.

CF-to-place map. CF versus distance from the stapes along the gerbil cochlear (CF range: 0.3 kHz–50 kHz) is shown in Figure 3. The gerbil CF-to-place map [Sokolich et al. 1976; Greenwood 1990] was measured with cochlear-microphonic recording. The maps from the passive model and measurement are in excellent agreement (Figure 3).

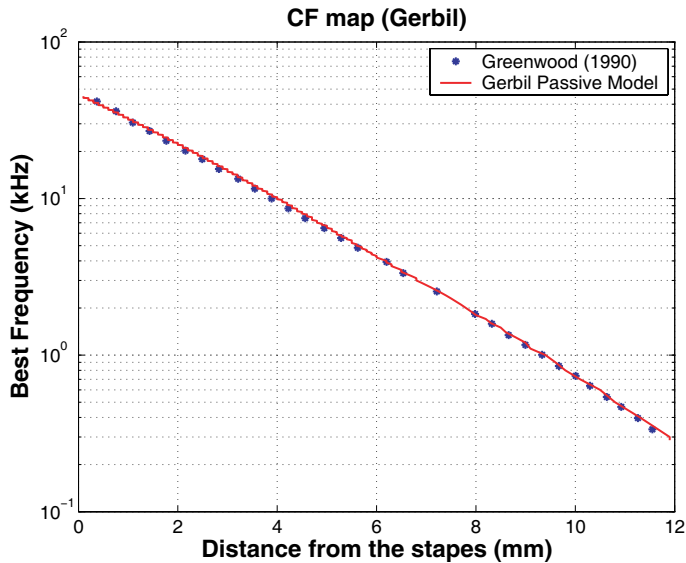


Figure 3. Characteristic frequency (CF) versus position for the passive cochlear model compared to measurements. The present three-dimensional cochlear model represents the gerbil cochlear CF-to-place map from 0.3 kHz to 50 kHz [Sokolich et al. 1976; Greenwood 1990] over a length of 12 mm.

BM velocity frequency response. The gerbil cochlear BM velocity magnitude and phase for 4.2 mm from the base (BF = 10 kHz) relative to the stapes displacement were computed up to 20 kHz and are compared with the gerbil experimental data from [Ren and Nuttall 2001] in Figure 4. The passive model shows quantitatively very good agreement with data which are measured at a high stimulus level (100 dB SPL at the ear canal).

Karavitaki [2002] gives the angle of tilt of gerbil OHC (θ_1) as 84° , closer to perpendicular to the BM (Figure 2). The active model results are calculated with parameters; $\theta_1 = 85^\circ$ (OHC angle), $\theta_2 = 25^\circ$ (phalangeal process angle), $\alpha_1 = \alpha_2 = 0.14$ (feedforward and feedback gain factor). The active model shows qualitatively and quantitatively good agreement with data at low stimulus level (30 dB SPL at the ear canal) with 27 dB gain.

In the left half of Figure 4, showing the magnitude of the relative BM velocity, the calculated BF place shifts from 10 kHz (passive model) to 13 kHz (active model), providing better agreement with measurements. The BF place shift (two fifths of an octave upwards) observed in the earlier feed-forward active model [Yoon et al. 2007] is resolved by using a push-pull mechanism in the active model. From the parameter study, we find that the BF place shifts to the low frequency by using a small phalangeal process angle in the active case.

The right half of Figure 4 shows that we obtain good agreement in the phase as well, at least in the region below the BF place (that is, up to 10 kHz). Reduced phase excursion is one of the most impressive improvements in the time-averaged Lagrangian model, compared to the 2.5 cycle phase difference near BF region in the earlier model. However, past the BF, the phase of BM velocity from the model shows a larger roll-off than the phase from the data, which represents over-fluctuation of the traveling wave after 10 kHz in the model.

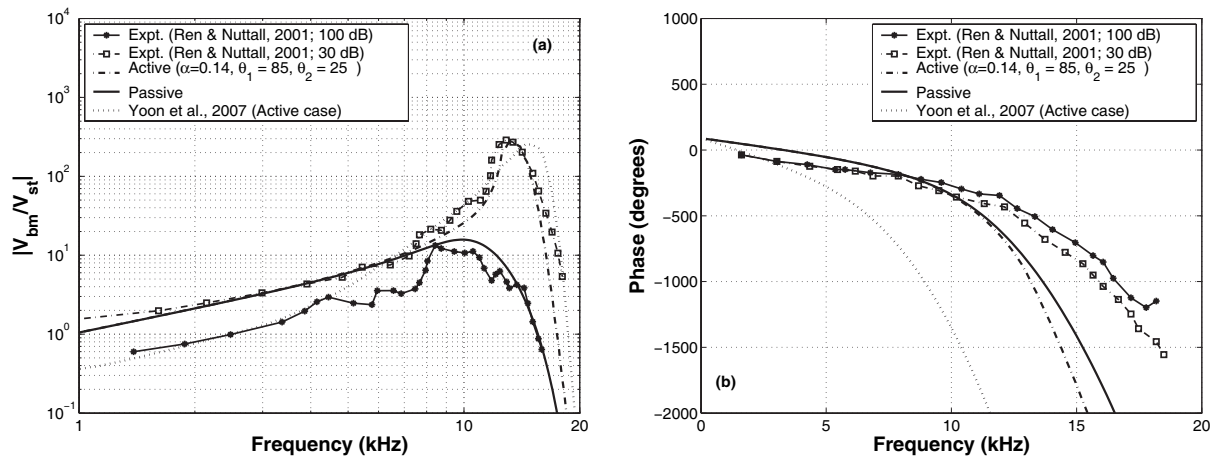


Figure 4. Basilar membrane (BM) velocity relative to the stapes: magnitude (left) and phase (right) for the gerbil cochlea at 4.2 mm from the base (BF = 10 kHz). For the active model, a value of 0.14 was used for the feed-forward and feedback gain factor. Experimental data from [Ren and Nuttall 2001] are included for comparison. Results from our earlier model [Yoon et al. 2007] are presented in dotted lines.

4. Conclusions

We presented a refinement of an earlier physiologically based three-dimensional cochlear model [Yoon et al. 2007] that resolved its two main deficiencies: a relatively large phase excursion near the best frequency region, which was addressed using the time-averaged Lagrangian method, and an overestimation of the best frequency (by about two fifths of an octave) observed in the earlier feed-forward active model, which was ameliorated by the implementation of a push-pull mechanism in the active case. Basilar membrane velocity simulation results for the gerbil cochlea now show excellent agreement in magnitude and good agreement in phase relative to physiological measurements. However, past the best frequency region, the phase in the current model still shows excessive roll-off. We hope that this can be addressed by incorporating into the model a more detailed treatment of the organ of Corti [Steele and Puria 2005].

List of symbols

BM	basilar membrane	L_2, L_3	width and height of fluid chamber
OHC	outer hair cell	α_1, α_2	feed-forward and feedback gain factors
BF	best frequency	l_{OHC}, l_p	length of OHC, length of phalangeal process
n	wave number	θ_1, θ_2	angle of tilt of OHC, phalangeal process
x, y, z	Cartesian coordinates	$F_{\text{PZ}}, F_{\text{BM}}^f$	forces acting on the pectinate zone and fluid
ω	angular velocity	F_{BM}^c	force exerted by OHC

References

- [Cohen et al. 1992] Y. E. Cohen, C. K. Bacon, and J. C. Saunders, “Middle ear development, III: Morphometric changes in the conducting apparatus of the Mongolian gerbil”, *Hearing Res.* **62**:2 (1992), 187–193.
- [Dannhof et al. 1991] B. J. Dannhof, B. Roth, and V. Bruns, “Length of hair cells as a measure of frequency representation in the mammalian inner ear”, *Naturwissenschaften* **78**:12 (1991), 570–573.
- [Edge et al. 1998] R. M. Edge, B. N. Evans, M. Pearce, R. C.-P., X. Hu, and P. S. Dallos, “Morphology of the unfixed cochlea”, *Hearing Res.* **124**:1–2 (1998), 1–16.
- [Geisler and Sang 1995] C. D. Geisler and C. Sang, “A cochlear model using feed-forward outer-hair-cell forces”, *Hearing Res.* **86**:1–2 (1995), 132–146.
- [Greenwood 1990] D. D. Greenwood, “A cochlear frequency-position function for several species: 29 years later”, *J. Acoust. Soc. Am.* **87**:6 (1990), 2592–2605.
- [Jimenez and Whitham 1976] J. Jimenez and G. B. Whitham, “An averaged Lagrangian method for dissipative wavetrains”, *Proc. R. Soc. Lond. A* **349**:1658 (1976), 277–287.
- [Karavitaki 2002] K. D. Karavitaki, *Measurements and models of electrically-evoked motion in the gerbil organ of Corti*, Ph.D. Thesis, MIT, 2002.
- [Lim 1980] D. J. Lim, “Cochlear anatomy related to cochlear micromechanics: a review”, *J. Acoust. Soc. Am.* **67**:5 (1980), 1686–1695.
- [Lim and Steele 2002] K.-M. Lim and C. R. Steele, “A three-dimensional nonlinear active cochlear model analyzed by the WKB-numeric method”, *Hearing Res.* **170**:1–2 (2002), 190–205.
- [Loh 1983] C. H. Loh, “Multiple scale analysis of the spirally coiled cochlea”, *J. Acoust. Soc. Am.* **74**:1 (1983), 95–103.
- [Naidu and Mountain 2007] R. C. Naidu and D. C. Mountain, “Basilar membrane tension calculations for the gerbil cochlea”, *J. Acoust. Soc. Am.* **121**:2 (2007), 994–1002.

- [Parthasarathi et al. 2000] A. A. Parthasarathi, K. Grosh, and A. L. Nuttall, “Three-dimensional numerical modeling for global cochlear dynamics”, *J. Acoust. Soc. Am.* **107**:1 (2000), 474–485.
- [Rabbitt 2008] R. Rabbitt, “Efficiency of outer hair cell somatic electromotility”, Poster session D9, Winter meeting (Phoenix, AZ) of the 31th Association for Research in Otolaryngology, 2008.
- [Ren and Nuttall 2001] T. Ren and A. L. Nuttall, “Basilar membrane vibration in the basal turn of the sensitive gerbil cochlea”, *Hearing Res.* **151**:1–2 (2001), 48–60.
- [Smith 1968] C. A. Smith, “Ultrastructure of the organ of Corti”, *Adv. Sci.* **24**:122 (1968), 419–433.
- [Sokolich et al. 1976] W. G. Sokolich, R. P. Hamernik, J. J. Zwislocki, and R. A. Schmiedt, “Inferred response polarities of cochlear hair cells”, *J. Acoust. Soc. Am.* **59**:4 (1976), 963–974.
- [Steele and Puria 2005] C. R. Steele and S. Puria, “Force on inner hair cell cilia”, *Int. J. Solids Struct.* **42** (2005), 5887–5904.
- [Steele and Taber 1979] C. R. Steele and L. A. Taber, “Comparison of WKB calculations and experimental results for three-dimensional cochlear models”, *J. Acoust. Soc. Am.* **65**:4 (1979), 1007–1018.
- [Steele and Zais 1985] C. R. Steele and J. G. Zais, “Effect of coiling in a cochlear model”, *J. Acoust. Soc. Am.* **77**:5 (1985), 1849–1852.
- [Steele et al. 1993] C. R. Steele, G. Baker, J. Tolomeo, and D. Zetes, “Electro-mechanical models of the outer hair cell”, pp. 207–215 in *Biophysics of hair cell sensory systems* (Paterswolde, 1993), edited by H. Duifhuis et al., World Scientific, Singapore, 1993.
- [Steele et al. 1995] C. R. Steele, G. Baker, J. Tolomeo, and D. Zetes, “Cochlear mechanics”, pp. 505–516 in *The biomedical engineering handbook*, edited by Z. D. Bronzino, CRC Press, Boca Raton, FL, 1995.
- [Thorne et al. 1999] M. Thorne, A. N. Salt, J. E. DeMott, M. M. Henson, O. W. Henson, Jr., and S. L. Gewalt, “Cochlear fluid space dimensions for six species derived from reconstructions of three-dimensional magnetic resonance images”, *Laryngoscope* **109**:10 (1999), 1661–1668.
- [Yoon et al. 2007] Y.-J. Yoon, S. Puria, and C. R. Steele, “Intracochlear pressure and derived quantities from a three-dimensional model”, *J. Acoust. Soc. Am.* **122**:2 (2007), 952–966.

Received 31 Jul 2008. Revised 16 May 2009. Accepted 17 May 2009.

YONGJIN YOON: yongjiny@stanford.edu

Stanford University, Mechanical Engineering, Durand Building, Room 262, Stanford, CA 94305, United States

SUNIL PURIA: puria@stanford.edu

Stanford University, Mechanical Engineering, Durand Building, Room 262, Stanford, CA 94305, United States

and

Stanford University, Otolaryngology — Head and Neck Surgery, Stanford, CA 94305, United States

CHARLES R. STEELE: chasst@stanford.edu

Stanford University, Mechanical Engineering, Durand Building, Room 262, Stanford, CA 94305, United States

SUBMISSION GUIDELINES

ORIGINALITY

Authors may submit manuscripts in PDF format on-line. Submission of a manuscript acknowledges that the manuscript is *original and has neither previously, nor simultaneously, in whole or in part, been submitted elsewhere*. Information regarding the preparation of manuscripts is provided below. Correspondence by email is requested for convenience and speed. For further information, consult the Web site at <http://www.jomms.org> or write to
jomms.steele@stanford.edu

LANGUAGE

Manuscripts must be in English. A brief abstract of about 150 words or less must be included. The abstract should be self-contained and not make any reference to the bibliography. Also required are keywords and subject classification for the article, and, for each author, postal address, affiliation (if appropriate), and email address if available. A home-page URL is optional.

FORMAT

Authors are encouraged to use L^AT_EX and the standard article class, but submissions in other varieties of T_EX, and, exceptionally in other formats, are acceptable. Electronic submissions are strongly encouraged in PDF format only; after the refereeing process we will ask you to submit all source material.

REFERENCES

Bibliographical references should be listed alphabetically at the end of the paper and include the title of the article. All references in the bibliography should be cited in the text. The use of B^IB_TE_X is preferred but not required. Tags will be converted to the house format (see a current issue for examples), however, in the manuscript, the citation should be by first author's last name and year of publication, e.g. "as shown by Kramer, et al. (1994)". Links will be provided to all literature with known web locations and authors are encouraged to provide their own links on top of the ones provided by the editorial process.

FIGURES

Figures prepared electronically should be submitted in Encapsulated PostScript (EPS) or in a form that can be converted to EPS, such as GnuPlot, Maple, or Mathematica. Many drawing tools such as Adobe Illustrator and Aldus FreeHand can produce EPS output. Figures containing bitmaps should be generated at the highest possible resolution. If there is doubt whether a particular figure is in an acceptable format, the authors should check with production by sending an email to:

production@mathscipub.org

Each figure should be captioned and numbered so that it can float. Small figures occupying no more than three lines of vertical space can be kept in the text ("the curve looks like this:"). It is acceptable to submit a manuscript with all figures at the end, if their placement is specified in the text by means of comments such as "Place Figure 1 here". The same considerations apply to tables.

WHITE SPACE

Forced line breaks or page breaks should not be inserted in the document. There is no point in your trying to optimize line and page breaks in the original manuscript. The manuscript will be reformatted to use the journal's preferred fonts and layout.

PROOFS

Page proofs will be made available to authors (or to the designated corresponding author) at a web site in PDF format. Failure to acknowledge the receipt of proofs or to return corrections within the requested deadline may cause publication to be postponed.

Journal of Mechanics of Materials and Structures

Volume 4, Nº 5 May 2009

Special issue

Tenth Pan American Congress of Applied Mechanics (PACAM X)

Preface	THOMAS ATTARD	779
Fractal elements	SAMER ADEEB and MARCELO EPSTEIN	781
Application and design of lead-core base isolation for reducing structural demands in short stiff and tall steel buildings and highway bridges subjected to near-field ground motions	THOMAS L. ATTARD and KITTINAN DHIRADHAMVIT	799
Homogenization and effective properties of periodic thermomagnetoelastic composites	JULIAN BRAVO-CASTILLERO, REINALDO RODRÍGUEZ-RAMOS, HOUARI MECHKOUR, JOSÉ A. OTERO, JOANKA HERNÁNDEZ CABANAS, LAZARO MAYKEL SIXTO, RAÚL GUINOVART-DÍAZ and FEDERICO J. SABINA	819
Deployment procedure for the Tetrahedron Constellation	PEDRO A. CAPÓ-LUGO and PETER M. BAINUM	837
Evolutionary control of structurally damaged steel buildings using an optimal state transition formulation	THOMAS L. ATTARD and ROBIN E. DANSBY	855
Effective elastic properties of nanotube reinforced composites with slightly weakened interfaces	MILTON ESTEVA and POL D. SPANOS	887
Continuum mechanics models of fractal porous media: Integral relations and extremum principles	MARTIN OSTOJA-STARZEWSKI	901
An endoscopic grasper with corrugated plate-shaped tactile sensors	MOHAMMAD AMEEN QASAIMEH, MOHAMMADREZA RAMEZANIFARD and JAVAD DARGAHI	913
A new earthquake-resistant concrete frame with fiber-reinforced plastic fabrics and shifted plastic hinges	M. SAID SAIDI, ERIK REINHARDT and FARAMARZ GORDANINEJAD	927
Nonlinear bending response of giant magnetostrictive laminated actuators in magnetic fields	YASUhide SHINDO, FUMIO NARITA, KOTARO MORI and TASUKU NAKAMURA	941
A dispersive nonlocal model for wave propagation in periodic composites	JUAN MIGUEL VIVAR-PÉREZ, ULRICH GABBERT, HARALD BERGER, REINALDO RODRÍGUEZ-RAMOS, JULIÁN BRAVO-CASTILLERO, RAÚL GUINOVART-DÍAZ and FEDERICO J. SABINA	951
A cochlear model using the time-averaged Lagrangian and the push-pull mechanism in the organ of Corti	YONGJIN YOON, SUNIL PURIA and CHARLES R. STEELE	977